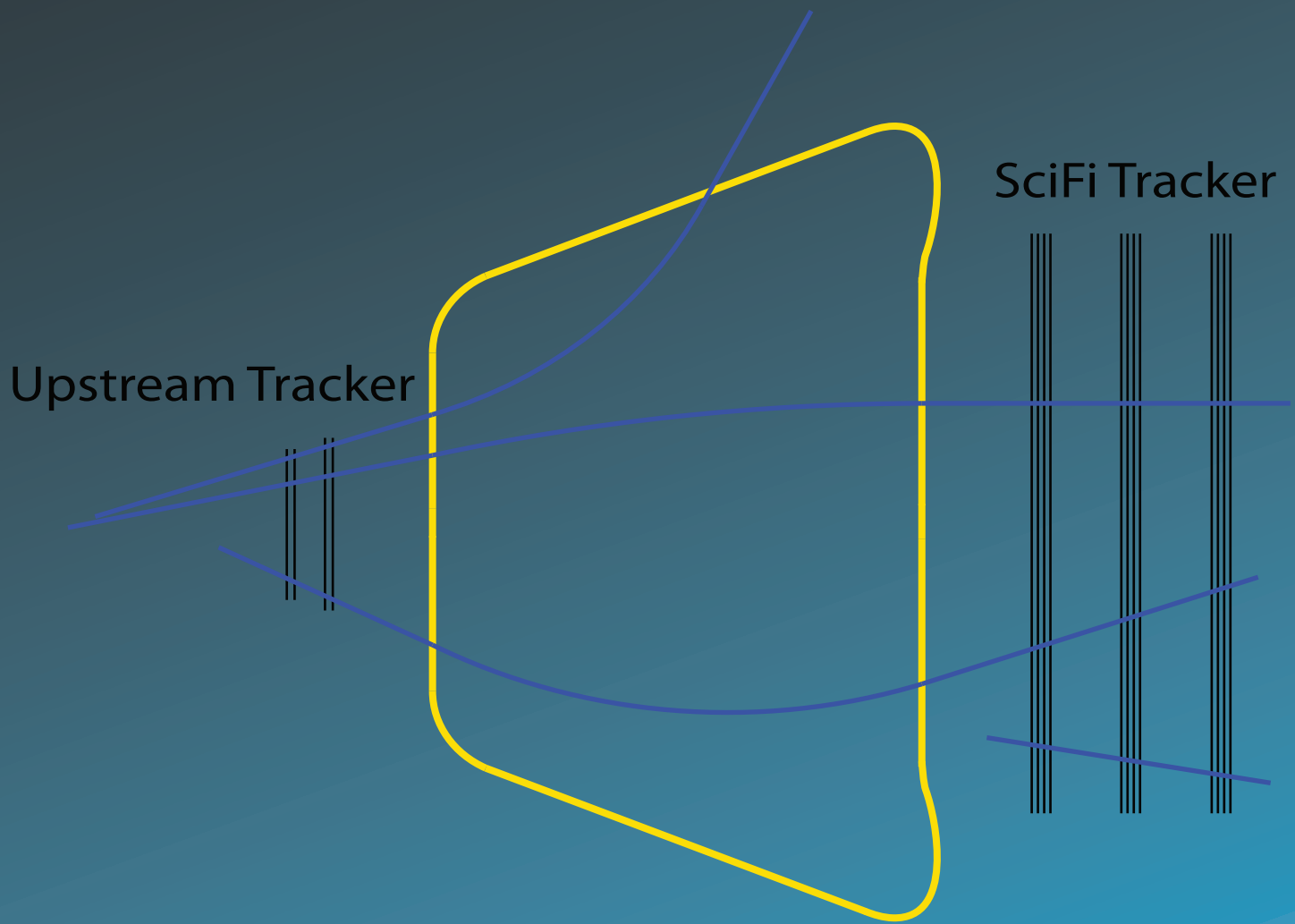


UPGRADE LHCb Tracker DR



Technical Design Report



CERN/LHCC 2014-001

LHCb TDR 15

21st February 2014

LHCb Tracker Upgrade Technical Design Report

The LHCb collaboration

Abstract

The upgrade of the LHCb detector will extend the physics reach of the experiment by allowing it to run at higher luminosity, $\mathcal{L}_{\text{inst}} = 2 \times 10^{33} \text{ cm}^{-2} \text{ s}^{-1}$, with increased trigger efficiency for a wide range of decay channels. This is facilitated by the implementation of new front-end electronics, designed such that complete events can be read out and sent to the LHCb data acquisition farm for selection by a full software trigger, every 25 ns. The upgraded LHCb detector is conceived to take physics data for an integrated luminosity of at least 50 fb^{-1} . This Technical Design Report describes in detail the upgrade of the two tracking subsystems, located just before and just after the LHCb dipole magnet. The tracking detector before the magnet (the Upstream Tracker) will be composed of new, high-granularity silicon micro-strip planes with an improved coverage of the LHCb acceptance. Behind the magnet, a Scintillating Fibre Tracker will be built, which is composed of 2.5 m long fibres read out by silicon photomultipliers at the edge of the acceptance. The performance of the two tracking detectors and of the LHCb tracking software are presented, as well as the cost, schedule and task sharing.

LHCb collaboration

A.A. Alves Jr⁴⁴, I. Bediaga, J.M. De Miranda, M. Féo Pereira Rivello Carvalho,
F. Ferreira Rodrigues, A. Gomes^a, A. Hicheur, A. Massafferri, I. Nasteva,
C. Pimenta Cheble Caplan, A.C. dos Reis, A.B. Rodrigues

¹*Centro Brasileiro de Pesquisas Físicas (CBPF), Rio de Janeiro, Brazil*

S. Amato, K. Carvalho Akiba, L. De Paula, O. Francisco, M. Gandelman, J.H. Lopes,
D. Martins Tostes, J.M. Otalora Goicochea, E. Polycarpo, M.S. Rangel,
V. Salustino Guimaraes, B. Souza De Paula, D. Szilard, D. Vieira

²*Universidade Federal do Rio de Janeiro (UFRJ), Rio de Janeiro, Brazil*

M. Cruz Torres, C. Göbel, J. Molina Rodriguez

³*Pontifícia Universidade Católica do Rio de Janeiro (PUC-Rio), Rio de Janeiro, Brazil*

Y. Gao, F. Jing, Y. Li, H. Lu, S. Wu, Z. Yang, X. Yuan, F. Zhang, Y. Zhang, L. Zhong

⁴*Center for High Energy Physics, Tsinghua University, Beijing, China*

Y. Xie

⁵*Institute of Particle Physics, Central China Normal University, Wuhan, Hubei, China*

D. Decamp, N. Déléage, Ph. Ghez, J.-P. Lees, M.-N. Minard, B. Pietrzyk, W. Qian,
S. T'Jampens, V. Tisserand, E. Tournefier⁶¹

⁶*LAPP, Université de Savoie, CNRS/IN2P3, Annecy-Le-Vieux, France*

Z. Ajaltouni, M. Baalouch, J. Bonnard, H. Chanal, E. Cogneras, O. Deschamps, I. El Rifai,
C. Gasq, M. Grabalosa Gándara, P. Henrard, M. Hoballah, R. Lefèvre, M. Magne, J. Maratas,
M.-L. Mercier, S. Monteil, V. Niess, P. Perret, N. Pillet, D.A. Roa Romero, R. Vandaele,
F. Yengui

⁷*Clermont Université, Université Blaise Pascal, CNRS/IN2P3, LPC, Clermont-Ferrand, France*

E. Aslanides, J. Cogan, W. Kanso, R. Le Gac, O. Leroy, G. Mancinelli, A. Mordà,
M. Perrin-Terrin, M. Sapunov, J. Serrano, A. Tsaregorodtsev

⁸*CPPM, Aix-Marseille Université, CNRS/IN2P3, Marseille, France*

Y. Amhis, S. Barsuk, M. Borsato, O. Callot, O. Kochebina, J. Lefrançois, F. Machefert,
A. Martín Sánchez, M. Nicol, P. Robbe, M.-H. Schune, M. Teklishyn, A. Vallier, B. Viaud,
G. Wormser

⁹*LAL, Université Paris-Sud, CNRS/IN2P3, Orsay, France*

E. Ben-Haim, M. Charles, S. Coquereau, P. David, L. Del Buono, J.-F. Genat, L. Henry,
O. Le Dortz, A. Martens, D.A. Milanes, F. Polci

¹⁰*LPNHE, Université Pierre et Marie Curie, Université Paris Diderot, CNRS/IN2P3, Paris,
France*

R. Greim, W. Karpinski, T. Kirn, S. Schael, T. Schateikis, A. Schultz von Dratzig,
G. Schwering, M. Wlochal

¹¹*I. Physikalisches Institut, RWTH Aachen University, Aachen, Germany*

J. Albrecht, T. Brambach, Ch. Cauet, M. Deckenhoff, M. Demmer, M. Domke, U. Eitschberger,

R. Ekelhof, L. Gavardi, P. Hebler, M. Kaballo, G. Kosian, S. Kralemann, F. Kruse, F. Meier, J. Müller, R. Niet, C.J. Parkinson, K. Rudloff, M. Schlupp, A. Shires, B. Spaan, S. Swientek, K. Warda, J. Wishahi

¹²*Fakultät Physik, Technische Universität Dortmund, Dortmund, Germany*

O. Aquines Gutierrez, J. Blouw, M. Britsch, M. Fontana, D. Popov, M. Schmelling, D. Volyansky, H. Voss, M. Zavertyaev^b

¹³*Max-Planck-Institut für Kernphysik (MPIK), Heidelberg, Germany*

A. Anjam, S. Bachmann, A. Bien, A. Comerma-Montells, M. De Cian, F. Dordei, S. Esen, C. Färber, E. Gersabeck, L. Grillo, X. Han, S. Hansmann-Menzemer, T. Herold, A. Jaeger, M. Kolpin, K. Kreplin, G. Krocker, B. Leverington, J. Marks, M. Meissner, M. Neuner, T. Nikodem, P. Seyfert, S. Stahl, U. Uwer, M. Vesterinen, S. Wandernoth, D. Wiedner, B. Windelband, A. Zhelezov

¹⁴*Physikalisches Institut, Ruprecht-Karls-Universität Heidelberg, Heidelberg, Germany*

O. Grünberg, T. Hartmann, M. Heß, C. Voß, R. Waldi

¹⁵*Institut für Physik, Universität Rostock, Rostock, Germany*

R. McNulty, R. Wallace, W.C. Zhang

¹⁶*School of Physics, University College Dublin, Dublin, Ireland*

A. Palano^c

¹⁷*Sezione INFN di Bari, Bari, Italy*

A. Carbone^d, D. Galli^d, U. Marconi, S. Perazzini^d, V. Vagnoni, G. Valenti, M. Zangoli

¹⁸*Sezione INFN di Bologna, Bologna, Italy*

W. Bonivento⁴⁴, S. Cadeddu, A. Cardini, A. Contu⁴⁴, A. Lai, B. Liu, G. Manca^e, R. Oldeman^e, B. Saitta^e

¹⁹*Sezione INFN di Cagliari, Cagliari, Italy*

M. Andreotti^f, W. Baldini, C. Bozzi, R. Calabrese^f, A. Falabella^f, M. Fiore^f, M. Fiorini^f, E. Luppi^f, M. Manzali^f, A. Mazurov^{44,f}, L. Pappalardo, M. Savrie^f, I. Shapoval^{51,f},

G. Tellarini^f, L. Tomassetti^f, S. Vecchi

²⁰*Sezione INFN di Ferrara, Ferrara, Italy*

L. Anderlini^g, A. Bizzetiⁱ, M. Frosini^{44,g}, G. Graziani, G. Passaleva, M. Veltri^h

²¹*Sezione INFN di Firenze, Firenze, Italy*

G. Bencivenni, P. Campana⁴⁴, P. De Simone, G. Lanfranchi, M. Palutan, M. Rama, A. Sarti, B. Sciascia, R. Vazquez Gomez

²²*Laboratori Nazionali dell'INFN di Frascati, Frascati, Italy*

R. Cardinale^j, F. Fontanelli^j, S. Gambetta^j, C. Patrignani^j, A. Petrolini^j, A. Pistone

²³*Sezione INFN di Genova, Genova, Italy*

M. Calvi^k, L. Cassina, C. Gotti, B. Khanji, M. Kucharczyk^{30,44,k}, C. Matteuzzi

²⁴*Sezione INFN di Milano Bicocca, Milano, Italy*

A. Abba^u, F. Caponio^u, M. Citterio, S. Coelli, A. Cusimano^u, J. Fu, A. Geraci^u, M. Lazzaroni^t,
M. Monti, N. Neri, F. Palombo^t

²⁵*Sezione INFN di Milano, Milano, Italy*

S. Amerio, G. Busetto^q, S. Gallorini, A. Gianelle, D. Lucchesi^q, M. Morandin, M. Rotondo,
G. Simi, R. Stroili

²⁶*Sezione INFN di Padova, Padova, Italy*

F. Bedeschi, S. Leo, P. Marino^s, M.J. Morello^s, G. Punzi^r, F. Ruffini, F. Spinella, S. Stracka⁴⁴

²⁷*Sezione INFN di Pisa, Pisa, Italy*

G. Carboni^l, E. Furfarol^l, E. Santovetti^l, A. Satta

²⁸*Sezione INFN di Roma Tor Vergata, Roma, Italy*

G. Auriemma^m, V. Bocci, G. Martellotti, D. Pinci, G. Sabatino^l, R. Santacesaria, C. Satriano^m,
A. Sciubba

²⁹*Sezione INFN di Roma La Sapienza, Roma, Italy*

P. Doroszⁿ, A. Dziurda, W. Kucewiczⁿ, T. Lesiak, P. Morawski, B. Rachwal, J. Wiechczynski,
M. Witek

³⁰*Henryk Niewodniczanski Institute of Nuclear Physics Polish Academy of Sciences, Kraków,
Poland*

M. Firlej, T. Fiutowski, M. Idzik, J. Moron, B. Muryn, A. Oblakowska-Mucha, K. Senderowska,
K. Swientek, T. Szumlak

³¹*AGH - University of Science and Technology, Faculty of Physics and Applied Computer
Science, Kraków, Poland*

V. Batozskaya, K. Kurek, M. Szczechowski, A. Ukleja, W. Wislicki

³²*National Center for Nuclear Research (NCBJ), Warsaw, Poland*

C. Coca, L. Giubega, A. Grecu, F. Maciuc, R. Muresan, M. Orlandea, C. Pavel-Nicorescu,
B. Popovici, S. Stoica, M. Straticiuc, E. Teodorescu

³³*Horia Hulubei National Institute of Physics and Nuclear Engineering, Bucharest-Magurele,
Romania*

G. Alkhazov, N. Bondar⁴⁴, A. Dzyuba, O. Maev, N. Sagidova, Y. Shcheglov, A. Vorobyev

³⁴*Petersburg Nuclear Physics Institute (PNPI), Gatchina, Russia*

V. Balagura, S. Belogurov, I. Belyaev, V. Egorychev, D. Golubkov, P. Gorbounov,
T. Kvaratskheliya, I.V. Machikhiliyan, D. Savrina³⁶, A. Semennikov, A. Zhokhov

³⁵*Institute of Theoretical and Experimental Physics (ITEP), Moscow, Russia*

A. Berezhnoy, M. Korolev, A. Leflat, N. Nikitin

³⁶*Institute of Nuclear Physics, Moscow State University (SINP MSU), Moscow, Russia*

S. Filippov, E. Gushchin, L. Kravchuk

³⁷*Institute for Nuclear Research of the Russian Academy of Sciences (INR RAN), Moscow,
Russia*

A. Gouskov, E. Korovaitseva, A. Malinin, V. Shevchenko, A. Ustyuzhanin

³⁸*National Research Centre Kurchatov Institute, Moscow, Russia*

A. Bondar, S. Eidelman, P. Krokovny, V. Kudryavtsev, L. Shekhtman, V. Vorobyev

³⁹*Budker Institute of Nuclear Physics (SB RAS) and Novosibirsk State University, Novosibirsk, Russia*

A. Artamonov, K. Belous, R. Dzhelyadin, Yu. Guz⁴⁴, A. Novoselov, V. Obraztsov, A. Popov, V. Romanovsky, M. Shapkin, O. Yushchenko

⁴⁰*Institute for High Energy Physics (IHEP), Protvino, Russia*

A. Badalov, M. Calvo Gomez^o, A. Camboni, L. Garrido, R. Graciani Diaz, E. Graugés, C. Marin Benito, A. Oyanguren, E. Picatoste Olloqui, C. Potterat, V. Rives Molina, H. Ruiz, P. Ruiz Valls, X. Vilasis-Cardona^o

⁴¹*Universitat de Barcelona, Barcelona, Spain*

B. Adeva, P. Alvarez Cartelle, A. Dosil Suárez, V. Fernandez Albor, A. Gallas Torreira, J.A. Hernando Morata, A. Pazos Alvarez, E. Perez Trigo, M. Plo Casasus, A. Romero Vidal, J.J. Saborido Silva, B. Sanmartin Sedes, C. Santamarina Rios, M. Seco, P. Vazquez Regueiro, C. Vázquez Sierra

⁴²*Universidad de Santiago de Compostela, Santiago de Compostela, Spain*

F. Martinez Vidal, J. Mazorra de Cos, C. Sanchez Mayordomo

⁴³*Instituto de Fisica Corpuscular (IFIC), Universitat de Valencia-CSIC, Valencia, Spain*

F. Alessio, F. Archilli, C. Barschel, J. C. Batista Lopes, J. Buytaert, D. Campora Perez, L. Castillo Garcia, M. Cattaneo, Ph. Charpentier, K. Ciba, X. Cid Vidal, M. Clemencic, J. Closier, V. Coco, P. Collins, G. Corti, B. Couturier, C. D'Ambrosio, E. Da Riva, G. Decreuse, A. Di Canto, H. Dijkstra, P. Durante, M. Ferro-Luzzi, C. Fitzpatrick, R. Forty, C. Fournier, M. Frank, C. Frei, C. Gaspar, V.V. Gligorov, H. Gordon, L.A. Granado Cardoso, T. Gys, C. Haen, J. He, T. Head, E. van Herwijnen, R. Jacobsson, O. Jamet, C. Joram, B. Jost, M. Karacson, T.M. Karbach, D. Lacarrere, E. Lanciotti, C. Langenbruch, B. Langhans, R. Lindner, C. Linn, G. Liu, S. Lohn, R. Matev, Z. Mathe, S. Neubert, N. Neufeld, J. Panman, M. Pepe Altarelli, N. Rauschmayr, M. Rihl, S. Roiser, L. Roy, T. Ruf, H. Schindler, B. Schmidt, T. Schneider, A. Schopper, R. Schwemmer, F. Stagni, V.K. Subbiah, F. Teubert, E. Thomas, D. Tonelli, M. Ubeda Garcia, J. Wicht, K. Wyllie, A. Zvyagin

⁴⁴*European Organization for Nuclear Research (CERN), Geneva, Switzerland*

A. Bay, F. Bernard, F. Blanc, J. Bressieux, M. Dorigo, F. Dupertuis, R. Frei, S. Giani', G. Haefeli, P. Jaton, C. Khurewathanakul, I. Komarov, V.N. La Thi, N. Lopez-March, R. Märki, B. Muster, T. Nakada, A.D. Nguyen, T.D. Nguyen, C. Nguyen-Mau^p, J. Prisciandaro, A. Puig Navarro, B. Rakotomiramanana, J. Rouvinet, O. Schneider, F. Soomro, P. Szczypka⁴⁴, M. Tobin, S. Tourneur, M.T. Tran, G. Veneziano

⁴⁵*Ecole Polytechnique Fédérale de Lausanne (EPFL), Lausanne, Switzerland*

J. Anderson, R. Bernet, E. Bowen, A. Bursche, N. Chiapolini, M. Chrzaszcz³⁰, Ch. Elsasser, F. Lionetto, P. Lowdon, K. Müller, S. Saornil Gamarra, N. Serra, O. Steinkamp, B. Storaci, U. Straumann, M. Tresch, A. Vollhardt

⁴⁶*Physik-Institut, Universität Zürich, Zürich, Switzerland*

R. Aaij, S. Ali, Th. Bauer, M. van Beuzekom, P.N.Y. David, K. De Bruyn, C. Farinelli, V. Heijne, W. Hulsbergen, E. Jans, P. Koppenburg⁴⁴, A. Kozlinskiy, J. van Leerdam, M. Martinelli, M. Merk, S. Oggero, A. Pellegrino, H. Snoek, P. Tsopelas, N. Tuning, J.A. de Vries

⁴⁷*Nikhef National Institute for Subatomic Physics, Amsterdam, The Netherlands*

J. van den Brand, F. Dettori, T. Ketel, R.F. Koopman, R.W. Lambert, D. Martinez Santos, G. Raven, M. Schiller, V. Syropoulos, J. van Tilburg, S. Tolk

⁴⁸*Nikhef National Institute for Subatomic Physics and VU University Amsterdam, Amsterdam, The Netherlands*

T.W. Hafkenscheid, G. Onderwater

⁴⁹*KVI - University of Groningen, Groningen, The Netherlands*

E. Pesen

⁵⁰*Celal Bayar University, Manisa, Turkey*

A. Dovbnya, S. Kandybei, I. Raniuk, O. Shevchenko

⁵¹*NSC Kharkiv Institute of Physics and Technology (NSC KIPT), Kharkiv, Ukraine*

O. Okhrimenko, V. Pugatch

⁵²*Institute for Nuclear Research of the National Academy of Sciences (KINR), Kyiv, Ukraine*

S. Bifani, P. Griffith, I.R. Kenyon, C. Lazzaroni, J. McCarthy, L. Pescatore, N.K. Watson

⁵³*University of Birmingham, Birmingham, United Kingdom*

M. Adinolfi, J. Benton, N.H. Brook, A. Cook, M. Coombes, J. Dalseno, T. Hampson, S.T. Harnew, P. Naik, C. Prouve, J.H. Rademacker, N. Skidmore, D. Souza, J.J. Velthuis, D. Voong

⁵⁴*H.H. Wills Physics Laboratory, University of Bristol, Bristol, United Kingdom*

W. Barter, M.-O. Bettler, H.V. Cliff, J. Garra Tico, V. Gibson, S. Gregson, S.C. Haines, C.R. Jones, M. Sirendi, J. Smith, D.R. Ward, S.A. Wotton, S. Wright

⁵⁵*Cavendish Laboratory, University of Cambridge, Cambridge, United Kingdom*

J.J. Back, T. Blake, D.C. Craik, D. Dossett, T. Gershon, M. Kreps, T. Latham, T. Pilař, A. Poluektov³⁹, M.M. Reid, R. Silva Coutinho, C. Wallace, M. Whitehead, M.P. Williams⁵⁷

⁵⁶*Department of Physics, University of Warwick, Coventry, United Kingdom*

S. Easo, R. Nandakumar, A. Papanestis⁴⁴, S. Ricciardi, F.F. Wilson

⁵⁷*STFC Rutherford Appleton Laboratory, Didcot, United Kingdom*

S. Benson, H. Carranza-Mejia, L. Carson, P.E.L. Clarke, G.A. Cowan, R. Currie, S. Eisenhardt, D. Ferguson, D. Lambert, H. Luo, F. Muheim, M. Needham, S. Playfer, A. Sparkes

⁵⁸*School of Physics and Astronomy, University of Edinburgh, Edinburgh, United Kingdom*

M. Alexander, J. Beddow, L. Eklund⁴⁴, D. Hynds, I. Longstaff, S. Ogilvy, M. Pappagallo, P. Sail, F.J.P. Soler, P. Spradlin

⁵⁹*School of Physics and Astronomy, University of Glasgow, Glasgow, United Kingdom*

A. Affolder, T.J.V. Bowcock, H. Brown, G. Casse, S. Donleavy, S. Farry, K. Hennessy, D. Hutchcroft, M. Liles, B. McSkelly, G.D. Patel, A. Pritchard, K. Rinnert, T. Shears, N.A. Smith

⁶⁰*Oliver Lodge Laboratory, University of Liverpool, Liverpool, United Kingdom*

G. Ciezarek, S. Cunliffe, U. Egede, A. Golutvin^{35,44}, S. Hall, M. McCann, P. Owen, M. Patel, K. Petridis, A. Richards, I. Sepp, E. Smith, W. Sutcliffe, D. Websdale

⁶¹*Imperial College London, London, United Kingdom*

R.B. Appleby, R.J. Barlow, T. Bird, P.M. Bjørnstad, S. Borghi, D. Brett, S. De Capua, M. Gersabeck, J. Harrison, C. Hombach, S. Klaver, G. Lafferty, A. McNab, D. Moran, C. Parkes, A. Pearce, S. Reichert, E. Rodrigues, P. Rodriguez Perez, M. Smith, A.D. Webber

⁶²*School of Physics and Astronomy, University of Manchester, Manchester, United Kingdom*

S.-F. Cheung, D. Derkach, R. Gauld, E. Greening, N. Harnew, D. Hill, P. Hunt, N. Hussain, M. John, D. Johnson, O. Lupton, S. Malde, A. Powell, E. Smith⁵⁷, S. Stevenson, C. Thomas, S. Topp-Joergensen, N. Torr, G. Wilkinson

⁶³*Department of Physics, University of Oxford, Oxford, United Kingdom*

I. Counts, P. Ilten, M. Williams

⁶⁴*Massachusetts Institute of Technology, Cambridge, MA, United States*

R. Andreassen, A. Davis, W. De Silva, B. Meadows⁶³, M.D. Sokoloff, L. Sun

⁶⁵*University of Cincinnati, Cincinnati, OH, United States*

J.E. Andrews, R. Cenci, B. Hamilton, A. Jawahery, T. O'Bannon, J. Wimberley

⁶⁶*University of Maryland, College Park, MD, United States*

M. Artuso, S. Blusk, A. Borgia, T. Britton, P. Gandini, J. Garofoli, B. Gui, C. Hadjivassiliou, N. Jurik, M. Kelsey, R. Mountain, B.K. Pal, T. Skwarnicki, S. Stone, J. Wang, Z. Xing, L. Zhang.

⁶⁷*Syracuse University, Syracuse, NY, United States*

^a*Universidade Federal do Triângulo Mineiro (UFTM), Uberaba-MG, Brazil*

^b*P.N. Lebedev Physical Institute, Russian Academy of Science (LPI RAS), Moscow, Russia*

^c*Università di Bari, Bari, Italy*

^d*Università di Bologna, Bologna, Italy*

^e*Università di Cagliari, Cagliari, Italy*

^f*Università di Ferrara, Ferrara, Italy*

^g*Università di Firenze, Firenze, Italy*

^h*Università di Urbino, Urbino, Italy*

ⁱ*Università di Modena e Reggio Emilia, Modena, Italy*

^j*Università di Genova, Genova, Italy*

^k*Università di Milano Bicocca, Milano, Italy*

^l*Università di Roma Tor Vergata, Roma, Italy*

^m*Università della Basilicata, Potenza, Italy*

ⁿ*AGH - University of Science and Technology, Faculty of Computer Science, Electronics and Telecommunications, Kraków, Poland*

^o*LIFAELS, La Salle, Universitat Ramon Llull, Barcelona, Spain*

^p*Hanoi University of Science, Hanoi, Viet Nam*

^q*Università di Padova, Padova, Italy*

^r*Università di Pisa, Pisa, Italy*

^s*Scuola Normale Superiore, Pisa, Italy*

^t*Università degli Studi di Milano, Milano, Italy*

^u*Politecnico di Milano, Milano, Italy*

Contents

1	Introduction	1
1.1	Overview	1
1.2	Evolution since the Framework TDR	4
2	The LHCb Upstream Tracker	6
2.1	Current System Overview	6
2.2	Requirements	8
2.2.1	Physics Performance Requirements	8
2.2.2	Irradiation Constraints	12
2.3	Geometry Overview	12
2.3.1	Geometry in the Simulation	13
2.3.2	Staves	15
2.3.3	Material Scan	17
2.4	Mechanics	17
2.4.1	Introduction	17
2.4.2	Stave Construction	18
2.4.3	Frame and Outer Box	19
2.4.4	Current and Planned R&D	20
2.5	Cooling	21
2.5.1	Requirements	21
2.5.2	Evaporative CO ₂ Cooling	22
2.5.3	Thermal Simulations and Prototype Test	23
2.5.4	Cooling System Architecture and Safety	26
2.6	Sensors and Hybrids	27
2.6.1	Silicon Sensors	27
2.6.2	Hybrids	30
2.7	The SALT ASIC	32
2.7.1	Analogue Front-end	33
2.7.2	SAR ADC	35
2.7.3	Digital Signal Processing Algorithms	38
2.7.4	Serialisation and Data Format	40
2.7.5	Control Interfaces	41
2.7.6	Ancillary Blocks – PLL, DLL, SLVS, DACs	41

2.7.7	Floor-plan and ASIC Integration	43
2.8	Electronics	44
2.8.1	Hybrid and Interconnect Cable	44
2.8.2	Periphery Electronics	47
2.8.3	System Power Distribution and Grounding Scheme	49
2.8.4	Interlock System	51
2.8.5	Prototyping	52
2.9	DAQ Integration	52
2.9.1	Data at ASICs	52
2.9.2	Data Process at DCB and AMC40	55
2.9.3	Timing and Slow Control	56
2.9.4	DAQ Slice Development	57
2.10	Integration and Testing	58
2.10.1	Quality Assurance Programme	58
2.10.2	Sensor Testing	59
2.10.3	Assembly of Read-out Hybrids	59
2.10.4	Stave Assembly	61
2.10.5	Radiation and Test Beam Studies	62
2.11	Project Organisation	62
2.11.1	Participating Institutes and Responsibilities	63
2.11.2	Schedule	64
2.11.3	Cost, Resources and Contingencies	67
2.11.4	Safety	68
3	The LHCb Scintillating Fibre Tracker	69
3.1	Introduction	69
3.2	Requirements	71
3.2.1	Detector Performance	71
3.2.2	Geometry Constraints	72
3.2.3	Radiation Environment	72
3.2.4	Cooling	74
3.3	Layout of the Scintillating Fibre Tracker	74
3.3.1	Geometry Description in Simulation	75
3.4	Scintillating Fibres	76
3.4.1	Properties	78
3.4.2	Radiation Tolerance of the Fibre	83
3.4.3	LHCb Radiation Damage Estimates	88
3.4.4	Summary	91
3.5	Silicon Photo-detectors	92
3.5.1	Signal Characteristics	92
3.5.2	Sensor Design and Packaging	93
3.5.3	Photon Detection Efficiency, Cross-talk, Gain, Temperature Uniformity and Signal Timing	95

3.5.4	Radiation Hardness and Measurement of Dark Current	98
3.5.5	Clusterisation	100
3.5.6	Cluster Amplitude and Size Distribution	101
3.5.7	Evaluation of Noise Cluster Rate	102
3.5.8	Hit Detection Efficiency and Spatial Resolution	102
3.5.9	Calibration of Gain	104
3.5.10	Summary	106
3.6	Module	106
3.6.1	Panels	108
3.6.2	Fibre Mats	111
3.6.3	Fibre-end Mirrors	115
3.6.4	Fibre Mat Performance	117
3.6.5	Read-out Box (ROB)	120
3.6.6	Summary of the Module Design	126
3.7	Electronics	128
3.7.1	Front-End Design	128
3.7.2	The PACIFIC ASIC	132
3.7.3	Data Processing	136
3.7.4	Back-end Processing	138
3.7.5	Voltage Distribution	139
3.7.6	Slow and Fast Control	140
3.8	Infrastructure	141
3.8.1	Support Structures and Module Frames	141
3.8.2	Cooling	142
3.9	Simulation Results	147
3.9.1	Material Description	147
3.9.2	Digitisation	147
3.9.3	Simulation of the Electronics	152
3.9.4	Data Format	152
3.9.5	Conclusion	152
3.10	Project Organisation	153
3.10.1	Tasks	153
3.10.2	Schedule	153
3.10.3	Costs	156
3.10.4	Operational Scenarios	156
3.10.5	Safety	158
4	Tracking Performance	159
4.1	Overview of the Tracking System	159
4.1.1	Track Types	159
4.1.2	Figures of Merit to Evaluate Tracking Performance	160
4.2	Pattern Recognition Algorithms and their Performance	164
4.2.1	VELO Tracking	165

4.2.2	Forward Tracking	165
4.2.3	Seeding	167
4.2.4	Track Matching	170
4.2.5	Adding UT hits to <i>long</i> tracks	172
4.2.6	Downstream Tracking	176
4.2.7	Upstream Tracking	177
4.3	Robustness Tests	180
4.3.1	Modified SciFi Tracker Performance	181
4.3.2	Modified UT Detector Performance	185
4.4	Conclusions	186
	Acknowledgements	188
	References	189

Chapter 1

Introduction

1.1 Overview

The LHCb detector [1], shown in Fig. 1.1, is a single-arm forward spectrometer covering the pseudorapidity range $2 < \eta < 5$, designed for the study of particles containing b or c quarks. The results from LHCb based on data collected during the LHC Run 1 have proved that measurements of excellent quality can be made in the heavy flavour sector in the extreme environment of high energy proton-proton collisions [2], and more results are expected from the LHC Run 2. Given that no physics phenomena beyond the Standard Model have emerged from Run 1, precision studies may become the only way to unravel new effects at the LHC. To maximise sensitivity, these studies must be performed at the highest possible LHC energy and luminosity that each LHC experiment can afford. The read-out and trigger scheme of the current LHCb detector limit the data rate that can be injected into the trigger farm, and therefore the precision that can be achieved. The upgrade of the LHCb detector [3], which will take place during the Long Shutdown 2 (LS2) from mid 2018 to the end of 2019, will extend significantly the physics reach of the experiment by allowing it to run at higher instantaneous luminosity with increased trigger efficiency for a wide range of decay channels. The sensitivity reach for a subset of key flavour physics observables that will be made possible by this upgrade has been recently updated in a dedicated report [4] on the basis of the latest LHCb upgrade developments and LHCb analysis results.

The LHCb upgrade relies on two major changes. Firstly, the full read-out of the front-end electronics, currently limited by a Level-0 trigger to 1 MHz, will be replaced with a 40 MHz trigger system. It will then be possible to feed complete events every 25 ns to the LHCb data acquisition farm and apply a full software trigger for every single bunch crossing. This change alone improves the trigger efficiency significantly for a broad range of LHCb physics channels. It requires the replacement of all front-end electronics which, for some subsystems, most notably the silicon tracking devices, implies that the sensitive elements of the detectors must also be replaced. Secondly, the upgraded LHCb detector will be designed to cope with an increase of the nominal operational luminosity by a factor five compared to the current detector. The LHC will collide protons at a centre-of-mass

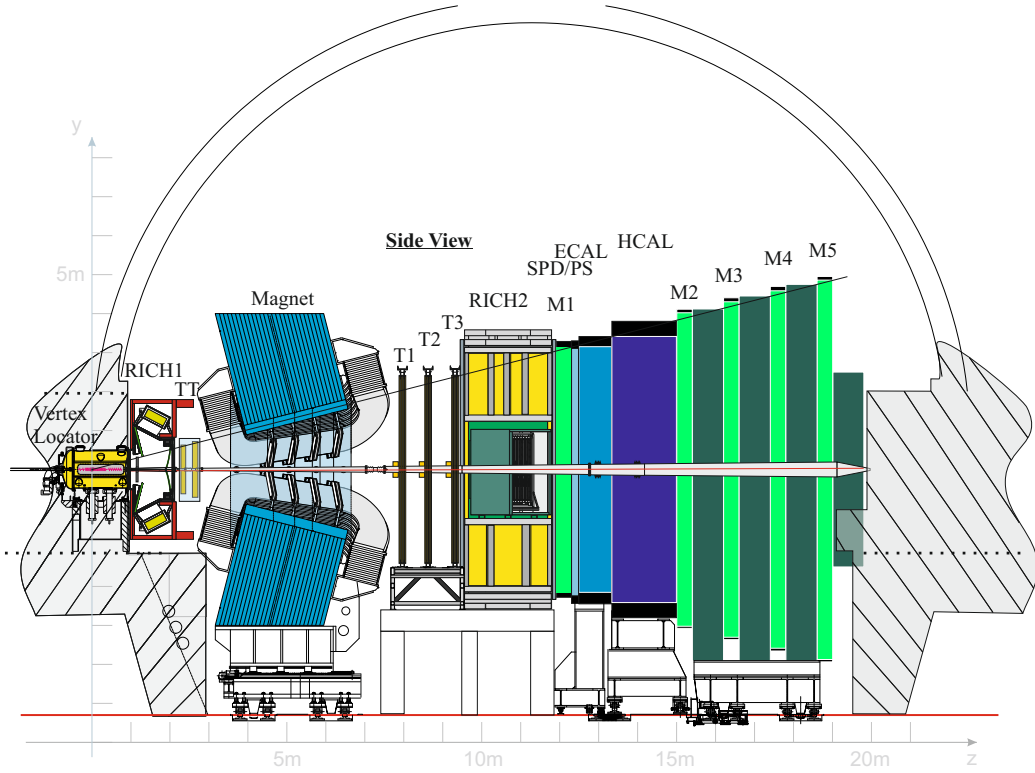


Figure 1.1: Schematic view of the current LHCb detector. RICH1, RICH2 = Ring Imaging Cherenkov detectors 1 and 2. TT = Tracker Turicensis. T1, T2, T3 = Tracking stations 1, 2 and 3. SPD/PS = Scintillating Pad Detector / Preshower. ECAL = Electromagnetic Calorimeter. HCAL = Hadron Calorimeter. M1, M2, M3, M4, M5 = Muon stations 1, 2, 3, 4, and 5.

energy $\sqrt{s} = 14$ TeV. The heavy flavour production cross-sections are expected to increase by almost a factor two compared to those at $\sqrt{s} = 8$ TeV. The instantaneous luminosity for the LHCb upgrade will be kept constant throughout a fill (levelled) at the nominal value $\mathcal{L}_{\text{inst}} = 2 \times 10^{33} \text{ cm}^{-2} \text{ s}^{-1}$. These conditions will be achieved with 25 ns separation between bunches and result in an average number of (visible) interactions¹ per bunch crossing $\nu = 7.6$ ($\mu = 5.2$). The experiment is designed to take data for an integrated luminosity of at least 50 fb^{-1} .

Figure 1.2 shows a side view of the LHCb upgrade detector. Compared to the current experiment several subsystems need to be partially rebuilt. Among these are the two

¹To minimise pile-up it is favourable to obtain the largest possible number of colliding bunch pairs, i.e. 2622 for LHCb in the nominal 25 ns filling scheme. There is too little experience with 25 ns bunch spacing in the LHC to predict what filling pattern will finally be used after LS2. To be on the safe side, 2400 colliding bunch pairs at Point 8 are assumed. In addition, a total (visible) cross section $\sigma_{\text{tot}} = 102.5 \text{ mb}$ ($\sigma_{\text{vis}} = 70.6 \text{ mb}$) is used.

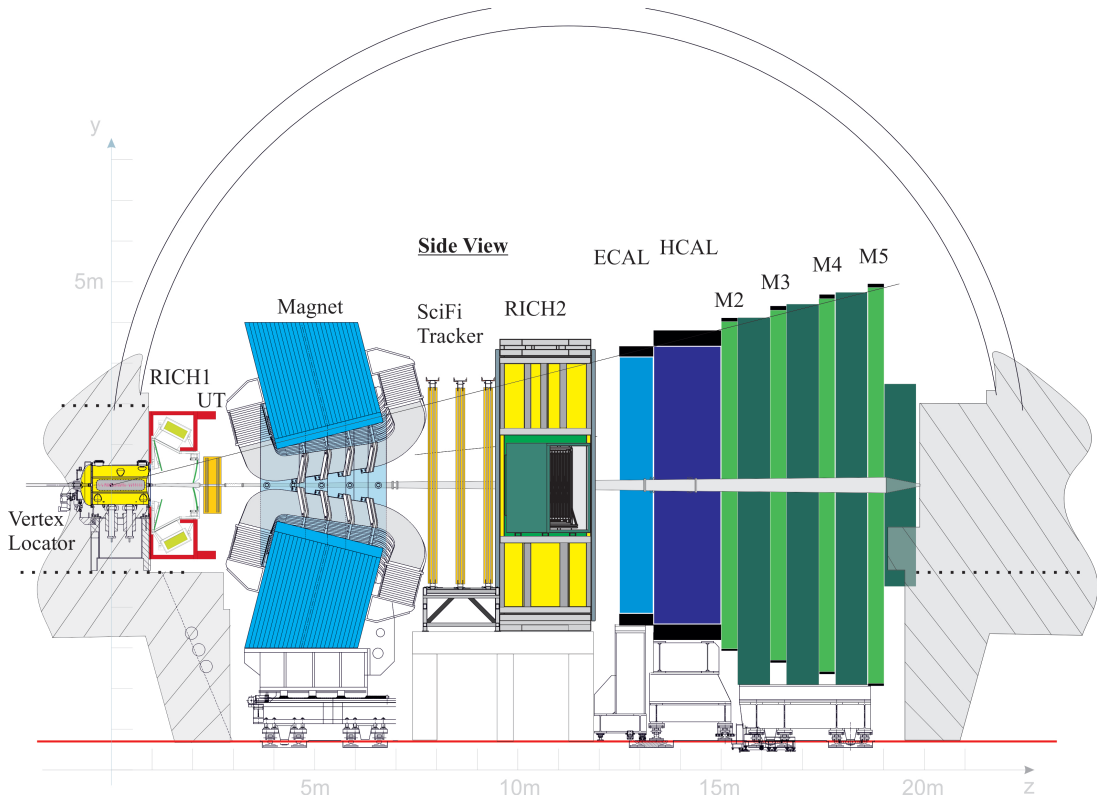


Figure 1.2: Schematic view of the LHCb upgrade detector. To be compared with Fig. 1.1. UT = Upstream Tracker. SciFi Tracker = Scintillating Fibre Tracker.

tracking subsystems, the Tracker Turicensis (TT) and the T-stations, located just before and just after the LHCb dipole magnet. These subsystems and their projected upgrade performance are the focus of this TDR. The four TT planes will be replaced by new high granularity silicon micro-strip planes with an improved coverage of the LHCb acceptance. The new system is called the Upstream Tracker (UT) and is the subject of Chap. 2. The current downstream tracker (T-stations) is composed of two detector technologies: a silicon micro-strip Inner Tracker (IT) in the high η region and a straw drift tube Outer Tracker (OT) in the low η region. The three OT/IT tracking stations will be replaced with a Scintillating Fibre Tracker (SFT), composed of 2.5 m long fibres read out by silicon photo-multipliers (SiPMs) outside the acceptance. The SFT is discussed in detail in Chap. 3. The performance of the UT and SFT detectors, as far as the individual detection planes are concerned, are addressed separately in their respective chapters, where also the cost, schedule and task sharing of these subsystems are presented. The charged particle tracking is an essential physics tool of the LHCb experiment. It must provide the basic track reconstruction, leading to a precise measurement of the charged particle momenta in the extreme environment of the LHCb upgrade over its entire lifetime. Therefore, the projected performance of the complete LHCb upgrade tracking system, which involves

both UT and SFT, has been thoroughly studied with an elaborate simulation package and is reported in Chap. 4.

1.2 Evolution since the Framework TDR

The details of the LHCb upgrade proposal and its evolution can be found in the Expression of Interest (EoI) [5], Letter of Intent (LoI) [6] and Framework Technical Design Report (Framework TDR) [3]. At the time of the Framework TDR, two replacement options for the LHCb tracker were being considered: a large area silicon-strip IT, requiring new (shorter) OT straw tube modules for the central region, or a Central Tracker (CT) made from scintillating fibres and complemented by OT straw tube modules on the sides. The CT option introduced the concept of 2.5 m long fibre modules which extend the active area of scintillating fibres to the detector periphery. The two options described in the Framework TDR required the development of new front-end electronics for the OT straw tube modules. The OT electronics architecture was developed at a relatively early stage (see a first description in the LoI [6]) and was reviewed in March 2013 [7].

Until 2013, the viability of the scintillating fibre option was not firmly established, mainly because of remaining uncertainties with regard to its performance in a high radiation environment. For this reason, it was felt that a fall-back solution based on established technologies was required, and R&D for the large area IT option was therefore pursued. The proposed IT/OT detector upgrade was implemented in the LHCb simulation framework. Based on simulation studies the OT occupancies were shown to be acceptable [8] up to the nominal LHCb upgrade conditions ($\sqrt{s} = 14$ TeV, $\mathcal{L}_{\text{inst}} = 2 \times 10^{33} \text{ cm}^{-2} \text{ s}^{-1}$). A prototype mock-up ladder for the enlarged IT was constructed and its vibrational properties studied [9]. The cooling strategy was investigated with a mock-up system and shown to work [10]. The signal-to-noise ratio of a three sensor ladder with a 15 cm long read-out cable was measured and found sufficient for the LHCb upgrade [11]. In brief, these recent simulation studies and laboratory tests demonstrated that the OT/IT option, with further developments, could be used for the LHCb upgrade as the fall-back solution.

Much progress was also made for the scintillating fibre option. The performance of the fibres and SiPMs was measured for radiation doses comparable to the dose expected in the LHCb upgrade. A review was held in February 2013 [12] to assess the viability of the fibre option, and it was concluded that the average number of detected photons for a fully irradiated detector (50 fb^{-1}) would be sufficient to qualify this technology for the LHCb upgrade tracker. Moreover, in the course of 2013, new SiPMs from two manufacturers were received which showed an improved performance with reduced cross-talk and higher quantum detection efficiency. This further strengthened the collaboration’s confidence in the SFT option. In the mean time, 2.5 m long fibre mats were produced with an acceptable geometric quality. The 5 m module design was further developed. The cooling strategy was reviewed and better defined. All these aspects led the collaboration to choose the fibre tracker option. A second review was held in November 2013 which validated this technological choice [13].

In parallel to the technical R&D, the collaboration has also considered the optimisation of the overall tracker layout, which meant re-optimising the positions of the individual tracking stations, the stereo angle, as well as their acceptance coverage. Detailed reconstruction algorithms were developed which fulfil the requirements from the trigger and physics analysis, in particular the challenging request to minimise processing time in the LHCb data acquisition farm. Based on these developments, the collaboration has reached the conclusion that the solution with fibre modules covering the entire LHCb acceptance is the best choice. Apart from simplifying track reconstruction, this single technology choice also removes the need for new OT electronics and considerably eases the mechanical integration challenges and the maintenance and operation of the detector after LS2. Chapter 3 describes the Scintillating Fibre Tracker in detail.

Chapter 2

The LHCb Upstream Tracker

2.1 Current System Overview

The Tracker Turicensis (TT), which is currently installed at the foreseen location of the UT in between RICH1 and the LHCb spectrometer magnet, has been described in Ref. [1]. It consists of four planar detection layers and employs 500 μm thick p⁺-in-n silicon sensors carrying 512 read-out strips with a length of about 10 cm and a strip pitch of 183 μm . The detection layers are composed of detector modules that are fourteen sensors long and span the full height of the detector acceptance, covering an area of approximately $1.5 \times 1.3 \text{ m}^2$ divided into top and bottom sections. The first and the last detection layer have vertical read-out strips, whereas the modules in the second and third detection layers are rotated by a stereo angle of +5° and -5°, respectively. To aid track reconstruction algorithms, the four detection layers are arranged in two pairs that are separated by approximately 27 cm along the LHC beam axis.

To reduce the cost of read-out electronics, the read-out strips of up to four consecutive silicon sensors on a detector module are bonded together to form effective strip lengths of approximately 10, 20, 30 or 40 cm. Following the distribution of charged particles, which falls off steeply with increasing distance from the beam axis, short strips are employed in the innermost region of each detection layer, just around the beam-pipe, while the longest strip lengths are employed in the regions farthest from the beam. With the chosen grouping, strip occupancies do not exceed a few percent at the current LHCb operating conditions. The read-out uses Beetle front-end chips [14] that are mounted on read-out hybrids at the upper and lower ends of the detector modules, outside the LHCb acceptance. Read-out strips in the inner parts of the detector modules are connected to their Beetle chips via flat Kapton interconnect cables that run along the detector module. This design was chosen since having the read-out hybrids outside of the acceptance removes all constraints on material budget and simplifies the design of the cooling.

The heat generated in the Beetle chips is removed by liquid C₆F₁₄ that is circulated at a temperature of 0°C through aluminium cooling plates, which are located above and below the sensitive area and onto which the detector modules are mounted. The cooling plates with the four detection layers are contained inside a common detector box, which

is light tight and provides thermal and electrical insulation to the ambient. The cooling plates, together with additional cooling elements to the left and right of the active region of the detector, also serve to keep the temperature inside the TT detector box below 8°C to reduce sensor leakage currents after irradiation to an acceptable level. No active cooling of the silicon sensors is required at the fluences that are expected to be accumulated in the TT. The detector box is flushed with nitrogen to avoid condensation on cold surfaces.

For the installation and maintenance of detector modules, as well as for bake-outs of the LHC beam-pipe, the detector box consists of two halves that are mounted on precision rails and can be retracted horizontally. One constraint for the design of the TT detector box was to keep a clearance of at least 5 mm to the LHC beam-pipe. This requirement limits the acceptance of the detector in the forward region. Moreover, to close the detector box in the region around the beam-pipe, a complicated insert consisting of two half cylinders had to be introduced. Despite being made of light-weight materials and designed to be as thin as possible, this insert contributes significantly to the dead material seen by particles at small polar angles, since it is crossed by these particles under a shallow angle.

The TT has performed very well during LHC Run 1. At the end of the run, 99.4% of all read-out channels were fully operational, a single hit efficiency of 99.7% and a single hit spatial resolution, including residual effects from imperfect alignment, of 61 μm were measured. The TT plays an important role for the reconstruction of K_S^0 mesons that decay outside of the acceptance of the VELO while adding TT hits to tracks reconstructed in the VELO and the downstream stations improves their momentum resolution by about 20%. Studies to use TT information in the HLT tracking algorithms are underway and yield promising results.

Studies of radiation damage are underway, making use of the evolution of measured leakage currents and full depletion voltages for the silicon sensors closest to the beam-pipe. Preliminary results show good agreement with expectations from a FLUKA [15, 16] simulation and established models of bulk damage (see Fig. 2.1).

However, despite its excellent performance, the current TT has to be replaced for the LHCb upgrade:

- The employed silicon sensors were not designed to be sufficiently radiation hard to survive the expected radiation damage, in particular in the inner region of the detector.
- The current read-out strip geometries will lead to unacceptably high occupancies under the foreseen running conditions.
- The Beetle chip is not compatible with the foreseen 40 MHz read-out, while the front-end hybrids carrying the Beetle chips form an integral part of the mechanical structure of the detector modules and cannot be replaced without damaging the module.

Furthermore, based on the positive experience from LHC Run 1 operation, requirements regarding the clearance to the LHC beam-pipe have been relaxed. This will make it

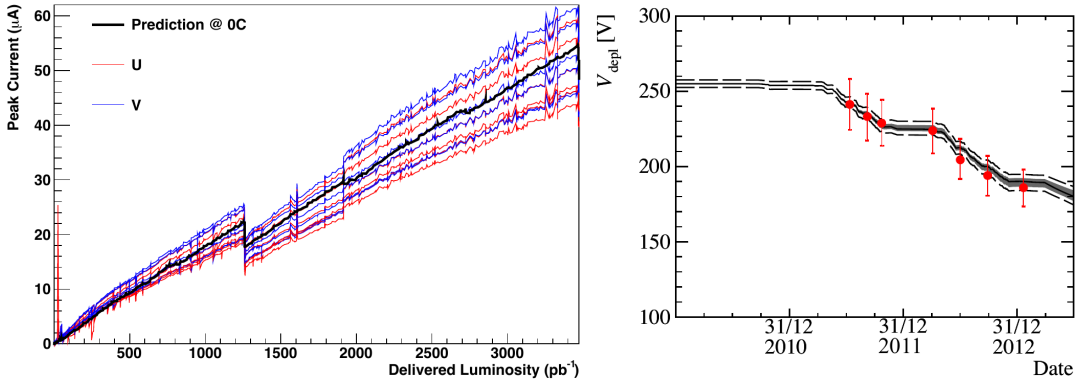


Figure 2.1: Estimation of radiation damage in TT: (left) Measured leakage currents in the innermost silicon sensors of two detection layers, normalised to 0°C and compared to expectations from a FLUKA simulation of the fluence. The jump in leakage currents at an integrated luminosity of about 1250 pb^{-1} corresponds to the annealing during the winter shutdown 2011/2012. (right) Measured effective depletion voltage in the innermost region of the sensors closest to the beam-pipe, compared to a prediction based on the full Hamburg model [17] and the actual running conditions of LHCb (both plots from [18]).

possible to significantly improve the forward acceptance of the detector and reduce the material budget in the very forward region.

2.2 Requirements

The design of the upgrade UT satisfies a set of performance requirements, that must be met throughout the detector operation, currently assumed to correspond to an integrated luminosity of at least 50 fb^{-1} . Thus, the evolution of the performance after considerable irradiation of the innermost components of this system need to be considered. Specific requirements are listed in individual sections of this report.

2.2.1 Physics Performance Requirements

The TT is a crucial element in track reconstruction. The reconstruction of $K_S^0 \rightarrow \pi^+\pi^-$ and $\Lambda \rightarrow p\pi^-$ is especially important as the majority decay after the VELO. In this case the decay tracks are reconstructed using the TT hits and the downstream tracker. An example is provided in Fig. 2.2 that shows the number of $\bar{B}^0 \rightarrow J/\psi K_S^0$ event candidates reconstructed using VELO and separately TT without VELO. Most of the events, 73%, are reconstructed from decays downstream of the VELO using the TT and the downstream tracker.

Adding TT hits to tracks also significantly improves the momentum resolution. Figure 2.3 (left) shows the invariant mass of di-muon pairs in the Υ mass region. The resolution is significantly improved, by $\sim 25\%$, if the tracks have TT hits as shown in Fig. 2.3 (right). Furthermore, the signal purity is improved appreciably if we require

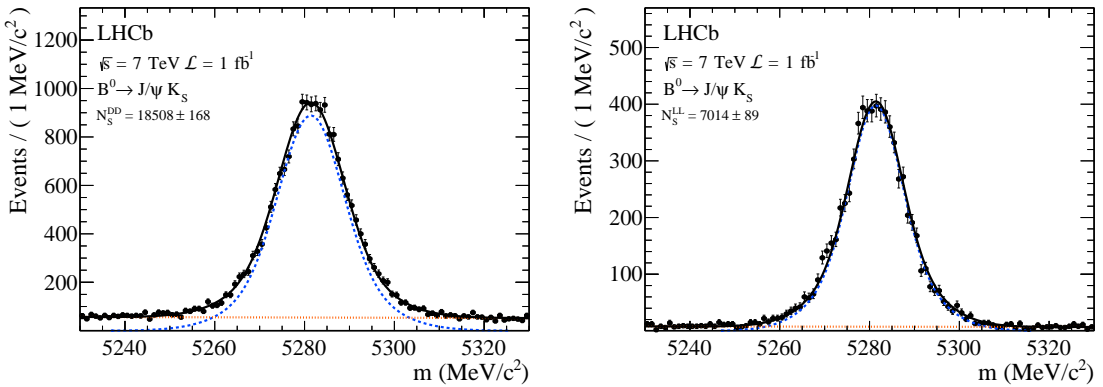


Figure 2.2: (left) The invariant $J/\psi K_S^0$ mass for candidates reconstructed using only the TT and downstream tracker, and (right) using the VELO and the downstream tracker, including TT hits if they exist. The red dotted lines show the background, the blue dashed lines the signal and the solid black lines the total.

at least three TT hits out of a possible four on the tracks. For example, in the decay $\bar{B}_s^0 \rightarrow D_s^+ \pi^+ \pi^- \pi^-$, with $D_s^+ \rightarrow K^+ K^- \pi^+$, the background/signal ratio is reduced from 12.2% to 8.4% when TT hits on all six final state tracks are required, and in the decay $B^- \rightarrow J/\psi \pi^+ \pi^- K^-$, $J/\psi \rightarrow \mu^+ \mu^-$, the background to signal ratio is reduced from 29% to 17% even though in this case we require TT hits only on the three hadrons. Currently, TT hits cannot be required for all tracks in the acceptance as this would result in a too low efficiency. It is one of the aims of the UT design to eliminate this inefficiency.

Tracks in LHCb have long segments in the VELO and the downstream tracker. It is possible however to mismatch these segments, that are 7 metres apart, and create false

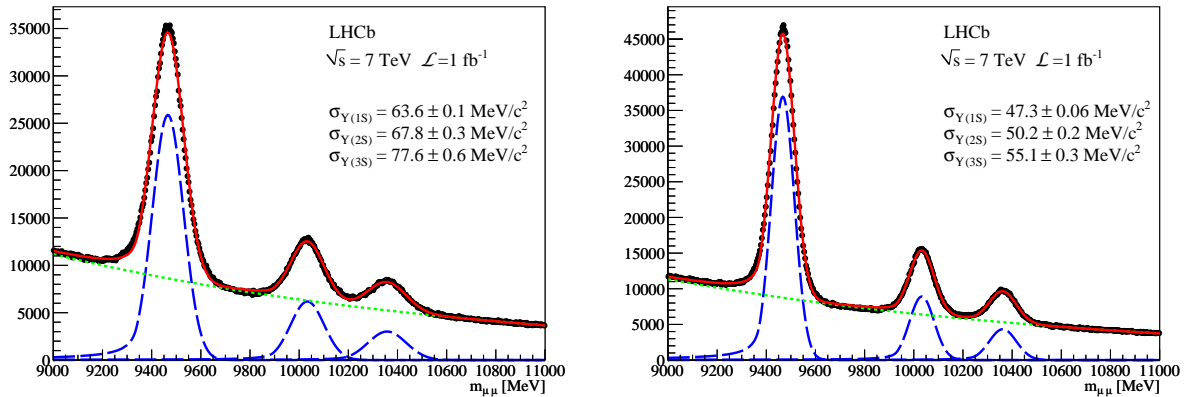


Figure 2.3: The invariant $\mu^+ \mu^-$ mass for candidates reconstructed (left) without TT hits and (right) candidates with both tracks having TT hits. The (green) dotted line shows the background, the (blue) dashed line the signals and the solid curves the sum. The σ 's are the r.m.s. widths of the signal Gaussians.

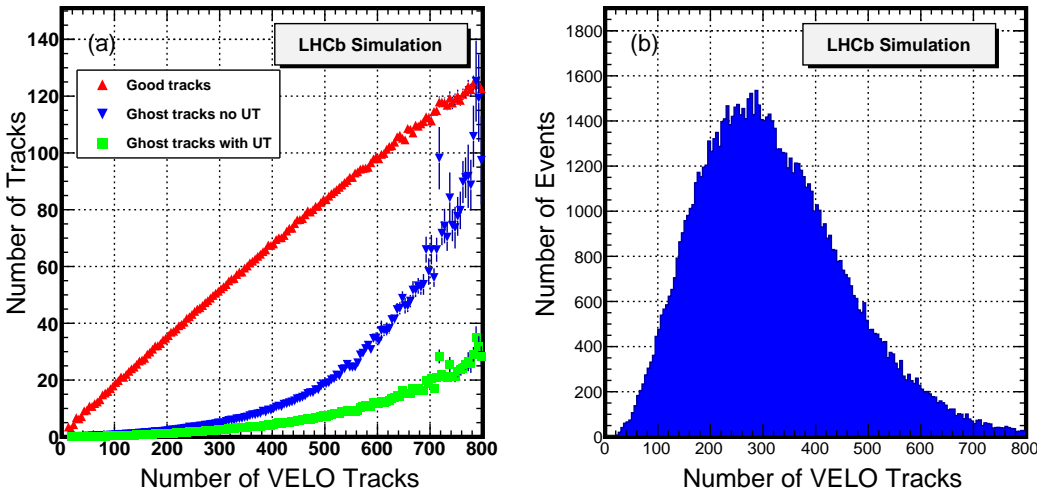


Figure 2.4: (left) Simulation of the number of real reconstructed downstream tracks and ghost tracks as a function of the number of VELO tracks at a luminosity of $2 \times 10^{33} \text{ cm}^{-2} \text{s}^{-1}$. The generated sample consists of events containing inclusive b -hadron decays at 14 TeV centre-of-mass energy. The ghosts are in two categories, one not requiring, and the other requiring a UT track match. (right) The distribution of VELO tracks.

tracks if the TT is not used. Requiring that the extrapolated hit positions at the TT match real hits reduces these track “ghosts” substantially. The ghost rate is a strong function of the track multiplicity. We chose to show this as a function of the number of tracks in the VELO. Figure 2.4 shows a simulation, using the upgrade geometry, of the number of good tracks, and ghost tracks both with and without the UT match requirement as a function of the number of VELO tracks. Here we require that hits in at least three out of four stations match the reconstructed track projections in the UT. Then for ~ 240 VELO tracks, the average multiplicity expected at a luminosity of $2 \times 10^{33} \text{ cm}^{-2} \text{s}^{-1}$, the ghost rate is reduced by about a factor of three. This reduction is important in speeding up trigger timings as well as for reducing backgrounds in all physics analyses.

To be used in the upgrade the electronics needs to be changed to be 40 MHz read out compatible, and the inner region of detectors needs to be made radiation hard, which can only be done by replacing the entire system. There are also gaps in the current geometry caused by (i) non-overlapping sensors, (ii) displacement of the top and bottom detector halves and (iii) the beam pipe plus clearance. It is our intention to eliminate gaps (i) and (ii) entirely and reduce (iii) as much as possible by significantly reducing the insulating material, and the clearance. These improvements will ensure that a track that is projected to the active UT area, outside of the beam pipe region, will have a signal. Taking three hits from the four layers as a requirement, the efficiency should be $>99.7\%$, for a 98% single hit efficiency. Our baseline requirement, however, is a 99% single hit efficiency, which we think is achievable. The improved acceptance will have several advantages: it will improve the K_S^0 and Λ reconstruction efficiency, the ghost track rejection, and will

allow the UT to be used as a crucial element in the upgrade trigger. As this is the critical element for the entire upgrade, we discuss it further.

In the software trigger one necessary element is to match track segments that do not project to the primary vertex in the Velo with downstream track segments in order to determine their momenta. Currently, all Velo tracks are projected, including ones that are outside of the downstream tracker acceptance, and low momentum tracks that have large multiple scattering, and thus are likely to appear not to come from the primary vertex, even if they do. To suppress these slow tracks, a momentum measurement is needed.

Currently, the momentum is determined by projecting all Velo tracks through the detector and matching to the downstream tracker. This is very expensive in computer time since all values of the momentum must be considered. Some time is saved by requiring tracks to have hits in the UT, since these tracks are all in the acceptance. It is also possible to use the stray magnetic field of about 0.02 T between the Velo and the UT to measure the track momentum much faster. Figure 2.5 shows the momentum resolution obtainable for the TT and the UT. Transverse momentum (p_T) resolutions, $\sigma p_T / p_T$, of $\approx 15\%$ are achieved, which is good enough to measure the sign of the charge, and exclude large multiple scattering tracks with $p_T < 400$ MeV. Knowing the sign of the charge means that only one charge is considered and not two. These changes decrease the time required by the forward tracking algorithm by about a factor of three. Due to ghost rate and inefficiencies

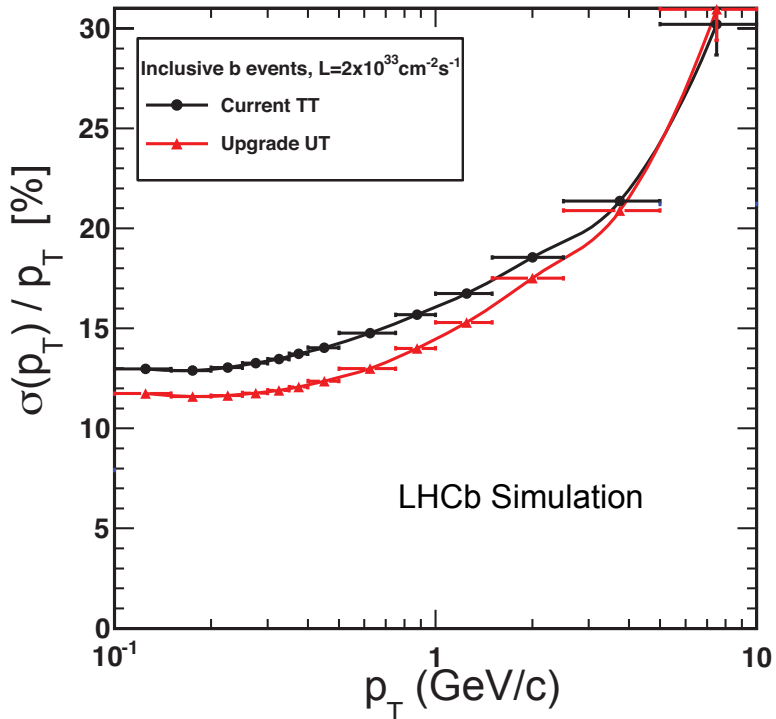


Figure 2.5: Resolution in p_T as a function of p_T in the current TT shown with (black) circles, the expected performance of the upgraded UT shown in (red) triangles.

in the VELO-TT pattern recognition in the current detector we do not presently use this method. It is an important goal of the upgrade design to make this feasible.

2.2.2 Irradiation Constraints

The current TT is designed to withstand an integrated luminosity of about 10 fb^{-1} . The UT detector needs to maintain its performance with an integrated luminosity at least a factor of five higher. The expected radiation dose in the upgrade is shown in Fig. 2.6 for a detector station slice at $x = 0$.

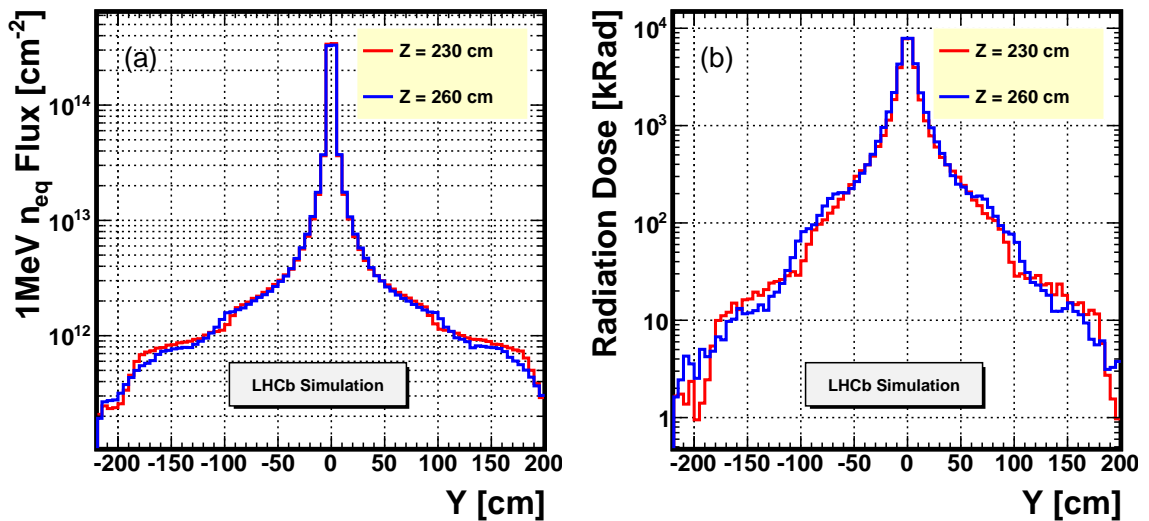


Figure 2.6: Expected fluence profile (left) and dose profile (right) after 50 fb^{-1} of total integrated luminosity as a function of the vertical coordinate Y for $X=0$. (The LHCb coordinate system is a right handed Cartesian system with the positive Z -axis aligned with the beam line and pointing away from the interaction point and the positive X -axis following the ground of the experimental area, and pointing towards the outside of the LHC ring.) This slice represents the highest fluence region throughout the UT system.

These studies imply that all the components in the region near the beam pipe need to be irradiated up to 40 MRad to validate their ability to sustain performance; this includes a safety factor of four. In addition, the electronics located near the detector box needs to be checked with a radiation level of the order of 100 kRad.

2.3 Geometry Overview

The UT detector is a replacement for the TT. It has four planes of silicon strips, same as in the TT, but with thinner sensors, finer segmentation and larger coverage. Signals are processed at the sensor rather than being taken out on long cables, allowing the system

to have lower electronic noise. The magnetic field bends tracks in the horizontal plane (X). Therefore, in order to measure track momentum, the strips run vertically in the Y direction. The middle two planes labelled U and V are at $\pm 5^\circ$ angles to the vertical in order to provide stereo measurements, allowing the Y coordinate also to be determined.

Each plane consists of staves staggered in Z to provide overlaps between adjacent staves in the X direction. Each stave supports silicon sensors about $10\text{ cm} \times 10\text{ cm}$ in size. These sensors are mounted on both faces of the stave alternatively, allowing for overlaps in the Y direction. The staggering in Z and X provides full detection coverage of the solid angle subtended by the UT.

Since the beam-pipe runs through the centre of the detector each plane has a hole in the centre. The UT planes have circular cut outs which provides better acceptance on tracks than square holes with the same allowed size. Reduction in material is also accomplished by having a thermal insulation layer surrounding the beam-pipe that is much thinner than that in the current system, and seals directly to the beam-pipe at the front and back faces.

The geometry configuration and material are optimised for best performance based on simulations. Such optimisation's will continue along with development of various components. The current configuration in the simulation and the material budget are explained in the following.

2.3.1 Geometry in the Simulation

The available space for the UT detector is roughly the same as for the current TT. Thus the plane arrangement and Z locations are similar to the TT, as illustrated in Fig. 2.7. There are four planes namely, UTaX, UTaU, UTbV and UTbX, progressing in the downstream direction. The first and the last planes have vertical strips, whereas the middle two are at $\pm 5^\circ$.

The centre of UT is at $Z = 2485\text{ mm}$ from the interaction point. The distance between the first and the last plane is 315 mm . Currently the Z-coordinates of the four planes are 2327.5 , 2372.5 , 2597.5 and 2642.5 mm .

The design consists of sixteen staves for the two upstream planes and eighteen staves for the two downstream planes. Each stave in turn has fourteen square sensors of $98.88\text{ mm} \times 98.88\text{ mm}$ size, except for the central region. Each sensor has guard rings of $800\text{ }\mu\text{m}$ width surrounding a nominal 512 strips of $190\text{ }\mu\text{m}$ pitch, 97.28 mm in length, and read out by four 128-channel SALT ASICs. Some sensors near the beam are of half pitch and some of half pitch and half length. (See Sec. 2.6.1.) These parameters are very close to those of UT prototype sensors that are already under characterisation.

There are 3.8 mm spatial overlaps between adjacent sensors within each stave. Thus the stave has active detection area of $97.28\text{ mm} \times 1336\text{ mm}$. The staves are staggered in Z by 10 mm to have overlaps in the X direction. The X locations of the staves are arranged in such way that there is 2 mm projection overlap on the middle plane for straight tracks from the centre of the interaction region. The UTaX plane detection coverage is thus

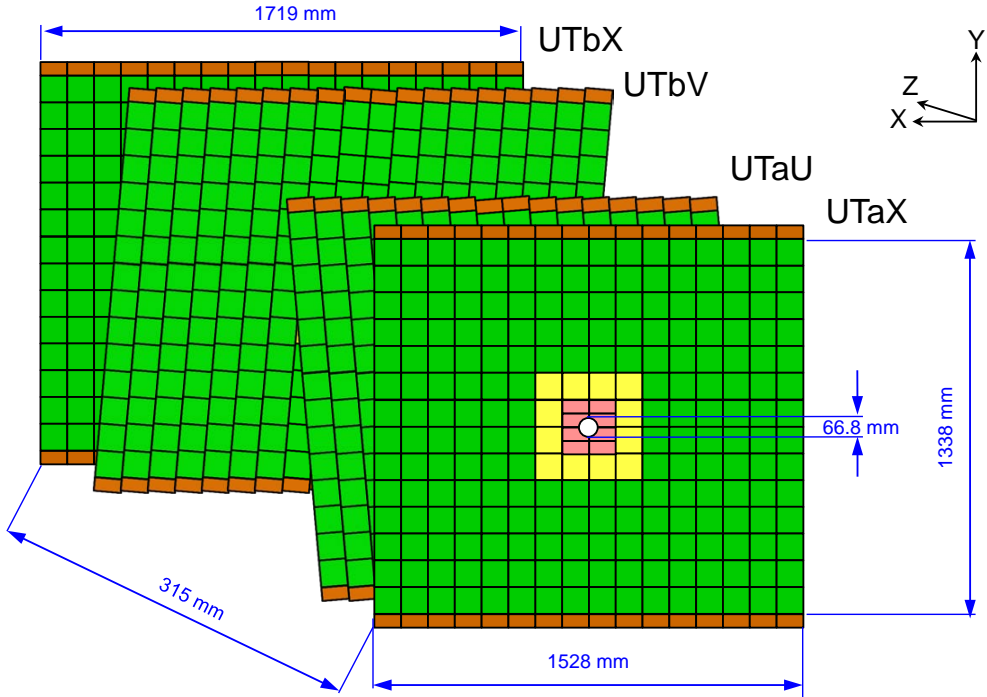


Figure 2.7: Overview of UT geometry looking downstream. The different sensor geometries are colour coded.

1526 mm in X and 1336 mm in Y, corresponding to θ_x between ± 317 mrad, and θ_y between ± 279 mrad. The UTbX plane covers wider in X of 1717 mm. Its angular coverage is ± 314 mrad and ± 248 mrad in X and Y directions, respectively.

The radius of the circular cutout in the innermost sensors is determined by the size of the beam-pipe, the thickness of thermal insulation layer, and the clearance required. The outer radius of the existing beam-pipe at UTbX is 27.4 mm. The current design of thermal insulation, presented in Ref. [19] is 3.5 mm thick aerogel heat shield. We allow for 2.5 mm clearance. These considerations lead to an inner radius of the silicon sensor of 33.4 mm. Due to the 0.8 mm guard ring, the active area starts at 34.2 mm. The central hole leads to an acceptance starting at roughly 14 mrad for straight tracks from the centre of the interaction region. We have verified by simulation that for the typical B decay of interest, we lose only about 5% of the events because one track is in the beam-pipe hole, when compared with tracks reconstructed in the VELO and the outer tracker.

Each UT sensors is composed of $250\ \mu\text{m}$ thick silicon and a $10\ \mu\text{m}$ metalisation layer. The sensors positions are shown as coloured squares in Fig. 2.7. In the central area the track density is very high. To deal with the high density, sensors of thinner strips, and also shorter lengths are used. Sensors shaded in yellow have nominal length, and $95\ \mu\text{m}$ pitch, half that of the nominal sensor. Sensors shaded in pink have both half the nominal pitch and the half nominal length, being about 5 cm long in Y direction. Thus, the central two staves have sixteen sensors each, instead of fourteen. Each of these fine pitch sensors

has 1024 strips which are read out by eight ASICs, rather than the normal four ASICs used to read out the majority of sensors (green) with 512 strips.

2.3.2 Staves

The planes are constructed with vertical strips, called staves, modified from the ATLAS upgrade design [20]. Each stave is the width of a full silicon sensor, approximately 10 cm. The sensors and front-end read-out chips (ASICs) are mounted on custom hybrids which in turn are mounted on thermo-mechanical support structures. The staves are about 1.6 m long and mounted vertically. The signals from the sensors are taken out to the top and bottom of the UT by (data) flex cables. Similarly, (power) flex cables bring voltage in to the sensors and electronics. The staves are supported by a rigid frame, well outside of the spectrometer acceptance. The cooling system will keep the sensor temperature below -5°C .

The stave structure is illustrated in Fig. 2.8. A silicon sensor and read-out ASICs are attached to a hybrid flex to form a UT hybrid. The hybrid flex is about 220 μm thick, same width as the sensor but 20 mm longer in order to accommodate the ASICs and wire bonds. An ASIC is 0.12 mm thick, 5 mm wide and 10 mm long.

The hybrids are mounted on both sides of the stave support and have a 2 mm spatial overlap in Y. The stave is 3.5 mm thick between the carbon fibre facing sheets. The stave

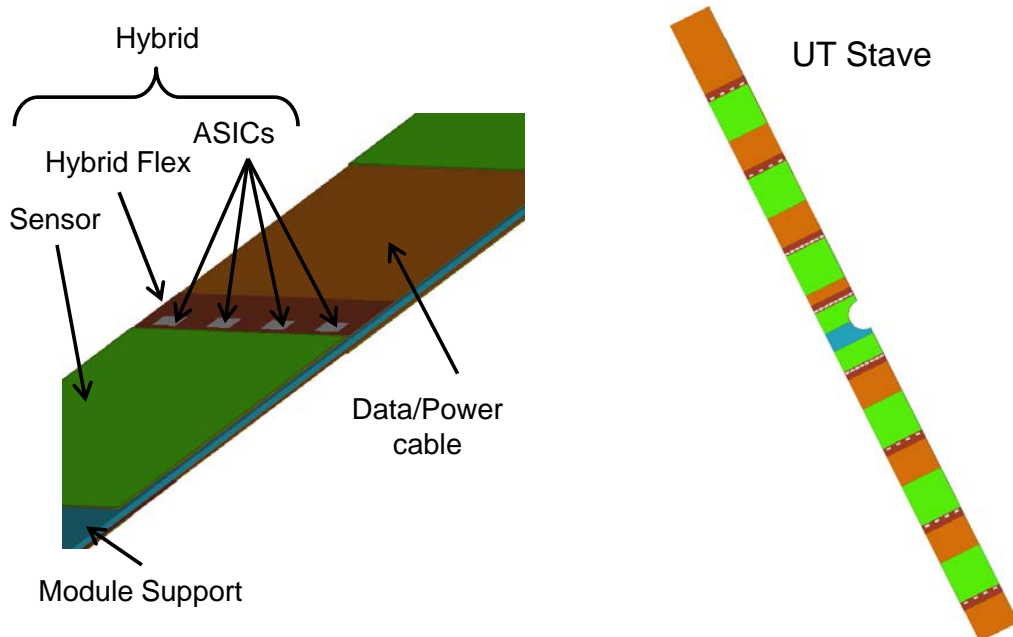


Figure 2.8: UT stave structure: (left) UT hybrid has silicon strip sensor, read-out ASICs attached to hybrid flex, (right) Hybrids are mounted on front and back faces of stave support alternatively, in between are flex cables that carries signal and power.

support also contains the cooling tube. Between the stave support and the hybrids are flex cables that carry power, ground and data lines. As explained in Sec. 2.8.1, each stave has four such cables for top and bottom halves, front and back faces. Each cable starts from the read-out edge of the innermost hybrids till the end of the stave where connections to periphery electronics are made.

The outer staves contain fourteen $10\text{ cm} \times 10\text{ cm}$ silicon sensor units, while the two inner staves have the sensors near the beam-pipe hole divided into two 5 cm pieces. The sensors are mounted on both sides of a given stave and adjacent staves are staggered in the Z direction in order to allow for sensor overlaps ensuring full coverage with no gaps in both the X and Y directions. The space between the silicon is used for the hybrids that contain the ASICs and are wire-bonded to the silicon and attached to the cables. The staves are mounted on the front and back of two rigid frames. The upstream frame has the X and U layers while the downstream frame has the V and X layers. Each layer has the staves staggered along the beam line allowing for the overlap of sensors in the X direction. For example one layer is shown in Fig. 2.9. The overlap in Y is achieved by the mounting of the sensors on the front and back of each stave. Both ends of each stave have aluminium blocks to facilitate mounting.

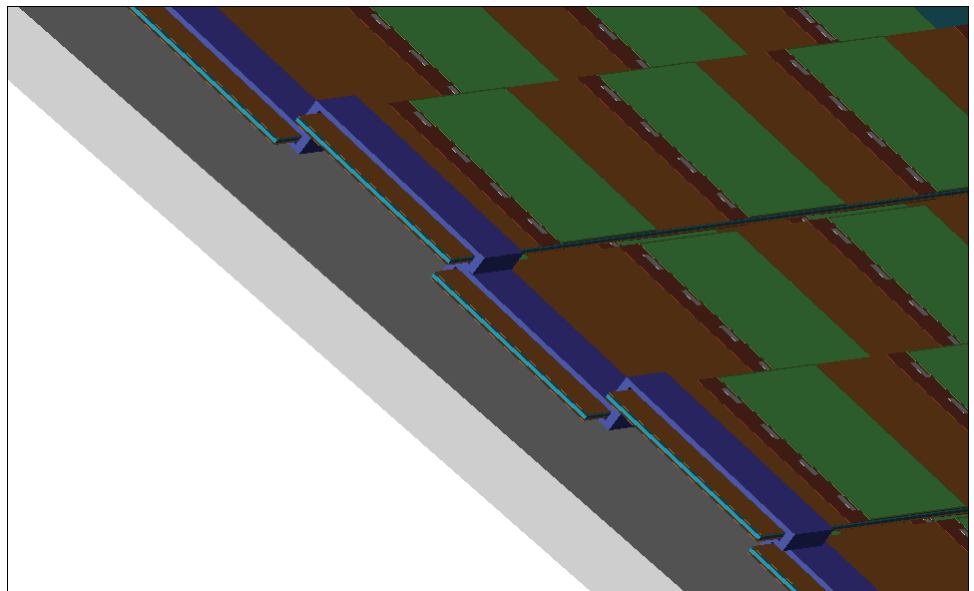


Figure 2.9: Mounting of one stave layer to the frame (grey). The dark blue shows part of the support structure. The brown indicates the Kapton cables and the green the silicon sensors. There are an equal number of sensors on the other side of the stave which cannot be seen in this view. The adjacent staves are staggered to allow for the overlap of sensors stave to stave. Another layer of staves is mounted to the other side of the frame.

2.3.3 Material Scan

The entire detector is enclosed in a light-tight and gas-tight box. The thickness of the UT in terms of radiation lengths compared with the TT is shown in Fig. 2.10 (right) as a function of the pseudorapidity, η . The detector acceptance covers $2 < \eta < 5$. There is a significant reduction in material in the forward, large η direction in the acceptance. This was done by changing the thermal insulation and sealing the box to the beam-pipe. The thickness of the UT in terms of radiation lengths affects the momentum resolution. Fig. 2.10 (left) shows the radiation length distributions with the current best design in the simulation. Note, the integral amount of material in the beam-pipe and heat shielding is about the same for the TT and UT but in the UT design it is pushed more out of the acceptance to higher η . This was done by changing the thermal insulation and sealing the box to the beam-pipe.

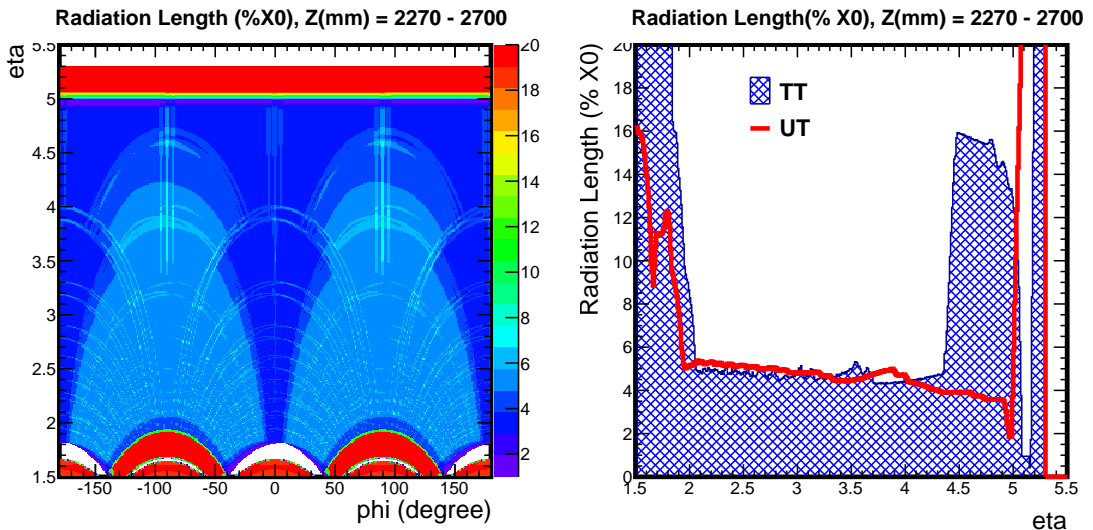


Figure 2.10: (left) Radiation length vs phi angle and η , (right) Radiation length as a function of η , compared with the present TT. The contribution from N_2 in the box is also included.

2.4 Mechanics

2.4.1 Introduction

The detailed requirements for the mechanical design are:

1. Structure must support the silicon sensors ($\sim 10\text{ cm} \times 10\text{ cm}$) including overlaps of sensors (2 mm in both directions perpendicular to the beam).
2. There must be fiducials on the structure that allow the silicon sensors to be aligned to a precision of $100\text{ }\mu\text{m}$ in the LHCb coordinate system.

3. Structure must be stable enough to prevent wire-bonds from breaking due to flexing or other motions.
4. Structure must not move during data taking, with position stability $< 20 \mu\text{m}$.
5. Minimal thickness in radiation lengths, no thicker than current TT, $\sim 4\%$ of a radiation length from $2 < \eta < 5$.
6. Provide cooling to silicon sensors and electronics keeping sensor temperature $< -5^\circ\text{C}$ and ΔT across any one sensor $< 5^\circ\text{C}$.
7. Ability to move detector out of the way when beam-pipe is baked.
8. Provide cable support.
9. Provide outer box for optical, thermal and gas isolation

2.4.2 Stave Construction

A schematic of the stave layout and its cross section are shown in Fig. 2.11. The stave consists of a sandwich structure made of thin, high-modulus carbon fibre reinforced

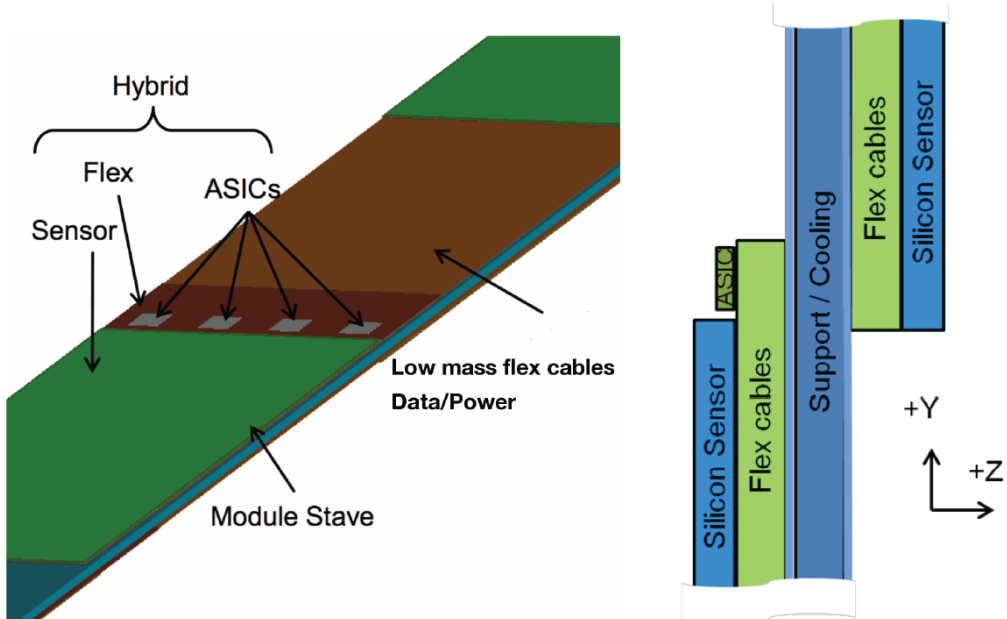


Figure 2.11: (left) A small section of a stave near the centre ($Y=0$) showing the relative position of the silicon and hybrid. (right) Cross section of a single UT stave. showing how sensors are mounted on both sides of the support structure (not to scale) allowing for sensor overlap.

polymer (CFRP) facing sheets surrounding a lightweight partially filled foam core interior. Embedded in the foam core are one or more thin-walled Ti cooling tubes which remove the heat generated principally by the ASICs. The foam core is a mix of thermal and structural foams, optimised to provide maximal heat transfer while maintaining minimal radiation length. The data and power flex cables are laminated on either side of the stave. Thus the stave structure provides stiff support, heat removal and signal transfer, with minimal mass.

The hybrids are precisely mounted on either side of the stave, and wire bonded to the data and power flex cables. The stave provides a stable support for sensors and for the delicate wire-bond connections. Stressing the wire-bonds either mechanically or thermally could cause the connection to break. Hence any motion or twisting of the integrated stave must be avoided. In order to mitigate thermal motion, mounting the hybrids in a balanced approach on either side of the stave minimises any relative thermal expansion. Kinematic mounting of the stave to the rigid outer frame will aid in minimising mechanical motion. These issues will be fully analysed by simulation and tested with measurements. The ends of the stave will contain fiducials as will the silicon sensors. These will allow alignment of the silicon to the LHCb coordinate system to an accuracy of $100\text{ }\mu\text{m}$.

After construction of the bare stave, it will be mounted into a “strong-back,” a frame-like structure which supports the stave during subsequent construction operations, such as the bonding of the data flex cables and mounting of the hybrids. This strong-back will also serve as a safety rig for shipping the integrated stave and as a mounting rig for attachment to the UT frame. The strong-back is envisioned to consist of several parts that can be added or removed. Connections of the strong-back to the modules can be made to aluminium blocks built into the top and bottom of the stave or to inserts on the edges.

2.4.3 Frame and Outer Box

The staves are mounted on the front and back of two rigid frames. The upstream frame has the X and U layers while the downstream frame has the V and X layers. Each layer has the staves staggered along the beam line allowing for the overlap of sensors in the X direction. The overlap in Y is achieved by the mounting of the sensors on the front and back of each stave. Both ends of each stave have kinematic mounting blocks, which will take up any motion along the long dimension of the stave. They will incorporate the staggering as well as facilitate the sequential mounting and (potential) removal of the staves.

The entire detector is enclosed in a light-tight and gas-tight box. It is being considered to seal the upstream face of the box to the RICH exit window, while the downstream face has a separate seal to the beam-pipe. Cables are fed through the box and glued to form a seal. The top and bottom of the box will be integrated with the cooling distribution manifold. The box is filled with dry N_2 gas to prevent any moisture condensation, either on the sensors or the beam-pipe. The box and the frames can be separated into two halves and moved horizontally away from the beam during the periodic bake-out of the beam-pipe.

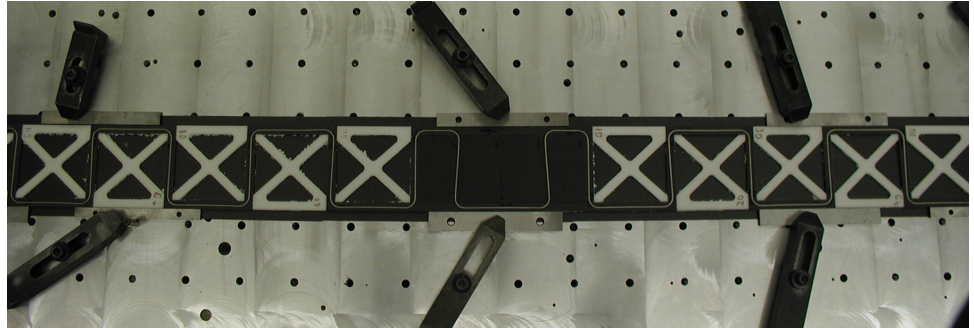


Figure 2.12: Photograph of the interior of the first stave prototype during construction. The white pieces are the Rohacell foam structural elements. They are glued to the carbon fibre sheet along with the carbon foam in which the bent titanium tube is situated. The area in the centre is filled with carbon foam to improve the heat conduction.

2.4.4 Current and Planned R&D

A full-sized stave test module has been constructed at Syracuse University that allows us to make measurements of the capability of evaporative CO₂ cooling for the heat loads involved in the conceptual design. A prototype CO₂ cooling system has also been constructed, and is used for testing.

The test module was constructed using real materials for the mechanical parts of the stave, approximate materials for the hybrids and flexes, and also allowed us to develop preliminary construction techniques. A photo of the internal stave parts is shown in Fig. 2.12. The stave was constructed using K13C2U/EX1515 carbon fibre reinforce polymer facing sheets and core materials Allcomp carbon foam and Rohacell structural foam. Mock data/power flex cables were made with a 50 μm thick copper layer surrounded by 50 μm thick Kapton HN on the reverse face and 150 μm on the obverse. Hybrid flexes were constructed in the same way. Sensors and ASICs were cut to shape from 250 μm and 100 μm brass alloy shim foil, respectively. The bonding in this construction was made with Hysol 9396 epoxy loaded with 30% BN for better thermal conductivity. Heaters were epoxied to both ASICs and sensors to simulate leakage current.

After the prototype construction was finished cooling tests started. The results of the first such test are reported in the cooling section.

During the coming year several other mechanical issues will be addressed. A second test module will be constructed to test variations on the baseline design, including cooling by straight tubes instead of the snake tube. Measurement techniques will be developed to determine thermo-mechanical deformations when the stave is cooled, and any degradation of the tube bonding to the carbon foam. This will be backed by thermal simulations. Also to be studied are dynamic mechanical effects, such as a vibrational frequency analysis of the stave bending stiffness and the effect of the mounting scheme on the vibrational modes. This will include study of the vibrational excitation of the wire bonds. Thermal cycling tests will be made, and development of the construction techniques and the assembly fixtures needed will also proceed.

2.5 Cooling

An efficient cooling system is necessary for maintaining the temperature of the sensors below -5°C in order to reduce the leakage current and prevent thermal runaway in presence of radiation damage. Sensors will be cooled down also during shut-down periods to avoid reverse annealing. CO_2 bi-phase cooling systems have successfully been built and operated for particle detectors for the LHCb VELO [21], which pioneered the use of evaporative CO_2 cooling in high energy physics, for the AMS tracker [22], and recently for the ATLAS IBL [23]. They have proved to be very efficient and reliable, providing effective cooling with reduced impact on the material budget. The heat load on the sensor is dominated by the power dissipation of the ASICs that are bonded directly to the sensor and positioned close to it in the active tracking volume. A dedicated simulation study described in Sec. 2.5.3, based on finite element analysis (FEA), has proved that evaporative CO_2 cooling is the optimal choice in terms of cooling efficiency and material budget. In the active region, the system consists of CO_2 cooling pipes embedded in the interior of the support structure of the UT stave where carbon foam provides good heat transfer from the sensor and the front-end electronics to the coolant.

2.5.1 Requirements

The cooling system has to maintain the temperature of the sensors at -5°C by removing the heat generated in the ASICs, assumed to be $0.77\text{ W}/\text{chip}$, in the silicon sensors due to self-heating, and in the cables that provide the power to the front-end electronics. The acceptable ΔT over the sensor is few degrees provided that the maximal temperature is below -5° . The temperature of the ASICs should be kept under 40°C for optimal functioning. The sensors need to kept cold even during shutdowns.

The heat load on the sensors depends on their radial position. The innermost sensors have finer granularity and hence a larger number of read out chips, and the leakage current due to radiation damage is expected to depend strongly on the radial coordinate. In UT the charged particle density per minimum bias event at $\sqrt{s} = 14\text{ TeV}$ can be approximated as $\Phi(r) \sim 3.8 \cdot r^{-1.68}\text{ cm}^{-2}$ according to Monte Carlo simulations. The radiation decreases rapidly with the radius r , varying over two order of magnitudes between the inner and the outer radius. The highest heat load is applied in the innermost sensors, at a radial distance of about 5 cm. They are read out by eight ASICs, dissipating a total of 6.2 W, and the maximal self-heating power is expected to be 0.26 W after ten years of operations. The outer sensors are read out by four ASICs, dissipating 3.1 W and the effect due to self-heating reduces to less than 60 mW at a radius larger than 20 cm. The contribution of the power cables is calculated to be about 10% of the power dissipated in the ASICs. The total power consumption of UT has been estimated to be about 900 W/plane for a total of 3.6 kW.

The radiation length of each UT plane should not exceed the value of $1\% X_0$, comparable with the present TT detector. This specification imposes a stringent limit on the mass of the cooling system in the active tracking volume. The cooling system design does not

tolerate leaks in the active region. A manifold based on a single piece metal pipe will be used avoiding weld joints. Dedicated connections for the stave cooling pipes will be designed. Particular attention to the mechanical distortion of the system is necessary since the operating temperature of the detector will be much lower than room temperature. Minimise the mismatch in coefficient of thermal expansion (CTE) between the various components of the module is beneficial to the system design.

2.5.2 Evaporative CO₂ Cooling

Evaporating CO₂ cooling is a well established technology that provides efficient cooling with a relatively low mass system. Large latent heat for liquid vaporising into gas means less flow needed to remove a given thermal power, which translates in a smaller diameter pipe. The thickness of the pipe, needed to cope with the internal pressure, is proportional to the diameter; hence a small diameter pipe is beneficial to the material budget of the detector. The temperature of evaporation, to be set in the UT stave cooling pipes, is fixed by the maximum operative temperature allowable for the sensors that is -5°C, and the temperature difference between the sensor and the coolant. The temperature of the coolant inside the cooling pipe is determined by the pressure. For example, the CO₂ evaporating temperature is around -35°C at 10 bar. The vapour stays compressed in a small volume, moving at low speed, with resulting low pressure drop along the cooling line. The low viscosity of CO₂ is also beneficial in this sense. The acceptable pressure drop of the CO₂ along the stave cooling channel is dictated by the acceptable temperature difference between stave inlet and outlet. A pressure drop of the order of 1 bar can be set as design goal, allowing to obtain a few degrees temperature difference along the cooling lines. Detailed studies of the cooling system with the CoBra Model (CO₂ BRAnch Model) and thermal tests on a stave prototype in scale 1:1 will be necessary to validate the design.

The nearly isothermal behaviour of a boiling flow adds beneficially to the large heat removal capacity giving a low temperature gradient, *e.g.* few degrees, along the stave. In order to exploit this cooling technique, the detector has to be designed and built integrating the evaporator into its structural support, so that the ASICs transfer the thermal power through the stave support materials up to the cold pipe embedded in the structure. The equipment needed outside the detector has to be designed yet. It will be a circulation system supplying the flow at the required fluid condition to the detector evaporator system; it is necessary to supply a sub-cooled CO₂ flow at a stable temperature and pressure. The temperature will be nearly constant along the cooling circuit since the absorbed heat is used only for the phase transition. In case the power to be dissipated would increase locally, it would increase only the fraction of gas at the pipe outlet but not the temperature of the coolant. The limit is imposed by avoiding that the CO₂ is completely evaporated, referred to as “dry out” of the channel, and a evaporated fraction of 50% is a practical guideline for the design. Evaporation of the coolant is controlled to start at the beginning of the detector cooling pipe, just outside of the tracking region, by a local pressure drop at the pipe inlet that can be obtained using a capillary junction. The 2-Phase Accumulator Controlled Loop (PACL) concept, developed at NIKHEF, and running stable and without

problems four years for LHCb VELO and two years in space for AMS is the baseline for the UT upgrade project.

Several stave structures have been analysed in the design phase using a FEA to evaluate the thermal performance, shortly described hereafter. The design aims at minimising these temperatures and the variation of temperature over the sensors that has an area of approximately $10 \times 10 \text{ cm}^2$.

2.5.3 Thermal Simulations and Prototype Test

A “snake pipe” design with bent tubes passing underneath the ASICs, see Fig. 2.13 (left), is currently considered as the baseline solution providing maximal heat transfer. However, several issues have still to be assessed and some R&D is needed, *e.g.* determine the optimal tube bending radius, the effect of the thermal contractions and the mechanical deformations of the stave. A solution with two parallel tubes combined with heat spreaders and thermal vias is considered as a valid alternative and is also under study, see Fig. 2.13 (right). In both cases the piping is embedded in the central core of the stave and it is in thermal contact with the two - upstream and downstream - faces of the stave, where the sensor and the ASICs are mounted. The candidate material for the pipe is titanium (Ti), for example a pipe with 2 mm inner diameter and 0.1 mm thickness. Stainless steel (S.S.), with relative magnetic permeability close to one, could be considered as a backup solution in case problems during Ti pipe construction would arise. Tests on Ti tube bending have been successful so far and thus Ti has been adopted for the baseline.

In order to improve the thermal performance while keeping low material budget, a carbon foam is used as conductive path between the pipes and the thermal sources. The thermal resistance Ω_{thermal} , a figure of merit (FoM) for estimating cooling performance, is defined as the ratio of the ΔT between the heater and the output, and the power dissipation per unit area. According to the simulations for the central stave, we obtain this range of values for the FoM in the region corresponding to the ASICs, where the power density is about 1.5 W/cm^2 :

- for the snake pipe solution, the ΔT between the ASICs and the cooling pipe ranges from 10 to 30°C and the relevant FoM varies from 7 to $20^\circ\text{C cm}^2/\text{W}$. The difference is driven by the fact that in the outer region the ASICs lay over the data/power tape, contrarily to the innermost ASICs.
- For the double pipe solution, the ΔT between the ASICs and the cooling pipe ranges from 4 to 38°C and the relevant FoM varies from 3 to $26^\circ\text{C cm}^2/\text{W}$.

The use of a snake pipe gives the best thermal performance, but the longer path than the straight tube causes concerns with the available CO_2 evaporation and concordant pressure drop. It also appears to be easier to construct the models with the straight tubes should the cooling be adequate.

The straight pipes solution needs to use high conductive insert, *e.g.* Thermal Pyrolytic Graphite (TPG), under the ASICs to improve the heat transfer; these have to be placed in

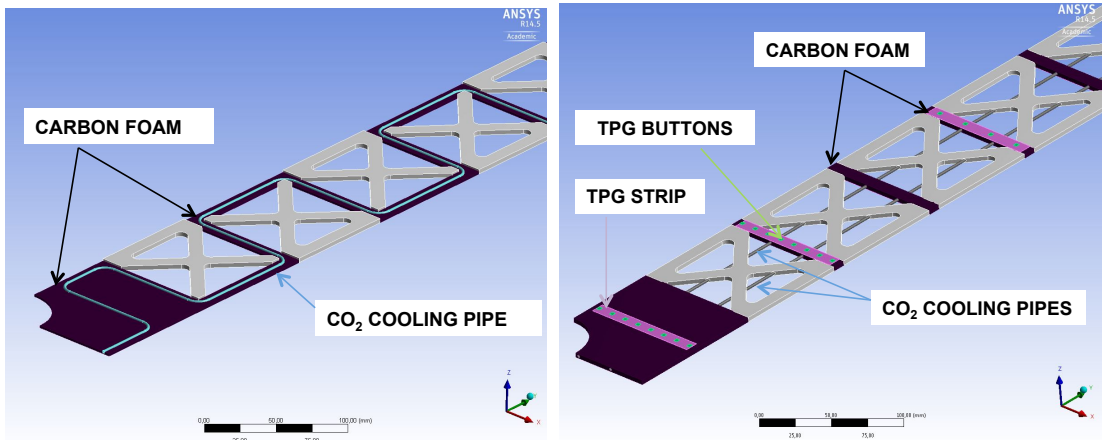


Figure 2.13: (left) “snake pipe” solution. The cooling pipes are embedded in the carbon foam and pass underneath the ASICs for maximal heat transfer. The chips are positioned horizontally at the end of each hybrid module and a bent pipe provides maximal overlap. (right) parallel pipe solution. The cooling pipes run parallel to the stave, embedded in the interior of the structure. The high conductive TPG inserts are placed underneath the ASICs to improved the heat transfer.

suitable cut outs in-between the most insulating layer, namely the carbon fibre face-plate and the hybrid.

An FEA thermal analysis has been performed with a detailed model of the central UT stave after 50 fb^{-1} (the most challenging conditions from the thermal point of view). Self-heating power was included and the cooling pipe internal wall temperature has been set to 0°C . The steady state solution was obtained in nominal working conditions. Thermal radiation and heat exchange with environmental gas will be included in the future, but their effect is expected to be small or negligible. According to the FEA an evaporation temperature of -30°C will satisfy the thermal requirements using both design options. Special attention has to be dedicated to the design and test of the central stave that matches the beam-pipe and features a larger number of ASICs and thermal power dissipated, nearly 85 W. In that case a special design with four additional bends of the pipe ($\sim 90^\circ$ bends) is needed to pass underneath the ASICs for the central sensors. The FEA thermal map of the central stave is shown in Fig. 2.14 for the snake pipe option. The temperature values are referred to the temperature of the coolant which is set to be 0°C in the simulation. The maximal temperature is reached on the ASICs near the sensors due to their high power density but still satisfying the requirement to be below 40°C . The maximum ΔT over the sensor is about 2°C and within specifications for the snake pipe, and 10°C for the parallel pipe solution. In the latter case further optimisation of the design is still possible and the results obtained so far are encouraging.

A prototype CO_2 cooling system has been constructed at Syracuse University. A full-sized stave demonstrator module has been constructed that will allow measurements of the capability of evaporative CO_2 cooling for the heat loads involved in the conceptual

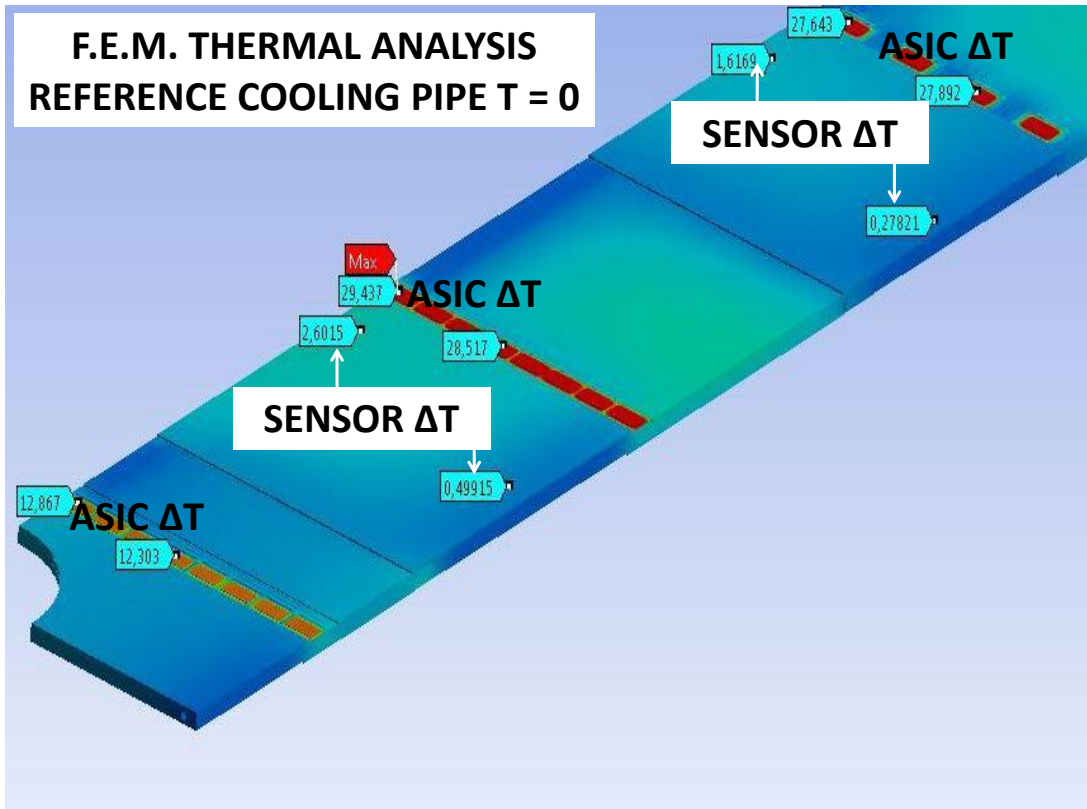


Figure 2.14: The FEA simulation results of the snake pipe solution. The temperatures shown refer to the temperature of the coolant which is set to 0°C in the simulation. The hotter spots (orange and red) correspond to the rows of eight SALT ASICs. The maximum temperature excursion on the sensor adjacent to the hottest SALT chips is about 2°C. The maximal ΔT over the sensor is about 2°C.

design. A photo of the internal stave parts is shown Fig. 2.12 in Sec. 2.4.

The prototype was completed with the top layer and sensors, some of which were silicon and some made of brass, since brass and silicon have comparable thermal properties. Heaters were glued on both at the ASIC positions and on each sensor to simulate leakage current. Temperatures were read off each sensor and at four separate locations on the central sensor and the next adjacent one. The stave was in a Styrofoams box except for the last sensor that was purposely placed outside of the box. The first results from the testing program are shown in Fig. 2.15. The system cooled all the sensors below -5°C, even the one outside the box. The temperatures increase along the stave but the temperature across each the sensor stays relatively constant. Further tests are needed and will include thermal cycling and detailed temperature maps of each sensor but preliminary results are encouraging.

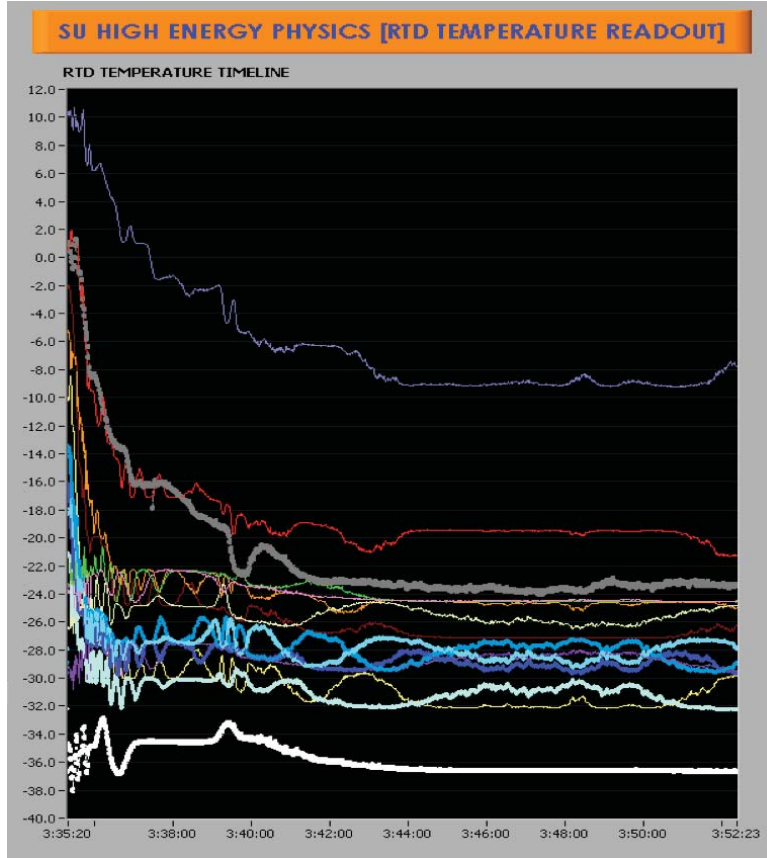


Figure 2.15: Temperature in Celsius degree as a function of time near the end of the cool down along the length of the stave. The thick white trace at the bottom is the input cooling tube temperature, and the thick grey trace the output tube temperature.

2.5.4 Cooling System Architecture and Safety

The net total power to be removed from the UT detector staves using the CO₂ plant is rated 3600 W at -35°C ; this comes from the sum of all the expected power sources: ASIC dissipation, sensor self-heating and power-data flex cables dissipation. A margin has to be applied and the environmental take off of the long connecting lines has to be added: giving a rated power of the order of 5000 W, and a total CO₂ flow rate of about 30 g/s. This can be compared to the actual 1500 W at -30°C for the VELO Thermal Control System, and to the 1500 W at -40°C cooling power of the Atlas IBL CO₂ system [23] that is going to be installed by the end of Long Shutdown 1.

CO₂ has a rather high critical pressure (73.8 bar) at 31°C . In case the plant loses the cooling power, the pressure can reach and even exceed this value. The maximum design pressure (MDP) has been therefore set to 100 bar, considering a safety margin. The triple point is at -56.5°C at 5.1 bar, at lower temperature the sublimation line starts and the phase is solid. While the operation temperature range is set by the sensor and electronics requirements, the temperature range for non-operational conditions depends

upon the failure scenarios: the triple point temperature on the lower side, and maximum foreseen temperature in case of failures. The design of the boiling channel focuses on two targets: minimise the material and the pressure resistance at 100 bar MDP. The deformation of the stave, induced by the cooling, has to be controlled without inducing unacceptable stress. A suitable pipe fixation and allowable clearance has to be taken in consideration in the stave design. The layout of the UT cooling plant has to be defined in the details. It is considered advantageous to share the cooling plant with the upgraded VELO [24] that will also use evaporative CO₂ cooling. A conceptual scheme for UT should foresee two separate supply lines from the CO₂ cooling plant towards the UT left box and the UT right box. The liquid cold supply of CO₂ travels inside a coaxial line, surrounded by the partially evaporated flow coming back to the CO₂ cooling plant. These lines are highly insulated. The UT box would need to be opened approximately once a year to access the detector, and a dedicated connection system must allow this movement; some space has to be allocated for the lines to give the necessary flexibility to open each of the two half detector box. Inside one half detector box the four planes will be supplied from the bottom with the liquid CO₂, and on the top of each plane the CO₂ liquid plus vapour mixture will be collected. To simplify the integration of the detector each half plane needs to be built with its own bottom and top manifolds; at a later stage these manifold have to be connected together in a circuit loop. Special attention has to be paid to the local pressure drop at the stave inlet that drives the boiling process to start inside the cooling channels. A capillary connection of each stave pipe can be designed and a thermal test of a complete prototype system has to be planned for the snake and the straight pipe design options. A dedicated engineering of the flow distribution between the parallel channels of a half UT plane is necessary to satisfy the different necessities. The cooling capacity for half detector box plane is close to 500 W, and the inlet and outlet manifold mass flow rate are about 3.0 g/s of CO₂. A first preliminary estimate of the central stave heat power is about 85 W and it would need a flow rate of 0.6 g/s; the adjacent stave heat power is about 68 W and it would need a flow rate of 0.45 g/s, while all the outer staves with nearly 50 W dissipated power would required a flow rate of 0.3 g/s each. The precise values of the flow rates have still to be determined and this will be part of the optimisation of the cooling system design.

2.6 Sensors and Hybrids

2.6.1 Silicon Sensors

The UT sensors are single sided silicon micro-strip devices. Their segmentation and technology are dictated by the expected radiation dose and occupancy. For an integrated luminosity of 50 fb⁻¹, detailed radiation background simulations [25] including safety factors motivated by previous experience predict a maximum dose of 40 MRad at the innermost edge of the silicon sensors and a fluence of $5 \times 10^{14} \text{ n}_{\text{eq}/\text{cm}}^2$, rapidly decreasing with the distance from the beam axis, as shown in Fig. 2.6. The occupancy follows a similar trend, as shown in Fig. 2.35 . Thus the segmentation is finer in the inner portion of the

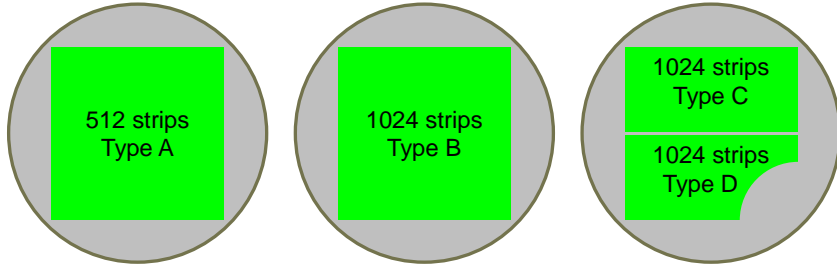


Figure 2.16: Sketch of the three mask designs for the UT upgrade. Sensors C and D are shorter and can be produced in a single 4 inch wafer, whereas sensors A and B require a full wafer.

plane, surrounding the beam-pipe, and is coarser in the rest of the detector. We envisage four kind of detectors, as illustrated in Fig. 2.16, referred to as type A, B, C, and D. Detectors C and D are only 5 cm high, in order to allow for a higher vertical segmentation without the need of a double metal layer to route the signals from the shorter strips to the contact pad row. This permits a simpler sensor design and reduces the probability of cross-talk. Most of the detector staves are populated with detectors of type A. These detector experience very modest radiation dose (100 – 300 kRad, depending upon the location), and thus can be safely implemented in the traditional “ p^+ -in-n” technology. Detectors of type B, C, and D are closer to the beam axis, and thus the technology chosen is the “ n^+ -in-p” demonstrated to be suitable to even more severe radiation environments [26]. Table 2.1 summarises the basic parameters of these silicon sensors.

There are two design feature that are unusual in our design. The first one is the implementation of the interconnection between strip and corresponding front-end electronics input channel (featuring a 73 μm pitch in the input pads) with a direct wire bond, without the use of an intermediate pitch adapter. While this can be implemented by adjusting the angle and the length of the wire bond for the B, C, and D sensors, this requires a “fan-in” circuitry built in sensors A. The pitch matching required is between 190 and 73 μm . The

Table 2.1: Basic parameters of the silicon sensors.

Property	Sensors B,(C,D)	Sensors A
Technology	n^+ -in-p	p^+ -in-n
Thickness	250 μm	250 μm
Physical dimensions	98 mm X 98 (49) mm	98 mm X 98 mm
Length of read-out strip	98 (49) mm	98 mm
Number of read-out strips	1024	512
Read-Out strip pitch	95 μm	190 μm
Sensor number (needed)	48 (16,16)	888

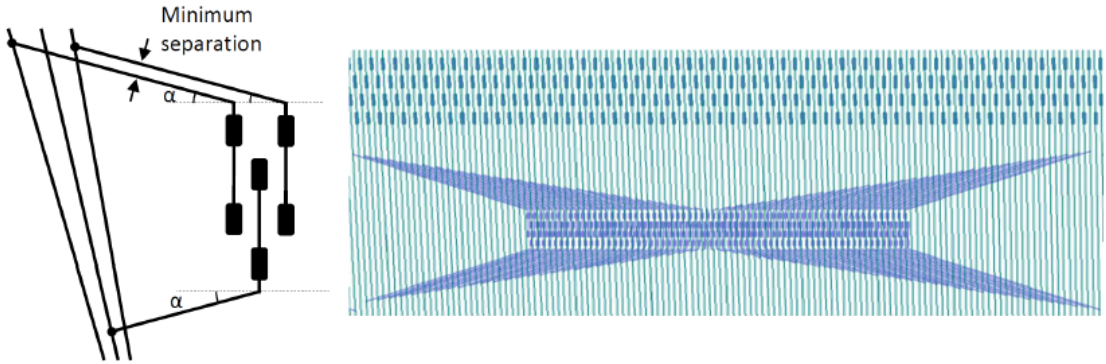


Figure 2.17: Sketch of the fan-in approach pursued in our design. The finer pitch pads represent the bonding pads to the front-end electronics. A prototype towards the ATLAS silicon tracker upgrade is shown here [27].

current plan is to implement this matching in a manner similar to the one studied for the ATLAS tracker modules described in Ref. [27], shown schematically in Fig. 2.17. Secondly, the outline of the detector shape is non-standard in sensors D. Motivated by the goal of maximising the angular acceptance matching with the VELO system, we are planning to shape one corner of these sensors with a quarter-circle cut-out, as shown in Fig. 2.16, to maximise the active area near the beam-pipe. The radius of this cut-out is 33.4 mm.

Currently, we are studying the performance of detector types B and C as fabricated by two different vendors. We utilise strip detectors of similar segmentation developed by Hamamatsu to validate their performance for our application [26]. These sensors have overall size equal to the one of our tiles, and comprise four rows of short strips (2.39 cm) that can be daisy chained to form 5.48 cm long detecting elements. The technology is n-in-p and the thickness is 250 μm . Currently we have completed current versus voltage measurements on these devices and we measure currents about 1 μA at 600 V at 29°C. We have ten such devices and they feature no oxide pin-holes. In parallel, we have developed prototypes of detectors B and C with Micron Semiconductors. These prototypes, designed for our application, are currently in the latest stage of production. We are expecting to receive them in February 2014. In this submission we have included smaller area detectors to study variation of the design, such as more aggressive guard ring design, involving less dead area at the sensor periphery, and a scaled-down version of the beam-pipe cut-out

described above. The measurements on these devices will guide the detailed design of the sensors that we will fabricate in the next R&D phase. In addition we will design and fabricate prototypes of type A detectors with built-in pitch adapter to verify that no excess cross-talk is added and that the performance is preserved at the irradiation levels expected for these devices.

2.6.2 Hybrids

The front end electronics (SALT ASICs) will be mounted on low mass flexible circuits that provide electrical connections of the ASICs to the data and power flexes. The unit comprising the front end hybrid and the Si sensor with the strips wire bonded to the corresponding input channels is named “UT module.” Currently we envisage two types of modules, that are distinct because of the different sensor segmentation. Hybrids providing read-out for sensors B, C, and D host eight SALT ASICs, while hybrids hosting read-out electronics for sensors A host four of them. Figure 2.18 shows the conceptual structure of a hybrid module: a thin flex circuit is instrumented with 8 (4) SALT ASICs, and subsequently a sensor is glued on it and wire bonded to the front end electronics.

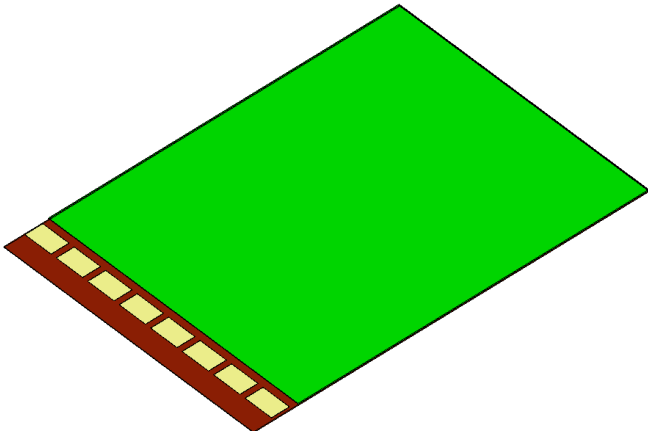


Figure 2.18: Sketch of an eight ASIC hybrid module. The Si sensor is depicted in green, and the eight SALT chips are shown in yellow. The brown layer represents the underlying flex circuit carrying the power and bidirectional communication to the back-end electronics to the individual ASICs.

The technology chosen relies on low-mass flex circuits. The overall design aims at minimising the radiation length of the design. Thus wire bonds are used to connect the flex circuit to the data/power tape. The hybrids and data/power tapes will be designed concurrently, thus enabling an optimisation of the technological choices for both. While the end product will be a module where only a thin flex circuit hosts the sensor and front end electronics, during the intermediate stages of integration there is a clear need for a rigid substrate supporting the module. We are planning to mechanically attach the flex circuit to a FR4 carrier which acts as a temporary substrate during assembly, wire

bonding and testing. The carrier allows for the machine placement and solder reflow of passive components. We are considering a panel capable of hosting multiple hybrids to allow for parallel electrical testing of multiple hybrids with only one data I/O and one power connection, to streamline the process of hybrid production and testing. More details on the planned procedure to mount the “sensor-hybrid module” on the stave are given in Sec. 2.10.

The hybrid provides thermal interface between the chips and the cooling system, the electrical interconnects among the chips and the electrical connections with other components. ASICs are aligned into a row in close proximity to the edge of the Si sensors near the signal bonding pads. The quality of the wire bonds are critical to our production chain, as the double sided stave makes it difficult to rework defective bonds during assembly. Once the detector is installed, access to the staves is possible only during extended shut-down.

Each hybrid has a rectangular shape, approximately $10 \times 3 \text{ cm}^2$, and the SALT ASICs are mounted in a row along the long side of the circuit so that the sensor strips can be directly wired bonded to the input pads of the SALT chips.

Special care must be taken in the mechanical requirement of the flex and of the technical realisation of the circuit:

1. accuracy in chip positioning: $\pm 50 \mu\text{m}$,
2. the planarity tolerance of the substrate in the bonding region: $\pm 10 \mu\text{m}$,
3. accuracy in the cut of the substrate: $100 - 150 \mu\text{m}$,
4. clearance region on the front part of the hybrid for bonding to the detector (maximum value): 2 mm ,
5. clearance region on the four corners of the hybrid for mechanical tools access (minimum value): $1 \times 2 \text{ mm}^2$.

On the opposite side of the rectangle, a series of bonding pads are placed to connect the hybrid to the interconnect cable. Care in aligning these pads must be built in the design as well, as we are planning to implement these connections with wire bonds.

The heat generated by the power dissipation of the SALTs has to be effectively transferred to the detector cooling system. For this reason a good thermal contact is obtained by inserting electrically isolated thermal “buttons” under the SALT chips by openings in the flex substrate layout. In the hybrid, the signals generated in the sensor are processed, digitised, formatted and serialised by the SALT ASICs. The output data are then transferred to the balcony electronics via low mass flex cables without further processing. The limited space available and the need to minimise material in the active region prevent mounting additional electronics on the hybrid. The signal preamplifier in the SALT, which is the first step in the signal processing, is particularly sensitive to noise. For this reason as a general rule, the layout must be developed to minimise the coupling of the analogue and digital sections. Cross-talk and noise coming from the power planes

must also be minimised. Furthermore power supplies have to be distributed in wide planes to reduce trace inductance as much as possible and achieve good coupling with current return. Each power line is filtered locally with capacitors to the common return. The capacitors have to be reliable for high frequency behaviour, ageing effects, temperature coefficients, dimension and values. Based on past experience surface-mount capacitors with X5R dielectric are proposed.

The hybrid must allow all functionality of the read-out chip. In particular:

1. provide separate analogue and digital power through low impedance planes,
2. two different current returns, one for the digital current and one for the analogue current,
3. each power line must be locally filtered,
4. differential command, control and data lines have to be properly distributed from each chip to the interconnection cable,
5. impedance of differential lines have to be controlled at 5% to guarantee SLVS communication between front-end chip and balcony electronics,
6. cross-talk of $\sim 1\%$ on adjacent traces of the same layer,
7. whenever possible control and command lines need to be redundant,
8. the detector bias voltage must be capacitive coupled to the analogue power (representing the analogue reference voltage of the read-out chip),
9. the hybrid must host and provide connection to one resistive temperature monitor,
10. the hybrid must provide connections for remote sensing lines for all the supply voltages,
11. gold plating of traces ($1.5 \mu\text{m}$) only in the pads used for bonding to minimise the radiation length.

While early prototyping is important to validate the overall electronics system design, the technology envisaged for this application has been widely used in current and planned silicon trackers, thus we do not anticipate that an extensive R&D effort on the hybrid technology will be necessary.

2.7 The SALT ASIC

The silicon micro-strip sensors of the Upstream Tracker (UT) will be instrumented with a novel front-end read out, an Application Specific Integrated Circuit (ASIC) called SALT (Silicon ASIC for LHCb Tracker), which is being developed by the AGH-UST Krakow LHCb

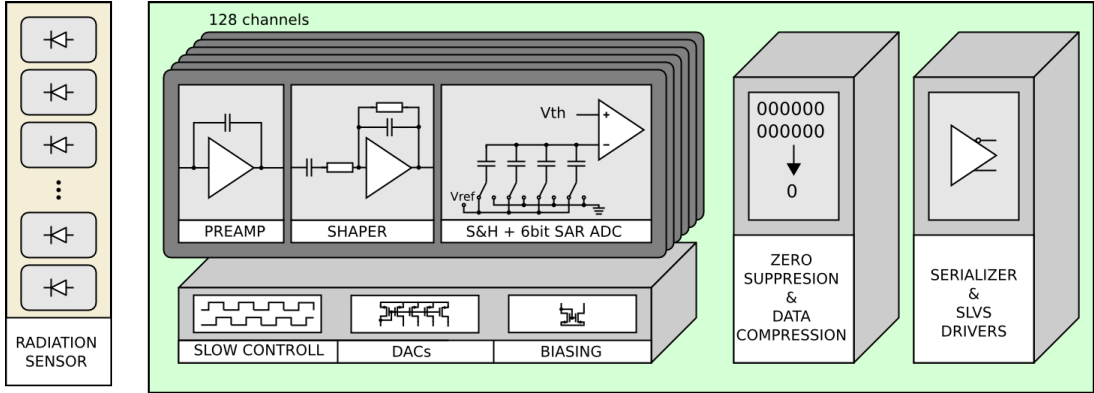


Figure 2.19: The SALT ASIC block diagram.

group. There are a number of technological challenges related to the design arising from the required performance and harsh environment of the 14 TeV pp collisions. The SALT ASIC will read out 128 channels and will be manufactured in IBM CMOS 130 nm technology. The ASIC main blocks are shown in Fig. 2.19. Each channel comprises an analogue block with a charge sensitive preamplifier, a shaper and a single-ended to differential converter. The differential analogue signal is then sent to an Analogue to Digital Converter (ADC) implemented as a 6-bit fully differential Successive Approximation Register (SAR). The digitised data is then fed to the digital signal processing block (DSP), which performs pedestal subtraction, mean common mode subtraction and zero suppression. After the DSP the data, with added header information, are placed into a de-randomising buffer [28] and transmitted to the consecutive parts of the read out system using serial links.

The ASIC is controlled via the LHCb common protocol consisting of two interfaces: the Timing and Fast Control (TFC) and the Experiment Control System (ECS) [28, 29]. The TFC interface delivers the 40 MHz clock and other crucial information and commands, synchronised with the experiments clock, while the ECS serves to configure and monitor the ASIC. The main specifications of the SALT ASIC are shown in Table 2.2.

2.7.1 Analogue Front-end

The analogue front-end has to be very fast with a peaking time ≤ 25 ns, have a very short tail to minimise pile-up and spill-over into the next bunch crossing, and also have very low power consumption (1–2 mW/channel). It should work with different strip sensors (capacitance range 5–15 pF), with input signal of both polarities and with good enough signal to noise ratio ($S/N > 10$), even with the worst operation conditions. One of the main challenges for the analogue block is to obtain a very short signal duration with the minimum possible power consumption. Preliminary studies showed that this is not possible with a standard semi-Gaussian shaping (with real poles in the transfer function), but that more complex shaping (using complex poles and zeros in the transfer function) is required. A first prototype of such a front-end was designed and fabricated in IBM CMOS

Table 2.2: Summary of the specification and overall requirements of the SALT ASIC.

Variable	Specification
Channels per ASIC	128
Input pitch	73 μm
Packaging	No side bonding on ASIC
Total ionising radiation dose	30 MRad
Total power dissipation	Below 1 W for 128 channels (room temperature)
Load capacitance on channel	5 – 10 typical, <20 pF max
Maximum leakage current	\sim 200 nA per channel
Noise	\sim 1000 e $^-$ at 10 pF
Maximum cross-talk	Less than 5% between channels
Signal polarity	Both electron and hole collection
Dynamic range	Input charge up to \sim 30 000 e $^-$
Linearity	Within 5% over dynamic range
Pulse shape	Pulse tail after $2*T_{peak}$ \sim 5% of amplitude (only in case of complex shaper) $<$ 20 beam-crossings
Recovery of baseline to within 1 ke $^-$ after 400 ke $^-$ signal	
Gain uniformity	Uniformity across channels within \sim 5%
ADC bits	6 bits (5 bits for each polarity)
ADC sampling rate	Up to 50 MHz (operation at 40 MHz)
Output formats	Non-zero suppressed, zero suppressed
Calibration modes	Analogue test pulses, digital data loading
Output serialiser	Serial links, several GBit/s Individual e-links at 320 MBit/s
Slow controls interface	I ² C, interface single-ended compatible with GBT-SCA
Digital signals	Data Interface: SLVS TFC interface and clock inputs: SLVS

130 nm. One of the main design goals was to verify whether a short symmetric pulse (with amplitude decreasing to \sim 5% 25 ns after the peak) could be obtained with an acceptable power consumption. The tests shown in Fig. 2.20 confirmed the theoretical expectations.

Although the power consumption of the prototype, around 1.8 mW, is still rather high, it was designed for significantly higher detector capacitance (up to 35 pF). These specifications were recently updated and a second prototype is currently being designed.

The analogue block includes also a single-ended to differential converter, since the front-end output is single-ended but the ADC input is differential. The first prototype of such a converter was also produced, and the results are promising. It will be studied in detail and updated in future prototypes.

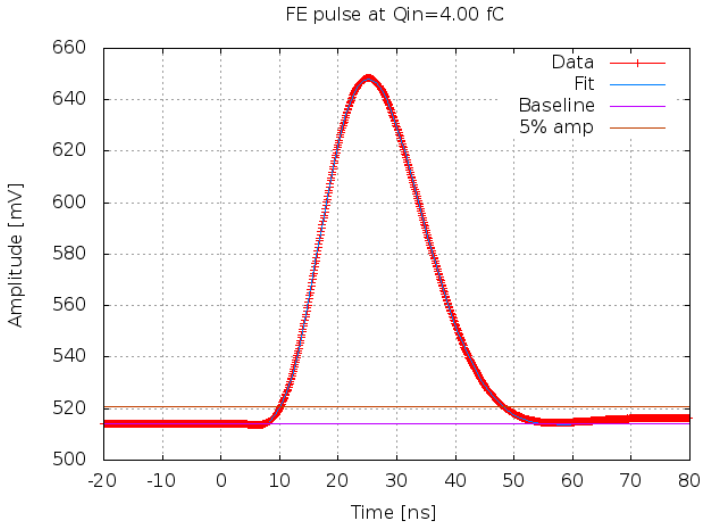


Figure 2.20: Example of the measured front-end impulse response, for a detector capacitance of 10 pF .

2.7.2 SAR ADC

2.7.2.1 Design

According to the SALT specifications a 6-bit resolution ADC, while sampling the signal with a rate of 40 MHz , is needed for the signal digitisation. The simulations confirmed that such a resolution is more than sufficient for the tracking purposes of the experiment. Again, one of the most important constraints of the ADC design is it should have a very low power consumption, much less than 1 mW at 40 MS/s (mega samples per second). This requirement has naturally led to the SAR ADC architecture. In order to further reduce the dissipated power, a Merged Capacitor Switching (MCS) scheme [30] has been chosen. Since in the given technology the best capacitance matching is offered by Metal-Insulator-Metal (MIM) capacitors, which are relatively large, a split capacitor Digital to Analogue Converter (DAC) approach has been used, as shown in Fig. 2.21. In order to increase the linearity of the ADC the input switches are bootstrapped, which reduces significantly their dynamic resistance.

In addition to the DAC switching scheme two other features are implemented to reduce the power consumption: a dynamic comparator and an asynchronous control logic, as shown in Fig. 2.21. The dynamic comparator dissipates power only during the bit cycling process, while the main power saving in the asynchronous control logic comes from the fact that the fast clock signal for the conversion of subsequent bits is eliminated. Finally, some more power is saved by implementing part of the logic with dynamic flip-flops.

The layout of a single ADC channel is shown in Fig. 2.22. The ADC pitch is currently $40\text{ }\mu\text{m}$ to match the analogue front-end pitch, but due to a change in the specifications, it will be modified in order to better match the pitch of the input pads.

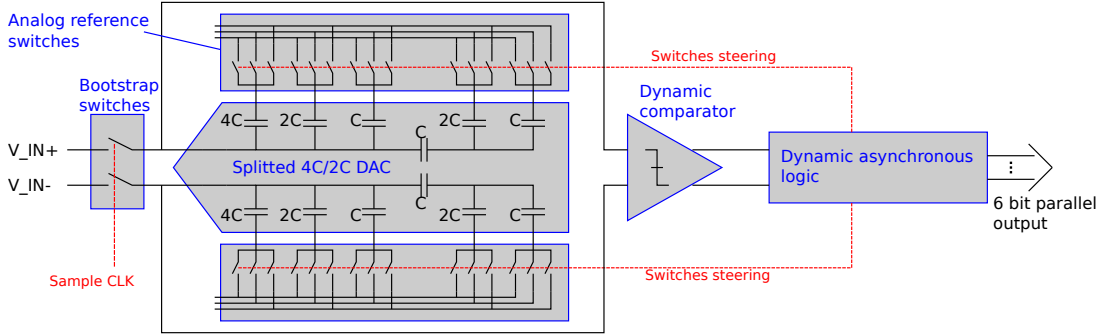


Figure 2.21: Block diagram of the 6-bit SAR ADC.

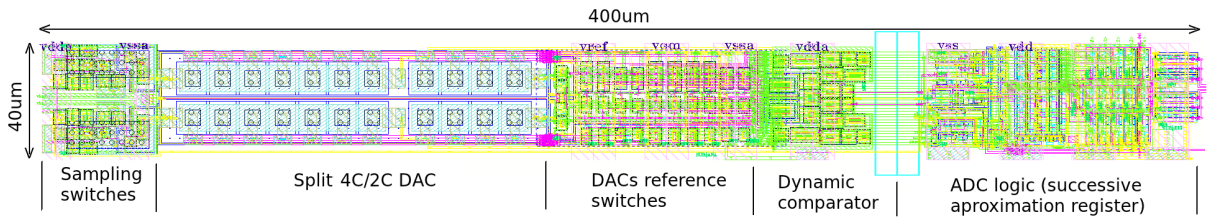


Figure 2.22: Layout of a single channel of 6-bit SAR ADC.

2.7.2.2 Measurements

A dedicated test setup, based on a Field Programmable Gate Array (FPGA) was developed in order to verify the performance of the ADC prototypes. Some basic functionality and power consumption tests were performed first, followed by detailed static and dynamic measurements. The ADC was fully functional at 40 MS/s, consuming around 0.35 mW.

Static measurements The static characterisation of the ADC channel was performed using the histogram method at 40 MHz sampling frequency with full range input signal. The differential (DNL) and integral (INL) non-linearities were measured at the nominal voltage supply of 1.2 V. The results are presented in Fig. 2.23. The maximum non-linearities are DNL < 0.35 LSB and INL < 0.25 LSB, which confirms excellent static performance.

Dynamic measurements To measure the dynamic parameters a sinusoidal differential signal was applied at the ADC inputs. Two types of scans were performed: an input signal frequency scan and a sampling frequency scan.

In both cases the standard dynamic ADC parameters were calculated: Total Harmonic Distortions (THD), Signal to Non-Harmonic Ratio (SNHR), Signal to Noise and Distortions (SINAD) and, based on the SINAD, Effective Number of Bits (ENOB).

The input signal frequency scan was performed with the ADC at a constant sampling rate of 40 MS/s, and changing the frequency from the input signal from a few Hz up to the Nyquist frequency. The measured results are shown in Fig. 2.24. Since the SINAD is

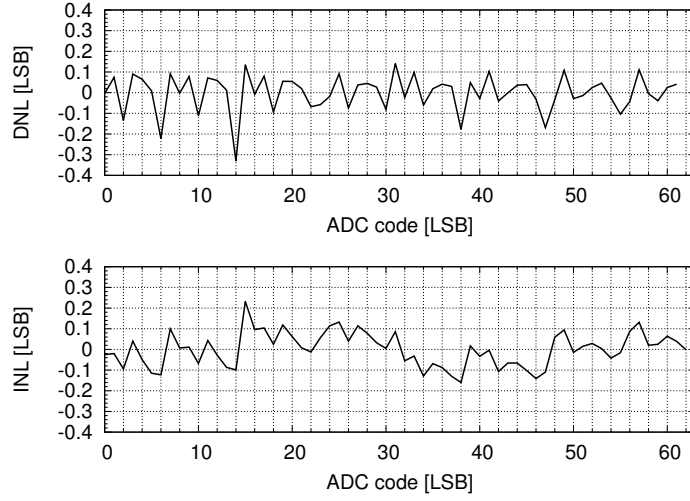


Figure 2.23: ADC static measurements result.

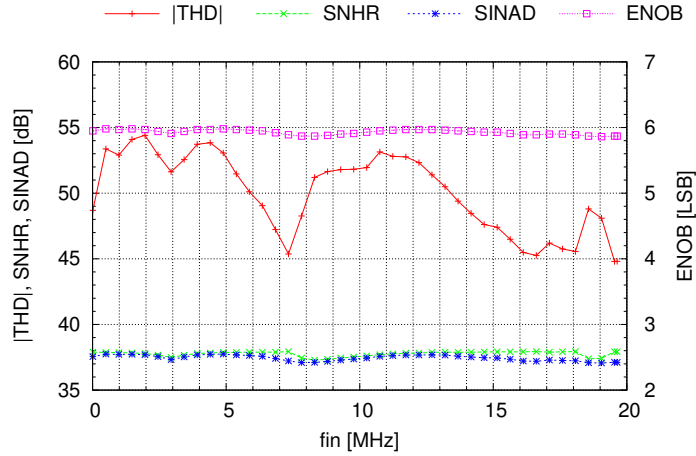


Figure 2.24: Input frequency scan at 40 MS/s; left vertical axis shows THD, SNHR and SINAD while right axis is ENOB.

almost identical to the SNHR we conclude that harmonic distortions are negligible. The ENOB is above 5.85 in the whole range confirming excellent dynamic performance.

The sampling frequency scan was performed to verify the maximum ADC sampling rate. The results of this scan are shown in Fig. 2.25. The input signal frequency and the sampling rate of the ADC were modified together in order to always keep the input signal at the Nyquist frequency. It was concluded that the ADC can work up to 80 MS/s with an ENOB above 5.85. The ADC is ready to be implemented in the multi-channel SALT ASIC.

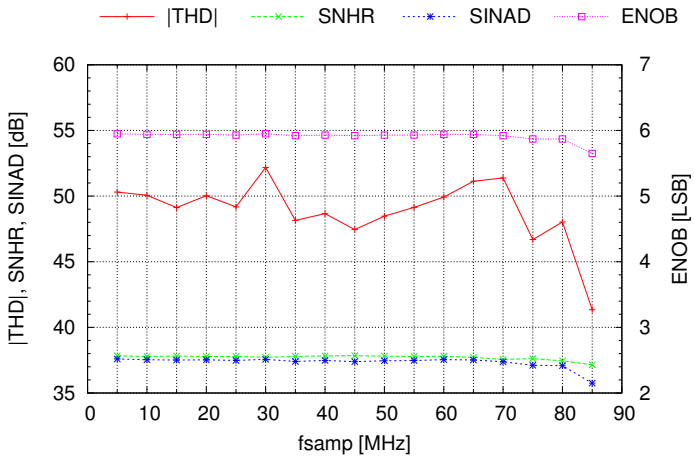


Figure 2.25: Sampling frequency scan with Nyquist input signal; left vertical axis shows THD, SNHR and SINAD while right axis is ENOB.

2.7.3 Digital Signal Processing Algorithms

Among the innovative solutions that are being implemented in the SALT design, which were not employed in the previous read out ASICs, is the DSP block. Its main goal is to reject the noise hits and perform the data compression. This functionality is critical for the UT detector and the data acquisition system (DAQ) of the upgraded LHCb spectrometer, since the transmission of the raw data is prohibited by cost.

2.7.3.1 Raw Data Processing Chain

A balanced approach needs to be pursued for the on-chip DSP procedure. It cannot be too complicated because of the validation and the power dissipation issues. On the one hand, complex processing algorithms are both cumbersome to debug (using the low level Hardware Description Language – HDL) and test and they require a large number of logical components. On the other hand, the algorithm must provide a sufficient ratio of raw data compression to minimise the data bandwidth to the optical links. Preliminary studies showed that the baseline processing chain, that fulfils these criteria, should consist of the following steps:

1. bad/noisy channel masking,
2. pedestal following (baseline calculation),
3. common mode suppression,
4. noise hit rejection and zero suppression,
5. raw bank encoding.

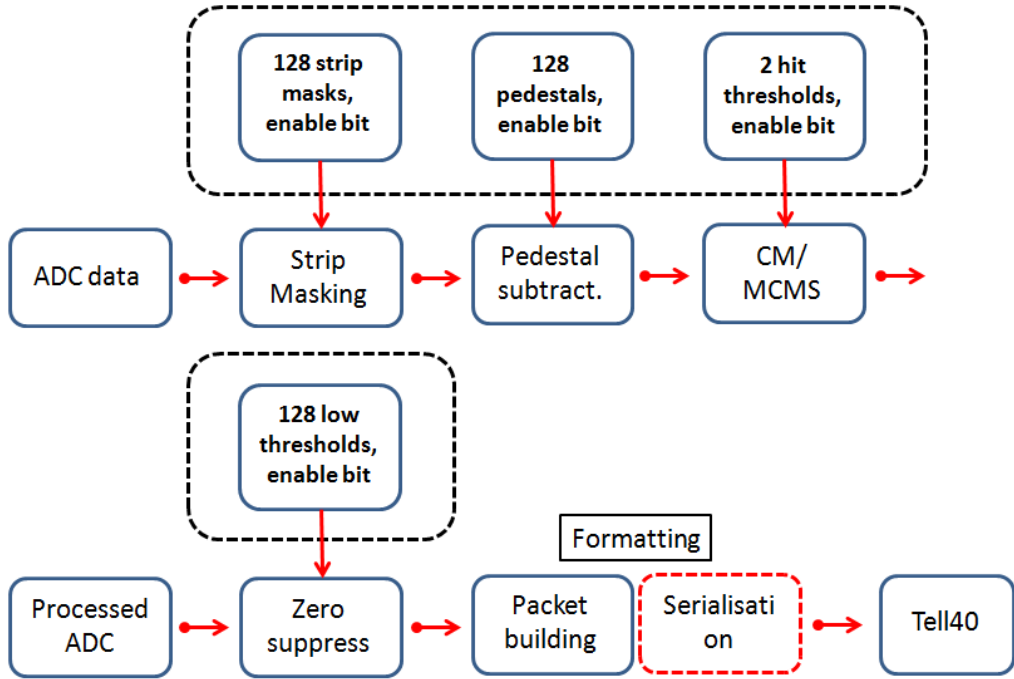


Figure 2.26: Baseline digital signal processing chain for the SALT ASIC. Dedicated calibration runs will be used to determine processing parameters for the DSP algorithms configuration. The calculated parameters will be then stored in the processing parameters data base and used by the Experiment Control System (ECS) to configure the read out ASICs

The processing chain is presented schematically in Fig. 2.26. In the first step of the processing a mask for each channel is applied to flag it as bad or noisy - such a channel is then excluded from further processing.¹ The masks should be determined in dedicated calibration noise runs. Next, the raw ADC samples are processed by the pedestal following block in order to calculate the baseline position in each channel. In practice it is quite difficult to implement the pedestal calculation in the ASIC. Instead the actual pedestal values will be calculated in the appropriate high level emulation software using the noise calibration data. These pedestals will be then uploaded to the ASIC memories and used in the baseline determinations. After the pedestal subtraction a common mode suppression algorithm is applied. For the baseline algorithm it is foreseen to use the simplest Mean Common Mode Suppression version, which assumes that the common mode noise is constant throughout the ASIC. All 128 channels (excluding the masked ones) will be used simultaneously by the algorithm to estimate the common noise value. The final step of the processing chain is the zero-suppression where the false hits should be rejected with highest possible efficiency. The zero suppression algorithm for the SALT applies one discrimination threshold tuned individually for each channel (the values of these thresholds

¹This should be treated with care, even if a value of charge in a given channel is set to zero it may change during the common mode suppression, so, it is vital to set the clustering thresholds properly for such channels as well.

will be determined by the emulation software using the noise runs). Dedicated studies must be performed to chose these thresholds properly in order to find the right balance between the raw data suppression factor and hit detection efficiency. Too low thresholds will result in a non-manageable data stream while too high ones may reject channels with lower signals (as a result of charge sharing, for example). This in turn could artificially degrade the single hit resolution and potentially worsen the physics performance of the UT.

The processed data must be encoded and formatted into the raw bank structure containing a header and an opaque data body as described in Sec. 2.9.1. Finally the transport frames are created (serialisation) using the GBT data protocol and sent out via optical links for further processing in the back-end TELL40 electronics boards [31].

2.7.3.2 DSP Emulation

Processing emulation will play an important role in both the ASIC development and subsequently in the detector daily operation. Since the DSP is going to be implemented directly in the ASIC a great deal of care must be taken to prepare and validate the algorithms. It was decided to take a two prong strategy using high and low level emulators. The former is implemented in C/C++ language whilst the latter would be run in an FPGA using an HDL language. In the future the high level emulator will be integrated with the experimental software platform and used to perform calibration and monitoring operations during the collision data taking.

2.7.4 Serialisation and Data Format

After the DSP the data will be kept in memory until they are transmitted to the DAQ back-end. The memory will have around 5 kBit. This memory block will be either described in HDL and synthesised or built from a macro block.

A single 40 MHz clock will be delivered to the ASIC. The higher frequencies needed for the data serialisation will be generated in a PLL. Both the PLL and a DLL for a precise adjustment of the ADC sampling clock are being designed.

The SALT ASIC will send data out using several serial links, known as e-links, each with a data rate of 320 MBit/s. All SALT ASICs will have five e-links. Depending on the location in the detector, which determines the amount of data (based on channel occupancy), the number of enabled e-links can be tuned to match the bandwidth requirements. Each ASIC will use at least two e-links and the unused data links will be disabled to save power.

The data will be organised in packets. Several packet types, responding to the number of hits, the buffer status and the different TFC commands are built in the ASIC. The specific data format is described in Sec. 2.9.1. In all cases the length of the data packet is always a multiple of six bits, which simplifies the implementation of the memory and the DAQ.

2.7.5 Control Interfaces

The SALT ASIC utilises two control interfaces, ECS and TFC. The ECS is a slow control interface mainly for configuration and monitoring while the TFC is a fast interface synchronised with main experiment clock.

The ECS commands will be transmitted to the ASIC via an I²C link at 400 kHz frequency. Out of the available seven bits of the I²C address, three will be configurable (via pads). The remaining four address bits will be either hard coded or used for other purposes. At the present design stage around 500 8-bit configuration and status registers are foreseen. All those registers will be triplicated to protect them against single event upsets (SEU).

It was decided that all the required TFC commands will be delivered to the ASIC via a single e-link at 320 MBit/s. At this data rate, up to eight different TFC commands can be delivered to the ASIC. A full list and description of the selected TFC commands can be found in Sec. 2.9.3. To ensure the synchronisation between the ASIC and the periphery electronics, a phase shift adjustment circuitry will be implemented.

2.7.6 Ancillary Blocks – PLL, DLL, SLVS, DACs

Many other analogue and digital blocks need to be designed to complete the SALT functionality. Some of them have already been agreed and specified and the others are being optimised together with the system design.

2.7.6.1 SLVS Interface

A differential interface is needed to enable fast data transmission. For low voltage supply technologies, as in CMOS 130 nm, a natural choice is the SLVS (Scalable Low Voltage Signalling) interface. A first version of an SLVS driver and receiver were implemented together with the ADC and PLL prototypes, and they have been tested beyond 1 GHz, way above the SALT requirements. In the first prototypes features such as tunable drive-current or pre-emphasis were not implemented. Those features will be added in the next prototype, and dedicated tests of data transmission will be performed in order to decide if the pre-emphasis is needed.

2.7.6.2 DACs

Various DACs are needed for setting different analogue biasing signals. They will be designed and included in the next prototypes.

2.7.6.3 PLL

As described in previous sections, a dedicated Phase-Locked Loop (PLL) is needed for the generation of the high frequency clocks needed in the ASIC. The first PLL prototype was designed and fabricated in IBM 130 nm CMOS technology [32]. The PLL block diagram is

shown in Fig. 2.27. It contains a Phase and Frequency Detector (PFD), a Charge Pump (CP), a Low Pass Filter (LPF), and a Voltage Controlled Oscillator (VCO). The layout of all the PLL blocks (analogue and digital) was drawn manually to obtain the lowest power and area. It has been designed and simulated for frequency ranges of 10 MHz–3.5 GHz. Four division factors i.e. 6, 8, 10 and 16 were implemented in the PLL feedback loop. The main PLL block, the voltage controlled oscillator (VCO), should work in 16 frequency ranges/modes, switched either manually or automatically.

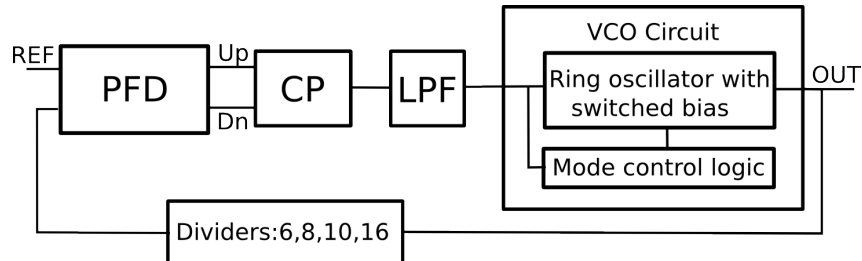


Figure 2.27: The SALT PLL block diagram.

Measurements done in the frequency range 20 MHz–1.6 GHz showed that the PLL is fully functional and generates proper clock signal. The PLL transfer function is presented in Fig. 2.28 where it is seen that all division factors are working properly. Power consumption of around 0.6 mW was measured at 1 GHz for a division factor equal to ten.

A new prototype fulfilling exactly the SALT specification is currently being designed. It should consume less than 1 mW. Particular attention is being given to radiation hardness issues. As an alternative, an existing PLL designed at CERN is also being considered, but it consumes much more power (30 mW).

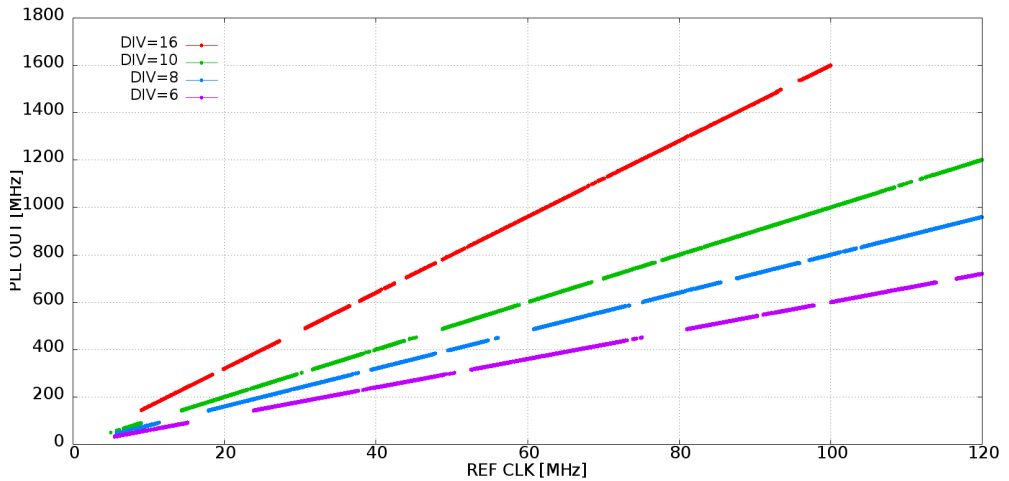


Figure 2.28: PLL output frequency vs reference clock for all division factors

2.7.6.4 DLL

A variable delay is needed for the adjustment of the analogue front-end output sampling time. This feature will be implemented by a dedicated Delay-Locked Loop (DLL) which is currently being designed.

2.7.7 Floor-plan and ASIC Integration

One of the most important issues concerning a multi-channel ASIC is the uniformity of the analogue parameters in the front-end and ADC blocks. Apart from an unavoidable statistical spread, arising from the production process, a systematic spread may also occur. The main source of the systematic spread is the heterogeneity of the voltage supply across the channels, due to the resistivity of the power busses. To minimise that spread the voltage supply is typically delivered from both sides of the ASIC. Since there will be no side bonding in the SALT, another power distribution scheme needs to be used. This drives the floor-plan of the ASIC.

The SALT ASIC is an example of a pad limited design since all pads (for control signals, data, bias voltages, power supplies) should be placed only on the back side of the ASIC. A reasonable solution is to split the front-end channels into two blocks of 64 channels each (see Fig. 2.29) and to deliver the voltage supply through the centre of the ASIC. All the required biasing circuitry will be placed between these two blocks. The front-end and ADC parts will be followed by the digital block (DSP, memory, serialisation, I²C, PLL, etc.) common for all channels. The input pads will be placed in a single row with a pitch of 73 µm. Apart from the input pad of each of the 128 channels, two additional ground pads will be added. The vertical dimension of the ASIC will be around 10 mm while the horizontal dimension is not yet fixed and depends on the final design implementation.

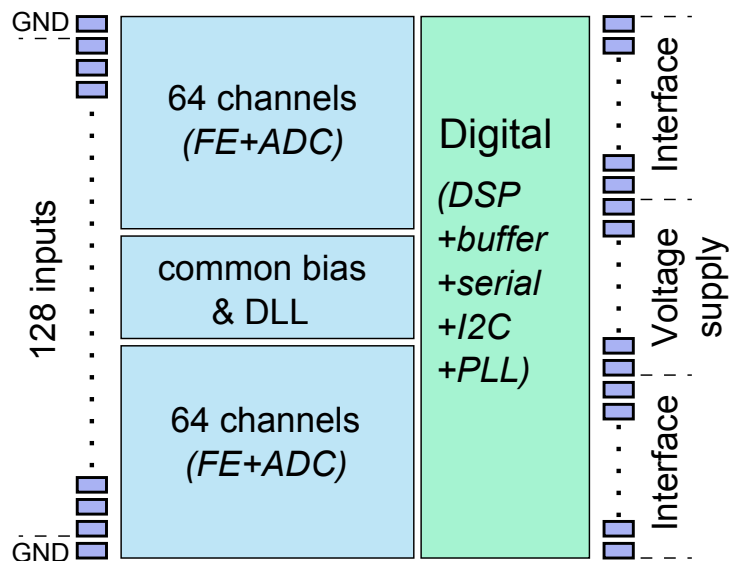


Figure 2.29: Preliminary floor-plan of the SALT ASIC.

2.8 Electronics

The design of the UT electronics and read-out chain follows the general LHCb electronics architecture [28], customised to the UT requirements as shown in Fig. 2.30. As discussed in previous sections, signal to noise considerations dictate the placement of FE electronics in proximity of the sensors. The FE ASIC also contains significant digital processing capability, including zero-suppression, in order to reduce the data flow rate to the back-end read-out boards (TELL40) and the data acquisition system. However, in order to reduce power dissipation near the sensors, thereby the cooling load, and avoid the additional mass and complications of extra electronics components, some of the digital processing functions, including the electro-optical transition and distribution of fast timing and slow control signals are designed to take place at the electronics boards placed at the periphery of the detector boxes (PEPI units- defined below). The electrical connectivity between the FE electronics and the PEPI units is achieved via low mass flex cables running along the staves, containing signal and control data lines as well as power lines. The data concentrator boards (DCB) combine the data received from FE ASICs on several e-links and transmit via optical fibres to TELL40 read-out boards in the counting rooms, which after additional processing and filtering by the Low Level Trigger (LLT) are transmitted to the data acquisition system. The functionality of the PEPI units, which contain all the DC/DC converters, also includes the conditioning and distribution of LV and HV to the FE ASICs and silicon sensors. Bulk power is supplied to the system from external units in the counting rooms and the experimental cavern.

2.8.1 Hybrid and Interconnect Cable

The design and specifications of the FE ASIC and the hybrid were described in previous sections. Here we discuss the requirements and specifications of the interconnect cable between the hybrids and the PEPI boards. The cable runs along the stave, with power and signal lines from the innermost sensors as long as ~ 0.7 m (half-stave length). Given the large number of interconnect lines ($\sim 20,000$ signal lines alone), the cable design, therefore, involves a trade off between low mass requirement (the overall UT mass budget per plane is $\sim 1\% X_0$) and low voltage drop and signal integrity. The 4,192 FE ASICs are estimated to require nearly 4,000 Watts of total power. The majority of the signals will be implemented using an enhanced version of the JEDEC-400 scalable low-voltage signaling (SLVS) standard. The enhancement will add the capability to selectively boost the drive current to better accommodate the longest signal runs. There will also be several low speed I₂C buses used for configuration and status monitoring. Lastly, there will be a number of environment sensors distributed throughout the detector planes to monitor temperature and humidity.

The fundamental requirement for the power lines is to have a voltage drop along the trace compatible with the maximum supply voltage allowed by the SALT chip with the minimum amount of material. On the other hand, the design of the differential line (needed for the SLVS transmission) requires not only a 100 Ohm nominal differential impedance,

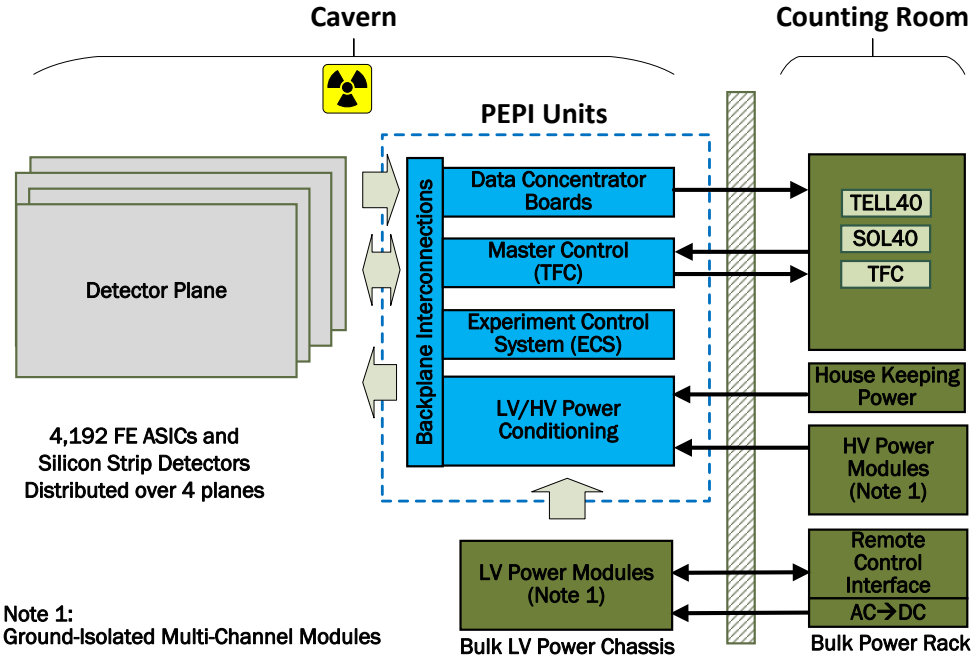


Figure 2.30: Conceptual Block Diagram of Primary UT Electronics System Functions.

but also a $\sim 5 \text{ Ohm/m}$ conductor resistance to allow small attenuation, skew between signal conductor as close to zero as possible and low cross-talk ($< 2\%$ on adjacent lines). Moreover, the material (conductor and insulator) in the cable should be spread over the full size of the stave for a uniform material distribution.

The design of the cable is currently underway and we anticipate several months of R&D work before finalising the selection of appropriate technology. A preliminary design study is carried out on a multi-layer flex circuit using a standard fabrication process based on 1 oz (35 μm) copper-polymide material (Altaflex, Molex and other) that offers also a panel size exceeding 70 cm in one dimension (maximum aspect ratio 10:1). The design parameters are summarised in Table 2.3.

Different cables (3 – 4 types) have to be designed to take into account the UT stave differences, both in term of number of ASICs to be powered and in signal lines. The proposed solution for the cable is illustrated for the C-type stave, which contains the largest number of power and signal connections (24 ASICs and 104 differential lines).

A preliminary layout of the design, Fig. 2.31, shows that the requirement can be fulfilled by a two-layer flex tape, 10 cm wide, with micro-strip-type signal traces on the top and power planes on the bottom layer. The differential impedance is estimated to $\sim 92 \text{ Ohm}$ and the 5 Ohm/m conductor resistance is achieved by a 175 μm signal trace width. Two large separate power strips, analogue and digital power, have been considered for a four ASICs multiplicity and each power has sense lines for precise voltage regulation.

Table 2.3: The parameters used in the preliminary design of the UT interconnect cable

Hybrid Supply Voltage (External input to SALT) (V)	1.75
Max Voltage Drop (round trip) (V)	0.5
SALT Operating Current (A)	0.6
Power cable max. length (round trip) (m)	>1.4
Minimum trace/space (μm)	125
Polymide thickness (internal layer) (μm)	50
Polymide thickness (outer layer) (μm)	16

The impedance and attenuation of the differential lines have also been simulated given the stated requirements above. The simulated data transfer at 320 Mbps is shown in Fig. 2.32.

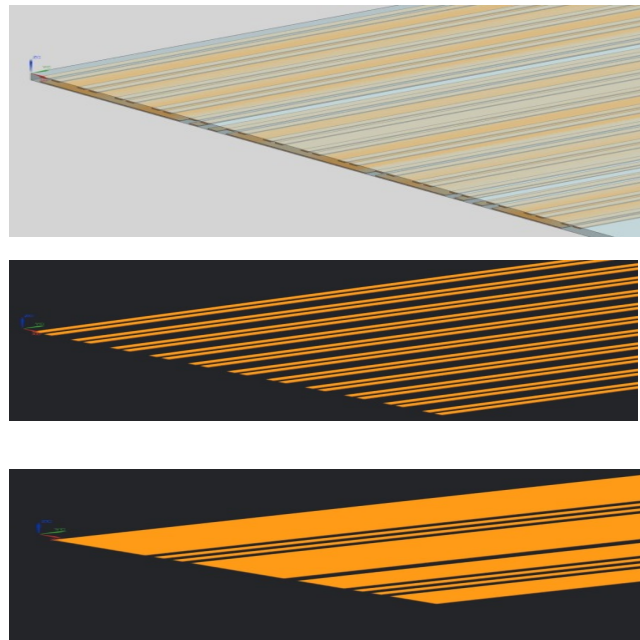


Figure 2.31: A two-layer interconnection cable (top). Top layer: micro-strip traces (middle). Bottom layer: power (bottom)

Different configuration of the flex cable are presently under study to optimise the design against uniformity, cross-talk etc. Prototypes of the flex cable will be produced and tested in the next months. We are also considering the possibility to separate the interconnection cable in two flat flex cables. One cable, 4 cm wide, would contain the power wires, while

the second cable (6 cm wide) will be only for signals and could guarantee better noise immunity from the noise coming from the digital power. Presently the material estimate of the interconnection cable is equivalent to $\sim 0.15\% X_0$. However a reduction in radiation length could be achieved by using a copper/aluminum mixed technology. The use of aluminum, limited to the power layer, is part of the on-going R&D.

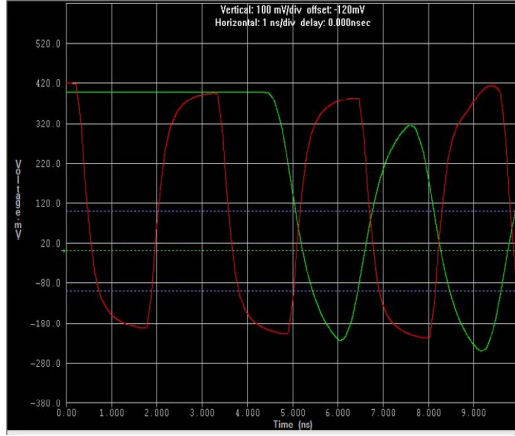


Figure 2.32: Signal 320 (Mbps) transmitted by a micro-strip. Red: input signal. Green: output signal (4.5 ns delay for a 80 cm long trace)

2.8.2 Periphery Electronics

The four UT detector planes are electrically connected to the periphery electronics processing interface (PEPI) units that will be physically located close to the detector outside the acceptance, with a total of 16 PEPI units, one for each quadrant (four quadrants per detector plane). The PEPI unit functionality will be accomplished with five primary types of board designs as shown in Fig. 2.30. These include the Master control board, Experiment Control System (ECS) board, Data Concentrator Board (DCB), and power distribution board along with a back-plane. These boards will be partitioned, replicated, and connected to back-planes. The staves are electrically split into the upper and lower halves to minimise the cable lengths. The signals are routed to the PEPI units located at the edges of the detector planes. The back-plane will be used to efficiently route the signals to the various boards in the PEPI units. The cavern area is subject to both significant radiation levels and stray magnetic fields that are highly dependent upon the proximity to the beam-pipe and the magnet. Consequently, the electronics must survive significant radiation doses, operate gracefully through single event upsets, and use components not influenced by strong magnetic fields.

The data received at the data concentrator board through e-links are logically grouped and combined within the PEPI units for transmission to the counting room via fibre

optic connections, each operating at 4.8 Gbps. The 16 PEPI units will utilise a total of approximately 1,500 fibre cables to route data to the counting room. A small subset will be used to receive control and configuration commands which will manage the operating modes, configuration, and resultant data flow.

The preliminary architecture plan for a single PEPI unit associated with a single detector quadrant is shown in Fig. 2.33. The PEPI unit architecture exploits several major custom ASICs that are presently completing development at CERN. These include the GBTx, GBT-SCA, and the Versatile link components. These components are all designed to operate reliably in the expected radiation environment of the cavern areas.

The GBTx ASIC, a dedicated high-speed serialiser/deserialiser (SERDES) communi-

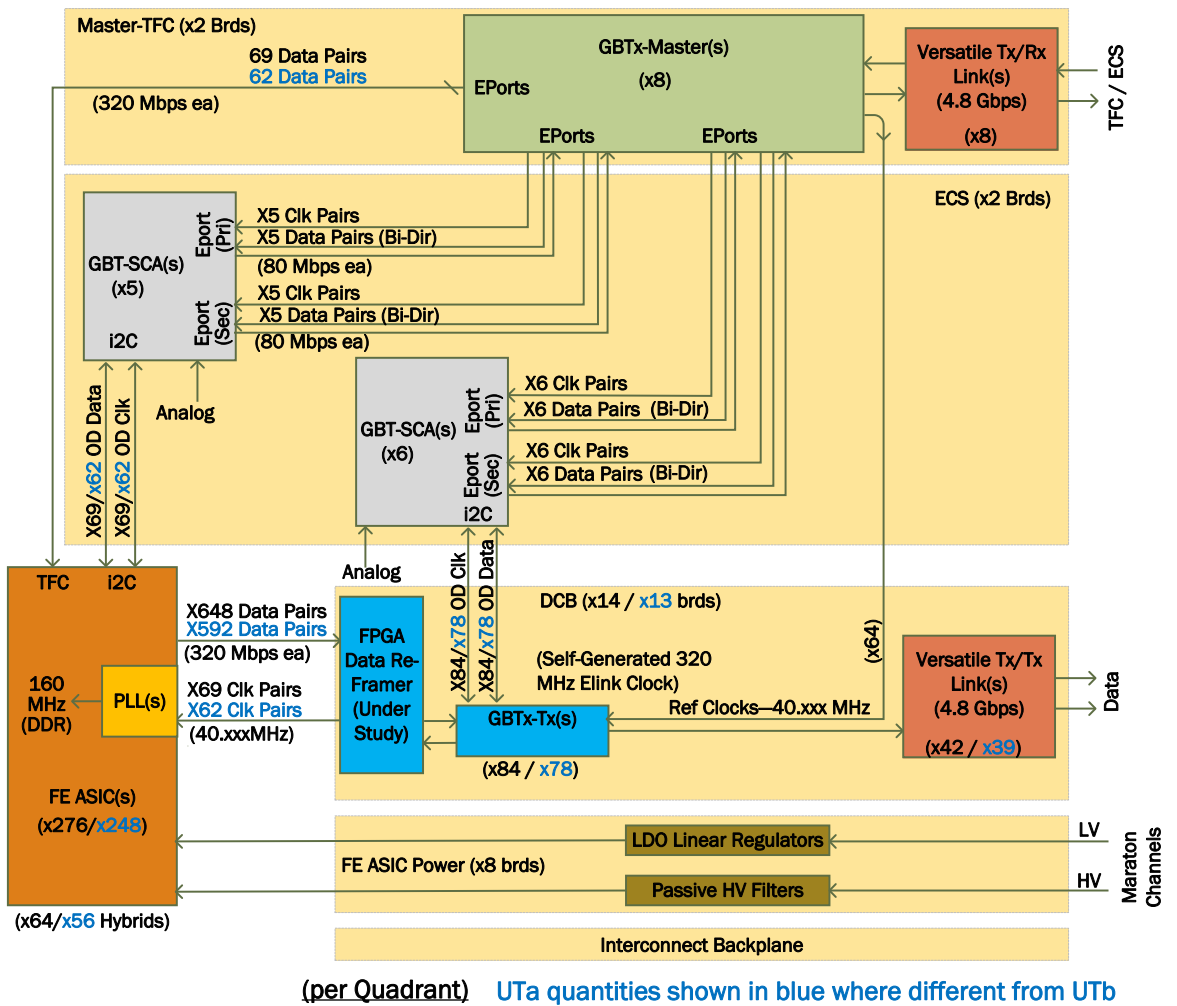


Figure 2.33: Block diagram of the PEPI architecture.

cations integrated circuit (IC), provides an effective communications foundation for the data concentrator and master control boards. It has a dedicated high-speed SERDES receive and transmit communication lane that can be routed to various lower speed serial links that will be configured to operate at 320 Mbps for the PEPI units. Consequently, a single GBTx can accommodate up to ten e-links (operating in standard-bus mode) of continuous data transmission. As described above, each FE ASIC will have a maximum of five e-links. The GBTx dedicated 4.8 Gbps SERDES Rx and Tx ports are designed to use the Versatile link components as fibre optic interfaces. The GBT-SCA is designed to provide experiment control and monitoring. These ICs reside on the master control board with direct interfaces to the GBTx masters. The I2C interface is the primary control bus that will be used amongst the various available options to communicate the configuration and status information. The global trigger and fast control (TFC) data for each bunch crossing is sent from the SOL40 [28,29] boards to dedicated GBTx-Masters and distributed to the FE ASICS as shown in Fig. 2.33..

2.8.3 System Power Distribution and Grounding Scheme

The power subsystem is divided into five distinct areas of source and distribution as shown in Fig. 2.30. The counting room contains the high voltage (HV) bulk power rack as well as the housekeeping power, while the bulk low voltage (LV) and PEPI unit signal conditioners are located in the cavern.

The low voltage power supplies will be located underground, partly in the counting rooms behind the shielding wall, and partly in the experimental cavern, in the balcony racks. The voltage drop in the cables can not be considered negligible due to the cable length (~ 80 m for the power supplies in the counting room; 20 – 30 m for those on the balcony racks) and the considerable expected current load. For that reason the MARATON (MAgnetic field and RAdiation TOleraNT) system from W.I.E.N.E.R is being considered. These power supplies provide low noise and low ripple floating channels with remote sensing capability. They have been widely used in high energy physics and have been shown to be very reliable. Moreover, the reuse of a pool of available MARATON power supplies in LHCb allows for significant cost reduction.

The MARATON power supplies will provide bulk power to the PEPI units via multiple ground-isolated channels, with outputs programmable between 1 and 8 volts with 50 Amps maximum per channel. The PEPI units will each have dedicated local power conditioning boards, employing L4913 radiation tolerant linear regulators, that serve as the interface for all DC power within the PEPI units and for the FE ASICS distributed throughout the UT planes.

The high voltage (HV) power supplies will also be located in the underground counting rooms behind the shielding wall. The UT sensors need a bias voltage in the range of 300 – 500 V, with the expected leakage current below 1 mA for the central region and below 0.5 mA in rest of the detector. Splitting the HV into 16 ground-isolated paths, one for each quadrant, further reduces the maximum current and corresponding voltage drop across the nominal 150 m cable path from the counting room to the cavern. To simplify

the grounding scheme, floating (ground-isolated) channels are preferred. A commercial system can be used in this scenario. Patch panels will be placed near the PEPI units to group and distribute the bias voltage to the sensors.

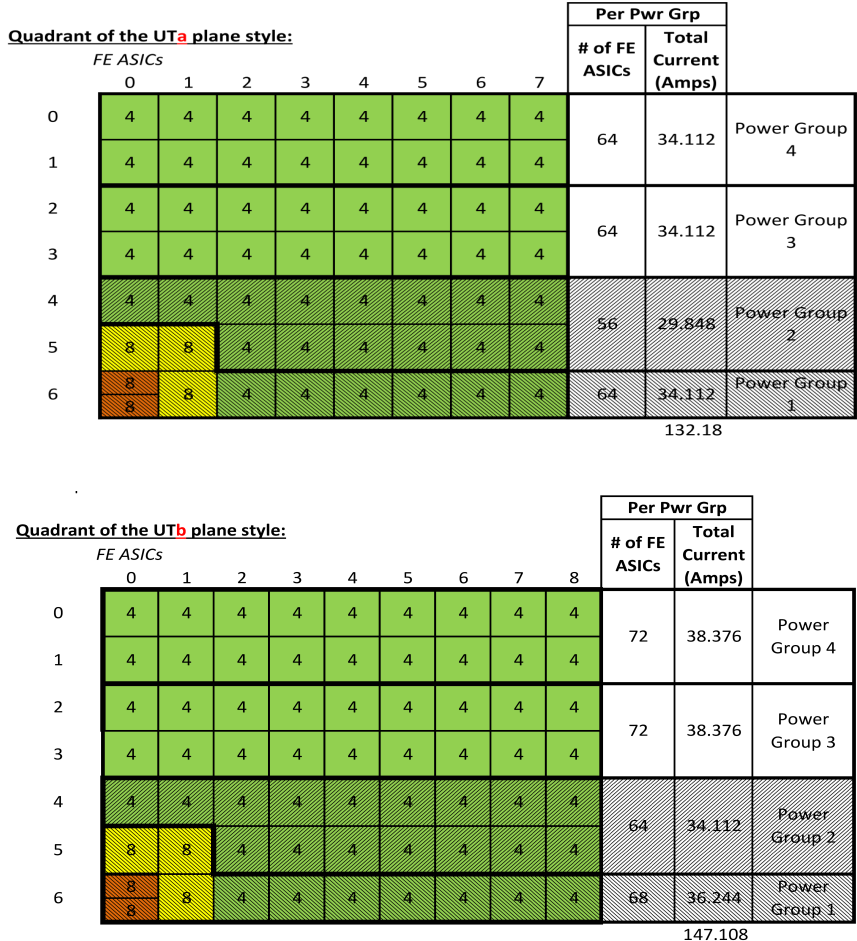


Figure 2.34: Ground isolation groups for two representative quadrants of the UTa and UTb planes.

The PEPI chassis primarily communicate with the FE ASICs using a modified SLVS differential interface. The SLVS common mode capability is more limited compared to other industry standard differential interface standards. Therefore, the common mode voltage between the PEPI chassis and FE ASICs must be managed to ensure robust signal communications. The return current through the ground return lines between the FE ASICs and the PEPI chassis back-plane can lead to an undesirable net difference between

the ground at the FE ASICs and the ground reference established at the back-plane for each PEPI chassis. Consequently, ground-isolated power channels will be exploited to manage the ground shifts by intentional design. The final design will represent a balance between using a reasonable number of isolated power channels and managing the worst case common mode voltage to within acceptable limits. The FE ASICs will be powered through wire pairs that are connected to groups of four adjacent FE ASICs. Therefore, each group of four FE ASICs will have an electrically equivalent wire pair running to the PEPI chassis back-plane. These will be further combined in the PEPI chassis back-plane according to grouping arrangement shown in Fig. 2.34. These larger groups have been selected primarily based on the nominal power return wire lengths. Each larger group will be powered by a dedicated ground-isolated power channel using dedicated source and return wire pairs. The loop area of each power distribution wire pair will be kept intentionally small to minimise electromagnetic interference (EMI) effects. Several independent ground sense wires will be resistively combined to provide both an accurate and redundant zero volt reference connection to the PEPI chassis ground planes. The ground sense connections will essentially pull the return leg of the floating power sent to the FE ASICs to nearly the same potential as the reference ground established at the PEPI chassis back-plane. The latter will effectively serve as the single point ground reference for the UT detector quadrant. The ground reference wires will have nearly zero current flowing through them to assure the ground reference is accurately maintained at the remote hybrid locations and that no current loops are created.

2.8.4 Interlock System

The UT system will employ several layers of fail-safes to protect the detector. The PEPI units will have internal fail-safes that work in concert with the overall detector interlock architecture. These fail-safes will include PLC sensors deployed around the detector to monitor parameters such as detector box temperature and humidity, PEPI units temperature, cooling, HV interlock, smoke detection, water leak detection, gas flow in the box, and possibly air flow around PEPI boxes, if they are air cooled. Failure or alarm in those sensors should trigger either an alarm to the expert on call and a power cut when there is immediate danger for the electronics. The smoke detection should also trigger an alarm to the fire brigade. The intent will be to prevent damage from faults rippling through the system in destructive manner. This will require sufficient redundancy in the sensor network as well as the fault decision tree implementation to avoid false shutdown events from radiation induced transients or invalid sensor inputs (e.g. failed). A dedicated and isolated DC power source that originates directly from the counting room will redundantly supply a small amount of power to a limited set of circuits necessary to obtain functional status without the full system powered. Items such as the UT plane operating temperatures and humidity and general power status will allow the state of the UT system to be evaluated remotely. This provides a flexible contingency operational mode in the event that there are unexpected events such as loss of system communications, unexpected power shutdown, or a detected fault condition.

2.8.5 Prototyping

Given the relatively long cable lengths ($\sim 0.7\text{ m}$) from hybrids to the PEPI units, studying the transmission properties of SLVS signals through the flex cable is of very high priority. Test boards will be developed, employing prototype SLVS drivers in SALT chips, to perform signal integrity studies.

Studies are underway of the properties of the CERN developed linear regulators. Prototypes of the five PEPI boards will be made and tested, as the CERN developed components, GBTx, GBT-SCA, VTTx and VTRx chips, become available. While these components have been designed for radiation exposures similar to the region occupied by the PEPI unit, the data concentrator board may be required to contain an FPGA to perform some of the digital processing that is currently planned for TELL40 boards. This would require employing a radiation hard FPGA, thereby radiation exposure studies of DCB boards will be necessary.

2.9 DAQ Integration

The UT DAQ follows the general LHCb data acquisition architecture. The information flow of event data transfer, timing and fast control (TFC), and experiment control system (ECS) is illustrated in Fig. 2.30.

Signals are digitised by the SALT ASIC and further processed by the DSP inside SALT ASICs. Zero suppressed data is packed and saved in a buffer and shipped out via e-links. At data concentrator boards that are located in the periphery of the UT planes, event data from multiple e-links are grouped by GBTx ASICs to form the GBT data frames. Then the data are sent to the AMC40 cards via optical fibres and processed there.

Information flow of TFC and ECS data follows a similar path but bi-directionally. TFC commands and ECS configuration and monitoring data are distributed from the SOL40 boards to the master GBTx at the periphery electronics, and further to the front end ASICs. Responses from the front end ASICs and periphery electronics, including monitoring data, are sent in reversed direction.

2.9.1 Data at ASICs

The SALT chip deploys six bit ADCs and operates in a bi-polar mode. After pedestal subtraction the signal of a channel has effectively five bits value. The ADC digitisation precision, range and zero-suppression (ZS) threshold affect hit position reconstruction and monitoring of the detector performance after irradiation. Preliminary optimisation suggests that the SALT chip should operate at $1000\text{ e}/\text{ADC gain}$, with a threshold of 6000 e . The maximum ADC value 31 corresponds to $31,000\text{ e}$, which is about 1.7 MIPs for $250\text{ }\mu\text{m}$ thick silicon.

The LHC beam upgrade will change the filling scheme. At the LHCb interaction point there will be up to 2400 out of 3654 bunch slots with beam-beam interactions. The system

is required to be able to operate at $2 \times 10^{33} \text{cm}^{-2}\text{s}^{-1}$, but should have a safe margin of operation above this luminosity.

The number of hits on each ASIC to be read out is estimated from a minimum bias simulation sample generated at a luminosity of $2 \times 10^{33} \text{cm}^{-2}\text{s}^{-1}$ ($\nu = 7.6$), and $\sqrt{s} = 14 \text{ TeV}$. The average number of hits per event is ≈ 1000 , with average cluster size of 1.44 strips. Considering all 4192 ASICs, the average number of hit strips per ASIC is 0.34. The hit density is much higher in the central region and falls off as roughly $r^{-1.68}$, where r is the radial distance from the centre of the beam-pipe. The sensors around the beam-pipe have better segmentation, and 1/4 of the size of the nominal strips. Even so, the average number of hit strips reaches 2.3 per event per ASIC, i.e. the occupancy is 1.8%, as shown in Fig. 2.35(a). In this figure, the four UT planes are presented with different colors, and the chip ID increments within each stave, starting from the left-most stave.

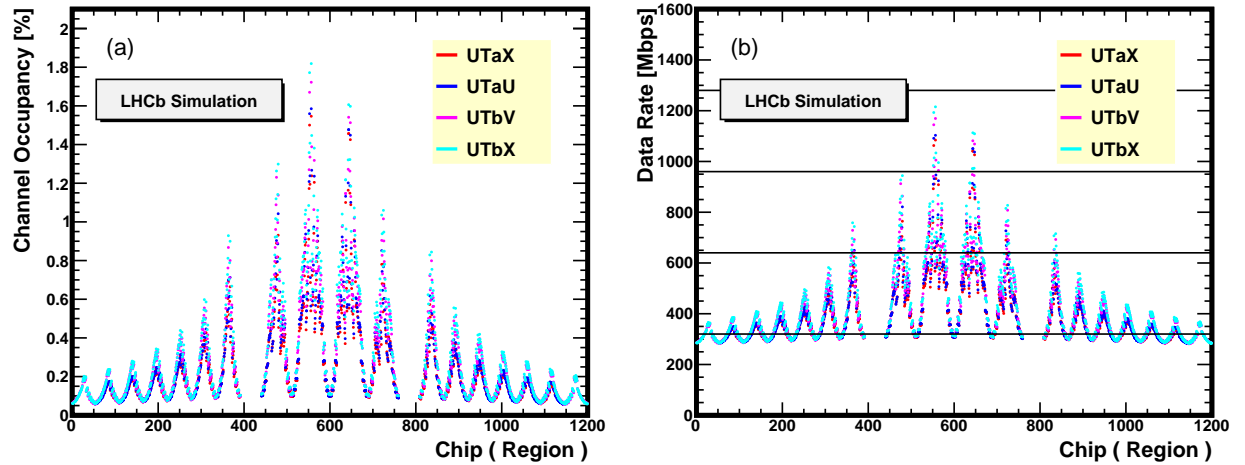


Figure 2.35: (a) Occupancy for each ASIC in minimum bias events ($\nu = 7.6$). (b) Data rate of each ASIC in dots. The horizontal lines show the data rate that can be handled by any given number of e-links.

The minimum number of bits to read out one hit strip is twelve, seven bits for the channel ID, from zero to 127, and five bits for the ADC value. Taking into consideration that only 2/3 of bunches have beam present in both bunches and hence interactions, the busiest chip needs to transfer about eighteen bits per 40 MHz clock cycle for hits alone.

The SALT ASICs will transfer data at 320 Mbits/s, i.e. eight bits per 40 MHz clock cycle. In order to transfer data, multiple e-links are needed for each ASIC, especially those at the centre. For each bunch crossing, besides the twelve bit hit data, there is also an event header to be transferred. Together they form an event packet. The event packet format is shown in Table 2.4.

As required by the LHCb general specification, the UT must transfer event packets for every bunch crossing, even if there is no beam-beam crossing or hit. The FE ASICs will therefore always be transmitting some kind of data. Thus a four bits bunch crossing ID

(BCID) is sufficient to tag each event. The value corresponds to the least significant four bits of the full twelve bits BCID.

For efficient data transfer, the size of the event packet changes. The ZS mode is used for normal data taking. The UT is also able to send non-ZS data whenever the NZS command is received. Two single bit flags, NoData and IsTrunc are used to distinguish different types of packet.

The first four packet types described in Table 2.4 are for normal data taking. When the ASICs receive a BX Veto for no beam-beam crossing, or a Header Only TFC command, or when there is no hit for a particular event, only a six bit header is sent. In the case that there is not enough data in the buffer to fill all active e-links, one or more idle packets are sent. For a normal event with some hits ($0 < \text{NumHits} \leq 63$), the header includes a “length” parameter to indicate the size of the hits data in units of twelve bits. Thus downstream electronics know where in the data stream the next event starts; a truncated event packet is sent in the case that the buffer is full, or in the case that the ASIC has too many hits, 64 or more out of 128, in which case the data is unlikely useful for the tracking reconstruction. No hit data is sent, but the field length contains the number of hits divided by four for monitoring purposes.

The NZS packet type is used mainly for monitoring, calibration or special runs. In this case, the SOL40 sends one NZS command followed by many HeaderOnly commands so that the buffer will not overflow. The data field has a fixed length for each ASIC with a few debug parameters followed by the six bit raw ADC values for each of the 128 channels. The “length” field has value 63 which distinguishes the NZS packet from truncated event packet.

During data taking the system periodically needs synchronisation. Whenever the ASICs receive a synch command, the data saved in the buffer will be discarded. The data packet sent out will comprise the full twelve bit BCID and a preset pattern that will be repeated several times to fill a frame with all active e-links.

With this event packet format, the data rate per ASIC is shown in Fig. 2.35(b). We use 10% more hits than in the simulation, based on a study of the current TT, to estimate the data rate. Also included are spill over effects and the fact that there may be more

Table 2.4: Event packet format at front end ASIC.

Header Field (6 or 12 bits)				Data Field	Comment
BCID	NoData	IsTrunc	Length		
4-bit 0000	1 1	0 1	- -	- -	BXVeto, HeaderOnly, or NumHits = 0 Idle packet
4-bit	0	0	6-bit	Hits	Normal event, $0 < \text{NumHits} \leq 63$
4-bit	0	1	6-bit	-	Truncated event, NumHits>63 or bufferFull
4-bit 12-bit	0 -	1 -	11 1111 -	Data Pattern	NZS packet, fixed length of data Synch packet, with preset pattern

noise hits in the real system. The horizontal lines in the figure indicate the data transfer capability of e-links. For most ASICs one or two e-links are sufficient, but the ASICs close to the beam-pipe need more.

The data buffer in the ASIC acts also as a *derandomizer*. In order to minimise the probability that the event is forced to be truncated, a reasonable buffer size is used, and enough e-links per ASIC are allocated so that the data rate is less than 95% of the e-links capacity. We also require that each ASIC has at least two active e-links to comply with the synchronisation protocol, as it should be wide enough to transmit the synch packet. The number of activated e-links per ASIC is shown in Fig. 2.36. With this assignment the system can handle data rate for luminosity up to $\approx 2.7 \times 10^{33} \text{ cm}^{-2}\text{s}^{-1}$.

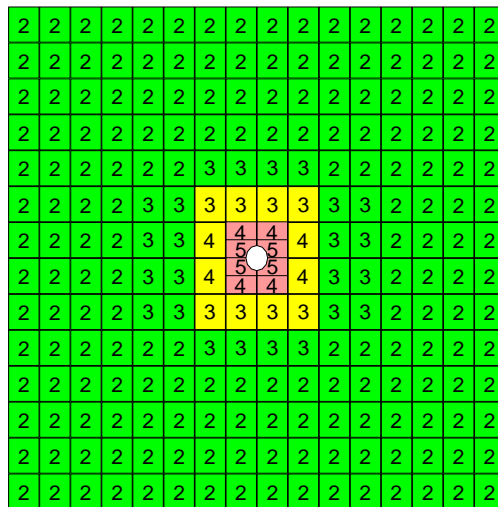


Figure 2.36: Number of active e-links per ASIC for each hybrid. Different hybrid types are colour-coded: (green) nominal four SALT hybrids, (yellow) eight SALT hybrids for sensors of type B, and (pink) eight SALT hybrids for sensors of type C and D (innermost, half length sensors).

2.9.2 Data Process at DCB and AMC40

One ASIC has two or more active e-links synchronously sending data at 320 MBit/s on the flex cable to the GBTx ASIC on the DCB. One GBTx ASIC takes input of up to ten e-links in 80-bit mode and forms a GBT data frame. The data is converted to optical signals and sent to the AMC40 card on TELL40 board through fibres. The data from each ASIC forms its own sub-GBT frame.

The TELL40 is currently conceived to contain four identical autonomous mezzanine cards known as the AMC40. One AMC40 takes input from 24 optical links. The AMC40 FPGA decodes data from each link, aligns them according to the BCID and builds each

event data packet. The event data is then processed by an UT-specific data process block before being sent to the computer farm.

It has been found, however, that there are not enough resources in the current AMC40 to perform the BCID alignment on data from 24 input links, with a few sub-frames per link. There are two options to deal with this issue. One option is to increase the number of AMC40 boards, so that the number of GBTx links per AMC40 and the number of sub-frames per link can be reduced. The other option is to repack the data at the DCB. In that case, the data from multiple ASICs would be decoded and BCID aligned in the DCB FPGA. For each BCID, one data packet would be formed, including hits from all connected ASICs. The GBTx ASIC built-in error correction would not be used. Thus, this option would need to implement its own error detection and correction mechanism to protect event headers.

Both options are currently being investigated, and the final choice will include the considerations that the DCB FPGA needed for the data repacking option is required to be radiation hard, as it would be placed very close to the UT planes, that specific firmware would need to be developed to handle the data repacking operation, and cost.

UT specific spill-over correction sand hit clustering needs to be developed and included in the AMC40 FPGA data processing block. The signal remainder height is expected to be <5%, 25 ns after the peaking time. If the signal height in a bunch crossing is big, it is possible to veto a hit in the same channel in the next bunch crossing. Hit signals are saved for each strip in the ASIC. One track hit may have more strips. They are grouped into one cluster hit at the AMC40 FPGA.

2.9.3 Timing and Slow Control

The UT timing and slow control has to comply with the front-end specifications defined for LHCb [28, 29]. The timing and fast control (TFC) signals, as well as the experiment control and monitoring will be handled by the SOL40 common board. The periphery electronics will house the master GBTx receiving and distributing the TFC information. Only eight TFC signals will be transmitted to the front-end electronics every LHC clock cycle. These include:

- Bunch Identifier Reset (BCID Reset): A configurable preset value will be loaded into the 12-bit BCID counters of the FE electronics. The preset value will be configured via the slow control interface.
- Front-End electronics Reset (FE Reset): Upon reception of this reset, all the data buffers, operational logic registers, counters and status bits will be cleared, with exception of the configuration and control registers.
- Header Only and Bunch Crossing Veto (BX Veto): The combination of this two commands will be transmitted as a single signal. For this particular BCID the FE electronics will only transmit the header information, and all data for this event will be discarded.

- Calibration: Only one calibration type so far has been identified for the UT FE electronics. Upon reception of this command, a test pulse signal will be injected into the analogue block of the ASIC. The amplitude of the test pulse signal can be configured using the slow control interface.
- Second calibration type: A second bit is reserved for a possible additional calibration command, detached from the test pulse calibration.
- Non-Zero Suppressed mode (NZS): On reception of this signal, the ASIC will send the full data corresponding to this event without zero suppression or compression.
- Status and Counter Snapshot command: On reception of the Snapshot signal, the ASIC, and possibly all sensitive front-end electronics, will capture the values of the essential internal counters and status registers. These captured values will be available to be read out using the slow control interface. The stored values will be overwritten on reception of a new Snapshot command.
- Synch command: When the synch command is received, the ASIC will send a predefined pattern on its serialisers. This is required to synchronise the front-end with the DAQ system. Also the FE buffers are zeroed.

For the experiment control system (ECS), several slow control adapter (SCA) chips will be connected to each master GBTx. The SCA, mainly its I²C and ADC modules, will be used to configure and monitor most of the system, including the SALT chip, the data GBTx, the low voltage regulators and the temperature and humidity sensors among others.

The control software will be developed using the Siemens WinCC framework commonly used in LHCb. All the detector hardware will be virtually controlled and monitored using the common representation, organised in a clear and structured hierarchy.

Extensive monitoring will be in place to check the status of the detector and ensure it is safe. The monitoring data will be collected and stored in a database and alarm levels will be defined. The control software will implement a safety system to perform automatic actions to protect the detector. Additional sensors, relays and thermo-switches will be installed to interface with the Detector Safety System (DSS) operating independently from the ECS and offering another level of protection.

2.9.4 DAQ Slice Development

The UT specific DAQ system development is split into three major parts according to its locations: DSP in the front end ASIC, periphery electronics including DCB, and AMC40 firmware.

The functionality of the SALT DSP has been described in previous sections. The algorithms have been optimised with simulated data at the nominal upgrade luminosity. A multiple purpose electronic board is under design which includes a basic version of the DCB. This board will be used to design the DCB FPGA repacking algorithm. The SALT

e-link data from MC samples will be used to model the whole data flow architecture, both in a system simulation and in the hardware implementation of a read out slice. The test board can also be used to test different flex cables and check the SLVS signal quality over various cable lengths. This board is designed to provide data to the AMC40 mini-daq included in the LHCb TELL40, and is meant to be scalable to different complexities of the bench tests and test beams planned for the duration of the electronics design and commissioning.

2.10 Integration and Testing

In this section we concentrate on issues related to integration of different sub-detector parts together and quality assurance steps (QA). The design of various sub-components have been already discussed in the previous sections.

The major mechanical and electrical components of the basic UT element, the stave, are the integrated carbon-fibre and cooling support structure, the power/data flex cable, the hybrids and the sensors. Each of these components need to be fully tested before a stave can be constructed. Silicon sensors will be manufactured in industry, and will be subjected to a series of QA tests, as described below. The hybrid is a Kapton substrate that provides support for the sensor and the (four or eight) SALT ASICs. Electrically, it provides the routing of the power, ASIC control and signals to/from the power and data tape (also a Kapton flex cable). The power and data flex carries power, data and signals to/from each hybrid to the balcony electronics, and will be either be glued or laminated to the carbon-fibre facing of the stave.

Construction of a single UT stave requires that the needed components are ready and fully tested beforehand.

2.10.1 Quality Assurance Programme

We will implement QA tests at every step of the production, assembly and integration. The QA program will allow us to catch and correct problems early, and ensure a well functioning detector as an end product. Some tests are intermediate steps of the planned production and assembly procedures. Other tests certify completion and functionality of each sub-element. Planning for QA tests is important for defining, and later managing the UT construction project. Early planning will allow us to establish common protocols between collaborating institutions and share designs of test set-ups. Not all technical details of the detector are already decided, thus the plan outlined here is tentative.

To maximise the benefits from the extensive QA testing we plan to deploy a database system to store electronic records from standard testing, including test results from manufacturer whenever feasible. Such records will be made easily accessible via a web interface. Web submission forms will also be used for input. Input format will be flexible to allow integration of heterogeneous sources. The database will possibly include electronic logs from the assembly procedures including signing off on a procedural checklist and

free format comments. The history of sub-elements will help diagnose problems during construction and detector operation. The database will also make it easier to monitor progress of various sub-projects. Other possible extensions of the database include a catalogue of parts to be purchased and their delivery. Ideally the database will be browseable from integrated parts to sub-elements and vice-versa, as well as searchable by unique component IDs. The database will be implemented in 2014.

2.10.2 Sensor Testing

Subsequent steps in detector integration are depicted in Fig. 2.37. One of the branches of detector construction activities is led by acquisition and testing of sensors. There are about 1000 sensors to test. A limited number of tests will be performed by the manufacturer for the large production runs. The received sensors will be visually inspected for scratches, anomalous discoloration and evident defects. Edges will be surveyed under a microscope to search for large defects ($> 40 \mu\text{m}$) from cutting. Metrology of sensors will include measurement of dimensions at a few points; thickness and flatness in particular. Electrical testing will be performed in a controlled environment (temperature, humidity, light-tight box). We will measure leakage current and capacitance as a function of bias voltage (IV,CV scans) for all strips together or groups of them. The depletion voltage will be determined from CV scans. Using a probe-station, we will then measure current and capacitance of each strip at the standard depletion voltage; initially for all sensors, later for at least a few sensors in each production batch. A long-term stability study will monitor current under depletion voltage for at least a week. Radiation hardness studies will also be performed on a small number of sensors during the R&D stage. Special test mini-sensors may also be tested during the production stage, where IV and CV tests will be performed before and after irradiation. We will also measure charge collection efficiency with laser and radioactive sources by coupling the sensors to Beetle electronics [14].

2.10.3 Assembly of Read-out Hybrids

The acquisition of the SALT ASICs and their testing are the first steps in the construction of the read-out hybrids. Both the digital and analogue domains will be tested. Because of the large number of ASICs (about 4,000), multiple institutes will be involved in bench testing the ASICs, with the test procedures defined by the design team at AGH-UST. We are considering using an external vendor as an alternative.

The ASICs will be attached to flex hybrids consisting of a multi-layer Kapton/copper integrated circuit, that will be about $150 \mu\text{m}$ thick. Since the flex hybrid is a very thin and delicate structure, a design similar to the one developed for the ATLAS strip upgrade project [ref needed] will be pursued. The flex hybrid will be mechanically attached to an FR4 printed circuit board carrier, accommodating either a single or possibly a few hybrids. The carrier provides a solid backing for handling and wire bonding, and is mechanically connected to the flex hybrid by several *hinge-like* structures that are easily cut to detach the encased hybrid. To enable testing of the hybrid(s) on a carrier board, temporary wire

bonds between the hybrid and the carrier board are made, and the signals are routed to a connector on the periphery.

The flex hybrid vendor will be responsible for constructing the hybrid carrier boards, mounting flex hybrids on them, populating them with ASICs and passive components, wire bonding the back end of the chip and the temporary test wire bonds. Basic functionality tests of the hybrids will be performed by the vendor, but most of the detailed testing will be performed at INFN Milan. The hybrid vendor will be supplied with fully tested SALT ASICs from the manufacturer as described above. During critical operations, such as wire bonding, or gluing/soldering components, the hybrid will be held flat with a vacuum jig. During shipping of the hybrids, the hybrid will be held flat using mechanical means, such as a pair of cross braces that are attached to the FR4 frame that can apply a small downward force to the hybrid.

Once the manufactured flex hybrid with ASICs arrives in Syracuse, it will be retested to ensure full functionality of the hybrid. QA tests of complete hybrids will include pedestal and noise measurements, pulse testing and testing with a laser and radioactive sources. In the beginning, longer burn-in tests will be performed. As we gain experience with the production, the longer-term burn-in tests will be done less frequently.

After re-qualifying the hybrid, the sensor needs to be attached. A pair of vacuum jigs, one to hold the sensor and one to hold the hybrid, with mating alignment and guide pins are used to align the sensor precisely to the hybrid. Both the sensor and the hybrid will have alignment targets, and the jigs will be designed so that they will be visible as the sensor is glued to the hybrid. A coordinate measuring machine (CMM) will be used to ensure that the relative silicon-hybrid alignment is within specification, before gluing the sensor down. A bow of $\sim 100 \mu\text{m}$ in the sensor would not be unusual. Any bow will be taken up by a thicker glue layer between the sensor and hybrid. That is, we do not want to induce a bow in the hybrid to accommodate bowing of the sensor. Sensors with larger bow can be placed further from the beam-pipe, where the cooling requirements are less stringent. After the sensor is attached and glued down, it is surveyed, and offsets between the hybrid and silicon targets are stored in the QA database.

Once the silicon is affixed, the channels at the front end of the SALT ASICs need to be wire bonded to the silicon strips. It is envisaged that this work is carried out with an industrial partner that has automated wire bonding capabilities. The hybrid, with the attached sensor, is shipped to the vendor for wire bonding. The hybrid needs to be held under vacuum while wire-bonding.

Once the wire bonding is complete, the hybrid is shipped back to Syracuse University, and a battery of QA tests are performed on the full hybrid. Longer burn-in tests are envisioned early on, and will be less frequent as experience is gained. Assuming all tests are passed, QA data is saved, the hybrid is put into storage for eventual mounting on a stave.

2.10.4 Stave Assembly

In parallel, other stave components will be manufactured and tested. Power and data flex cables will undergo visual inspection and measurements of resistance will be made to test for open and shorted lines. For stave facings we will measure mass, dimensions, flatness (bow, twist). We will also measure mass and dimensions of the structural and thermal foam. In addition to such measurements for the cooling tubes, we will also perform pressure-tests and pass/fail tests of their shapes. When put together, they will constitute a bare stave unit. We will measure their total mass and perform metrology including pass/fail test of the flatness in normal and cool-down conditions. Then data and power flexes will be glued on a stave and tested for their position.

The final stage is to populate the stave, which has the power and data flex already attached, with the hybrids. Before mounting, each hybrid is first re-tested to ensure that it is still fully functional. The fully tested hybrid is picked up from the temporary holder with a vacuum fixture and prepared for connection to the stave. A stencil is used to put a precise amount of epoxy on the power/data flex in the location where the hybrid will be mounted. A strong-back, or frame, holds the stave, allowing for handling of the stave while keeping it flat and rigid. The strong-back has precise alignment dowels that match the holes in the vacuum fixture, and enable the hybrid to be precisely located on the stave. Optical alignment markers on the stave, the strong-back and the hybrid allow for an optical *in situ* survey, ensuring accurate placement of the hybrid position. A CMM will be used to check the positioning before gluing the hybrid down. The hybrids are then glued down one-by-one until one side of the stave is fully populated. Once this is done, a protective cover is placed over the finished side, and the stave is flipped over for mounting the hybrids on the other side. Once the second side is finished, a second cover is placed on the opposite side, encasing the stave.

Once both sides are populated with hybrids, the hybrids on both sides of the stave need to be wire bonded to the power/data flex. Again, this will be carried out by a wire bonding company. A local company in Syracuse has been identified, which has the capabilities to handle large devices like a UT stave, and is eager to work on the project. Each pair of wire bond pads that carry power, control and data will have at least 2 wire bonds in case of a single wire bond failure.

Once the full stave is wire bonded, it is shipped (or driven) back to Syracuse University for the full set of QA tests to be performed on the fully populated stave. Final certification of the hybrid-loaded stave unit will include a measurement of its total mass, cooling tests, and high and low voltage tests. The read-out electronics will be checked for digital connectivity and the channel pedestals and noise will be recorded. A test DAQ setup will be used and cooling will be provided to the stave by a small-scale blow-through CO₂ cooling system that uses the integrated cooling channels. Each stave will be burned-in for approximately 48 hours, where the sensors are at a pre-defined voltage, and the hybrids are read out continuously. The data will be saved and summary plots will be uploaded or linked to the QA database. Once the testing is complete, the fully loaded stave is stored until it is ready to be shipped to CERN.

Electric testing will be repeated after shipment to CERN and installation into UT support structure. The staves are positioned on the detector frame using precise mounting pins on top, but the stave is not rigidly fixed at the bottom to allow for thermal expansion and contraction in the vertical direction.

A common electronic test set-up will be used for tests of hybrids at different stages of detector integration as described above. A flexible Mini DAQ system developed by Marseille group for testing all upgrade electronics will be used. The system will be connected to a hybrid or stave via Balcony Electronics (BE) emulator board. The final BE boards will be tested with a hybrid emulator before actual hybrids are available.

2.10.5 Radiation and Test Beam Studies

In addition to sensors, also SALT ASICs, flex hybrids, power/data flex cables will be tested for radiation hardness. Several irradiation facilities are under consideration: reactor neutrons at Maryland, 220 MeV protons at Massachusetts hospital used previously by the Syracuse group, as well as spray from high-energy protons on target at a mixed-field irradiation facility at the CERN PS.

In addition to QA tests during detector production and assembly, we plan a vigorous test beam program to validate the design concepts and check the detector integration process. In late 2014 we will test sensors using a read-out chain using Beetle chips. In 2015 prototype hybrids with complete SALT ASIC prototypes will be tested, attached to prototype read out electronics, and read out with the Mini-DAQ system. In 2016 prototype stave units will be tested with a refined read out system prototype.

2.11 Project Organisation

The UT project is organised into seven work-packages:

1. **Sensor and hybrid module production**, including sensor production, front-end hybrid production, development of the QA procedures to assess the performance of these components during the R&D phase, and the acceptance tests in the course of the production phase.
2. **SALT ASIC**, including design and production of the dedicated front-end ASIC (SALT) for UT sensor read-out, and the development of a testing protocol for the QA procedures during the production phase.
3. **Electronics**, including the design and production of the cables providing the bi-directional communication between the balcony electronics and the hybrids, as well as the high voltage bias lines for the sensors and the low voltage distribution to the SALT chips, the development of the balcony electronics boards providing communication between the data acquisition crates and the hybrids, and the high voltage and low voltage system.

4. **Data acquisition and Experiment control**, including all the tasks needed to adapt the general LHCb data acquisition, timing and experiment control system to the UT needs. In view of the unique properties of our detector, being a very large system with significant spatial variation of the expected data rates, this task involves a delicate optimisation of the data flow architecture, and extensive firmware development. In addition, a scalable testing system to be used at different stages of system development is implemented in the early stage of this task.
5. **Mechanics and cooling**, including the design and production of the staves and embedded cooling, and the coordination for the design and production of the CO₂ cooling plant with its and circulation and monitoring circuit.
6. **Integration and testing**, including the development of assembly procedures between hybrids and sensors, as well as between instrumented modules (hybrid+sensor combinations) and the flex cables, and the validation and documentation of the QA tests developed for the individual components, as well as the development of a comprehensive data base documenting the performance assessment of the components of the instrumented staves at the various stages of their production and integration. In addition, this task involves the design and coordination of the irradiation and test beam studies in the early part of the project.
7. **Integration with LHCb**, including the planning of the procedures to be adopted to receive the instrumented staves in LHCb, the design of the frame where the staves are mounted, and of the detector box enclosing the UT system. An important component of this task is the implementation of the requirements posed by the beam-pipe thermal insulation, and the detector lateral retraction during the yearly beam-pipe bake-out.

Tasks concerning the integration of the UT in the tracking software and in the trigger algorithm are part of the tracking software and trigger projects. We have designated coordinators that provide coordination between the project described here and its exploitation in the data taking and data analysis of the experiment.

Figure 2.37 shows the plan on production and testing of the various components of the instrumented staves. The various steps in this process have been described above.

2.11.1 Participating Institutes and Responsibilities

The institutes currently working on the UT project comprise four US institutes, Syracuse University, Maryland University, the University of Cincinnati, and Massachusetts Institute of Technology (MIT), and four European institutes, AGH University of Science and Technology (AGH-UST), CERN, INFN Milano, and the University of Zurich. Table 2.5 shows how the institutes are currently planning to contribute to the work-packages. All the groups contributing to the UT construction are also involved in software tasks, and

Table 2.5: Project sharing of responsibilities.

Sensor and hybrid module	INFN Milano, Syracuse
SALT	AGH-UST
Electronics	INFN Milano, Maryland, Syracuse
DAQ, ECS & TFC	Maryland, Syracuse, Zurich
Mechanics and Cooling	CERN, Cincinnati, INFN Milano, Syracuse
Integration and Testing	All Institutes
Integration in LHCb	CERN, INFN Milano, Syracuse, University of Zurich
Software	All Institutes

we have identified coordinators responsible for maintaining communications between the hardware and software activities related to the UT detector. The collaborating institutions are currently negotiating the funding allocated to them for the UT project. The exact distribution of responsibilities may be adjusted when the results of the requests to the funding agencies have become clear.

2.11.2 Schedule

The upgraded UT detector is scheduled for installation in Q1 2019, and the schedule shown in Figs. 2.38 and 2.39 show the time-line of the major sub projects in the UT R&D and construction.

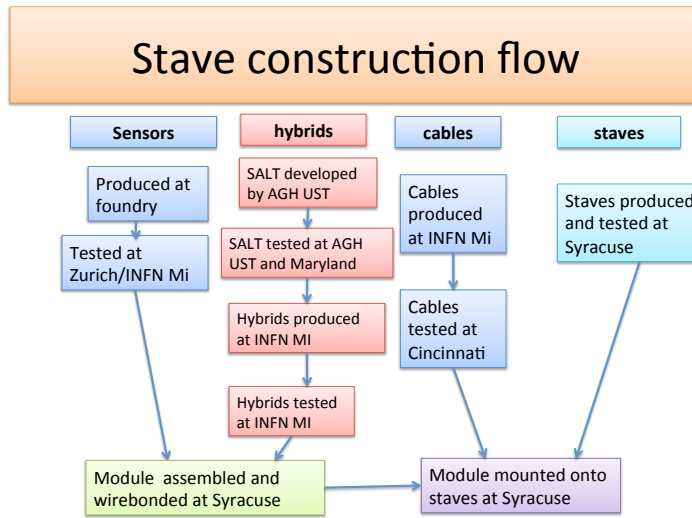


Figure 2.37: Flow diagram of the construction and testing of the various components of the instrumented stave. Upon construction the staves will be shipped to CERN and be handled and tested according to the procedures developed in the “Integration with LHCb” work-package.

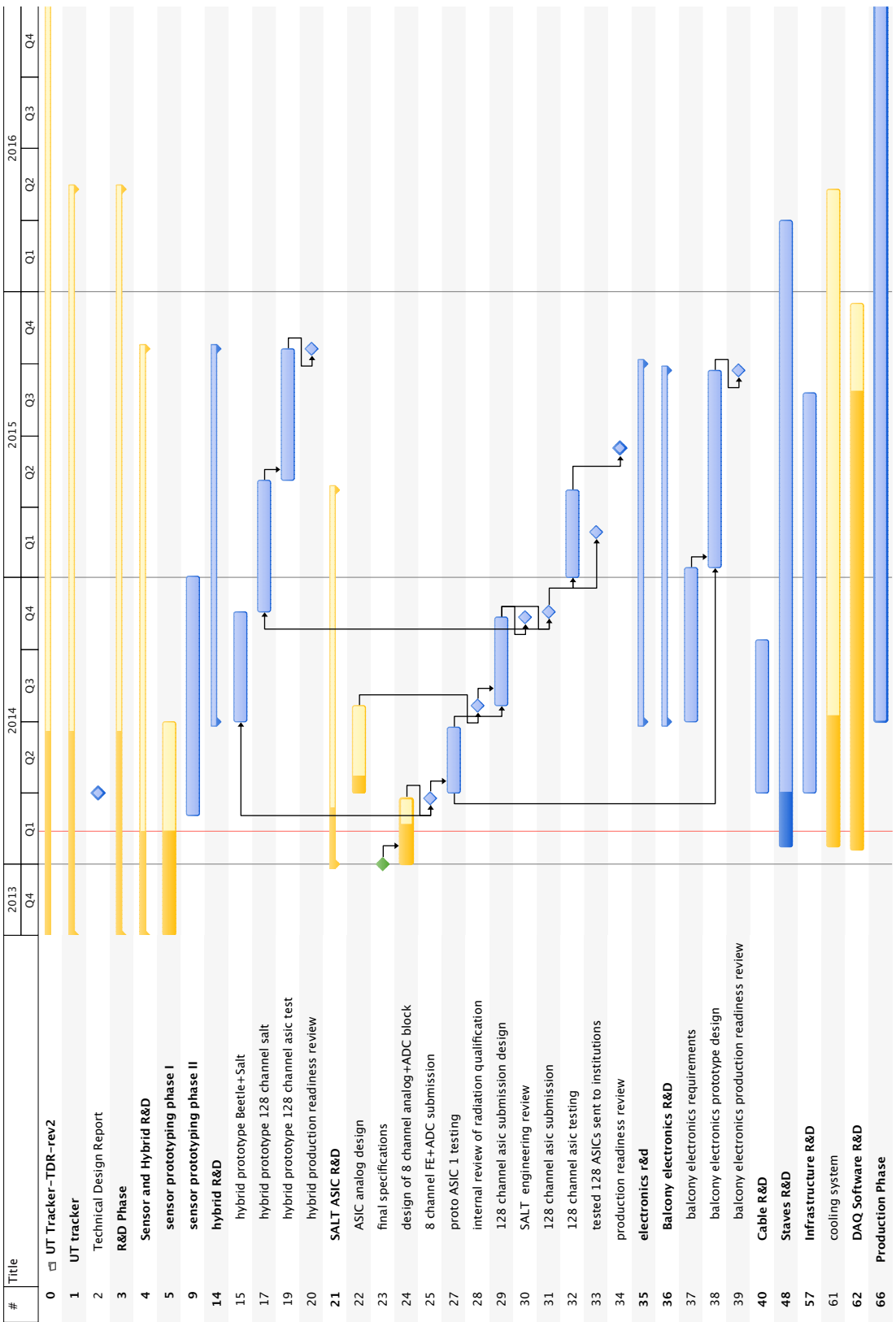


Figure 2.38: Planned R&D schedule for the LHCb Upstream Tracker. All the work packages have R&D activities planned for 2014, some of them extend into 2015.

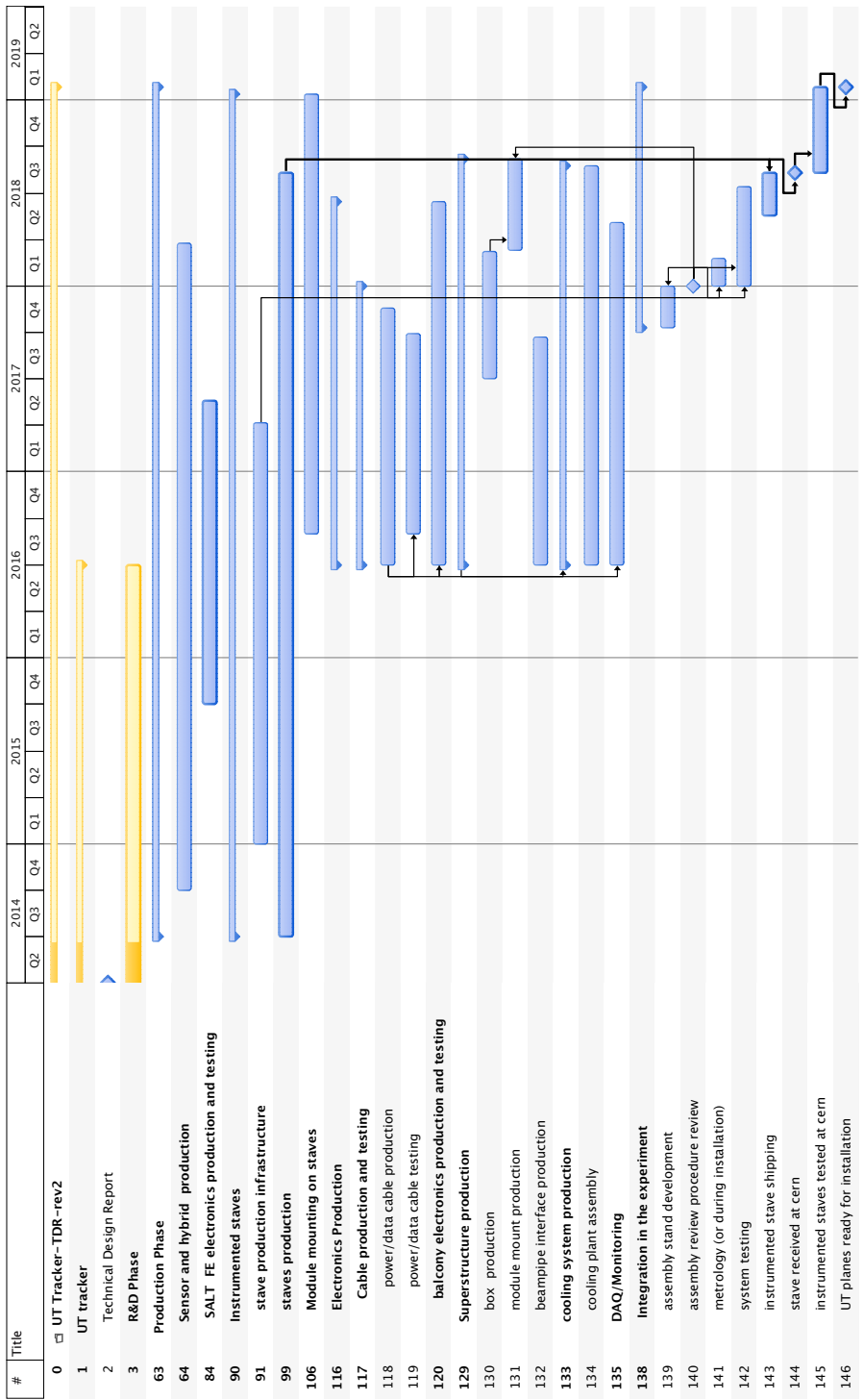


Figure 2.39: Project schedule for the LHCb UT upgrade from the start of 2013 to the beginning of 2019. The commissioning period is expected to extend up to Q4 2019.

2.11.3 Cost, Resources and Contingencies

The estimated core cost of the UT upgrade is 6.5 MCHF. The estimate is based on quotes from industry whenever possible, or extrapolation from similar projects if the items required a more detailed design to submit to industry for bids. This is the case, for example, for the hybrids and flex cables, where the cost was derived from similar components in other upgrade projects. In the case of mechanical components, such as the staves, the cost was derived from quotes on the material needed to assemble these devices, as well as a detailed assessment of the shop time required to fabricate the parts according to our design. Finally, for US institutes, an additional 430 kCHF is requested for US technical personnel (engineers, technicians and undergraduate students) that need to be supported with project funds. The UT core cost breakdown is given in Tab. 2.6.

The silicon sensor cost estimate is based on quotations by two different foundries. The number of spares included in this estimate is 13%, which is the minimum amount that is considered adequate for the construction of the double-sided staves. The hybrid and cable estimate is based on previous experience, but needs to be corroborated by quotations, once the design of these components is in a more advanced stage. The cost of the PEPI electronics has been assessed quite carefully, but needs to be fine tuned once the power consumption of the SALT ASICs and the data flow architecture are finalised. The DAQ and HV/LV cost are estimated on the basis of a conservative model of the number of channels needed for our application. The mechanics estimates are based on a careful analysis of all the materials needed to assemble the instrumented staves, as well as on a detailed analysis of the amount of shop time needed to manufacture the individual components needed for the instrumented staves and the associated fixtures. Finally, the cost of the CO₂ cooling plant has been estimated on the basis of the cost of comparable

Table 2.6: Summary of the UT project core cost. Cost to support US faculty members, post-docs and graduate students working on this project are not part of the core cost. In addition to the core cost, the US institutes request a 430 kCHF for US technical personnel (engineers, technicians and undergraduate students) that need to be supported with project funds.

Work Package	Cost (kCHF)
Si sensors and hybrids	2700
SALT ASICs	1300
Cables	160
PEPI Electronics	620
DAQ & HV/LV	780
Staves& Hybridisation	510
Infrastructure	130
Cooling	300
Total	6500

systems such as the VELO cooling plant or the ATLAS IBL cooling plant.

The cost described here accounts for a reasonably conservative amount of spare components. The only contingency included is the possibility of a second production run for the SALT chip.

2.11.4 Safety

In accordance with CERN’s safety rules and regulations defined by SAPOCO/42 [33], the Upstream Tracker project will follow the CERN safety codes which also allow the use of international construction codes for structural engineering as described in EUROCODE 3.

The detector makes use of technologies and components which have already been used in high energy physics detectors. No major risks to the environment or to personnel have so far been identified. Much of the conceptual design of the cooling system is based on that of related cooling projects, such as the present LHCb VELO and therefore the risk is considered low.

The electrical circuits of the UT will be subject to an electrical reception prior to operation (Code C1). Electrical protection will be assured by the ECS/DSS that will be able to cut the power source when necessary. Interventions on the circuits will require the primary power source to be switched off by means of the DSS. Interlocks to the electronic equipment will be activated by over-temperature.

All work conducted at CERN, in preparation and during the installation, and for the periods of commissioning and operation of the UT detector will comply with CERN safety regulations. The UT will require particular attention to the radiological hazards during the de-installation of the existing TT and its replacement with the upgraded detector, and attention to damage avoidance during (de)-installations. The group will conduct an initial safety review as part of its Engineering Design Review and a separate Safety Review will be conducted by CERN prior to start of decommissioning.

Chapter 3

The LHCb Scintillating Fibre Tracker

3.1 Introduction

The tracking detectors upstream and downstream of the LHCb dipole magnet provide a high precision estimate of the momentum of charged particles. This leads to a precise mass resolution for decayed particles. The reconstructed trajectories of charged particles are given as inputs to photon-ring searches in the RICH detectors which are used for particle identification. The momentum resolution is mainly limited by multiple scattering for tracks with momentum up to about $80\text{ GeV}/c$, while the detector resolution is the limiting factor for tracks with higher momentum. This chapter describes the upgrade of the tracking detectors downstream of the magnet.

There are three downstream tracking (T-)stations: T1, T2, T3. They were designed to provide standalone pattern recognition with a high efficiency together with high resolution in the bending plane of the magnetic field. The tracking stations of the current detector consist of two separate sub-detectors: the Outer Tracker (OT) and the Inner Tracker (IT). The OT is constructed using large straw detectors and covers around 99% of the 30 m^2 detector surface. The IT is a silicon micro-strip detector covering an area of 0.35 m^2 in the high track density region around the beam-pipe. Each station consists of four detection planes which provide measurements of the co-ordinates (x, u, v, χ) , with strips or straws orientated at $(0^\circ, +5^\circ, -5^\circ, 0^\circ)$ with respect to the vertical axis.¹ The performance of the IT is described in Refs. [18, 34]. The IT spatial resolution was measured to be $50\text{ }\mu\text{m}$ with a hit efficiency greater than 99%. The performance of the OT is described in Refs. [35, 36]. The OT spatial resolution is about $200\text{ }\mu\text{m}$ and the hit efficiency is above 99%. The momentum resolution, $\Delta p/p$, of the current tracking system ranges from 0.4% at $5\text{ GeV}/c$ to 0.6% at $100\text{ GeV}/c$, and invariant mass resolutions of around $8\text{ MeV}/c^2$ have

¹LHCb follows a right-handed co-ordinate system with positive z defined as the average direction of the beams away from the interaction point at $z = 0$ where positive y points “upward”, and positive and negative x point towards the access cavern and the LHC cryogenics respectively. Positive and negative x are thus labelled A-side and C-side.

been achieved for $B \rightarrow J/\psi X$ decays with a constraint applied to the J/ψ mass.

The design of the current tracking detectors was optimised to provide the best performance in proton-proton collisions at a centre-of-mass energy of 14 TeV with 25 ns bunch spacing, and instantaneous luminosities in the range $\mathcal{L} \approx 2 - 5 \times 10^{32} \text{ cm}^{-2}\text{s}^{-1}$. The LHCb upgrade is planned to run with an increased luminosity of $1 - 2 \times 10^{33} \text{ cm}^{-2}\text{s}^{-1}$. This will be achieved using 25 ns bunch spacing with the average number of proton-proton interactions per bunch crossing $\nu = 3.8 - 7.6$. Collecting data at this luminosity will only be possible if the current so-called “Level-0” hardware trigger is removed, and the detector is read out at the full 40 MHz bunch-crossing rate.

The geometry of the current tracking system was chosen such that the maximum occupancy in the hottest regions of the OT was limited to 10% for an instantaneous luminosity of $2 \times 10^{32} \text{ cm}^{-2}\text{s}^{-1}$ [37]. Improvements were made to the track reconstruction algorithms so that LHCb could collect data at an instantaneous luminosity of $5 \times 10^{32} \text{ cm}^{-2}\text{s}^{-1}$. In this case, the occupancy in the OT increased up to a maximum of 25% with no loss in track finding efficiency. However, it was shown in Ref. [6] that the occupancy in these regions in OT would be too large at the upgrade luminosity and some OT modules would need to be replaced. All of the read-out electronics, in both the IT and OT, would have to be replaced to enable the LHCb detector to read out complete events at 40 MHz.

The integrated luminosity collected over the lifetime of the upgraded detector is planned to be at least 50 fb^{-1} . The different options for the upgrade of the downstream tracking system were described in the LHCb Letter of Intent (LoI) [6] and the LHCb Framework TDR [3].

The tracking stations will be replaced by a Scintillating Fibre Tracker (SciFi Tracker/SFT) which will cover the full acceptance after the magnet. The detector modules will have 2.5 m long scintillating fibres with a diameter of 250 μm . The fibres will be read out by Silicon Photomultipliers (SiPMs) contained in the so-called “Read-out Boxes” at the top and bottom of the detector. The conceptual design of the modules is similar to that described in Ref. [38].

This TDR describes the development of the project since the LoI, and the design of the upgraded tracker. Several important design choices have been made:

- Following the Tracker Technology Validation Review [13], it was decided that the complete tracker will be replaced by the Scintillating Fibre Tracker. The modules will contain six layers of scintillating fibres in the region around the beam-pipe and five layers everywhere else.
- Mono-phase cooling with serial module interconnections will be used for the silicon photomultiplier cooling. This decision was made after an independent review of different cooling technologies in October 2013 [39].
- Following an Electronics review in December 2013 [40], the digitisation will use a 2-bit pulse-height information using three comparators with three thresholds.

The design of the upgraded detector is based on the set of requirements given in Sec. 3.2. The layout and detector geometry are shown in Sec. 3.3. The scintillating fibres and

silicon photo-detectors are described in Secs. 3.4 and 3.5 respectively. The design of the scintillating fibre module and the read-out electronics will be described in Secs. 3.6 and 3.7 respectively. The infrastructure and services required for the construction and operation of the detector are discussed in Sec. 3.8. The expected performance of the detector estimated from simulation studies is presented in Sec. 3.9. Finally, the organisation of the project will be discussed in Sec. 3.10.

3.2 Requirements

The track reconstruction requires that the detector has high hit efficiency, good spatial resolution in the bending plane of the magnet, and low material budget in the acceptance. The LHCb upgrade requires that the read-out electronics operate with 40 MHz sampling frequency. The detector must be able to operate for the full lifetime of the upgraded LHCb detector to ensure that the performance of the track reconstruction is good enough for the duration of the experiment.

The main requirements on the detector performance are given in Sec. 3.2.1, and the geometrical constraints are described in Sec. 3.2.2. The radiation environment in the tracker volume is presented in Sec. 3.2.3.

3.2.1 Detector Performance

The main requirements on the upgraded tracking detector are given below:

- The hit detection efficiency should be as large as possible ($\approx 99\%$), while keeping the reconstructed noise cluster rate at any location of the detector well below ($< 10\%$) the signal rate at that same location.
- The single hit spatial resolution in the bending plane of the magnet must be less than or equal to $100 \mu\text{m}$. A better resolution is not needed as the extrapolation of tracks from the VELO would be dominated by the effect of multiple scattering in the detectors upstream of the magnet.
- The material in the acceptance region should be minimised such that the effects of multiple scattering in the tracker are smaller than those due to the material upstream of the magnet. This requirement is achieved when the radiation length is such that $X/X_0 \leq 1\%$ per detection layer.
- The read-out electronics should be able to run at a frequency of 40 MHz, and the recovery time of the read-out channels should be short to minimise inefficiency due to dead-time.
- The detector should be able to operate with the required performance for an integrated luminosity up to 50 fb^{-1} .

Table 3.1: Nominal z positions of the tracking stations in the current LHCb detector.

Station	Inner Tracker		Outer Tracker	
	z_{\min} (cm)	z_{\max} (cm)	z_{\min} (cm)	z_{\max} (cm)
T1	767.3	782.8	783.8	803.8
T2	836.0	851.5	852.5	872.5
T3	905.0	920.5	921.5	941.5

3.2.2 Geometry Constraints

The current detector has three tracking stations placed at equidistant positions along the beam-line between the LHCb magnet and RICH2. The nominal z positions are listed in Table 3.1. The space available for the SciFi Tracker is constrained by that currently used by the IT and OT. The supporting structure, including the suspension bridge, can be reused.

The position of hits produced by particles traversing the detection layers must be well determined. A precision alignment of the detector will be made using particles, but this procedure will be complicated if the shape of the detector is not well known. The fibres must be straight and aligned within $50\text{--}100\,\mu\text{m}$ in the x -direction, and the detection layers should be flat within $300\,\mu\text{m}$ in the z -direction, to ensure that the requirements on the resolution can be satisfied.

3.2.3 Radiation Environment

The radiation level expected at the tracker stations was estimated using a FLUKA [15, 16] simulation of the LHCb detector. The simulation was made using the latest version of the detector geometry for the expected upgrade conditions at $\sqrt{s} = 14\,\text{TeV}$ assuming an integrated luminosity of $50\,\text{fb}^{-1}$ and a proton-proton cross-section of $100\,\text{mb}$. The details are described in Ref. [41].²

The estimated 1-MeV neutron-equivalent fluence in T1 ($z = 783\,\text{cm}$) is shown in Fig. 3.1, and the dose is shown in Fig. 3.2. The expected fluence and dose were also estimated for T3 ($z = 920\,\text{cm}$). The maximum fluence at the position of the SiPMs ($y = \pm 250\,\text{cm}$) after an integrated luminosity of $50\,\text{fb}^{-1}$ is estimated to be $9.5 \times 10^{11}\,\text{n}_{\text{eq}}/\text{cm}^2$ and $13 \times 10^{11}\,\text{n}_{\text{eq}}/\text{cm}^2$ for T1 and T3 respectively. The integrated ionising dose in the SiPMs is 40 Gy in T1 and 80 Gy in T3. The peak dose absorbed in the fibres is expected to be around 35 kGy and 25 kGy at T1 and T3, respectively. The simulations also showed that a technically feasible shielding, constructed from Polyethylene with 5% Boron, can reduce the neutron fluence in the region of the SiPMs by at least a factor of two.

²Initial simulation studies assumed a proton-proton cross section of $72\,\text{mb}$ and the maximum neutron fluence in the region of the SiPMs was found to be $6 \times 10^{11}\,\text{n}_{\text{eq}}/\text{cm}^2$ in T1 after an integrated luminosity of $50\,\text{fb}^{-1}$. The new simulations were only available from October 2013 so the measurements of irradiated SiPM detectors presented in Sec. 3.5 were made assuming a neutron fluence of $6 \times 10^{11}\,\text{n}_{\text{eq}}/\text{cm}^2$.

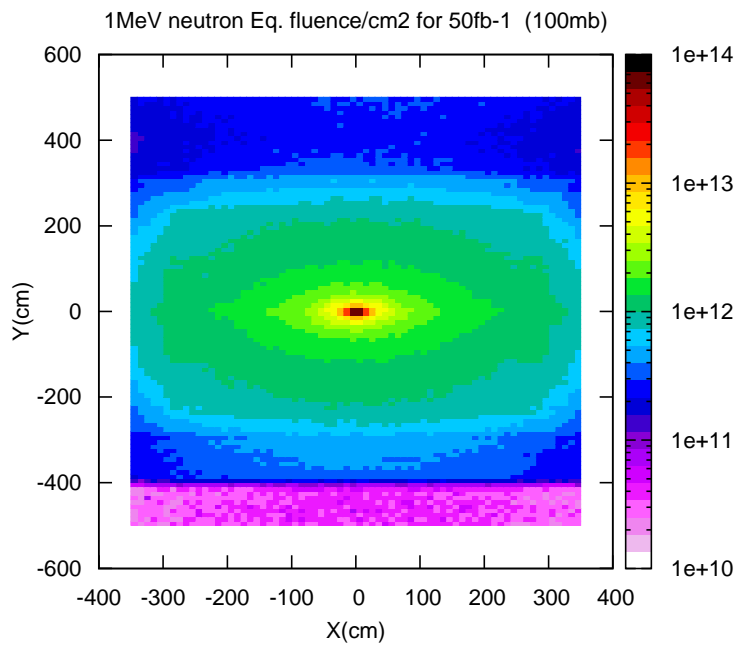


Figure 3.1: The expected 1- MeV neutron equivalent fluence per cm^2 at $z = 783 \text{ cm}$ after an integrated luminosity of 50 fb^{-1} .

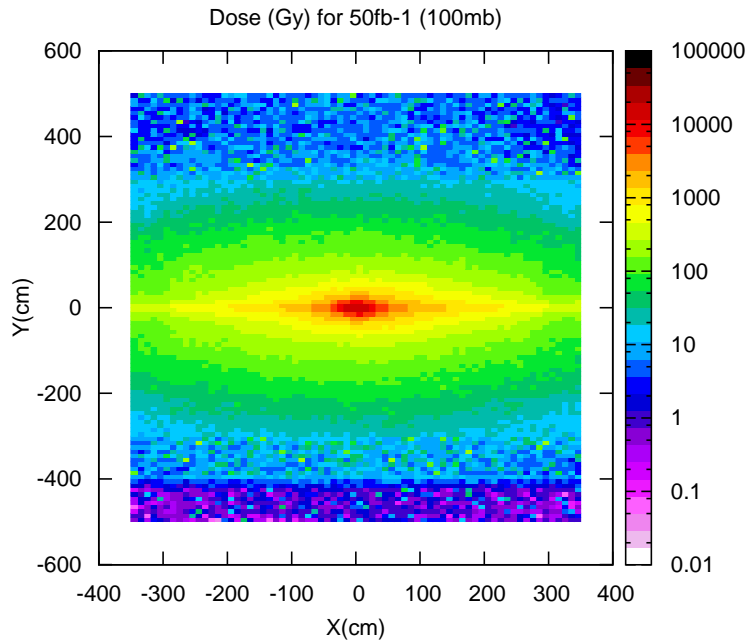


Figure 3.2: The expected dose in the $x - y$ plane at $z = 783 \text{ cm}$ after an integrated luminosity of 50 fb^{-1} .

3.2.4 Cooling

The performance of the SiPMs will degrade with increasing luminosity. The effects of radiation damage can be mitigated by cooling the SiPMs to -40°C . The cooling temperature must be stable within 1K. The cooling of the SiPMs will be discussed in detail in Sec. 3.6.5.3 and the design of the cooling plant is presented in Sec. 3.8.2.1.

3.3 Layout of the Scintillating Fibre Tracker

The Scintillating Fibre Tracker consists of three stations (T1, T2, T3) located between the dipole magnet and RICH2 as shown in Fig. 3.3. The three stations of the SciFi Tracker are each composed of four detection layers. Figure 3.4 shows the arrangement of the 12 detection layers in the current simulation. The three stations are centred at the same z position as the current Outer Tracker in the LHCb cavern. There is a gap of 20 mm along the z -axis between the detection layers of a given station. The detection layers have a circular hole in the centre to account for the beam-pipe structure. The first and the last layer in each station have no stereo angle with respect to the y -axis (“ x -layers”), while the middle two layers are tilted by $\pm 5^{\circ}$ (“ u -” and “ v -layers”). There are 12 modules in each detection layer, and a total of 144 modules will be required to build the complete detector. The module design is described in Sec. 3.6.

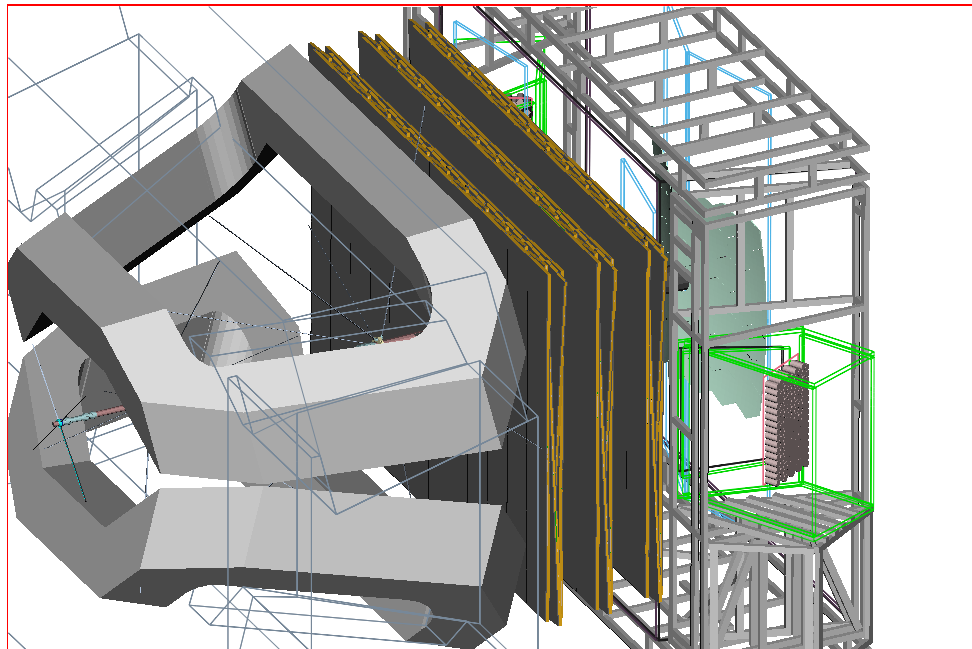


Figure 3.3: The three stations of the scintillating fibre tracker shown between the dipole magnet on the left and RICH2 on the right.

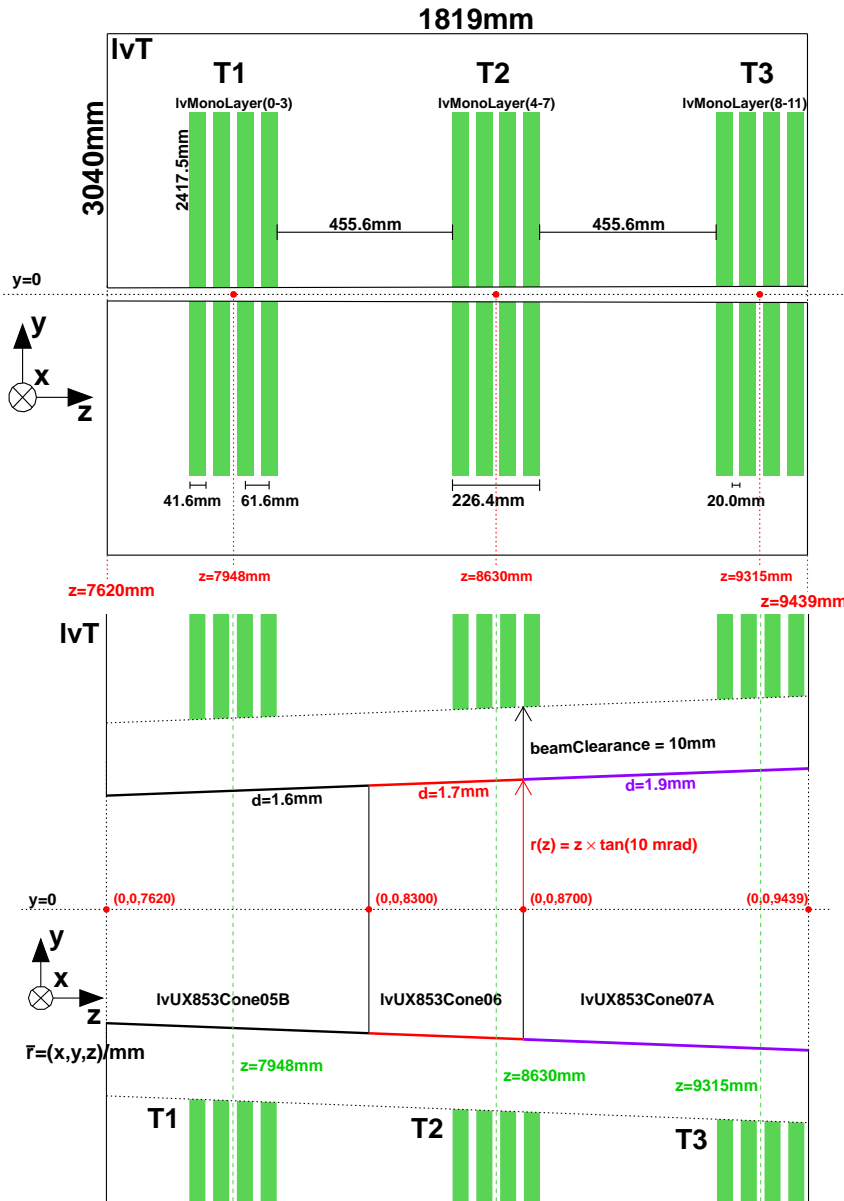


Figure 3.4: Arrangement of the detection layers within the full tracker volume (top) and their position relative to the beam-pipe (bottom).

3.3.1 Geometry Description in Simulation

The layout of the SciFi Tracker was implemented in the LHCb detector description database and used to study the performance of the detector. Standard LHCb packages were used for the detector simulation and new algorithms were developed to perform the digitisation and track reconstruction. Results from these studies will be shown in Sec. 3.9 and Chap. 4. The description of the geometry in the simulation is based on input from the hardware side, and includes the modular structure and dead material between sensitive regions.

The use of stereo angles allows the y co-ordinate to be determined for particles passing through the tracker. This is a key feature which reduces the quantity of fake tracks. Figure 3.5 shows the design of a detection layer displayed for a $+5^\circ$ stereo angle. The two central modules have cut-outs to allow the beam-pipe to pass through the detector.

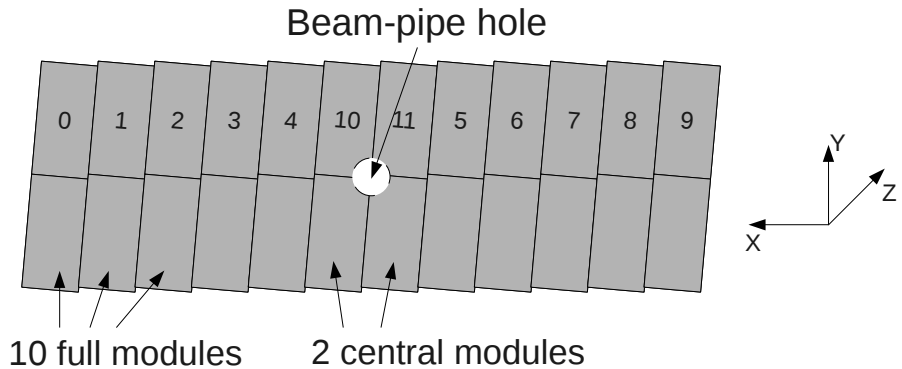


Figure 3.5: The structure of one detection layer is made up of 12 fibre modules. The modules 10 and 11 have a cut-out to allow the beam-pipe to pass through the detector.

The module in the simulation is a seven layer sandwich structure consisting of carbon fibre, honeycomb and Kapton outside of the scintillating fibre mat. The module has two large active regions (*i.e.* top and bottom) with a non-active region around the outside. The total size of one fibre module is 540 mm \times 4835 mm. The fibre materials cover of 99.2% of this area. The fibre mat in the module described in the simulation is a single volume covering the full region. This is different from the fibres mats which will be used to build the final modules (see Sec. 3.6.1). The dead regions that will exist between the mats in the final module are added during the digitisation process in the simulation.

3.4 Scintillating Fibres

Scintillating plastic fibres are considered as the active detector elements for the SciFi Tracker project. A signal of optical photons is produced through a multi-step process. Ionisation energy is deposited in the polymer core of the fibre; a few eV of deposited energy is required to produce an excitation of the polymer [42].³ However, the relaxation time and light yield of the base material is quite poor. An organic fluorescent dye with matched excitation energy level structures is added to the polystyrene base ($\sim 1\%$ by weight) to improve the efficiency of the scintillation mechanism. Energy is transferred quite rapidly (sub-ns) from the base to the dye by means of a non-radiative dipole-dipole transmission, known as the Förster Transfer, where the excited energy state of the dye will subsequently relax by emission of a photon. The fluorescent dye is chosen to have a high quantum efficiency ($> 95\%$), a particular emission wavelength spectra, and fast decay

³More specifically, the p-electrons of the benzene ring of an aromatic polymer chain

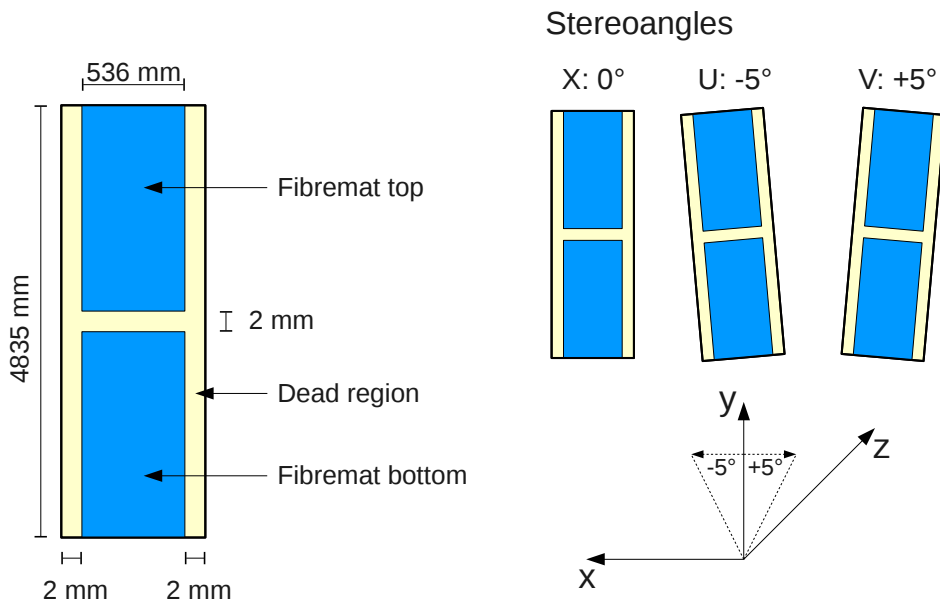


Figure 3.6: The dimensions of a module as described in the simulation and the definition of the stereo angles. The size of the dead material is increased to be visible. The simulation describes one full fibre mat in each module whereas the final module will be constructed using eight separate 13.5 cm fibre mats placed side by side.

time (less than a few ns). Single dopant fibres that emit in the blue-region (such as PMP, or p-terphenyl (PT) dye) typically have a shorter attenuation length of ~ 1 m, due to the self-absorption of the light by the dye. Dyes that exhibit a larger separation between their absorption and emission spectra (Stokes' Shift), such as 3HF which emits in the green, have longer attenuation lengths (> 2 m). A second approach is to use two scintillating dyes. The primary dye has a high quantum efficiency to absorb the energy from the base material and the second dye is a wavelength shifter ($\sim 0.05\%$ by weight). It absorbs the emission of the primary dye, via radiative or non-radiative transfer, and fluoresces at a longer wavelength where re-absorption in the fibre is less likely to occur [43].

For the time being, all experimental work has been concentrated on the multi-clad blue emitting fibre of type SCSF-78MJ⁴ from Kuraray⁵. It uses p-terphenyl (PT) as a primary dye, plus tetraphenyl-butadiene (TPB)⁶ as a wavelength shifter [44–47] and was chosen as the baseline because of previous experience and knowledge gained from using the scintillating fibres in other experiments. Co-operation with a second fibre supplier,

⁴The M indicates multi-clad. The J indicates a high purity distillation process was used. This results in an extended attenuation length.

⁵Kuraray Co., Ltd., Ote Center Building, 1-1-3, Otemachi, Chiyoda-ku, Tokyo 100-8115, Japan.

⁶The dyes have not been confirmed directly by Kuraray, but are based on private communications in the references. In addition, the spectra and timing signatures correspond well to published literature for PT and TPB. A derivative of these scintillators is also possible, but less likely.

Saint-Gobain,⁷ is at an early stage. Saint-Gobain offers the fibre type BCF-12 which is advertised to have similar specifications to the SCSF-78MJ from Kuraray. The delivery of a qualification batch of BCF-12 fibre (several km) is expected in early 2014. The 3HF-type scintillating fibre, known to be radiation tolerant with a long attenuation length and produced by both manufacturers, has been discarded from consideration due to its lower light yield and slow timing characteristics. The known properties of the SCSF-78MJ scintillating fibre from Kuraray and its impact on the SciFi Tracker are presented in the following sub-sections.

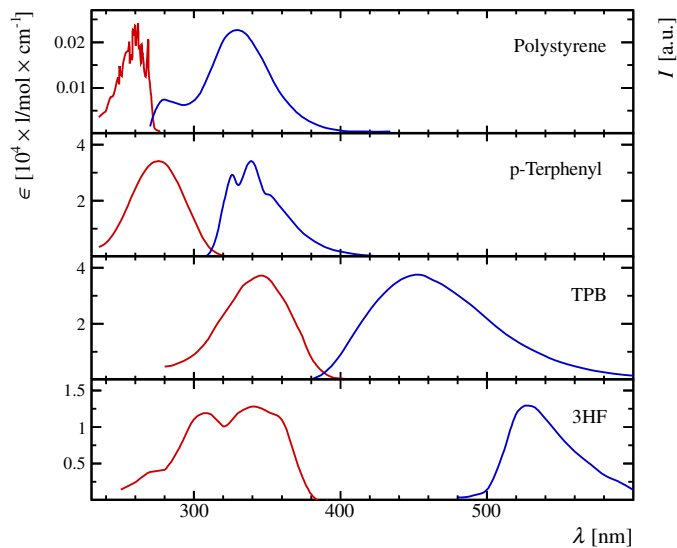


Figure 3.7: Absorption and emission spectra of compounds used in plastic scintillators. Red curves show the decadic molar extinction coefficient ϵ , blue curves show the emission intensity (number of photons) I per unit wavelength in arbitrary units. The data for polystyrene, p-terphenyl (PT) and tetraphenyl-butadiene (TPB) refer to solutions in cyclohexane and are obtained from [48]. 3HF is dissolved in polystyrene, data adapted from [49]. Figure taken from [50].

3.4.1 Properties

Plastic scintillating fibres with a circular cross-section and a total diameter of 250 μm , which includes two cladding layers nominally 3% total thickness each, are intended to be used. A schematic of the fibre is shown in Fig. 3.8. The core of the fibre is doped polystyrene having two claddings with lower, decreasing indices of refraction. The inner cladding is made of PMMA and the outer cladding is made of a fluorinated polymer. The light yield is typically around 8000 photons/MeV of deposited ionisation energy (BCF-10,12,20 [51]) though no value is listed by Kuraray for SCSF-78MJ fibres.

⁷formerly Bicron, Saint-Gobain Crystals 17900 Great Lakes Pkwy, Hiram, OH 44234-9681, United States.

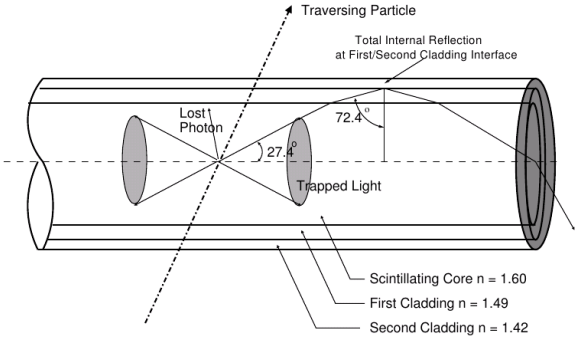


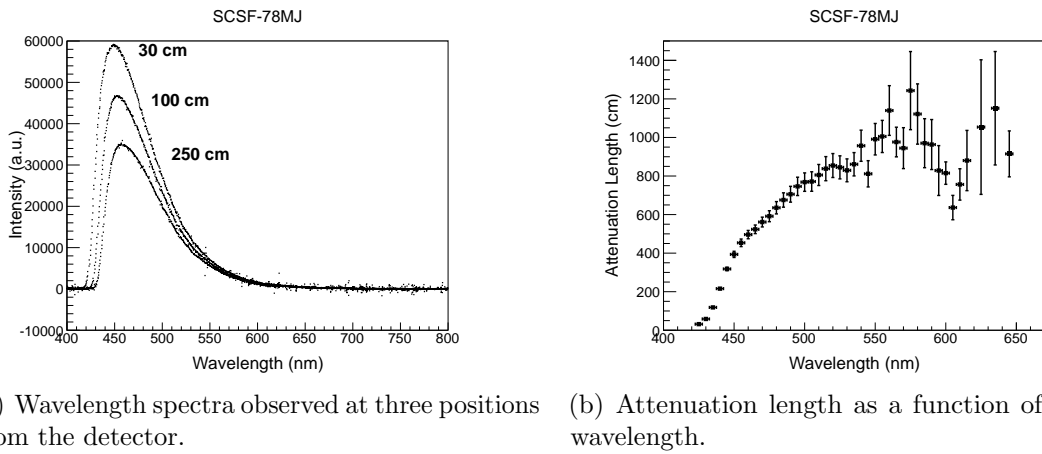
Figure 3.8: Fibre schematic. Light is produced in the core material and then trapped and propagated within the fibre through total internal reflection. The claddings have decreasing indices of refraction.

The trapping efficiency for isotropically emitted (scintillation) light in a single hemisphere is 5.34% (helical path or non-meridional light rays will further increase this number, but are highly attenuated) and the numerical aperture of the fibre is 0.72. The nominal emission spectrum (for emission near to the detection point) for the SCSF-78MJ fibre extends from about 400 to 600 nm and peaks at 450 nm near the source, as shown in Fig. 3.9(a) with a bulk optical absorption length of > 3.5 m. Typically, there are short and long components to the attenuation length, due to geometrical effects in the fibre, as well as a strong wavelength dependence on the attenuation length due to re-absorption of the shorter blue wavelengths by the scintillation dyes, Rayleigh scattering, and some discrete absorption of higher wavelengths by the polystyrene, as shown in Fig. 3.9(b). The effect on the emission spectrum and the optical absorption length by radiation will be further addressed in Sec. 3.4.2.

The decay time constant of the scintillation light signal is nominally 2.8 ns [52] and is dominated by the excitation decay of the TPB. The mean propagation time of light along the length of the fibre is 6 ns/m. This number results from the permittivity of the core and cladding material as well as from the isotropic emission of scintillation light. The emitted photons undergo multiple reflections at the material interfaces and follow helical paths instead of the shortest distance from the point of excitation to the fibre end.

Typically, one observes between 15 – 20 photoelectrons per mm of scintillating fibre traversed by a charged particle near the source as seen by a SiPM. This light yield and timing appears to be sufficient for the needs of the SciFi Tracker. Measurements of the light yield with an SiPM photo-detector will be shown in Sec. 3.6.4.

The so-called S -parameter ($0 \leq S \leq 1$) describes the degree of axial alignment of the polystyrene chains in the fibre core. These S-type fibres with a high (> 0.7) degree of alignment have better mechanical properties (bendability) but also a reduced optical attenuation length. It is difficult to produce two distinct types (S-type and non-S-type) for small diameter fibres. The 250 μm fibres from Kuraray have an S -parameter of about 0.4.



(a) Wavelength spectra observed at three positions from the detector. (b) Attenuation length as a function of photon wavelength.

Figure 3.9: The attenuation of discrete wavelengths seen in Kuraray SCSF-78MJ scintillating fibres. The attenuation length is found from a single exponential fit of the measured intensities along positions from 50 cm to 270 cm. A 370 nm LED was used to stimulate the fibre and was read out with an intensity calibrated Hamamatsu C10083CA-2050 photospectrometer.

The minimum bending radius recommended by the supplier for this fibre type is about 12.5 mm.

3.4.1.1 Geant4 Simulation

Knowledge of the time distribution of photons arriving at the SiPM is crucial for the design of the read-out electronics and in the context of spill-over determination (see Sec. 3.7). Therefore, simulations employing the GEANT4 [53, 54] toolkit and measurements were performed to illuminate these fibre properties.

In a first step, a basic implementation of the fibre in GEANT4 was used to determine the time distribution of exiting photons for different points of excitation with minimum ionising particles (MIPs) [55]. A single photon wavelength and thus single discrete absorption and scattering lengths were used to describe the propagating light. However, the result of this study is in good agreement with measurements of the propagation time in a fibre with Aluminium metallisation at the end opposite from the detector and excited by an UV LED (see Fig. 3.10).

To achieve a more realistic description of time distributions and light attenuation, especially after irradiation of the fibre, a much more detailed implementation of the fibre in GEANT4 has been developed [56]. This simulation can deal with different emission and absorption spectra, decay times, geometries, radiation doses and many other properties provided via parameter files, so that different scenarios can be studied easily. Detailed information about the produced and detected photons such as wavelength, time, path length, momentum direction, *etc.* is recorded. A virtual fibre mat can be built, additional light loss factors within the fibre can be applied and the number of detected photons with different wavelength dependent SiPM sensitivities can be investigated. The outputs and

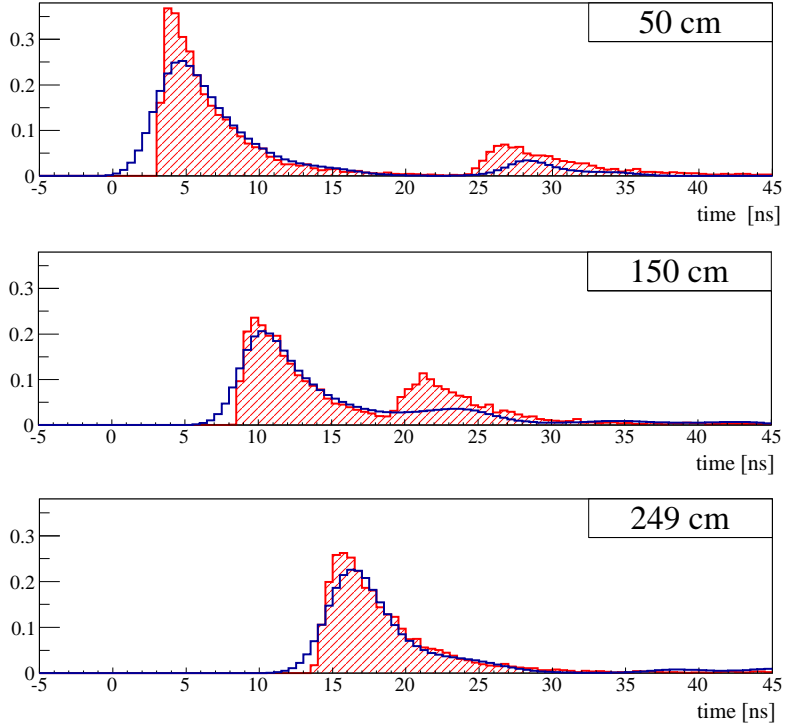


Figure 3.10: The arrival time of photons within a 250 cm long scintillating fibre for positions 50 cm (top), 150 cm (middle) and 249 cm (bottom) from the photo-detector in simulation (red) and experimental measurements (blue) [55]. The secondary peak is a result of photons reflected from a mirror at 250 cm.

results of this simulation serve as inputs to the timing information needed for signals in the front-end electronics.

3.4.1.2 Fibre Diameter

Our current understanding of the technical specification of the fibre is summarised in Ref. [57]. The extrusion of dual-clad scintillating plastic fibres from a preform is a delicate process requiring the control of a multitude of parameters. The temperature of the furnace and the rotation speed of the mandrel which receives the fibre have a direct impact on the fibre diameter. The producers monitor the diameter during production (with cm sampling intervals) and achieve average diameters within about 1% from the nominal value. The measured nominal fluctuations are tolerable for production. However, according to information from Kuraray, inhomogeneity of the base material can lead to fibre diameter variations on small length scales (order of cm) which cannot be controlled by regulating temperature and speed. These bumps become a concern if their size exceeds about 300 μm . The fibres are delivered on 12.5 km long spools. Every spool of fibre will be checked by the

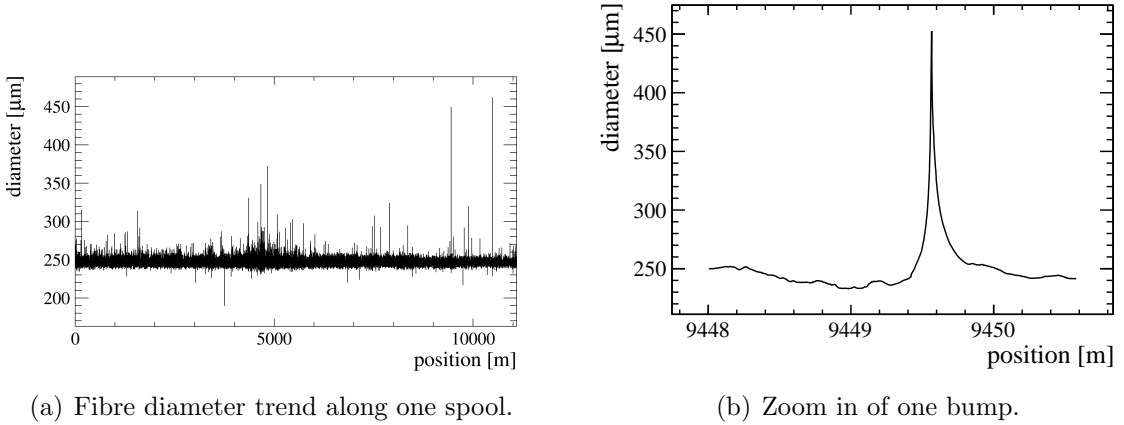


Figure 3.11: The trend of the diameter of one spool. Spikes in the left plot are bumps in the fibre and one of them shown in the right plot.

manufacturer before shipment for quality. Spools which contain fibres above the tolerance limit (presumably $< 300 \mu\text{m}$) with intervals below 1500 m will not be shipped. These bumps (diameter $300 - 500 \mu\text{m}$) would cause serious disorder of the fibre matrix.

All the delivered fibres are checked again by the collaboration in view of the diameter and light guidance with the help of a dedicated machine. It has been developed to control fibres of spooled fibres of several kilometres length during rewinding. The diameter is measured by a laser micrometer and UV-LEDs excite the fibre. The data from one spool is shown in Figs. 3.11 and 3.12. A mechanically damaged fibre region is identified via the measurement of lateral light losses.

The fibres are to be bonded into a matrix structure forming long ribbons consisting of five and six staggered layers with a horizontal pitch of $270 \mu\text{m}$, and a total length of

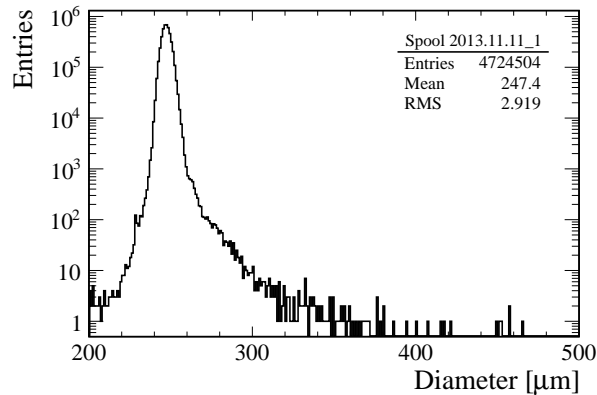


Figure 3.12: The fibre diameter measured over 11 km of continuous fibre. It is visible that some bumps exist beyond $300 \mu\text{m}$. Multiple entries may correspond to the same bump.

about 2.5 m. They are covered with a thin epoxy layer (Epotek 301-2)⁸ during ribbon production, and again during final ribbon moulding. Titanium-dioxide will be added to the epoxy to reduce channel-to-channel cross-talk. The difference between fibre diameter and positioning pitch mitigates the effect of fibre diameter variations or other imperfections (e.g. dust grains).

3.4.2 Radiation Tolerance of the Fibre

The scintillating fibres are exposed in the innermost region of the detector, at about 8 cm from the beam-pipe axis, to an accumulated radiation dose of approximately 35 kGy after an integrated luminosity of 50 fb^{-1} . The expected dose drops rapidly, both in the horizontal and vertical direction, and becomes relatively marginal ($< 1 \text{ kGy}$) at distances of about 50 cm [41], as shown in Sec. 3.2.3. Radiation damage to plastic fibres was systematically investigated in the early 1990s [58], and the optical changes to the base material resulting in transmission loss were identified as main cause for the degradation of their light output. Radiation damage leads to a reduction of the optical attenuation length and the viability of a fibre at a given radiation load depends crucially on its length. However, the basic scintillation and wavelength shifting fluors, as well as other additives, could also suffer damage and contribute to the performance degradation, though this is not expected for the Kuraray SCSF-78MJ fibre.

From the beginning of radiation damage studies on fibres, the impact of radiation dose rate, radiation type and environmental effects (presence of oxygen) as well as recovery effects were controversially discussed in the literature. Analysis of the publications of a number of irradiation experiments which have been performed for the baseline fibre or similar polystyrene based blue emitting fibres revealed results partly disagree where the conclusions are vague or contradictory [59]. It was therefore considered mandatory to perform a series of radiation experiments with baseline fibre of the SciFi Tracker in a configuration which comes close to the one in the final detector. While some of the experiments are completed, further complementary tests will be performed in 2014 on completed fibre ribbons and modules in conditions as similar as possible to the LHCb upgrade.

The different fibre irradiation experiments that have been conducted by this collaboration occurred under differing conditions but all used the same fibre type.

3.4.2.1 24 GeV/c Proton Irradiation

A radiation test was performed in the CERN PS T7 area with 24 GeV/c protons on a plexiglass test plate which contained an arrangement of 8 SCSF-78MJ fibres of 2.94 m length on a 1 m polycarbonate plate. The fibres are laid in straight channels on the plate and then turned back at the ends of the plate with a bending radius of ~ 12 cm, resulting in four 75 cm long segments. Details of this test and the performed characterisation measurements can be found in Ref. [60]. An identical sample, which did not receive any

⁸EPOTEK, Epoxy Technology, Inc., 14 Fortune Drive, Billerica, MA 01821, USA.

Table 3.2: Dose profile and rates of the fibre irradiation in the CERN PS area with $24 \text{ GeV}/c$ protons.

	section (cm)	dose (kGy)	dose rate (Gy/s)
1	$0 - 75$	0	0
2	$75 - 150$	0	0
3	$150 - 225$	3	6.25
4	$225 - 294$	22	1.4

radiation, was kept as reference. The irradiation was programmed to reproduce the ionising dose profile expected in the LHCb environment coarsely along the fibre bundle length in four 75 cm long sections. The irradiated sections and dose are described in Table 3.2.

Sections 1 and 2 received only background radiation from neutrons. This resulted in a neutron fluence of about $(5 \times 10^{12} \pm 20\%) \text{ n/cm}^2$ which represents a negligible ionisation dose. The measured radiation doses and fluences were extracted from the forward currents of a set of four PIN diodes and the activation of aluminium foils which were attached to the sample right above the fibre locations (see Table 3.2). In accordance with the rules in place at CERN, the sample could be extracted from the irradiation zone after a cool down time of seven days.

The characterisation of the fibre samples was performed with two different methods:

- Lateral excitation of the wavelength shifting fluor in the fibre with a UV-LED (DC mode) and read out at one fibre end either with a calibrated photodiode or with a spectrometer. These measurements yielded the emission spectrum and the (averaged or wavelength resolved) attenuation lengths in the four irradiation sections as a function of the dose.
- Exposure to an energy filtered Sr-90 source (electron-gun) and read out at one end with a SiPM detector (Ketek 1 mm²). These measurements are sensitive to a possible damage of the scintillation mechanism. The absolute photoelectron yield is, however, not representative as the geometrical arrangement of the fibres in the test sample differs from the SciFi Tracker geometry.

In both cases, a removable aluminised glass mirror was attached to the non-read-out fibre end to study mirror effects. For a comparison of photodiode and SiPM data, the different spectral responses of the photo-detectors were taken into account.

The effective attenuation length, Λ , is typically extracted from a single exponential fit to the data, $I(d) = I_0 \exp(-d/\Lambda_{abs})$, for positions from the photo-detector, d , greater than 50 cm. A double exponential fit is needed to account for the short attenuation components less than 50 cm owing to geometrical path and wavelength effects in the fibre. More complex parameterisations are needed when including the mirror at the far end.

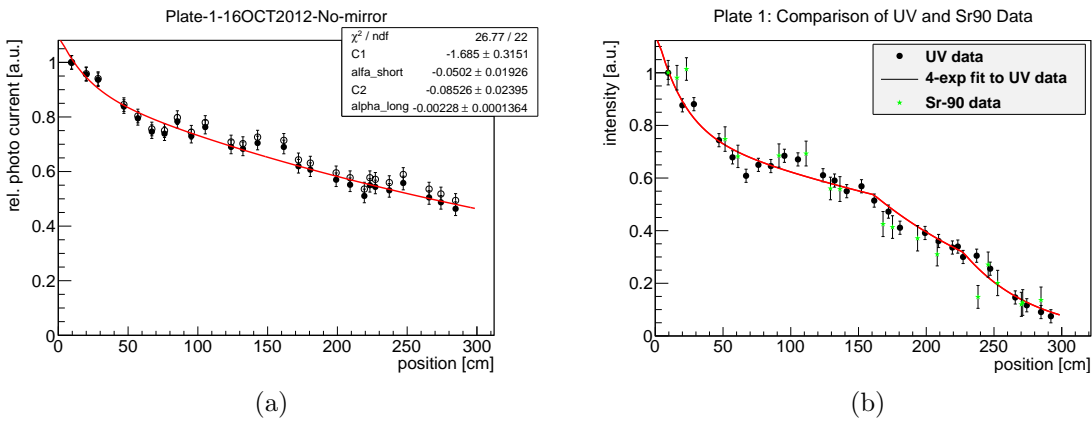


Figure 3.13: Relative light yield with UV excitation as function of the excitation distance of the scintillating fibres before and after irradiation. (a) Before irradiation. Open symbols: As measured with the PIN diode. Full symbols: Scaled to the spectral response of a KETEK SiPM detector. (b) After irradiation: Relative light yields resulting from UV excitation and exposure to electrons from the Sr-90 source.

Data from measurements before and after irradiation are shown in Fig. 3.13. The measurements after irradiation are described by a combination of exponential functions, where the individual segments of the fit in Fig. 3.13(b) were defined such that they coincide at the turn point positions of the plate. The fits resulted in the attenuation lengths summarised in Table 3.3. The long and short components of the attenuation length are shown. The short attenuation length describes the rapid loss of helical light rays and/or possible 'cladding' light along with losses in the shorter wavelengths.

The Sr-90 data in Fig. 3.13(b) shows a very similar dependence on the excitation distance as the UV-LED data (after scaling the latter to the spectral response of the SiPM). It therefore appears that both, the scintillation and wavelength shifting mechanism of the fibre are, if at all, only marginally affected by the applied radiation levels. The main effect of the radiation damage is a wavelength dependent degradation of the transparency

Table 3.3: Optical attenuation length Λ before and after irradiation. The data for sections 1 and 2 include the long/short attenuation length, while 3 and 4 only contain the long component. The errors are statistical only.

section	dose (kGy)	sample 1 non-irrad. (cm)	sample 2 (cm)	sample 1 irrad. (cm)	Λ/Λ_0
1 and 2	0	$439^{+28}_{-25} / 20^{+8}_{-5}$	$346^{+13}_{-12} / 10^{+40}_{-5}$	$422^{+97}_{-66} / 20^{+8}_{-5}$	0.96
3	3	439^{+28}_{-25}	346^{+13}_{-12}	126^{+13}_{-10}	0.29
4	22	439^{+28}_{-25}	346^{+13}_{-12}	52^{+6}_{-5}	0.12

of the fibre core.

3.4.2.2 22.9 MeV Proton Irradiation

Scintillating fibres were also irradiated at the Karlsruhe Institute of Technology (KIT) using 22.9 MeV protons from the Compact Cyclotron.⁹ The samples were placed in a box on an XY stage and moved laterally in front of the beam. The fibres were arranged in two configurations in shallow channels on a PVC board, as shown in Fig. 3.14. The geometries of the boards were defined by the irradiation facilities and the XY stage used at KIT which had a 20 cm × 40 cm window. Precision holes for the base of a UV-LED light holder allowed for simple and reproducible measurements for each position of the board. Similar to the CERN PS measurements, small bundles of four or six 250 µm diameter Kuraray SCSF-78MJ scintillating fibres were embedded in Epotek 301-2 epoxy arranged on boards with 1 mm × 0.5 mm shallow grooves. Boards were prepared for unirradiated control samples as well. Details of this test and the performed characterisation measurements can be found in Ref. [61].

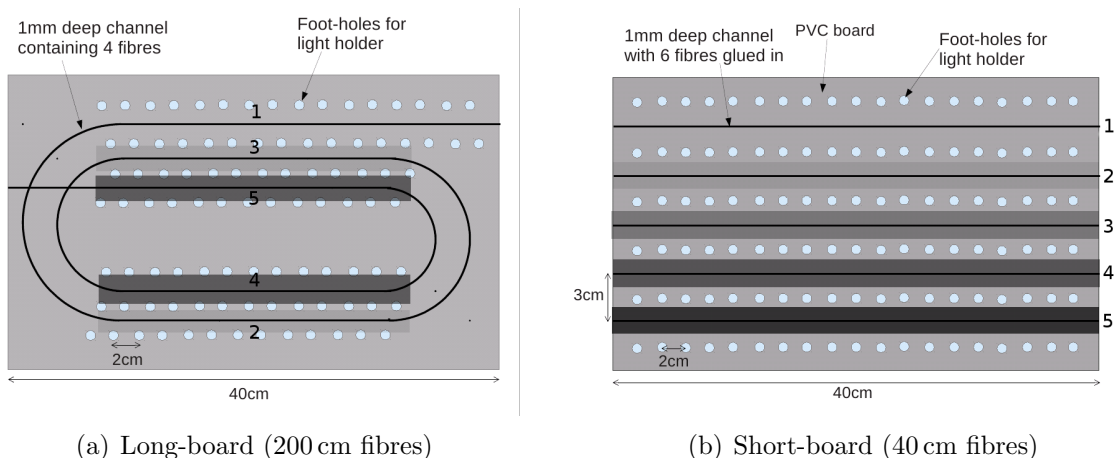


Figure 3.14: PVC boards with channels for (a) the 200 cm and (b) the 40 cm long fibre bundles. The shaded and numbered regions indicate the regions irradiated.

A minimum stable beam current of $\sim 0.2 \mu\text{A}$ meant that the lowest dose achievable was approximately 7 kGy. The highest dose applied of 60 kGy was chosen to be higher than the FLUKA simulations for the upgrade by a factor of two.¹⁰ The dose was applied at an approximate rate of 5 kGy/s which is much faster than in the CERN-PS or the *in situ* measurements mentioned below. A range of doses over multiples of the minimum dose were tested due to the scanning method and fixed beam current. The integrated proton fluences were measured with Nickel foils and with calibrated silicon PIN diodes on selected

⁹KIT Campus North.

¹⁰Based on early LHCb upgrade dose estimates (*cf.* Sec. 3.2.3).

channels. The uncertainties in the nickel foil measurements were estimated to be 20% [62], and 30% for the PIN diodes.

The light yield of the scintillating fibre bundles for both the long and short boards was measured before and after irradiation and the transmission from each board position was compared. The fibres were stimulated laterally with a 370 nm UV LED operated in DC mode. By taking the ratio of the measured light output, local variations in the board due to reflections and epoxy coverage were removed. Assuming the data fits well to a single exponential containing only the long component after a few cm, one can fit the ratio of the data to

$$I'(x)/I(x) = K'e^{-x\left(\frac{1}{\lambda'} - \frac{1}{\lambda_0}\right)}$$

to extract the attenuation length after irradiation. Data showing the ratio of after to before irradiation as measured by a calibrated photodiode are shown in Fig. 3.15. The results of the dose and attenuation length measurements are given in Table 3.4 and are consistent with the CERN-PS measurements.

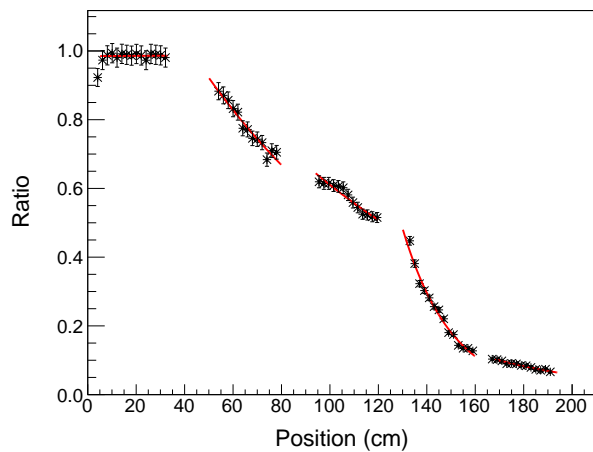


Figure 3.15: Ratio of current measurements after irradiation to before irradiation of the 200 cm long fibres. Each group of ≈ 15 data points represents a single dose region, with gaps in between corresponding to the curved sections of the fibre bundle, which were not irradiated. Statistical errors in the ratio data points are $\pm 2.8\%$ and ± 0.5 mm for the position.

3.4.2.3 Irradiation in the LHCb Cavern

Irradiations of three sets of 1.1 m long fibres were performed *in situ* in the LHCb cavern to study the damage for low doses and dose rates. The samples were installed in 2012 during LHC Technical Stop 1 on the shielding wall close to the VELO. The doses were in the sub-kGy range (70 Gy to 800 Gy). Measurements of the relative light yield as a function of the position of a Sr-90 source were performed during subsequent technical stops. The measurements and the analysis suffer from a number of limitations inherent to

Table 3.4: The mean dose measurement and the ratio of the measured attenuation length after to before irradiation for the 200 cm and 40 cm fibre bundles using Nickel foils and PIN diodes.

Long-board Fibres (200 cm)			Short-board Fibres (40 cm)	
Sec.	Dose (kGy)	$\Lambda'(D)/\Lambda_0$	Dose (kGy)	$\Lambda'(D)/\Lambda_0$
1	0	1 ± 0.16	0	-
2	8.8 ± 1.5	0.20 ± 0.04	9.5 ± 1.9	0.26 ± 0.03
3	10 ± 2	0.23 ± 0.05	18 ± 3	0.15 ± 0.02
4	43 ± 7	0.052 ± 0.02	37 ± 7	0.067 ± 0.012
5	36 ± 7	0.13 ± 0.11	60 ± 10	0.048 ± 0.012

the *in situ* set-up, such as a non-uniform dose profile and the shorter fibre length. Further measurements, simulations and analysis will reduce the uncertainties. The relatively low dose levels make it difficult to derive a conclusive result but are overlaid, though not used, with the combined analyses below (see Fig. 3.16).

3.4.3 LHCb Radiation Damage Estimates

The empirical model of the radiation damage to the scintillating fibre (the reduced attenuation length) used in the Viability Assessment Review [60] was constructed in the same manner as in Ref. [63]. A logarithmic function $\Lambda'(D)/\Lambda_0 = \alpha + \beta \log(D)$ is used to describe the ratio of the attenuation length after irradiation to before, where D is the received dose in kGy. Using only the three data points available at the time from the CERN-PS measurements, values of $\alpha = 0.38 \pm 0.04$ and $\beta = -0.20 \pm 0.04$ were found. First predictions, made in February 2013 for the Viability Assessment Review, for the light yield after irradiation in the full SciFi Tracker were based on this model, folding in the expected radiation field of the LHCb upgrade and predicted a reduction in the light yield of 40% from the most damaged region of the detector, which also happens to be the furthest from the photo-detectors, near the beam-pipe.

Including the new data from the 22.9 MeV proton measurements at KIT into this fit results in values of $\alpha = 0.44 \pm 0.04$ and $\beta = -0.23 \pm 0.03$, which predicts less light loss than before for the same maximum dose after 50 fb^{-1} . However, this logarithmic description has two failings. The ratio of attenuation lengths goes to infinity near zero dose and becomes negative at large doses. Other empirical models were proposed and describe the data as well or better and do not have the same problems. The combined data and model fits are shown in Fig. 3.16. Model 1 assumes a linear damage with dose effect ($\Lambda'(D)/\Lambda_0 = 1/(1 + (D/A))$). Model 2 assumes a power law relationship for the damage from irradiation ($\Lambda'(D)/\Lambda_0 = 1/(1 + (D/A)^B)$). Model 3 is the logarithmic dependence similar to the study in Ref. [63]. Model 4 is another non-linear model which has an exponential-like behaviour ($\Lambda'(D)/\Lambda_0 = \exp((D/\alpha)^\gamma)$).

Using these models, an updated prediction of light loss in the scintillating fibre at the

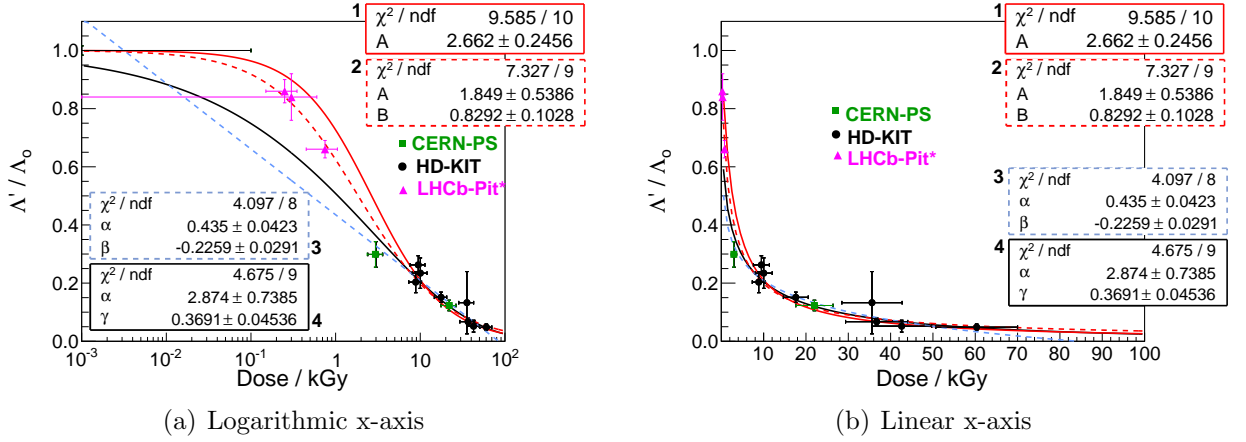


Figure 3.16: The combined attenuation length data versus dose from three fibre irradiation studies and fits to 4 models. Model 1 assumes a linear damage with dose effect ($\Lambda'(D)/\Lambda_0 = 1/(1 + (D/A))$). Model 2 assumes a power law function ($\Lambda'(D)/\Lambda_0 = 1/(1 + (D/A)^B)$). Model 3 is the logarithmic function $\Lambda'(D)/\Lambda_0 = \alpha + \beta \log(D)$. Model 4 has an exponential-like behaviour ($\Lambda'(Dose)/\Lambda_0 = \exp(-(D/\alpha)^\gamma)$). The LHCb-Pit data are not included in these fits.

full 50 fb^{-1} is shown in Fig. 3.17. The data is simulated in a ROOT [64] based parametric Monte Carlo with Model 4, a more pessimistic model than Models 1 – 3, which predicts greater losses at low doses, where $\Lambda(D)/\Lambda_0 = \exp(-(D/\alpha)^\gamma)$. The parametric Monte Carlo is based on the current knowledge of the detector components. It steps virtual photons (no ray tracing) along a defined distance in Y, with the dose profile based on FLUKA simulations described in Sec. 3.2.3 and the subsequent attenuation lengths based on the above measurements are checked after each step. The photon survival probability after each step is determined from the reduced attenuation length. The photons are also given wavelengths based on measured spectra and matched against the photon detection efficiency of measured SiPMs to determine their detection probability at the end of the stepping.

The expected fraction of signal loss is seen to be $27 \pm 3\%^{11}$ after 50 fb^{-1} with 35 kGy of dose near the beam pipe. The irradiation dose at a given position is based on a parameterisation of dose curves presented in the Viability Assessment Review, and scaled to the higher expected dose at the 100 mb cross-section. If the received dose is greater by a factor of two, then Model 4 predicts a loss of $43 \pm 17\%$. A summary of the expected signal loss in the fibre after irradiation over multiple doses is presented in Table 3.5. The lack of measurements at doses less than 1 kGy is an issue that needs to be resolved as this is where the models show the largest deviation. Combined with the inherent uncertainties in the dose estimations, a loss of 40% near the beam-pipe after 50 fb^{-1} will be assumed. The four models predict a variation from $10 - 20\%$ reduction of signal away from the beam-pipe, as

¹¹The uncertainties are the RMS of 100 toy Monte Carlo samples of 100 events each with parameters having a Gaussian distribution based on uncertainties in Model 4.

Table 3.5: This table describes the dose and signal seen near the beam-pipe: given the maximum dose seen in the fibre, the expected relative signal loss near the beam-pipe is shown over multiple peak doses along with the fraction of the signal lost due to irradiation, the fraction of final dose expected and the fraction of the total loss of signal relative to 35 kGy, the maximum dose expected after 50 fb^{-1} of data collection.

Max. Dose (kGy)	frac. of signal lost	frac. of final dose	frac. of total loss
1	0.031	0.03	0.12
8.75	0.11	0.25	0.41
17.5	0.16	0.5	0.61
26.25	0.22	0.75	0.81
35	0.27 ± 0.03	1	1
70	0.43 ± 0.17	2	1.6

the damage can be quite significant at lower doses, especially when spread over a large area. A more detailed examination of the dose distribution around the beam-pipe and its implications on signal loss are also needed. Additional simulations and irradiation tests at lower doses will be conducted in 2014.

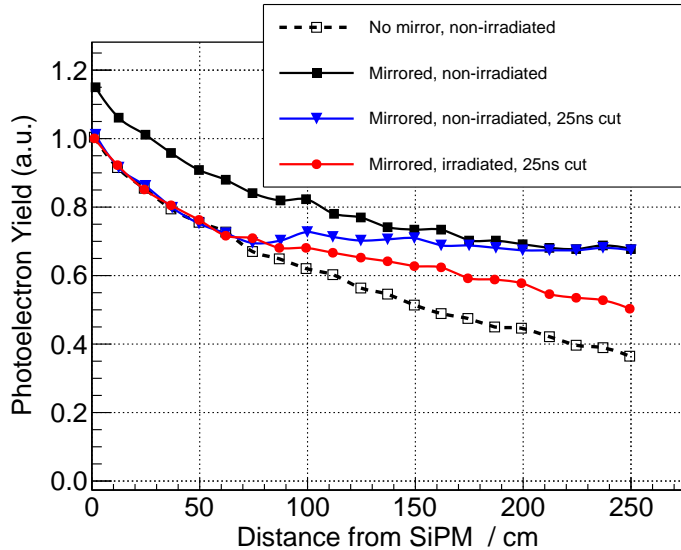


Figure 3.17: The relative photoelectron yield from a ROOT-based parametric Monte Carlo of the SciFi Tracker. The model estimates the signal yield from (1) a non-irradiated, mirror-less fibre, (2) an non-irradiated, mirrored fibre, (3) a non-irradiated, mirrored fibre after cutting photons that arrive after 25 ns and (4) an irradiated, mirrored fibre after cutting photons that arrive after 25 ns. The signal loss is estimated to be $27 \pm 3\%$ after 50 fb^{-1} with 35 kGy of dose in the worst region.

The wavelength spectrum after irradiation can also be estimated using the measurements above. The peak emission of the fibre specified by the manufacturer is 450 nm and has been confirmed by measurement. Strong attenuation of the short wavelengths over distance produces a spectrum near the mirror with a peak near 490 nm (with mirroring) as shown in Fig. 3.18(a). The mean wavelength value at the mirror is estimated to shift slightly again from 490 nm to 495 nm after 35 kGy (Fig. 3.18(b)). The signal from fibres can be maximised by ensuring the peak quantum efficiency of the photo-detector matches the irradiated fibre spectrum where the majority of the tracks reside in the lowest signal amplitude region. The photon-detection efficiency of the SiPM photo-detectors is discussed in Sec. 3.5 (see Fig. 3.21) and is relatively flat over 420 – 550 nm.

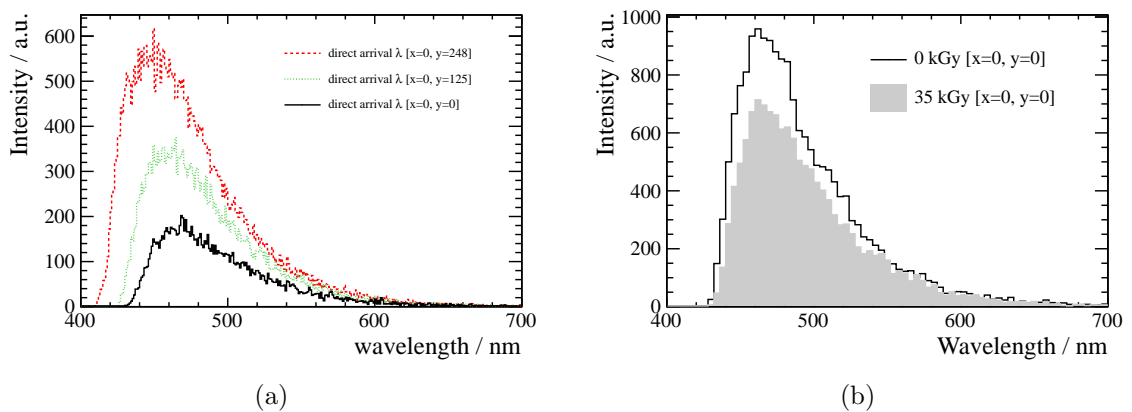


Figure 3.18: The wavelength spectra (as seen at the photomultiplier) expected from the scintillating fibres based on a parametric Monte Carlo simulation in ROOT. (a) Wavelength spectrum after 35 kGy at 0, 125 and 248 cm from the beam-pipe (without mirroring). (b) Wavelength spectra at 0 and 35 kGy at 0 cm from the beam-pipe.

3.4.4 Summary

The SCSF-78MJ from Kuraray should produce a sufficient light yield and has a long enough attenuation length for this detector. It is also of sufficient quality to produce the fibre mats needed. The wavelength spectra of the fibre overlaps well with the photo-detector. The radiation damage to the fibre material results in degraded transmission but it is expected to result in less than 40% loss of signal from the worst regions near the beam-pipe after 50 fb^{-1} . The worst case scenario (Model 4 with losses up to 43%) is currently assumed to allow for a safety factor. Further irradiation studies at lower doses are needed to constrain the damage models to understand the behaviour over the whole detector over time. Measurements at low dose rates will be made to evaluate possible annealing effects. The mirror at the end of the fibres is a very necessary part of the design to increase the signal after irradiation near the ends of the fibre far from the photo-detector. However, this has implications for the timing of the signal and spillover.

3.5 Silicon Photo-detectors

Silicon photomultipliers (SiPMs) are solid state photon detection devices that combine all of the features necessary for the photon detection of a high resolution scintillating fibre tracker. A good overview of the most important characteristics is given in Ref. [65]. Two SiPM manufacturers, Hamamatsu¹² and KETEK¹³, have developed dedicated devices for the SciFi Tracker. These custom devices provide high photon detection efficiency (PDE) in a large wavelength range, high reliability due to its simple mechanical construction, a high density multi-channel package and are of sufficiently low cost to allow the construction of a large area tracking device. There are several challenging requirements placed on the photo-detector mainly due to the neutron radiation environment and the low light output of the long scintillating fibres. The development of customised devices is required to adapt to the dimensions of the detector channels and the packaging suitable for low temperature operation. New devices with the latest technological improvements implemented will be available in spring 2014.

The two most important characteristics of the tracker are the hit detection efficiency and spatial resolution. These characteristics are dominated by the overall light yield¹⁴ of the detector and fibre module once the mechanical dimensions, such as channel size and fibre diameter, are fixed. The noise of the detectors has three contributions: dark noise, pixel cross-talk and after-pulsing. The dark noise produced by random avalanches in the amplifying silicon region creates signals with amplitude equal to one photon. The rate of dark noise or Dark Count Rate (DCR) increases strongly after irradiation. It is the only radiation damage observed for the detectors at the level of irradiation required for LHCb. Each avalanche produced can induce an avalanche in a neighbouring pixel which is called pixel to pixel cross-talk. The cross-talk, as well as after-pulsing, depends strongly on the detector technology.¹⁵ The after-pulse noise is accounted for in the random DCR as after-pulses with significant amplitude compared to one pixel signals can only occur after a large fraction of the pixel recovery time ($> 10\text{ ns}$). After-pulsing has been significantly reduced in the latest technology and contributes only a minor fraction to the total noise.

3.5.1 Signal Characteristics

The characteristics of the signal and the noise have been studied to evaluate the hit detection efficiency and spatial resolution. A realistic simulation of the signal generation in the fibres and the collection in the photon detectors has been made. The detector model accurately reproduces the signal distribution among the fibres and, as a consequence,

¹²Hamamatsu Photonics K.K., 325-6, Sunayama-cho, Naka-ku, Hamamatsu City, Shizuoka Pref., 430-8587, Japan.

¹³KETEK GmbH, Hofer Str. 3, 81737 München, Germany.

¹⁴The overall light yield is understood as the most likely value for the number of detected photons per cluster for a MIP. A cluster is formed by combining the signals from neighbouring channels and the clusterisation algorithm is described in Sec. 3.5.5

¹⁵The Dark Count Rate is measured by counting the number of noise counts above the signal height of half a photoelectron (0.5 PE).

allows the efficiency and resolution to be estimated. A cosmic ray telescope was used to verify the simulation results.

The dominating characteristic for the performance of the detector is the light yield. It has been measured for modules with different lengths (see Sec. 3.6.4). The most recent measurement was made on a five layer fibre mat with a length of 2.5 m. To produce mono energetic electrons of 1.8 MeV, a so-called “electron-gun” with a Sr-90 source was used, and a scan over the length of the detector was performed. The signal for a perpendicular particle is typically recorded by two detector channels. A clustering algorithm is necessary to combine the signals from several channels to form clusters. The signal generation is illustrated in Fig. 3.19. The ionising particle produces photons in each fibre along its trajectory and, after the propagation of the light to the detector, the photons are detected on the SiPM photo-detector. The illustration is taken from an example of a GEANT4 simulated event where the coloured pixels on the detector are pixels with signal due to a photon which hit the detector at the position indicated by a small black dot. Depending on the exit angle at the fibre end, a small displacement from the exit point of the fibre is possible as there is an approximately 100 μm thick optical window between the fibre end and the silicon surface.

3.5.2 Sensor Design and Packaging

The multi-channel detector arrays are designed for a channel pitch of 250 μm and a channel height that can cover the stack height for six layers of fibres. The detector read-out pitch is 250 μm which is slightly smaller than the fibre pitch of 270 μm . The active area is 200 μm higher than the total stack height of the fibres to cope with misalignment due to manufacturing tolerances, for example thickness of glue and mounting tolerances. The detector designed for six layers can also be used in the region with five layers. The number of channels per detector module is maximised to keep geometrical inefficiency due to gaps between detectors as low as possible. Due to mechanical constraints, the maximum number of channels per array is 128. The 128 channel detectors are built out of two 64 channel silicon dies which are assembled into one package as shown in Fig. 3.20. The gap on the sensor is minimised by cutting tightly around the edge of the silicon, and allowing small tolerances for the mounting process. A 250 μm gap between two silicon dies, or from a dead channel, can be recovered in 80 – 90% of the cases by the signal in the neighbouring channels. This is possible because the majority of the clusters have signals large enough for detection in more than one channel. A slight degradation in spatial resolution in these regions is expected. The gap between two detector arrays is 400 μm wide. The inefficiency due to geometrical gaps and single dead channels is expected to be 1%.

An epoxy protection layer for Hamamatsu, or a glued thin glass plate for KETEK detectors, with a thickness of 100–120 μm is placed between the end of the fibres and the silicon surface. This thin protection layer ensures that the cluster size is not significantly increased due to the light propagation between fibre end and silicon surface. The protection layer is advantageous for the handling of the detectors and to prevent ageing effects, such as corrosion, during long term operation. The packages for the two manufacturers are

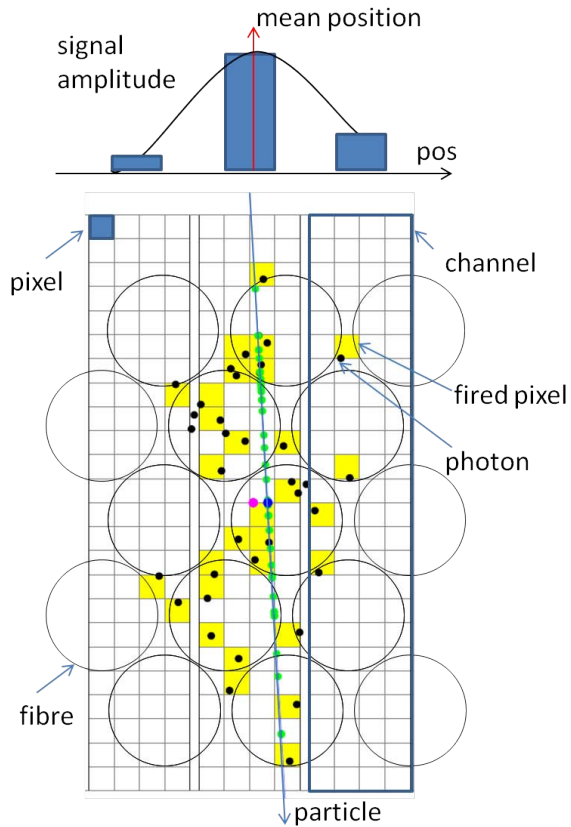


Figure 3.19: The photons produced along the trajectory of the particle are propagated to the fibre end and further to the detector. Each pixel of the detector can detect one photon and the signal proportional to the total number of pixels with signal (coloured pixels) is the signal amplitude per channel illustrated in the top part of the figure. The particle position can be calculated with a weighted mean value of the channel signal. Note that the fibres are not aligned to the detector channels and the photons can arrive at the detector outside the fibre area.

made for a low temperature soldering process. The pixel size was maximised for the latest generation of detectors to increase the PDE for the low signal, and thereby reduce hit detection inefficiency. Larger pixels allow the ratio between the dead area on the border of the pixels and the active pixel ratio to be reduced. This effect is especially important for new detectors which have so-called *trenches* between pixels to reduce the pixel to pixel cross-talk, as shown in Fig. 3.20. The number of pixels is 96 per channel with a pixel size of $57.5 \mu\text{m} \times 62.5 \mu\text{m}$ for the latest (2014) trenched detectors from Hamamatsu. Three versions with different pixel size and active area height were produced by KETEK in 2014, $82.5 \mu\text{m} \times 62.5 \mu\text{m}$ (1.32 mm high, 64 pixels), $60 \mu\text{m} \times 62.5 \mu\text{m}$ (1.32 mm high, 88 pixels) and $60 \mu\text{m} \times 62.5 \mu\text{m}$ (1.62 mm high, 104 pixels). The drawbacks of the increased pixel size are the increase of pixel to pixel cross-talk¹⁶ and saturation (one pixel can detect only

¹⁶The gain, and therefore the number of produced photons, is increased.

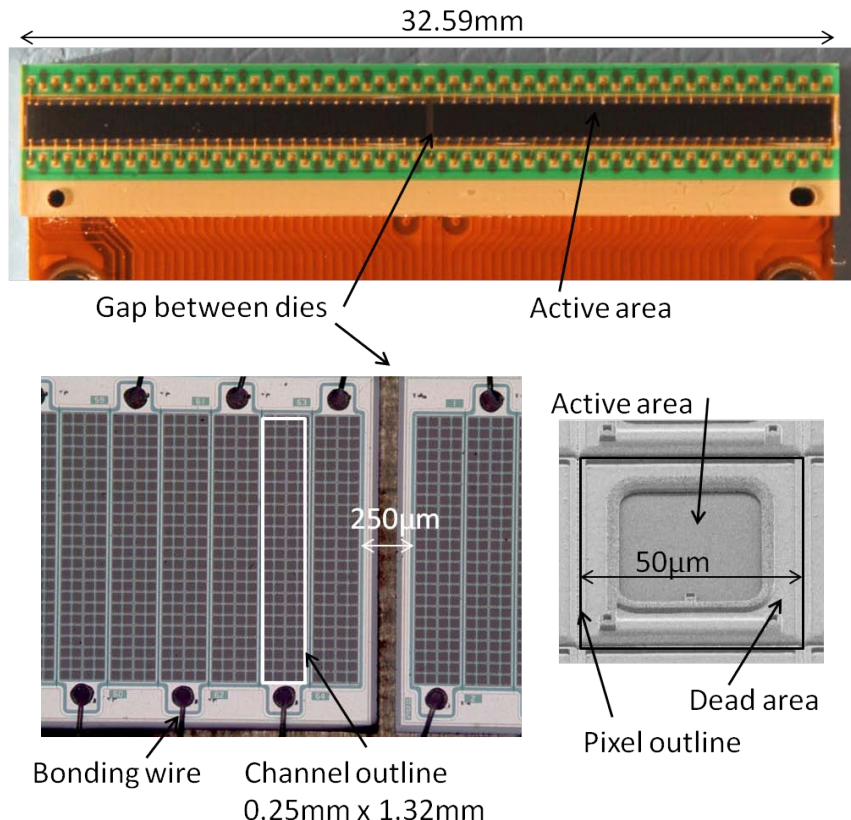


Figure 3.20: Top: Package with two 64 channel silicon dies. Electrical contacts are on the bottom side of the FR4 like base material. There are alignment holes on the package to ensure precise positioning. Bottom left: the gap between two silicon dies is shown under the microscope. Bottom right: a pixel with optical trenches is shown.

one photon). The detectors with the best performance should be chosen for the inner region of the detector. Since the detectors have very similar dimensions and electrical characteristics, a mixture of the detectors from both manufacturers could be used.

3.5.3 Photon Detection Efficiency, Cross-talk, Gain, Temperature Uniformity and Signal Timing

The PDE is the key parameter for the detector. It directly influences the overall light yield of the module (*cf.* Sec. 3.6.4) and has to be maximised. It is limited by two factors: the geometrical fill factor (FF) which is the ratio between the active area compared to the total area; and the avalanche probability which is the probability that an avalanche is produced once a photon arrives on the active area. The PDE also depends strongly on the wavelength with peak sensitivity in the blue wavelength region. A monochromator based set-up was used to characterise and compare the various devices as a function of the

applied over-voltage [66]. In the case of the Hamamatsu 2012 non-trenched technology, the FF is 61% and a peak PDE of 30% was achieved at 1.3 V over-voltage.¹⁷ A cross-talk of 17% was reached with the old technology at 1.3 V over-voltage. In 2013, Hamamatsu and KETEK developed new technologies with trenches between pixels which have been demonstrated to reduce pixel to pixel cross-talk. The over-voltage can be increased for the detectors with trenches to increase the avalanche probability and therefore the PDE. The Hamamatsu 2013 trenched samples with 50 μm square pixels have FF=60% and a peak PDE of 38% at an over-voltage of 3.5 V. The KETEK 2013 samples with trenches have FF=50% and a peak PDE=42% at 3.5 V over-voltage. They have a narrower sensitivity around the peak at 410 nm than the Hamamatsu detectors as shown in Fig. 3.21. In summary, the two technologies have very similar PDE; the higher peak sensitivity for the KETEK detector is compensated by higher PDE at longer wavelengths for the Hamamatsu detectors.

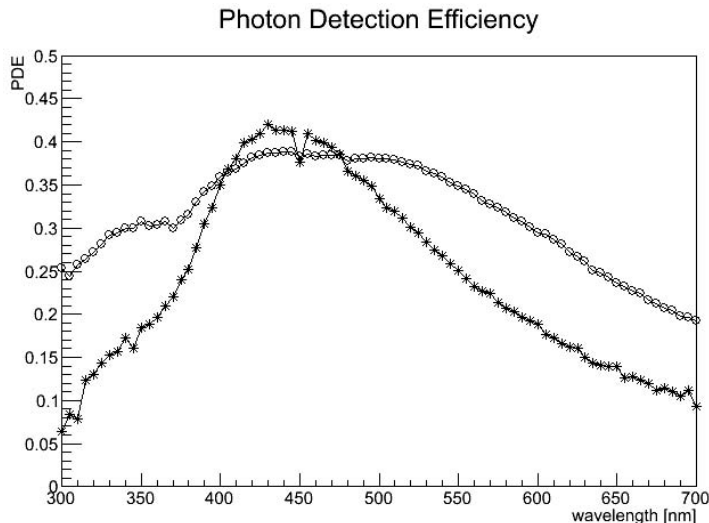


Figure 3.21: Comparison of the PDE for a KETEK (*) multi-channel array and a Hamamatsu (o) single channel 50 μm square pixels. Both detectors have trenches to suppress cross-talk and were operated at 3.5 V over-voltage. The important wavelength region is from 400 nm to 550 nm as it corresponds to the fibre emission spectrum for signals produced close to the mirror.

An important characteristic of the detector is the pixel to pixel cross-talk. The effect of cross-talk can be seen in the noise distribution shown in Fig. 3.22. The highest peak, representing the pedestal value, is about 50 times higher (more likely) than the value for one pixel of noise for the non-irradiated detector. This situation occurs when the integration and shaping time is 50 times faster than the mean interval in which a noise pulse occurs. Each fired pixel can produce pixel to pixel cross-talk which is observed simultaneously to the initially fired pixel. Two pixel noise is therefore reduced by the

¹⁷The PDE values are cross-talk corrected and therefore lower than typical values given in the data sheet by Hamamatsu.

cross-talk probability which is $\approx 10\%$. Note that without cross-talk the two pixel noise would be expected to be 50 times lower than the one pixel noise. The slope of the curve is defined by the cross-talk probability. Higher cross-talk results in more noise signals with high amplitudes. It is a feature of the SiPM principle that the signal from a pixel fired by noise has the same size and shape as the signal from a pixel fired by a photon. Reducing the temperature reduces the DCR, and therefore all random or cross-talk related high noise amplitudes.

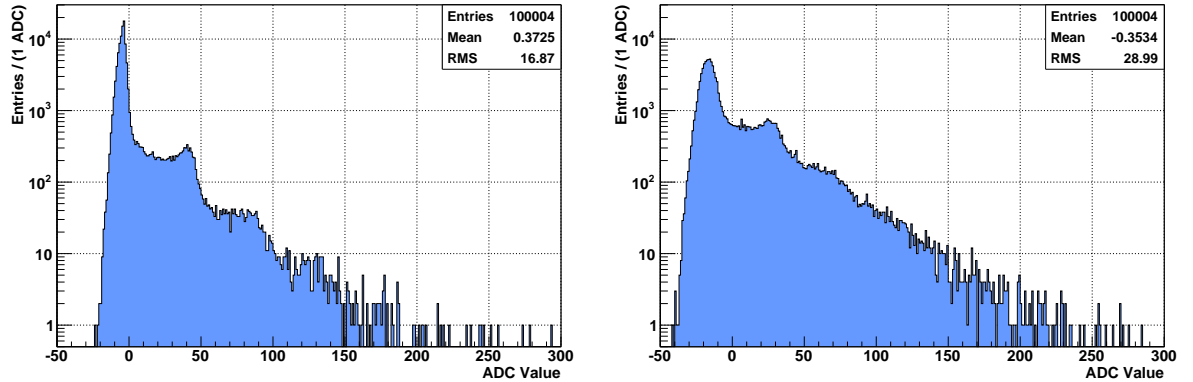


Figure 3.22: Left: Measured dark noise amplitude for a non-irradiated standard technology Hamamatsu detector at nominal operation voltage and 25°C. Note the exponential decrease of the probability of large amplitude events. The relative intensity of the second and third peak, corresponds to the sum of the cross-talk and after-pulse probability of the SiPM. The probability of two random noise pulses is very small in a non-irradiated detector. Right: Measured dark noise amplitude of the same detector at nominal operation voltage and -60°C after irradiation to $2 \times 10^{11} n_{eq}/cm^2$. The relative intensity of the second and third peak is almost unchanged which confirms that the cross-talk is not changed due to irradiation. However, a small change can be explained by the fact that, at this DCR, random pulses can overlap in time. The ratio between pedestal and one photon noise is reduced in this case to about 10.

To maximise the PDE, the detectors with trenches are typically operated with an over-voltage of 3.5 V which is around three times higher than that used in measurements of devices from earlier experiments [67]. This results in better channel to channel gain uniformity which was seen in the multi-channel arrays produced by KETEK in spring 2013. First measurements from the KETEK 2014 detector confirm a break-down voltage¹⁸ uniformity better than 50 mV which corresponds to a gain uniformity of 1.4%.

Good uniformity allows the detectors to be operated without channel-by-channel gain adjustment via an on-chip DAC circuit. The implementation of a 1 V dynamic range DAC per channel has been studied and found to have a large impact on the complexity of the

¹⁸The break-down voltage is the voltage where the amplification starts. It is typically 60 V and 30 V for the Hamamatsu and KETEK detectors with trenches, respectively. The over-voltage is the voltage above the break-down voltage and is typically 1 to 4 V. The gain is proportional to the over-voltage.

analogue FE-design. The break-down voltage has a temperature dependence of 56 mV/K for the Hamamatsu technology resulting in a gain variation of 1.6%/K if operated at 3.5 V over-voltage. A non-uniform temperature of 1 K over the multi-channel arrays attached to the same bias voltage is therefore acceptable. Four multi-channel arrays are connected together in a super-array to limit the number of bias voltage channels required. Therefore, a temperature uniformity of 1K over the super-array must to be provided by the cooling. Small gain variations can be compensated by individual channel cuts in the clustering. The main disadvantage of using variable gain in the detector operation is that the noise, PDE and cross-talk also depend on the gain.

The time response for the SiPM is an important characteristic to achieve fast signal shaping and integration, as well as a fast recovery of the pixels. The fast part of the signal pulse (rise and fast fall) has been minimised in order to allow for a complete collection of the signal, and will be described in detail in Sec. 3.7. The recovery time constant for the pixel (20 ns for Hamamatsu and 100 ns for KETEK) was chosen to suppress after-pulsing and ensure that no significant dead time occurs due to the signal and noise¹⁹ induced discharge rate of the pixel. The highest expected cluster occupancy is 2.5 clusters per event per 128 channels (see Sec. 3.7.1.4) and the light yield of 20 PE per cluster leads to an estimated average dead region (96 pixels per channel) of 0.4% for Hamamatsu and 1.6% for KETEK detectors. From the cluster signal and the occupancy, the DCR and the gain of the detector, the total bias current for one detector is below 1 mA for a bias voltage of about 60 V.

3.5.4 Radiation Hardness and Measurement of Dark Current

The SiPM photo-detectors are located in a region with a low level of ionising radiation. A moderate ionising dose of 40 to 80 Gy after 50 fb^{-1} is estimated to be present in the worst case region.²⁰ The dominating radiation effect on the SiPMs comes from a large neutron fluence present in this region which is up to $13 \times 10^{11} \text{ n}_{\text{eq}}/\text{cm}^2$ after an integrated luminosity of 50 fb^{-1} . A neutron shield can reduce the neutron fluence by a factor two as shown in the FLUKA [16] simulation described in Ref. [41]. The results presented below are for a maximum integrated luminosity of 50 fb^{-1} and assume the presence of shielding for the SiPMs.

The main effect on the SiPM is the increase of the dark current of the detector proportional to the neutron fluence received as shown in Fig. 3.23. The increase of the dark current can be understood as an increase of the dark count rate whose frequency depends on the following parameters: temperature, bias voltage, pixel to pixel cross-talk, after-pulsing and neutron fluence.

Operation of the detector at -40°C will be necessary to reduce the DCR to an acceptable level towards the end of the lifetime of the experiment. The required working temperature

¹⁹The pixel noise rate (4 MHz) is about five times lower than that due to signal in the highest occupied region.

²⁰This value refers only to the location of the SiPM detectors. The worst case region is located in the centre, 2.5 m above and below the beam-pipe.

of the detector depends on several parameters such as neutron fluence and neutron shield efficiency, detector cross-talk and light yield.

Fluences up to $6 \times 10^{11} \text{ n}_{\text{eq}}/\text{cm}^2$ were applied during the neutron irradiation, and irradiation studies were made in the LHCb cavern, the neutron irradiation facility at Ljubljana, and with a Pu-Be neutron source. The neutron fluence was measured with neutron sensitive pin diodes. The energy spectrum of the Pu-Be source and the FLUKA spectrum for LHCb are very similar, and both have a peak energy $\approx 2 \text{ MeV}$. The increase of the dark current was found to depend linearly on the total fluence as shown in Fig. 3.23 (left). No irradiation rate dependence and no measurable change in gain and cross-talk was observed.

The I-V curve was measured as a function of temperature, neutron fluence, detector type and annealing.²¹ The relation between temperature and dark current has an exponential character. Figure 3.23 (right) shows that the dark current is reduced by a factor of two when the temperature is lowered by 10°C .

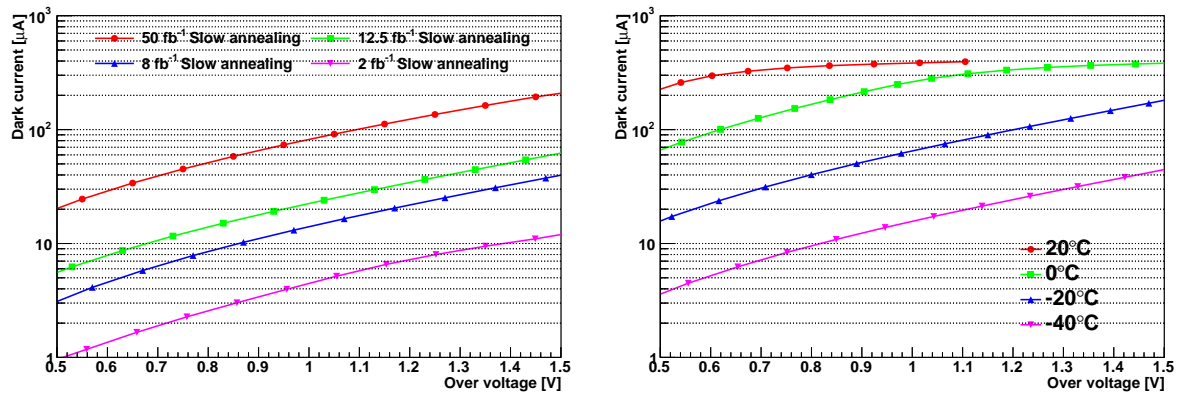


Figure 3.23: Left: Multi-channel arrays (Hamamatsu no trenches) irradiated with neutrons to an equivalent fluence of up to 50 fb^{-1} . The nominal operation point of this detector is 1.3 V at -40°C . Right: Same detector irradiated to equivalent of 8 fb^{-1} . The dark current changes by a factor of two every 10°C over a large temperature range. Current limitation in the test electronics is observed for high currents. All plots are given for fully annealed detectors after slow annealing one week at $+40^\circ\text{C}$.

The measurements with irradiated detectors show that the dark current can be reduced by a factor of 2.5 after annealing the detector at a temperature of 40°C for one week. Heating the detectors to 40°C for one week during long shutdown periods, once a year, is a possible way to take advantage of this recovery. The I-V curve before and after annealing is shown in Fig. 3.24 (left). Fast annealing of the detector was performed during 80 minutes at a temperature of 80°C . It should be noted that slow annealing exhibits a larger healing effect. The effect of annealing was the same for standard and new technology devices.

²¹Annealing is observed for many radiation damage. It can often be accelerated by increasing the temperature.

A comparison of the increase in DCR²² between the standard technology and the new trench technology with respect to the over-voltage is shown in Fig. 3.24 (right). The new detectors with trenches are typically operated with an over-voltage of 3.5 V. The DCR for the trench technology (Hamamatsu single channel 2013) is half the dark current of the standard (Hamamatsu single channel 2012) at 1.3 V over-voltage, which is the nominal operational over-voltage for the standard detector. However, the new detector operated at 3.5 V over-voltage has twice the DCR of the standard detector operated at 1.3 V.

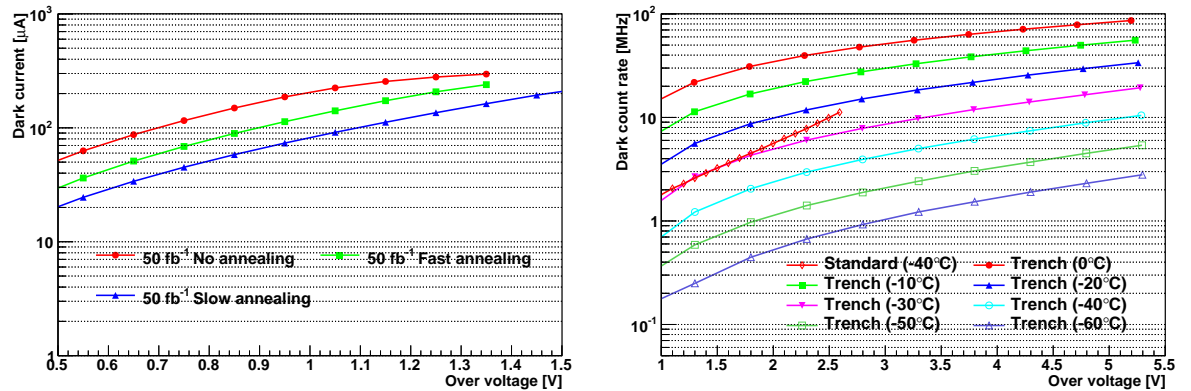


Figure 3.24: Left: Hamamatsu with trench, dark current as a function of over-voltage for different annealing scenarios. The dark current is decreased by a factor 2.5 after one week of annealing at 40°C. Right: Two types of detectors irradiated to an equivalent fluence of 25 fb^{-1} . Here the DCR can be compared for the standard Hamamatsu at 1.3 V at -40°C and the trenched detectors at different temperatures. The desired operation point for the trenched technology is 3.5 V in order to reach a high PDE. The DCR changes by a factor of two every 10°C over a large temperature range. The expected DCR at -40°C is 5 MHz at the desired operation point. The DCR for an irradiated detector is expected to double after an integrated luminosity of 50 fb^{-1} . All plots are given for fully annealed detectors after slow annealing during one week at 40°C.

3.5.5 Clusterisation

The full bunch crossing read-out scheme for the LHCb Upgrade requires data reduction by zero suppression in the FE electronics. This will be achieved in the SciFi Tracker by grouping the signals from several channels to form a cluster. The front-end ASIC is required to implement three comparators and three individual channel thresholds for this purpose. The thresholds are implemented via DAC circuits. Reducing the data with three comparators allows the information for each channel to be described by four possibilities. It can be encoded into two bits and this method is referred to as threshold read-out.

²²The DCR was calculated as the dark current divided by the gain and scaled to the 128 channel array surface.

The clustering is performed on 128 detector channels which is the total number of channels processed in one front-end chip. Clusters over the border of 128 channels are very unlikely due to the 400 μm dead region present between two 128 channel SiPM chips. However, it is important to allow clusters over the region between channels 64 and 65 where a dead region of 250 μm is present (*cf.* Sec. 3.5.2). Over 90% of the clusters contain two or more channels, and a large fraction of the clusters can be found over a dead region of 250 μm . The cluster size in the algorithm is limited to four channels. Restricting the maximum cluster size to a small number is important to minimise the logic resource usage in the downstream FPGA. Only around 2.6% of the clusters in the cluster size distribution shown in Fig 3.25 contain more than four channels. It is possible to merge clusters in the offline analysis.

3.5.6 Cluster Amplitude and Size Distribution

The signal created by a MIP is dispersed over several detector channels and must be assembled into a cluster. The centre-of-gravity of this cluster is the best estimate of the hit position. A typical distribution of the cluster size and the cluster signal in photons per cluster is shown in Fig. 3.25. The signal is a Landau distribution where the lowest signal has been cut to suppress noise. The cluster size depends on the distribution of the incident angle and the light yield. The distributions in Fig. 3.25 are from measurements made with a cosmic ray telescope where the incident angle of the muons was restricted to 30° from the vertical axis. The gain was reduced to obtain a light yield of 14.5 PE which is close to the expected signal in the beam-pipe region.

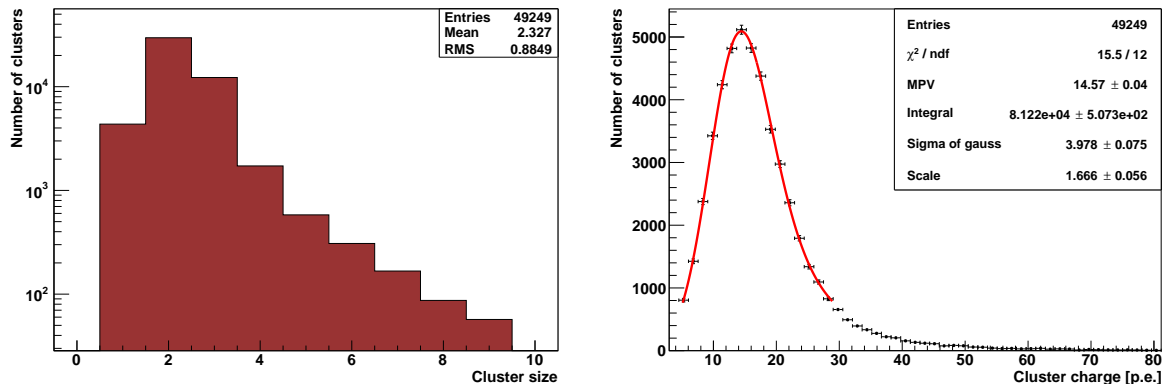


Figure 3.25: Cluster size distribution (left) and cluster signal distribution (right) for data collected with a cosmic ray telescope and a light yield of 14.5 photons per MIP. The result from the fit of a Landau convolved with a Gaussian to the data is shown in red, and the most probable value of the Landau is 14.5 PE. Single channel clusters contribute 9% of the total; two channel clusters, 60%; three channels, 25%; and four channels, 3%. Only 2.6% of the clusters contain more than four channels.

The dynamic range of the signal for digitisation can be restricted to 16 PE without

losing significant information as only a small fraction of channels saturate. An adjustable gain is implemented in the FE-amplifier that can be used to reduce the saturation effect for the outer detector region where there is less radiation.

3.5.7 Evaluation of Noise Cluster Rate

A large number of parameters influence the noise behaviour of the SiPM and need to be studied in order to control the noise cluster rate. A model of the detector has been built and combined with the clustering algorithm which was developed for the analysis of test beam data. The model includes the effects from temperature, over-voltage, irradiation, cross-talk, after-pulse, detector pulse shape and electronic shaping. The model has been used to predict the dark noise spectrum at different temperatures and different pulse shaping. An excellent agreement with the data was observed. The validation of the model is given in Ref. [68].

The clustering algorithm for the SciFi Tracker is identical to the clustering used for the current VELO and ST detectors [69] except that it does not include common mode suppression. After the pedestal subtraction, seed channels above a threshold (typically 2.5 or 3.5 PE) are selected. Neighbouring channels above a “neighbour threshold” (~ 1.5 PE) are subsequently included in the cluster. Only clusters with sum above 4.5 to 5.5 PE are accepted as signal. The most important parameter is the seed threshold. The two other thresholds are typically set 1 PE lower for the neighbour threshold and 2 PE higher for the sum threshold. The noise cluster rate depends on the threshold values chosen, and these values can be varied in order to understand the effect of noise. The simulation of the noise cluster rate for a 128 channel detector read out with an LHCb like integration and shaping time is shown in Fig. 3.26 for different cross-talk and temperature values.

The noise cluster rate was measured with a fast read-out system based on the Beetle [14] read-out chip and a signal attenuator. The measurements suffer from the non-linear response of the read-out and the low dynamic range which limits the signal measurement to only a few photons. The measurement demonstrates that the signal of the detector after 50 fb^{-1} (fully annealed) with a fast read-out has single photon peaks in the low light spectrum as shown in Fig. 3.27. The noise cluster rate was measured at different temperatures as a function of the threshold settings (Fig. 3.27).

3.5.8 Hit Detection Efficiency and Spatial Resolution

The hit detection efficiency depends strongly on the overall light yield and the acceptable noise cluster rate. The inefficiency is mostly due to low signal events that are below the third threshold of the clustering algorithm. The simulation shows that the module with six fibre layers has a slightly higher hit detection efficiency than the one with five layers at the same light yield (Fig. 3.28).

The simulated hit detection efficiency agrees very well with the hit efficiency for five layer modules measured using the cosmic ray telescope. It shows that it will still be possible to operate with a seed threshold of 2.0 PE, even at the end of the lifetime of

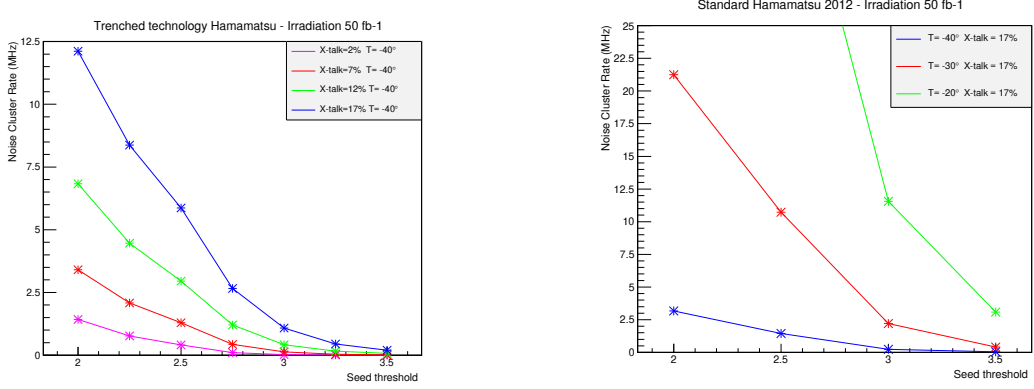


Figure 3.26: Left: Simulation of the cluster noise rate for different cross-talk probabilities. Note that the expected cross-talk for the new trenched devices is 7%. operation at 3.5 V over-voltage and -40°C was assumed. Right: Simulation of the noise cluster rate at different temperatures for the standard Hamamatsu detector with 1.3 V over-voltage and 17% cross-talk. These results can be compared with the measurements shown in Fig. 3.27 (right).

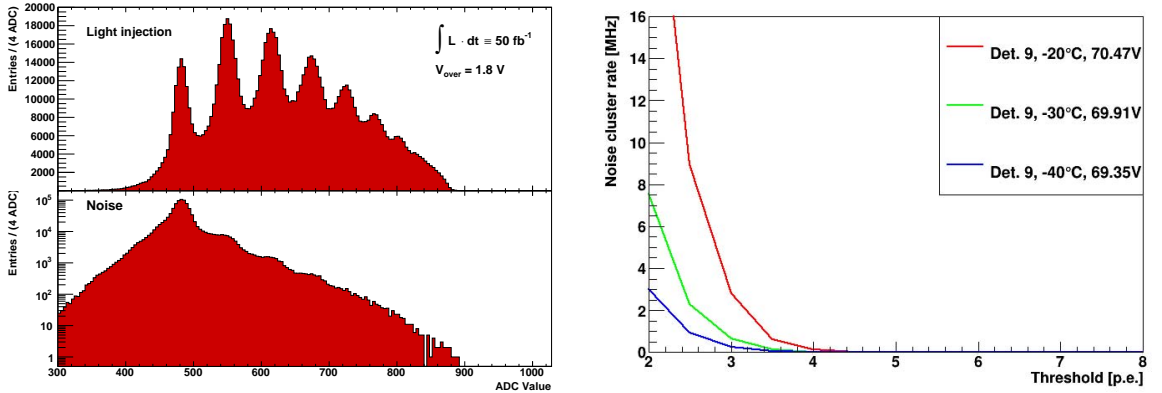


Figure 3.27: Left: Signal and noise spectrum for an irradiated sensor at 1.8 V over-voltage measured using the Beetle read-out system. The fast read-out system allows the low light intensity photon spectrum to be recorded after irradiation up to 50 fb^{-1} , and that the gain can be measured from this spectrum. Right: Noise cluster rate for a Hamamatsu (standard technology 2012) 128 channel array at nominal operation voltage (1.3 V) measured at different temperatures with a Beetle based read-out.

the detector, when the light yield is expected to be 12.4 PE (see Sec. 3.6.4, Table 3.9 for details). This allows the hit detection efficiency to be kept above 97.4% for a six layer module. Note that in the outer regions, and in the central regions during the first half of the lifetime of the experiment, the light yield is above 16 PE which allows for a hit

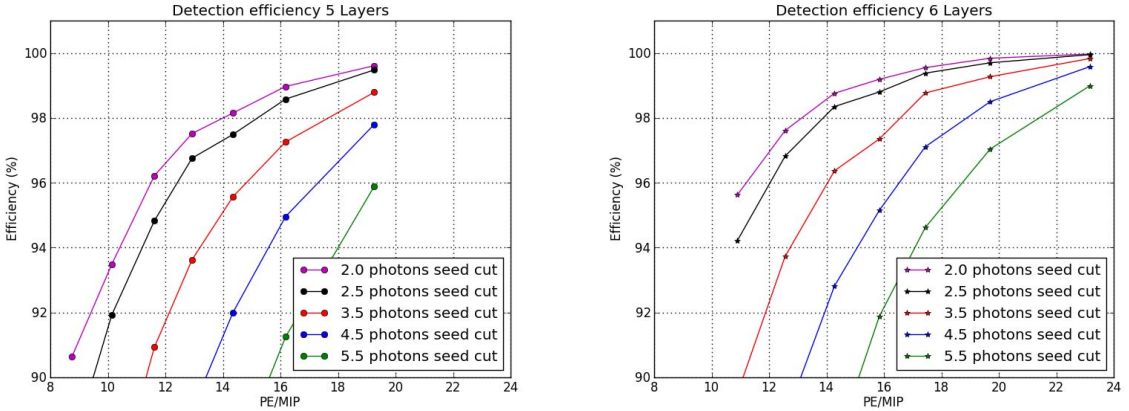


Figure 3.28: Left: Simulated hit detection efficiency for five fibre layers depending on the light yield and for different seed threshold (second threshold). Right: Efficiency for a six layer module. The two plots are simulated with 8 fb^{-1} equivalent of noise.

Table 3.6: The simulated spatial resolution for five and six layer modules and different light yield. The table shows also the result for three different versions of clustering algorithm, the full precision 12-bit ADC, a 6-bit ADC where saturation occurs at 14 PE, and a threshold only based version with saturation at 4.5 PE.

Module type	6 layer			5 layer		
Light yield	16.6 PE			13.7 PE		
Clustering	12-bit	6-bit	Threshold	12-bit	6-bit	Threshold
Resolution	50 μm	54 μm	60 μm	54 μm	56 μm	63 μm

detection efficiency above 99%.

The spatial resolution was simulated for fibre tracker modules with five and six fibre layers and measured in a test beam [38]. The test beam results show that the spatial resolution of the detector is better than 60 μm for a light yield of 15 PE, which is the value obtained with the simulation. The simulation allows the resolution for five and six fibre layers to be obtained for different light yields as shown in Table 3.6. The simulation of the spatial resolution assumes perfect alignment and straightness of the fibres.

3.5.9 Calibration of Gain

The gain calibration of the SiPM is an important monitoring tool during non-physics periods. Uniformity in break-down voltage is required for the four adjacent 128-channel detector arrays placed on one super-array to allow a common bias power supply. No gain adjustment is foreseen for the individual channels. The break-down voltage uniformity

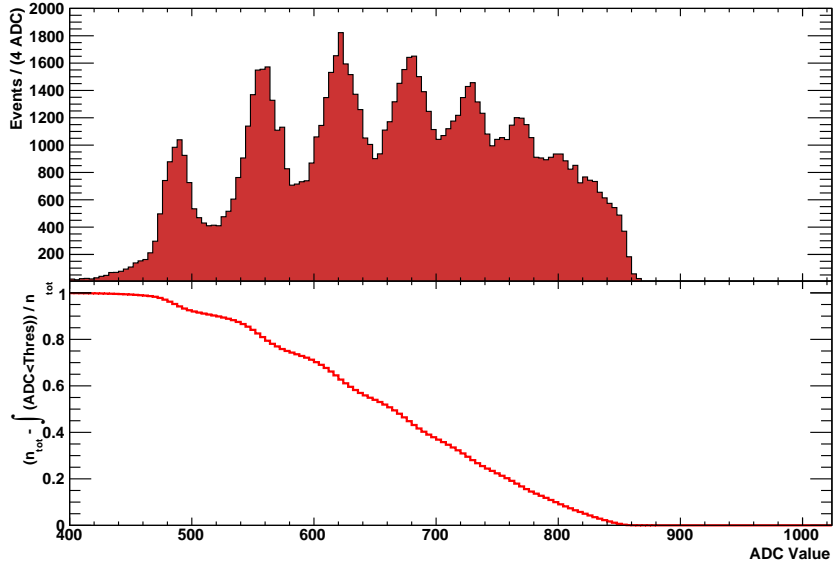


Figure 3.29: Top: light spectrum of an irradiated detector recorded with the Beetle [14] read-out system (fast shaping). Bottom: conversion of the light spectrum to a threshold scan. The photon peaks can be reconstructed by differentiating the threshold scan curve. The resolution is 1/16 PE in these plots.

needs to be better than 350 mV to achieve a gain uniformity of better than 10%, at an over-voltage of 3.5 V. Homogeneous gain is not a main requirement for the tracker. However, inhomogeneous gain can increase the noise cluster rate or reduce the PDE for channels operated at lower gain. The individual channel thresholds can be tuned offline to cut at the desired number of photons.

The gain can only be measured approximately from the dark noise spectra shown in Fig. 3.22. The “photon peak” positions are smeared due to the high level of random noise which is read out asynchronously. A precise measurement of the gain requires a light injection system (see Sec. 3.6.5.2) which allows the photon spectrum and the distance between two or more photon peaks to be measured. The light intensity should be of the order of a few photons (less than 5) per SiPM channel, without a strong requirement on channel-to-channel uniformity. If the uniformity is not sufficient then the light intensity has to be scanned, and the threshold scan repeated. This method was successfully tested and used in a test set-up for an ECAL development in the context of the PEBS [70] balloon experiment in 2012. Figure 3.29 (top) shows a signal spectrum measured with an irradiated SiPM sensor using fast read-out electronics synchronised to the pulsed light source. The photon peaks can clearly be seen and the gain per photon, defined as the distance between photon peaks, can be measured. This is the distribution that can be recorded if the ADC values of the signal are available. The result of an emulated threshold scan is shown in Fig. 3.29 (bottom) and a soft step function is observed. The threshold scan was emulated by plotting the integral of the light spectrum (normalised to one). The photon peaks can be measured again by taking the derivative of the threshold scan curve.

This means that the threshold scan, as well as an ADC spectrum, can be used to measure the gain between photon peaks. Note that the calibration of the irradiated detectors is more difficult due to the larger noise.

The calibration of a threshold circuit is expected to take longer than the calibration of an analogue system as every data point requires a new threshold to be set. The total number of sample points (threshold settings) is limited by the DAC defining the threshold. The total time needed for a full threshold scan is dominated by the time taken to change the thresholds for all channels as this requires a reconfiguration of the front-end chip registers. It is expected that a complete threshold scan will take around one hour.

3.5.10 Summary

The detector development with Hamamatsu and KETEK is leading to the fabrication of SiPMs that fulfil the requirements of high PDE, low cross-talk, and sufficient radiation hardness. The fast signal response and recovery time of the detector makes the SiPM particularly suitable for the fast LHC interaction rate. Short signal shaping and integration time enable the SiPMs to cope with high noise rates. A large increase in DCR is expected due to the radiation environment which can only be reduced to an acceptable level by cooling the SiPMs to -40°C . A temperature uniformity of around 1 K over four multi-channel arrays is required to limit the gain and, therefore, the PDE and noise non-uniformity.

3.6 Module

To achieve the goals set in Sec. 3.2.1, the following technology choices have been made and are described in detail in the paragraphs below:

- Sufficient signal amplitude and hit resolution in the X-coordinate is produced by a layered ribbon of 250 μm diameter scintillating fibre .
- Low occupancy is provided by the small width of the photo-detector channel and spacing of the scintillating fibre matrix.
- The LHCb detector acceptance will be covered by 12 planes divided into modular sub-detectors.
- A light and stable detector is provided by a carbon fibre sandwich-based module design.
- The photo-detectors will be cooled to reduce the noise and false clusters.

The description of the module in this section is based on the improving knowledge of prototypes, mechanical tolerances and available materials for this detector, and is likely to be improved in the future.

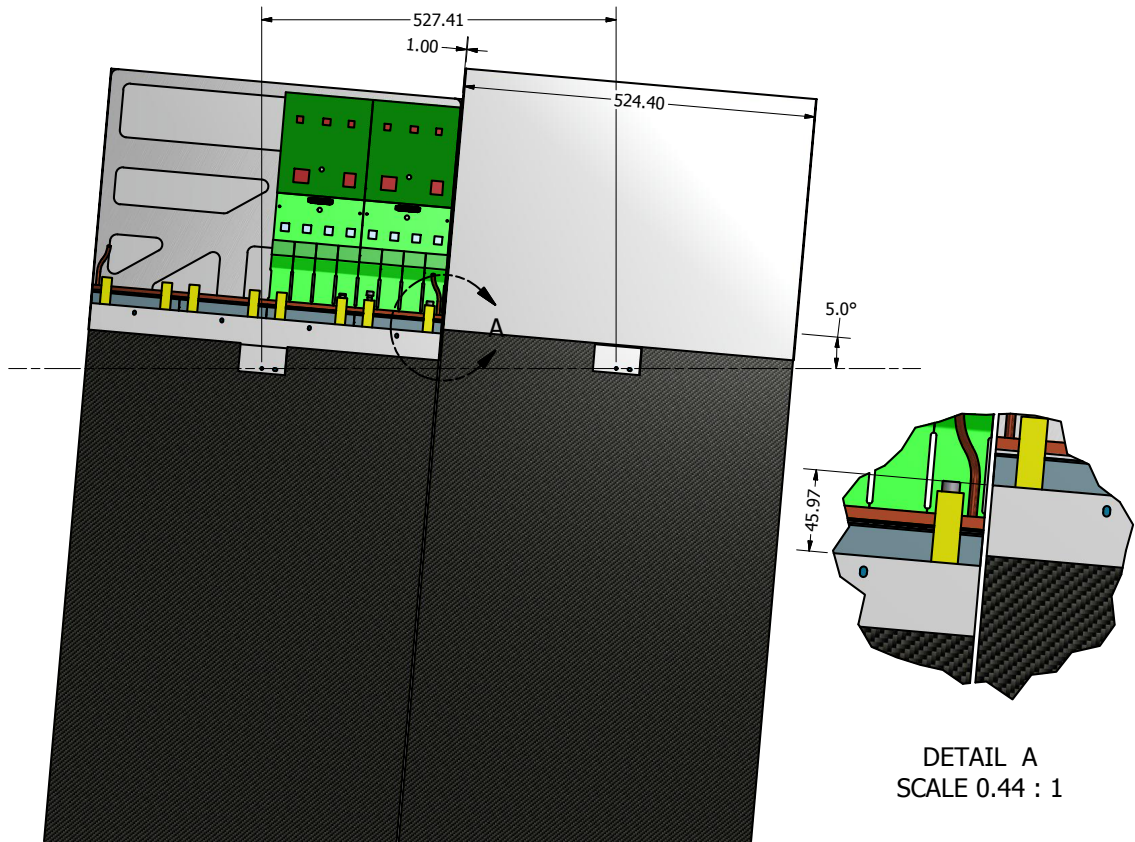


Figure 3.30: An illustrative view of two adjacent stereo modules. There is a 3 mm gap between modules. The space between ROBs is roughly 1 mm. The cold pipe will introduce a cold spot at the side of the module that will need to be insulated. The insulation filling the cold-volume and surrounding the cooling pipe are not shown.

The full span of each detector plane will cover 6 m by 5 m in the X-Y coordinate system respectively.²³ The plane is broken into modules that are 5 m in height, with a width of 0.52 m, resulting in 12 modules per plane. The placement of two adjacent stereo modules is shown in Fig. 3.30. The module width is dictated by integer values of the width of the SiPM array. At a single end of one 0.52 m module, 16 SiPM arrays will be placed. This number was chosen as a reasonable compromise between handling size, operability and maximising detector coverage. Each SiPM array will be grouped into 'super-arrays' of four, having an outer active detector width of 130.19 mm. It was deemed feasible to produce fibre mats which cover this width. Each module consists of eight 2.5 m long mats of 130.45 mm width; four on the top and four on the bottom. A mat of half this width, or even one quarter could be used and would introduce very little extra inefficiency in

²³It should be noted that the geometry and material described in this section differ slightly from the simulated geometry stated in Sec. 3.3.1 and Sec. 3.9.1. Simulation work is been based on earlier estimates of module widths and materials, and will be updated to more exact descriptions in due course.

detector coverage as the gap between SiPM arrays is a constant 400 µm. However, the alignment of twice the number of mats adds difficulty and degrades precision, as well as the additional waste from mat cutting and finishing would be more expensive. The fibre mat production is discussed below.

There will be two basic types of modules: beam-pipe and non-beam-pipe modules. The beam-pipe modules will require special modifications to accommodate the beam-pipe and have six sub-types ((X and U) × 3 station radii) to accommodate the beam-pipe.²⁴ The beam-pipe cut-outs will not be perfectly circular as the fibre ends must be cut and polished at nearly 90 degrees. An approximation of a circle using steps of SiPM array widths will be used such that the resulting damaged fibres from cutting will lie in the gap regions between SiPM arrays. As the radii are only different by 3 mm over one station, the largest radius will be used for the module cut-outs at that station for all four layers. This will reduce the number of different flavours of module required. Each station would require four identical X and four identical U beam-pipe modules. It is also foreseen to implement a sixth layer of fibres in the fibre mats for these modules, as they will degrade the most from radiation damage over time. Aside from this, they are identical in width, length and operation to the non-beam-pipe modules. Non-beam-pipe modules will have five fibre layers and comprise the majority of the modules. A schematic of the three basic module types is shown in Fig. 3.31. The opposite side of the beam-pipe is accommodated by a rotation of the module about the module's central z -axis by 180° for both X and U beam-pipe modules. The location of the mirror, alignment pins and other components are indicated in the drawing.

Table 3.7: Module types. Stereo modules are indicated by U. The cut-out radius includes the 10 mm beam-pipe clearance.

Type	Quantity	Cut-out radius (mm)
Non-Beam-pipe X&U	120	—
Beam-pipe X TS1	4	81
Beam-pipe U TS1	4	81
Beam-pipe X TS2	4	88
Beam-pipe U TS2	4	88
Beam-pipe X TS3	4	95
Beam-pipe U TS3	4	95

3.6.1 Panels

The panel material has been chosen to provide the maximum strength while having the lowest material budget. A sandwich of two 0.2 mm carbon-fibre reinforced polymer (CFRP,

²⁴The 5° rotation of the stereo modules about their centre requires the cut-out to accommodate the beam-pipe being shifted vertically by $(0.52 m/2 \cdot \sin(5^\circ))$, compared to the X-modules, to avoid collisions with the beam-pipe.

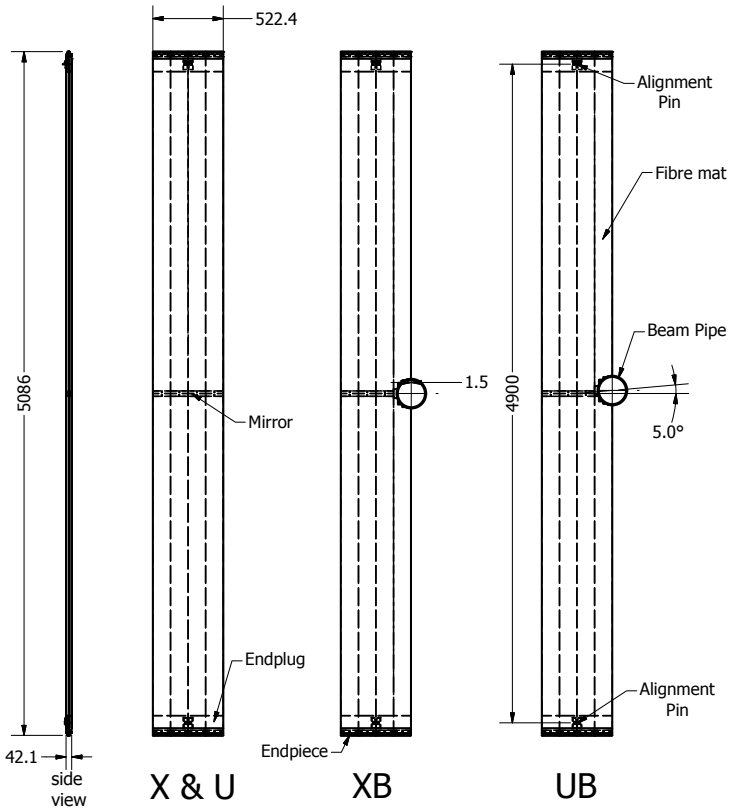


Figure 3.31: A schematic of the three basic module types, non-beam-pipe X & U modules, and the beam-pipe modules for the X (XB) and stereo (UB) layers. The XB and UB modules must accommodate the beam-pipe radius at the three different stations.

70%/30%) layers separated by two 20 mm layers of light core material (Nomex® honeycomb, Airex® R82 foam or Divinycell®F40 foam)^{25,26,27} on either side of the scintillating fibre mats will produce a light and robust tracking module. Given the large amount of material, the core product types are chosen for their low density, good strength, low water absorption, and their excellent fire, smoke and toxicity (FST) properties. Differences are based on cost, bonding, open/closed cells and finishing. A cross-section drawing of a 5 m panel is shown in Fig. 3.32. The first 1 m prototype panels are currently under construction along with the required tooling.

The prototype module material budget²⁸ is shown in Table 3.8. The lowest total

²⁵Nomex is a registered trademark of E.I. du Pont de Nemours and Company (DuPont®).

²⁶Airex is a trademark of 3A Composites International AG.

²⁷Divinycell is a trademark of DIAB International AB.

²⁸The radiation length for the Nomex® core is calculated as in Ref. [71]. The foam core radiation lengths are found similarly by molecular weighting. Divinycell is assumed to be the same material or similar as Airex (Polyetherimid, $C_{37}H_{24}O_6N_2$), but of lower density.

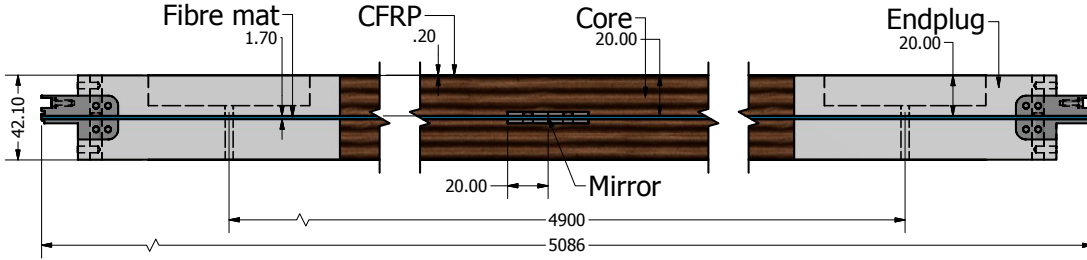


Figure 3.32: A drawing of the cross-section of a SciFi Tracker module.

radiation length for this design is $X/X_0 = 0.99\%$ for one layer or 4% for one tracking station of four layers. The majority of the material budget is a result of the six layers of fibres and the casting glue²⁹ as described in Fig. 3.34. The glue used during winding contains TiO_2 while the casting glue does not. Total radiation lengths should be compared to the Inner and Outer Tracker material budgets. The OT has a material budget of 0.744% per layer plus 0.191% for sidewalls, which is 3.17% per station [72]. The IT contributes between 2 and 7% per station. Averaged over the T-stations,³⁰ a particle sees around 17.5% of a radiation length coming from the IT and OT material [73]. The IT and OT would be replaced completely by the nearly uniform SciFi Tracker which would contribute approximately 11% of a radiation length to the LHCb detector.

Table 3.8: The material budget for a single module. Core material budgets for 24 kg/m^3 Nomex (N), 60 kg/m^3 Airex (A), and 40 kg/m^3 Divinycell (D) are listed. The fibre mat is the current cast 6 layer prototype thickness as described in Fig. 3.34. The fibre mat glue contains TiO_2 while the casting glue does not.

Material	Thickness(μm)	Layers	$X_0(\text{cm})$	$X/X_0 (\%)$
Core(N/A/D)	20000	2	1750/689/1050	0.229/0.580/0.381
CF skin	200	2	23.3	0.172
Panel glue	75	4	36.1	0.083
Fibre mat	1350	1	33.2	0.407
Casting glue	175	2	36.1	0.097
Total	4220			0.99/1.34/1.14

The modules will be assembled on a vacuum table template such that all eight fibre mats can be aligned with respect to a single plane and reference axis. The fibre mats have aligned polycarbonate “end-pieces” bonded to them during the casting process to provide

²⁹The glue added to the fibre mat currently contributes approximately $2 \times 0.175 \text{ mm}$ to the total thickness and will be minimised.

³⁰Averaged over ϕ and for $2.0 < \eta < 4.8$ for minimum bias events.

mounting for the SiPM arrays and additional Rohacell-based end-pieces near the middle of the module to mount a mirror to. Larger polycarbonate blocks, called “end-plugs”, are added to the ends of the module panels to provide mounting support and contain the final alignment holes of the module with respect to the frame. The materials are bonded to the fibre mats at room temperature to ensure no thermal stresses are introduced. Measurements of a 2 m dummy module have indicated they are more resistant to bending than the current OT modules.³¹ The dummy module has a Young’s modulus of 1.73 GPa compared to the OT which is 1.24 GPa. The finished modules will have only a thin optical barrier as a sidewall, unlike the OT which required a thicker carbon-fibre sidewall for support.

3.6.2 Fibre Mats

Winding: The scintillating fibre mats form the active component of the SciFi Tracker and must be assembled with precision and be of high quality. The single 250 μm fibres are arranged in multi-layer mats in order to produce a sufficient light yield at the photodetector. The fibres are packed together as a long regular matrix by winding them on a 1 m diameter wheel where each successive layer is shifted by half the horizontal pitch with respect to the lower. A prototype machine has been developed to produce these mats, controlling the speed, tension and winding of the fibre onto the winding wheel (see Fig. 3.33). A spool of 12.5 km of fibre is fed as a single continuous fibre into the machine. A small weighted wheel defines the tension of the fibre and regulates the speed of the feeding spool. The winding wheel provides precision alignment and guidance to the fibre by means of a milled screw thread on its surface. The thread has a channel depth nearly half the fibre diameter and a 270 μm horizontal pitch to guide the fibre of the first layer. Once one layer is complete, the fibre is cut and placed again at the beginning of the screw. The fibre of the first layer becomes the guide for the fibre that produces the second layer and so forth. Mats are wound to a width of approximately 135 mm.

A schematic of a complete fibre matrix is shown in Fig. 3.34. A thin layer of stable, optically transparent epoxy with white, optically diffusive titanium dioxide is added on top of each fibre layer on the wheel to bond adjacent fibres and the subsequent layer together. The epoxy has a pot-life of eight hours which provides sufficient working time. After the epoxy has hardened enough, the fibre mat forms a cylindrical shell which is cut perpendicularly to the fibres and taken off the wheel to be flattened. The principle of producing fibre ribbons this way was proven to work with shorter modules (80 cm) in the serial production for the PERDaix detector (\approx 80 fibre mats) [67]. An image from an optical coordinate measurement machine (CMM)³² of a cross-section from a 3 m long fibre mat, used for the measurements described in Sec. 3.6.4, is shown in Fig. 3.35. The pattern recognition software can measure the diameter of both the core and cladding of the scintillating fibre, as well as the relative position of each fibre. The fibre mat shown

³¹Fibre mats have been replaced by a single 1 mm polystyrene sheet in the 2 m dummy module. Nomex honeycomb core has been used.

³²OGP SmartScope, available in the CERN Departmental Silicon Facility.

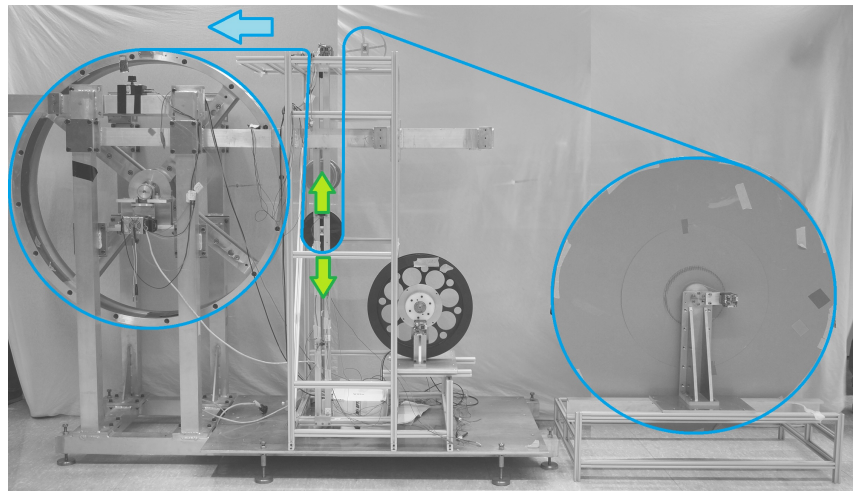


Figure 3.33: A prototype fibre winding machine used to produce 3 m long fibre mats.

has an average horizontal pitch of 0.27 mm and a vertical pitch of 0.21 mm. The inter-fibre variation is approximately 8 – 16 μm , increasing from first to fifth layer respectively. Fibre mats of over 2.5 m in length with five layers have successfully been produced by two separate institutions within the collaboration using similar techniques extensible to serial production.

As an alternative to the thread on the wheel, a second approach is being developed. It is based on a thin ($\approx 100 \mu\text{m}$) Kapton substrate foil on which a photo-imageable coverlay (Dupont) is laminated. Exposure through a mask, photographic processing and thermal hardening lead to a foil with a fine line pattern (64 μm high) which acts as guides for the fibre winding. Stretched over a wheel, the foil replaces the thread. After the winding process, the substrate remains attached to the fibre mat which has the advantage that it can provide precise ($< 10 \mu\text{m}$) alignment marks. Furthermore the winding is always performed on a fresh substrate of constant quality, making thread cleaning and the use of an anti-stick agent obsolete. Industrial producers for substrate sizes up to 3.5 m have been identified. Both methods to guide the fibres have been successfully tested.

Casting: In both approaches, the mat is still fragile after it is taken off the wheel. The fibre mat has a tendency to split between adjacent fibres as the glue layer is quite thin and can separate from the smooth surface of the fibre. Fibres near the edges are particularly prone to becoming separated from the ribbon. For this reason, the ribbon is cast in a bath of glue to ensure a thin protection film around the mat, which also creates a precise flat surface. Protected like this, the fibre mats can be cut along the fibre axis to achieve the correct width and rectangular cross-section with less risk of fibre separation. The mat becomes robust and handleable without fear of damage from moderate movements. Special tooling and procedures are required to repeatedly produce a mat with a surface more precise than 100 μm without defects and holes due to surface tension. Work is being done to reduce the excess thickness the glue adds to the fibre mat from the current value

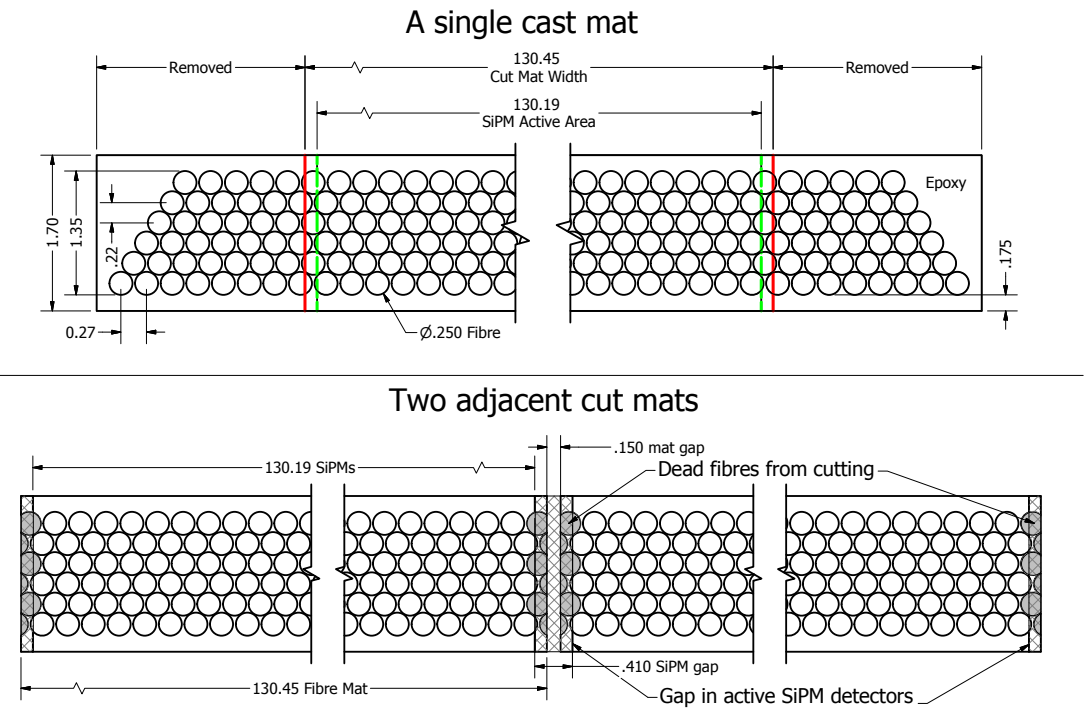


Figure 3.34: A schematic of the cross-section of a single cast fibre mat (top) and two adjacent cut fibre mats (bottom). The shaded region indicates where no active SiPM read out occurs. Any fibres cut at the edge of the mat will lose the majority of their light during transmission and are effectively dead.

of 0.35 mm to 0.2 mm.

Alignment: While the inter-fibre alignment is assured by the winding process, the overall alignment of the fibre mats within the detector requires additional care. It has been seen that fibre mats of over 2.5 m will deviate by more than 100 μm from a central axis in its plane under minimal load, despite being fixed at either end. A wire was placed between adjoining fibres and measured with respect to a taut reference wire. Optically aligning and affixing 1152 fibre mats with precision is not feasible.

A more robust and repeatable alignment procedure has been developed and is currently being implemented for further prototype fibre mats. Precision holes of approximately 2 mm in depth and 3 mm in diameter are drilled into the winding wheel, following the threaded screw pattern. Within the hole, a plastic or metal pin is placed and a small amount of glue is applied to the exposed surface. Alternatively, the pins are made by filling the hole with epoxy. The method ensures that mechanical alignment pins are bonded to the underside of the fibre mat and are guaranteed to follow the axis of the fibre mat. The pins can then be placed in alignment holes in subsequent machining and detector assembly tooling with minimal human intervention. A schematic drawing of a fibre mat with pin

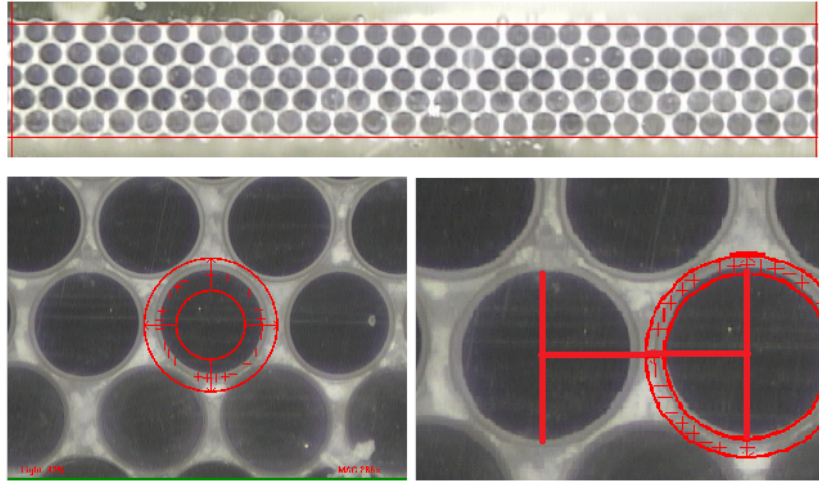
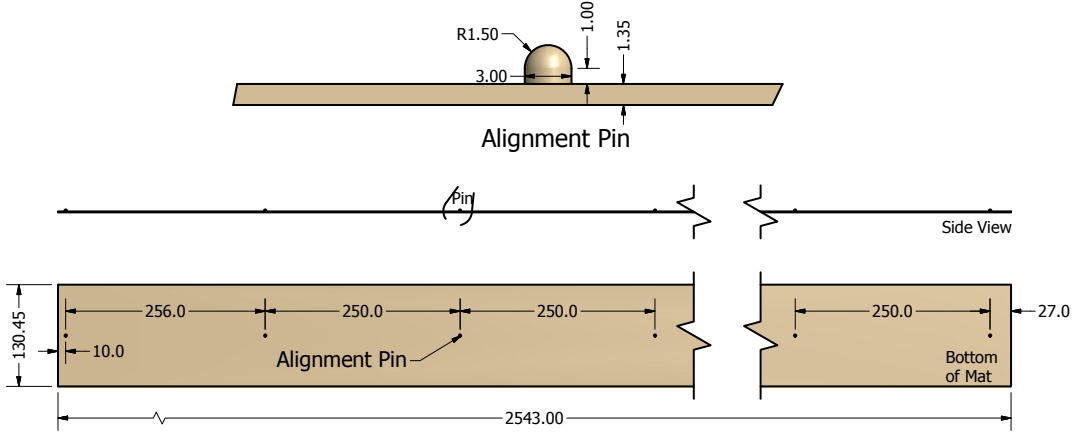


Figure 3.35: An image taken by an OGP 3D Optical Coordinate Measurement Machine of the fibre mat measured in Sec. 3.6.4. Pattern recognition software can measure the diameters and position of each fibre.

and images of the alignment pins foreseen for mass production are shown in Fig. 3.36.

A measurement of the straightness of a prototype 7 cm mat with pins attached to the mat after winding is shown in Fig. 3.37. As a large diameter wheel with pin holes has not been produced yet, the pins have been positioned with respect to a reference wire that has been embedded in the mat. The extruding pins are then aligned against a straight edge and the position of the embedded wire is compared to a straight reference wire. The RMS of the deviations from the reference wire after being aligned is $25 \mu\text{m}$, and is compatible with the measurement accuracy and four times better than the upper limit for the position resolution ($< 100 \mu\text{m}$) of the SciFi Tracker. A 1 m mat has been wound with pins as shown in Fig. 3.36, but only on a small wheel as proof of concept and has no measurements as of the writing of this document. A similar hole and pin concept could also work for the overlay winding substrate.

Cutting: The fibre mats must be cut in two ways once they are cast and hardened. The edges of the mats are cut parallel to the aligned central axis on a vacuum table to produce a straight and precise detector element. Cutting will inevitably produce dead fibres on the long sides, as indicated in Fig. 3.34. The precision of the edges is expected to be better than $100 \mu\text{m}$, such that the fibre mats can be packed as close as possible in the module. The packing of the detector is also limited by the photo-detector geometry. The fibre mats must also be cut at the ends of their length to optical quality. A single-point diamond milling of the ends of the fibre mats provides a good quality finish and no grit-type polishing is performed.



(a) Schematic drawing.



(b) Sample pins made from epoxy.

Figure 3.36: The fibre mats will be aligned on a template by means of alignment pins bonded to the fibre mats.

3.6.3 Fibre-end Mirrors

The relatively low light yields for tracks close to the mid-plane ($y=0$) of the SciFi Tracker, in particular after radiation damage, suggests to mirror the fibre ends. A series of tests and measurements were performed in order to establish a viable mirror technology which fulfils the following requirements [74]:

- High reflectivity over the full emission spectrum of the fibre (400–600 nm). In first approximation, the mirror reflectivity R determines the light yield gain for tracks which pass close to the mirror end $Y = Y_0 \cdot (1 + R)$. A more detailed consideration accounts for the absorption losses and Fresnel reflections at the various interfaces (discussed in the appendix of Ref. [74]).
- Compatibility with the expected radiation dose (up to 35 kGy).
- Minimal use of space in both the y and z direction. The discontinuity of the fibres at

$y = 0$ leads to a small inactive region. In the interest of maximum tracking efficiency, the extension of this zone should be kept as small as possible. A value below 1 mm is considered as acceptable.

- Ease of implementation and low cost. The mirroring is foreseen to be applied before the fibre ribbons are mounted on the support module, either on individual 13 cm wide ribbons, or jointly on a set of four ribbons (52 cm width). This step should not introduce long delays in the overall production sequence and its cost should be small.

The following technologies were evaluated: Aluminised Mylar film glued to the fibre ends, 3M Enhanced Specular Reflectance (ESR) film glued to the fibre ends, Thin Film Aluminium vacuum coated on the fibre ends.

The tests showed that Aluminised Mylar film is a viable solution fulfilling all SciFi Tracker requirements. The tests were performed with samples prepared in the CERN PH-DT thin film lab. They consisted of a 50 μm thick Mylar foil on which a 90 nm thick Aluminium layer was vacuum coated (PVD) and protected by a 32 nm thick MgF_2 film. The film reaches a reflectivity of $R \geq 0.8$, when glued to a machined fibre end, corresponding to a relative light yield gain factor for tracks close to the mirror of about 1.75. The glue interface layer between the fibres and the mirror film mitigates the requirements on the surface quality of the fibre end machining. The technology has been proved to be radiation hard up to 60 kGy. The Mylar foil can be less than 100 μm thick and its rear side is mechanically robust. It can easily be integrated in the production sequence of the fibre modules, and could reduce the space between upper and lower fibre mats.

The ESR film leads potentially to around 5 – 10% higher reflectivity but this gain could not (yet) be demonstrated when glued to machined fibre ends. The Thin Film Aluminium

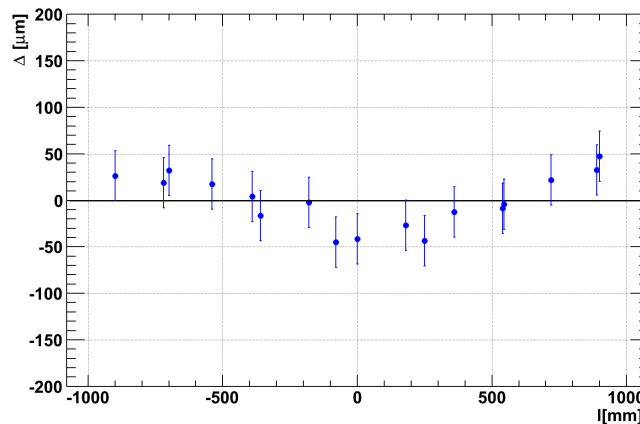


Figure 3.37: Measurement of a fibre mat aligned with pins that have been applied by hand. The RMS is 25 μm .

coating was disqualified for reasons of cost and complexity without any performance gain compared to Aluminised Mylar films.

3.6.4 Fibre Mat Performance

A 3 m long and 3 cm wide fibre mat with five layers underwent metrological tests and was also characterised with an electron beam from a Sr-90 source, available at CERN. The mat was left uncasted and equipped with two end-pieces made of black POM (Polyoxymethylene) which allowed the fibre ends to be machined with a single-point diamond tool to optical quality. The final length of the mat including end-pieces was 2.5 m after machining.

Samples of 2 cm length and 3 cm width were produced from the excess length of the fibre mat. These samples were fully immersed in epoxy glue and the fibre ends machined to optical quality. The samples were inspected with an optical 3D coordinate measurement machine. The pattern recognition of the CMM recognises the boundaries of the fibres and calculates parameters like diameter, eccentricity and positions, which allows the fibre pitch to be deduced (see Fig. 3.38). The average pitch, given by the thread, was found to consistently be 270 μm for all five layers and it was constant over the width of the mat. The RMS of the pitch increases from the first layer, which is in direct contact with the thread, $RMS_1 = 8.8 \mu\text{m}$, to the fifth layer, $RMS_5 = 16 \mu\text{m}$. These values are small compared to the expected position resolution of the final detector ($< 100 \mu\text{m}$) and are therefore considered acceptable.

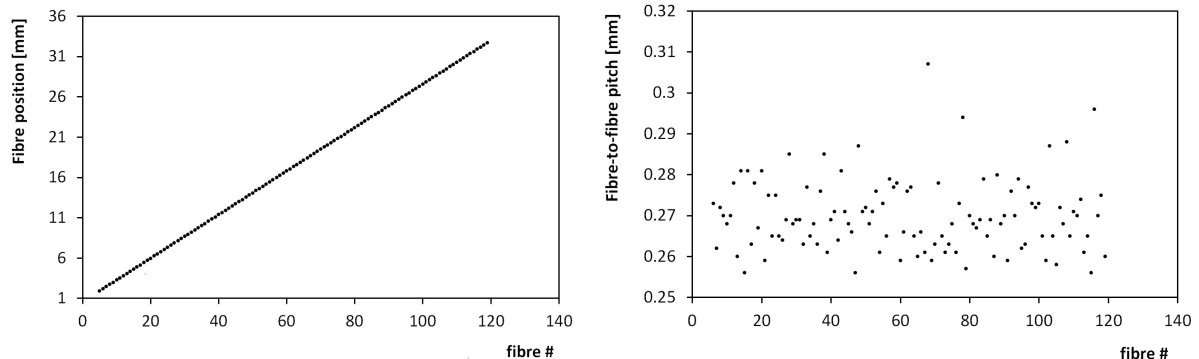


Figure 3.38: Result of the automatic position measurement with the optical CMM for the 3 cm wide mat. Left: Fibre x- positions. Right: Fibre-to-fibre pitch with an average of 270 μm and an RMS of 8.8 μm .

The 2.5 m long fibre mat was mounted in a so-called “electron-gun” set-up available at CERN. It consists of a 370 MBq Sr-90 source with magnetic energy filter, which provides a collimated beam of electrons up to the end point energy of 2.2 MeV with a resolution of $dE/dx \approx 0.1 \text{ MeV}$. A crossed arrangement of two scintillating fibres (1 mm, square cross-section), read out by two SiPM detectors defines a 1 mm^2 beam spot and coincidence trigger. The fibre mat was mounted in between the exit slit of the electron-gun and the

trigger counters. The electron energy was chosen to be 1.7 MeV. The most probable energy loss dE/dx of 1.7 MeV electrons in plastic scintillator is 1.52 MeV/cm.³³ The fibre mat was read out at one end by a 128 channel Hamamatsu SiPM array identical to the model used in 2012 test beam experiments. The SiPM array was visually aligned to the fibre ends. However, the required precision of better than 0.1 mm was found to be difficult to achieve. Full overlap of fibre ends and active SiPM area could therefore not be guaranteed. The SiPM was read out by a 128 channel VATA128 ASIC via a custom designed USB board. At the opposite end of the mat, a mirror could be attached. The mirror consisted of an aluminised glass plate with MgF_2 protection layer. Alternatively, an aluminised Mylar foil was also used. As the fibre mat could be longitudinally displaced relative to the electron beam, the optical attenuation length of the fibres could also be assessed. A transverse scan by means of a linear motion table also allowed the uniformity of the fibre mat to be measured. The results are summarised in Fig. 3.39.

The photoelectron yield of the mat is similar to the results obtained from 2012 test beam measurements on a 2.5 m hand-wound fibre mat. The longitudinal scan indicates an effective attenuation length of ~ 5.8 m, though the fit is not ideal. The transverse scan shows excellent uniformity across the mat. Application of a mirror (without optical glue or grease) was found to increase the photoelectron yield by a factor of 1.7 – 1.8 when the fibre was excited 10 cm from the mirror. This is in agreement with the results of dedicated mirroring studies described in Sec. 3.6.3. The yield was not improved by attaching the mirror by means of optical glue. Similarly, at the detector side, the SiPM window (epoxy) was in mechanical contact (*e.g.* air gap) with the fibre ends. Adding a thin layer of optical grease had no noticeable impact on the photoelectric yield.

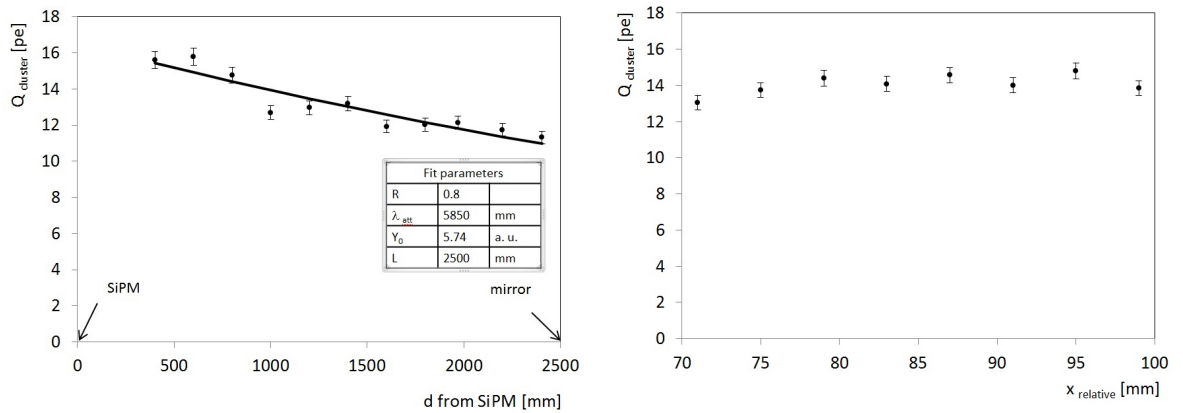


Figure 3.39: Photoelectron yield measurements of the 2.5 m long fibre mat. Left: Longitudinal scan. Right: transverse scan.

³³Most Probable Value (MPV) of Landau fit to GEANT4 generated dE/dx distribution. The maximum range of 1.7 MeV electrons is 1.1 g/cm² or about 1 cm in plastic.

Table 3.9: Expected light yield in photons (PE) at different locations in the detector before and after irradiation. The base for this table is a light yield of non-irradiated fibres with six layers at the mirror of 20.7 PE. The attenuation of the light from the mirror to the detector is 32%. A 40% signal loss is assumed near the mirror in the irradiated region and the radiation has a smaller 10–20% effect in the outer region.

6-layer region inside $\pm 0.5\text{m}$				5-layer region outside $\pm 0.5\text{m}$			
Non-irradiated		Irradiated (up to 35 kGy)		Non-irradiated		Irradiated (up to 35 kGy)	
Mirror	Detector	Mirror	Detector	Mirror	Detector	Mirror	Detector
20.7	27.3	12.4	16.4	17.3	22.8	14 – 16	22.8

3.6.4.1 Light Yield in the SciFi Tracker

Estimates of the light yield for the SciFi Tracker here are based on the above measurements of the light yield and previous estimates of the radiation damage. The detected light yield can be split into four regions: two regions near the mirror in the horizontal beam-pipe plane, and two near the photo-detector. Each of the two cases are split into a highly irradiated region with six layer fibre mats and a less irradiated region with only five layer fibre mats. The light yield for the four regions before irradiation and at the end of the lifetime of the experiment are given Table 3.9. The scintillation light arriving at the SiPM is exponentially attenuated on its path through the fibre. Furthermore, in the region around the beam-pipe the transparency of the fibre degrades due to the ionising dose present in this area leading to an additional signal loss of up to 40% [61, 68] (from approximately twice the expected dose). The low light yield in the worst region can be partially compensated by using six fibre layers per detection plane in the region $\pm 0.5\text{ m}$ from the beam-pipe whereas five fibre layers are used in the rest of the detector.

The calculation of the expected signal is based on the results of the measurement of a non-irradiated 2.5 m long fibre mat with a Hamamatsu multi-channel array from the generation currently available (lower PDE and higher cross-talk compared to the new generation). Its light yield close to the mirror was measured to be 11.2 PE for five fibre layers using signals produced by an electron gun. The typical light yield for a heavy high energy particle is 10% higher (12.3 PE). The next generation of detectors, optimised for high PDE and larger pixel size, will produce 40% more signal leading to a signal of 20.7 PE for six layers of fibres before irradiation near the mirror. At the end of the lifetime of the experiment, the light yield will be reduced by up to 40% (a safe estimate, similar to the worst dose damage model) due to the radiation damage of the fibres, and this gives the worst case light yield of 12.4 PE. A smaller reduction in light yield of about 10 – 20% is expected in the outer regions due to radiation, depending on the dose damage model used.

The expected light yield after 50 fb^{-1} will be sufficient for the lifetime of the experiment, given the current understanding of the radiation dose, fibre damage behaviour and expected increases in performance of the photo-detectors. However, the FLUKA simulations predict a radiation environment composed of neutrons and ionising dose which primarily affects

the performance of the central detector region. In this region, the low light yield and high detector noise rate may at a certain point no longer allow for an efficient detector operation. Given the uncertainty of the models, the replacement of the innermost two modules per layer, *i.e.* 24 modules in total, is being considered as a possible measure to guarantee the optimum detector performance over the full lifetime of the experiment.

3.6.5 Read-out Box (ROB)

At the ends of the module, the scintillating fibre ribbons are connected to the SiPM arrays, which in turn are connected to the front-end electronics through flex-PCB cables, as shown in Fig. 3.40. Cooling pipes for a liquid cooling system (see Sec. 3.8.2.1) must also be fed through this enclosure to keep the silicon photo-detectors at -40°C (see Sec. 3.5).

This relatively small volume, with a high density of interfaces at the end of the module, is referred to as the “Read-out Box” (ROB), and is shown schematically in Fig. 3.41. The Read-out Box design is technically challenging not only because of the limited space and the large density of cooling, electronic and mechanical interfaces, but also because

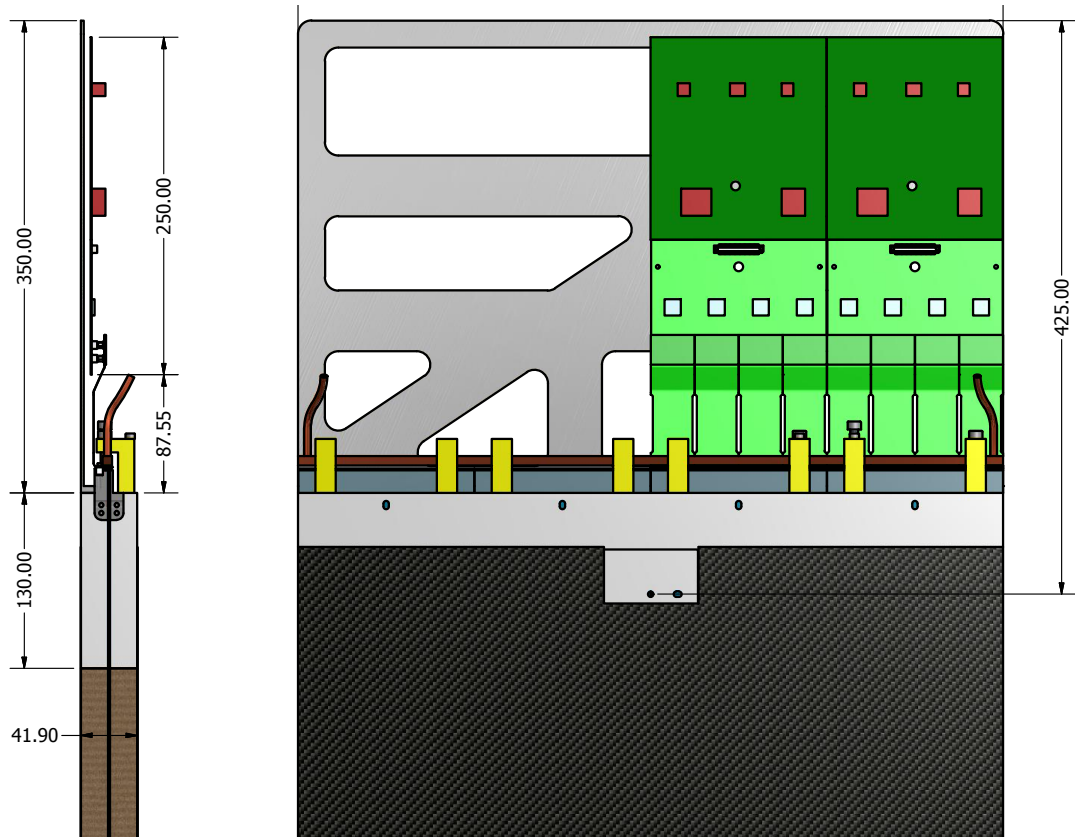


Figure 3.40: Side- and front-view of the end of a scintillating fibre module, showing the SiPM arrays, cooling pipe, flex cables and front-end electronics.

of the requirements that the Read-out Box be light-tight, with its interior well insulated (thermal) and isolated (moisture) and flushed with a dry gas having the frost and dew points below -70°C at the inlet and below -50°C at the exhaust to prevent condensation and frost build-up on the cold surfaces of the interior of the cold volume.

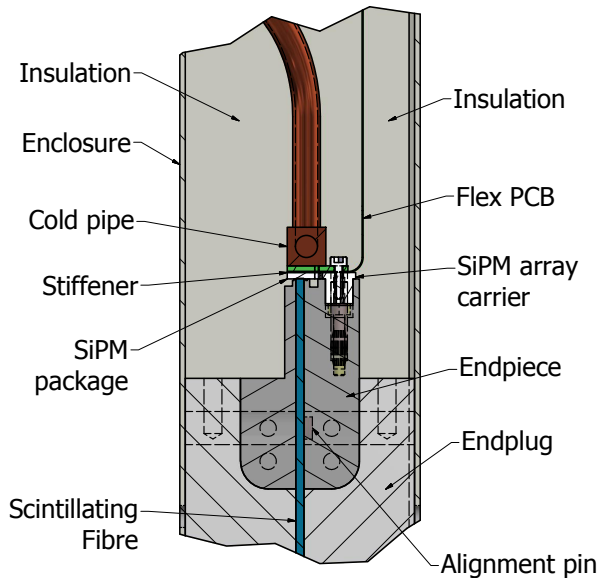


Figure 3.41: Schematic view of the cold volume within the Read-out Box at the end of a scintillating fibre module. The front-end electronics sit above and are separated by insulation from the cold volume.

Access to the ROB will be through two access panels in the front face of the box, one for the Front-End Electronics, and another for the cold volume where the SiPMs reside. Access to the ROB for replacement of electronics and SiPMs, and to repair connections, should be possible while the detector is in the closed position in the pit. The modularity of the electronic cards and SiPM super-arrays should allow for easy replacement with minimal fine work. Connectors for the electronics and power supplies will feed through the top end of the ROB. An illustration of how the box might appear is shown in Fig. 3.42.

Significant amounts of insulation ($\sim 5\text{ cm}$) will be needed to separate the cold region of the Read-out Box where the SiPMs are located from the warm region containing the front-end electronics. The small distance (2 cm) between the cooling pipe and the front and back faces of the ROB will also provide a challenge to prevent condensation and frost inside and outside the ROB.

3.6.5.1 Flex-PCB, Temperature Sensor and Super-Arrays

The SiPM multi-channel array is mounted on a Kapton flex-PCB which has a length of about 100 mm (Fig.3.43). The flexibility is required to make a 90° bend in order to connect the SiPMs to the Front-end (FE) boards located outside the cold volume. Each detector

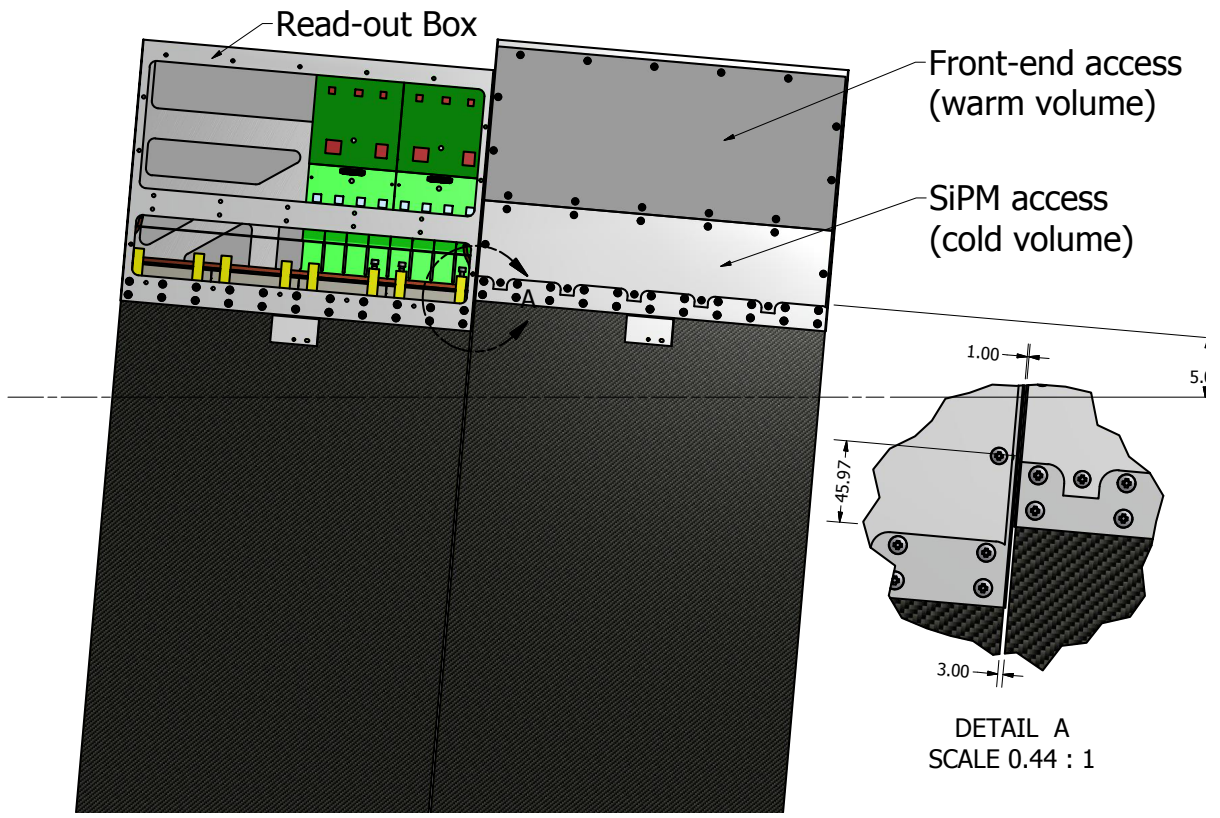


Figure 3.42: An illustrative view of two adjacent stereo modules with closed ROB (right) and open access panels (left). The access to the electronics and SiPM zones will be through access panels in the front face. The insulation filling the cold-volume and surrounding the cooling pipe are not shown.

is mounted on a separate flex-PCB and attached with connectors to the FE board. This allows single detectors to be tested and increases the overall yield. The connectors of the flex-PCB do not require soldering the connection of the SiPMs to the front-end electronics.

An aluminium stiffener is glued to the back side of the SiPM flex-PCB and detector region where it allows a good thermal contact to be made with the cooling pipe. The stiffeners also play a role of “heat spreaders”, providing a uniform temperature profile over an SiPM array. If required, the stiffener could also be implemented with a material that matches the detector substrate. A passive temperature sensor (NTC or PT1000) is mounted on the back side of the detector where a cut-out in the stiffener is foreseen. The temperature sensor is connected via the flex-PCB to the FE board and can be accessed by the slow control. The temperature difference between detectors over four arrays needs to be within 1K to ensure good gain uniformity while using only one bias voltage per four arrays. The bias voltage ($\sim 60 \text{ V}/1 \text{ mA}$) is provided via the flex-PCB to the detector.

The four flex-PCBs are connected to one FE board to form a so-called “super-array”.

The four SiPM arrays will also be pre-aligned together and fixed to a polycarbonate support carrier for ease of handling, installation and alignment.

The SiPMs must be aligned with respect to the fibre mats, and this relative alignment must remain stable over time as this end region is subject to thermal expansions and contractions. The alignment concept is shown in Fig. 3.44. They are aligned to the mat by means of dowel pins on the carrier matching the outer end-piece of the casted fibre mat, as shown in Figs. 3.40 and 3.41. Optical grease that does not crystallise at cold temperatures will be used as an optical interface between the SiPMs and the fibres.

It is foreseen that super-arrays will be exchanged by opening the ROB access panels, removing the insulation, displacing the cold pipe and disconnecting the old super-array.



Figure 3.43: One 128 Channel SiPM array mounted on a flex-PCB cable with connectors for the Front-end electronics.

3.6.5.2 Light Injection System

The gain of the SiPMs must be measured in order to calibrate the detector (see Sec. 3.5.9). The calibration of the photo-detectors will be made using a synchronous light source with short low intensity light pulses. The light injection system has to provide a low intensity long light pulse ($\mathcal{O} 5\text{ ns}$) where the intensity can be tuned such that 1–2 photons on average are detected per channel.

A possible implementation is to inject the light into the transparent polycarbonate end-piece with the help of a light leaking fibre. A leaking fibre can be produced by generating small damages on the cladding of the fibre as shown in Fig. 3.45. The light is then coupled via scintillating fibres to the detectors.³⁴ Transporting the light via a fibre into the cold region is advantageous since the light intensity of the LED is strongly temperature dependent, and the driver can generate electronic noise. The LED driver and the LED coupled to one end of the fibre can be placed outside the cold region in the FE-electronics region of the ROB. A prototype equipped with such a light injection system has been tested in the laboratory.

³⁴A compromise will have to be found regarding the coating of the scintillating fibres with TiO_2 .

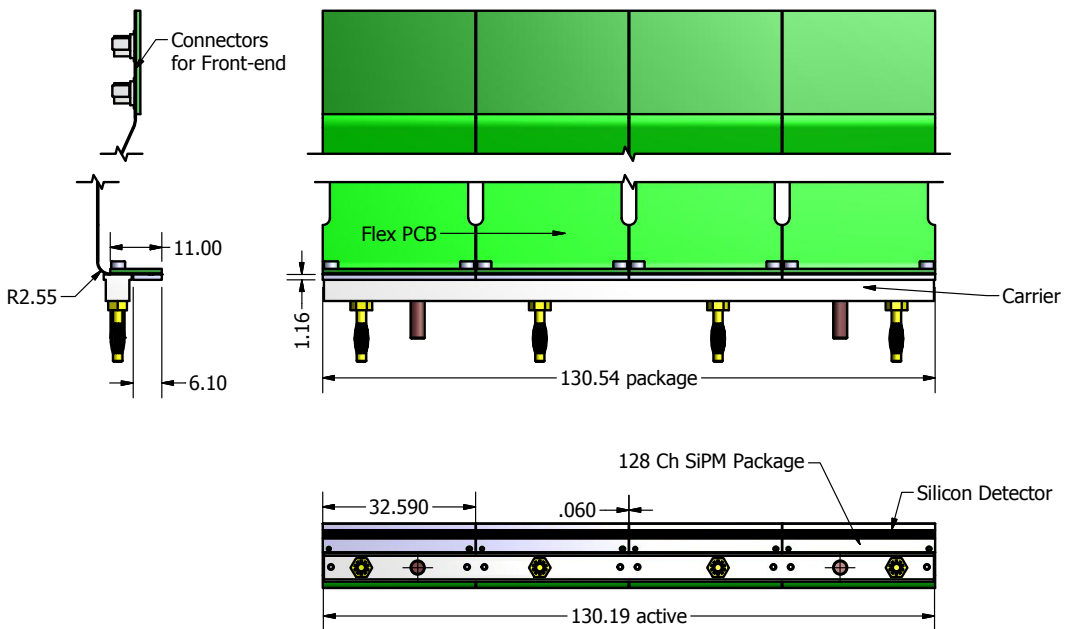


Figure 3.44: A super-array: four SiPM arrays mounted on one carrier spine. Four of these packages will be needed to read out one end of a SciFi Tracker module.



Figure 3.45: Light leaking fibre introduces light in the transparent polycarbonate end-piece.

3.6.5.3 SiPM Cooling

The SiPMs must be operated at sub-zero temperatures, down to -40°C , in order to keep the dark count rate at an acceptable level during the entire lifetime of the upgraded experiment, especially in the most irradiated inner modules ($|x| < 0.5 \text{ m}$). The temperature gradient across the 130 mm long super-array should be greater than $\Delta T < 1\text{K}$.

Because the SiPM arrays dissipate a negligible amount of heat, the system heat load will be dominated by parasitic heat influx through the insulation of the ROB and connecting lines. Thermal analysis [75] and direct measurements [76] have shown that the heat load of one ROB with the SiPM temperature of -40°C is below 20 W. This corresponds to a total heat load of maximum 6 kW for the entire SciFi Tracker (not including the heat pick-up along insulated pipes, discussed in Sec. 3.8.2).

Inside the ROB, a square copper or aluminium tubular heat exchanger (a "cooling pipe") with a 4 mm bore for a cooling fluid, is pressed by spring-loaded screws against the

array of SiPM stiffeners. A thin thermal interface of alumina-loaded silicone or pyrolytic graphite provides a sufficient thermal contact between the cooling pipe and the SiPM array and, at the same time, eliminates or reduces the shear stresses due to the difference in their thermal contraction. The aluminium SiPM stiffeners perform as heat spreaders ensuring a uniform temperature over every single SiPM package.

The limited space in the z-direction (6 – 7 cm) for each tracker module imposes stringent requirements on the thermal design of the ROB. The narrowing of the end-pieces glued at the end of the fibre mat is designed to limit the thermal exposure of the SiPM and to maximise insulation. Cavities in the end-plugs of the modules will provide additional insulation and slightly reduce the temperature gradient over the fibre end. All remaining space within the Read-out Box will be packed with a closed-cell foam insulating material, like Rohacell³⁵. The module edges remain thermally non-insulated. Therefore, the gaps (dead spaces) between the modules will be protected by the insulating shells of the module interconnection pipes.

As stated before, dry gas will be flushed through the read-out box to prevent frost and condensation in the interior. The flushing gas (air) should have a frost point of less than -55°C , which corresponds to a relative humidity of $<0.09\%$ at normal conditions (water concentration below 13 ppmw). To prevent condensation on the outside of the ROB, the temperature of its outer surface must be above the dew point of the LHCb cavern. A strong thermal gradient will exist within the module as demonstrated in an ANSYS³⁶ thermal simulation of a ROB prototype shown in Fig. 3.46. The cold zones where frost and condensation are expected are mostly contained within the end-plugs and insulation, with some problem areas appearing on the front and back faces of the ROB. The 2 mm thick aluminium plates on the outer surfaces of the ROB are effective heat spreaders which have been shown to mitigate some of the cold-spot problems. However, the calculated coldest spot of the aluminium ROB enclosure is still barely above the average dew point of 11°C . Active heating might be required to raise the surface above the dew point if additional insulation cannot be added.

The overall design of the SiPM cooling system is fairly conservative, but it faces a few important challenges that still require solutions related to:

- the thermal insulation of the connection lines and the ROBs, especially in the dead regions between the modules;
- the thermal expansion/contraction (and the corresponding deformations) of 0.52 m wide objects under the temperature variations of over $\pm 40\text{K}$;
- the requirement of a rigorous condensation and frost formation control at all levels (including multiple humidity barriers in the ROB insulation).

The SiPM cooling plant and infrastructure are discussed further in Sec. 3.8.2.1.

³⁵Rohacell® is a trademark of Evonik Röhm GmbH.

³⁶ANSYS, Inc., Southpointe, 275 Technology Drive, Canonsburg, PA 15317, USA

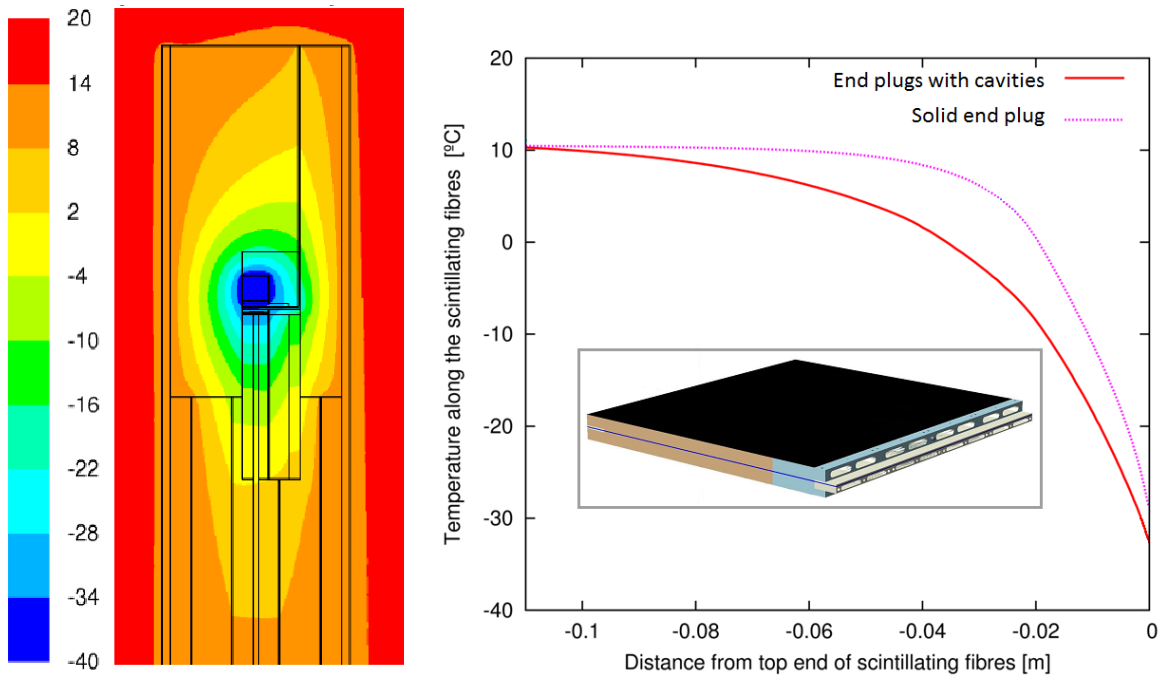


Figure 3.46: An ANSYS thermal simulation of a simplified SiPM compartment of the Read-out Box. Left: The temperature distribution around the SiPM array. Right: fibre temperature profiles as function of the position along the mat with and without cavities in the end-plugs (position 0 corresponds to the contact between the mat and the SiPM, position -0.11 corresponds to the bottom of the end-plug). A detail of a simulated module is shown in the insert.

3.6.6 Summary of the Module Design

Based on the above considerations, a functional module design can be produced for the full SciFi Tracker. The light yield of a serial-like production fibre mat has been measured including mirroring. Estimates of the irradiated detector light yield are shown. Challenges have been identified in the mechanical design regarding the cooling of the Read-out Box, thermal expansion, and preventing condensation and frost build-up and will be addressed in the future Engineering Design Report. Production of prototype modules and tooling are in progress and will include one or more fibre mats that can be read out by the proposed SiPM package scheme, as well as implementing the cooling system where possible. A list of all prototypes which have been produced is given in Table 3.10.

Table 3.10: A summary of the items, production status, characteristics, and measurements done for the SciFi Tracker module development. (GW) = grooved wheel, (C) = Kapton coverlay substrate

Item	Comment	Status	Measurements
Fibre Mats			
3 cm (GW)	3 m, 5 layers	Completed	light yield, atten. length, fibre alignment
4 cm (GW)	1 m, 3 layer	Completed	align. pins in wheel
7 cm (GW)	3 m, 5 layers	Completed	mat&fibre align.
7 cm (C)	3 m, 4 layers, multi-sheet	Completed	fibre align.
13.5 cm (GW)	3 m, 5 layers	Completed	fibre align.
13.5 cm (GW)	3 m, 6 layers	Spring 2014	
13.5 cm (C)	3 m, 6 layers, single sheet	Mar. 2014	
13.5 cm	275 cm winding wheel	Autumn 2014	
Module Panels			
2 m dummy	poly. sheet, honeycomb	Completed	Young's modulus
1 m dummy	cast poly. + 7 cm mat	Feb. 2014	assembly
1 m fibre	13 cm fibre mats	Spring 2014	mat align, readout, cooling tests
2.5 m dummy	poly. sheets, 7 cm fibre mat	Late Spr. 2014	mat align., assembly
2.5 m fibre	13.5 cm fibre mats	Sum. 2014	mat align., test beams
5 m	cast 13.5 cm fibre mat	Autumn 2014	assembly, test beams
Read-out Box, Cooling			
Mock-ups 1,2	No elec., no hum. seal	Completed	thermal simulation and measurements
Mock-ups 3+	realistic design, serial connect	Spr./Sum. 2014	Thermal load, assembly
Test-beam proto	sealed, mounted, func. elec.	Autumn 2014	Functional
Final	final geometry	Early 2015	
SiPM super-arrays			
BGV-version	short flex-PCB	Completed	functionality
SciFi-version	longer flex-PCB, other adj.	Summer 2014	
Completed Modules			
PERDaix [67]	7 cm mats, 1 m long	Completed	light yield, test beam
	hybrid SiPM-FE	10 modules	temp. cycle, operated over months

3.7 Electronics

3.7.1 Front-End Design

The Front-End boards are located in the warm side of the ROB. They interface to the SiPMs on one side, and to the experiment data-acquisition and control system on the other. Each FE Board also has a complete interface for the distribution of bias voltages to the integrated circuits and to the SiPMs. It also distributes Timing and Fast Control (TFC) signals, and signals from and to the Experiment Control System (ECS) [29].

The architecture of the SciFi Tracker FE electronics follows the guidelines defined in the *Electronics architecture for the LHCb upgrade* document (Ref. [28]). At the functional level, it can be summarised by the block diagram shown in Fig. 3.47. All SiPM signals are amplified, shaped and digitised in the PACIFIC ASIC which is described in detail in Sec. 3.7.2. The data are routed to an FPGA that executes a fast clusterisation algorithm and zero-suppression to reduce the data volume. The cluster data from various SiPMs are gathered by a “concentrator” FPGA, which formats them and transfers them to a fast serialisation algorithm according to the specifications of the GBT project [77]. This algorithm can be run either on the same FPGA or on a dedicated GBTx ASIC. Serial data are then transmitted to the counting house via optical links [78]. A “Master GBT”, connected to the SOL40³⁷ [79] via bi-directional optical links, is responsible for the distribution of TFC signals to the FE, and ECS signals to and from the FE through the SCA chip [80].³⁸ Dedicated DC-DC converters are also placed on the FE Board to provide the voltages for the PACIFICs, the FPGAs, and the optical links.

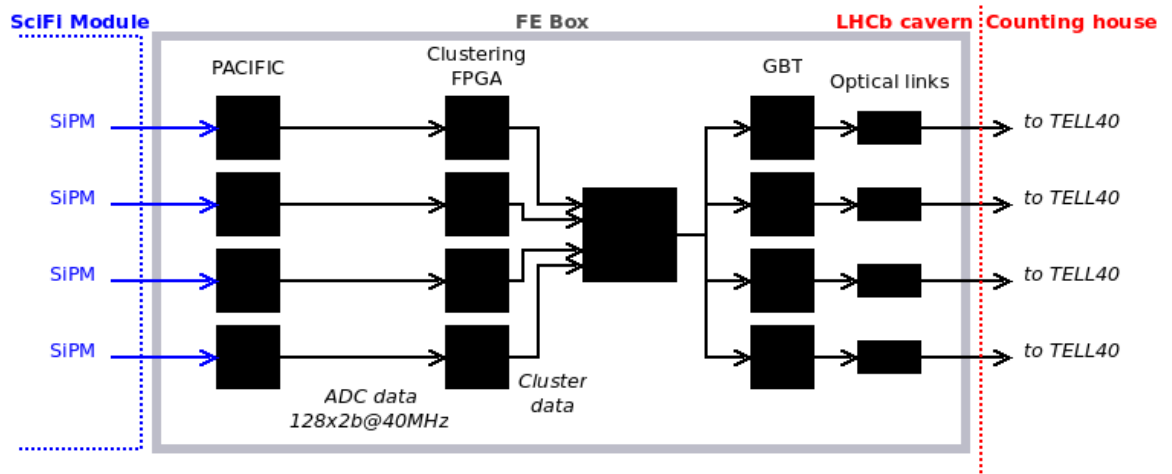


Figure 3.47: Functional diagram showing the data flow in the FE electronics. It corresponds to one quarter of a ROB.

³⁷The SOL40 is an electronic board devoted to the distribution of the slow control and the TFC signals.

³⁸The SCA chips decode and encode the data encapsulated by the GBT for the SOL40 slow control signals (I2C, JTAG, SPI, clocks, slow ADC).

The implementation of these concepts into a concrete design based on a combination of ASICs and printed circuit boards will be discussed in the following sections. The discussion will also take into account the mechanical constraints imposed by the scintillating fibre modules and the surrounding infrastructure (cables, pipes, support frames, *etc.*).

3.7.1.1 Geometrical Constraints

The FE Board will be connected by flex cables to SiPMs at each end of the scintillating fibre modules and attached to the detector frames for mechanical support. This defines a tight geometrical envelope for the FE design. The mechanical structure is still in the design phase, but an estimate of this geometrical envelope, shown in Table 3.11, can be obtained assuming that the present Outer Tracker C-Frames are re-used and the scintillating fibre modules have a width of about 522.4 mm, corresponding to 16 SiPMs with 128 channels each and a pitch of 250 μm .

Table 3.11: Geometrical envelope in a ROB for the FE Boards.

Dimension	Max (m)
Width (LHCb x co-ord.)	0.52
Height (LHCb y co-ord.)	0.25

The final design will take into account the fact that some services, most notably the SiPM cooling pipes and possibly some dry-air pipes, will have to be fed through this volume.

3.7.1.2 Inputs and Outputs

The single ended analogue signals from the SiPMs will be transmitted to the FE electronics through flex cables together with readings from small temperature sensors placed close to the SiPMs. These sensors are required as variations in the temperature lead to variations in gain. The SiPM bias voltage is also transmitted through the flex cable. In addition, a signal will be sent to control the intensity of a calibration LED placed close to the SiPM (see Sec. 3.6.5.2). Each FE Board will have power inputs for the FE chips (LV) and the SiPM bias voltages.

Several optical links will transmit the cluster data to the TELL40 in the counting house. The exact number of links required depends on the occupancy in the modules handled by the FE Board. Bi-directional optical links will provide the interface between the GBT Masters in the FE electronics and the TFC and ECS systems.

3.7.1.3 Design and Layout

A straightforward way to implement the FE Board design is to distribute all read-out elements in one plane over the full width of the scintillating fibre module. One ROB will

contain two of the FE boards shown in Fig. 3.48. Each of these units consists of several identical boards hosting the PACIFICs and the clustering FPGAs interconnected with high-density high-pin-count connectors to one “Master Board”. The Master Board will contain two Concentrator FPGAs, the GBTx data serialisers, a Master GBT, the optical links and the DC-DC converters.

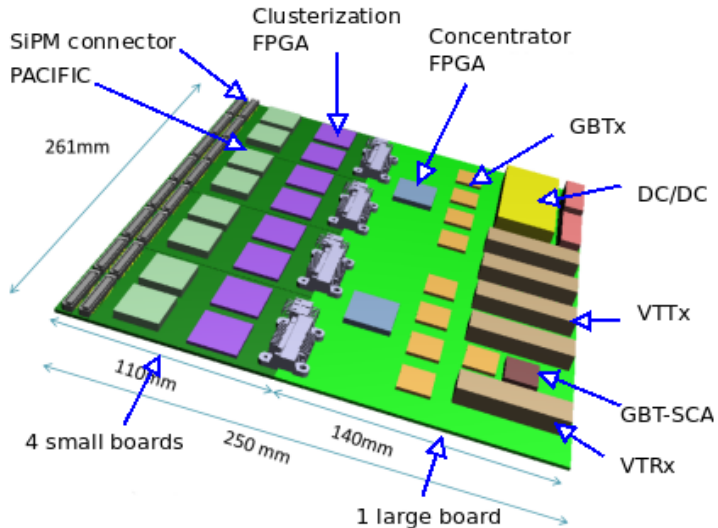


Figure 3.48: FE board of half module width, hosting the complete FE electronics for 8×128 SiPM channels. Each ROB will contain two of these units.

The main feature of this layout is the high density of input channels. The PACIFICs and clustering FPGAs will be placed with a pitch of 32 mm (corresponding to 128 SiPM channels). Preliminary studies have demonstrated the feasibility of a PCB hosting the PACIFICs and the clustering FPGAs. A 16-layer PCB, in combination with chip packages not exceeding $26 \times 26 \text{ mm}^2$, allows the routing of the 128 analogue signals from one SiPM to a PACIFIC, the 32 differential output signals from the PACIFIC to the FPGA, and several control signals.

The number of the main components used for a detector plane is given in the Table 3.12. The GBT are always mounted on the FE boards while the number of Versatile Transceiver (VTRx) and Twin-Transmitter (VTTx) modules [81] depends on the occupancy. Hence, the number given here represents the order of magnitude required, and it will change when the detector will be optimised.

3.7.1.4 Occupancy Simulations

A first estimation of the detector occupancy was made using a preliminary model of the LHCb detector [82]. The results indicate that the maximum mean occupancy in the

Table 3.12: Number of components used for the FE boards.

	PACIFIC	Clust. FPGA	Conc. FPGA	GBT	SCA	VTRx	VTTx
Board Plane (24 modules)	8 384	8 384	2 96	9 432	1 48	1 48	2-8 112

detector is 2.5 clusters per SiPM per event near the beam pipe corresponding to a cluster rate of 100 MHz. The occupancy then falls quickly to around 0.1 clusters per SiPM per event at the edge of the detector, a rate of about 4 MHz.

The simulation results have been converted to a bandwidth requirement using the data format given in Sec. 3.7.3.2. The number of bits per event for an SiPM was computed as:

$$N_{bits} = 16b \text{ (header size)} + 16b \text{ (coded cluster size)} \times N_{clusters} \quad (3.1)$$

The maximum number of clusters $N_{clusters}$ is 15 which leads to a 256 b frame size. In this case, the event data is split within two GBT frames. The simulation results are shown in Fig. 3.49. The offset (0.64 Gb/s) is generated by the headers which have to be sent even with empty events.

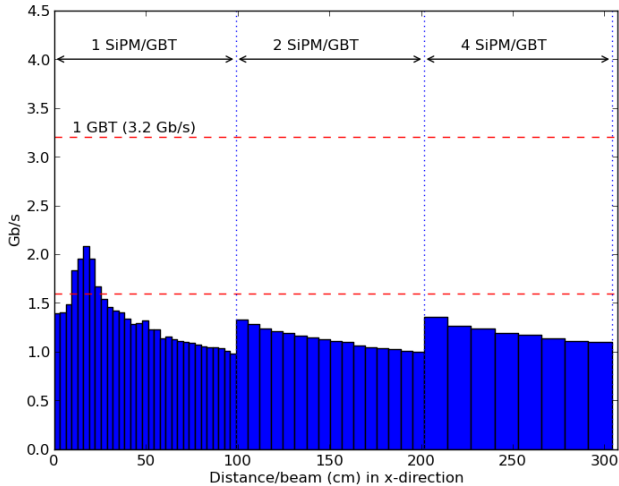


Figure 3.49: Bandwidth needs in one quadrant of the hottest detector plane given in Gb/s. The two red lines represent the bandwidth of 1/2 GBT and 1 GBT. One GBT per SiPM is used for the first 32 SiPMs, then one GBT every two SiPMs for the next 32 SiPMs, and finally one GBT every four SiPMs for the last 32 SiPMs ; the bin width is used to illustrate this division.

The detector can be split into three zones. The first uses one SiPM per GBT, the second uses two SiPMs per GBT and the third use four SiPMs per GBT. This drastically reduces the number of links required per quarter from 96 to 56. The simulations show that there is still room for optimisation as the accuracy of the physics simulation improves.

3.7.2 The PACIFIC ASIC

A new low-power front-end ASIC, called PACIFIC, is being developed to process and digitise the analogue signal from the SiPM. The hit position of the particle needs to be computed with a spatial resolution less than $100\text{ }\mu\text{m}$. Four functions will be required to achieve this: amplification, shaping, integrating and digitisation.

3.7.2.1 General Overview

The PACIFIC chip will include all of the elements required to process the data from one SiPM. Hence, it will have the same granularity. *i.e.* 128 channels per chip. It will be low power with 1 W per chip or 8 mW per channel, and radiation tolerant. The chip will use the IBM 130 nm technology. The functional view of the ASIC is presented in Fig. 3.50. It is composed as follows:

1. an input stage.
2. a fast shaper.
3. two interleaved gated integrators.
4. a 2-bit ADC sampling at 40 MHz.

Moreover, the chip has an analogue switch for each channel at its input such that the bias voltage of the SiPM can be switched off. This feature provide a protection against individual channel short-circuits which have been observed during irradiation tests of the SiPMs. The design is a compromise between area occupancy, power consumption, and precision on the detector.

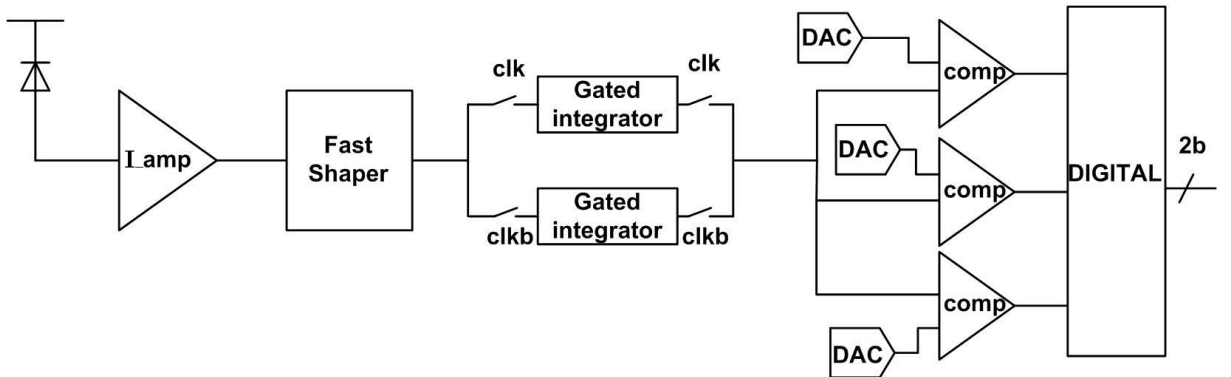


Figure 3.50: Fast shaper solution.

3.7.2.2 Input Stage

The input stage is a current conveyor with the current flowing from the SiPM anode to the circuit [83]. The goal is to achieve the following specifications in this block:

- High bandwidth (≈ 250 MHz).
- Low power (< 2 mW, maximum of 8 mW per channel including the whole ASIC).
- Low input impedance ($20 \Omega < Z_{in} < 40 \Omega$).

The current conveyor, shown in Fig. 3.51, is based on a novel approach of double feedback, and is optimised for SiPM arrays with anode connection. The current conveyor is followed by a closed loop transimpedance amplifier that transforms the input current into a voltage and provides impedance isolation to drive the first stage of the shaper.

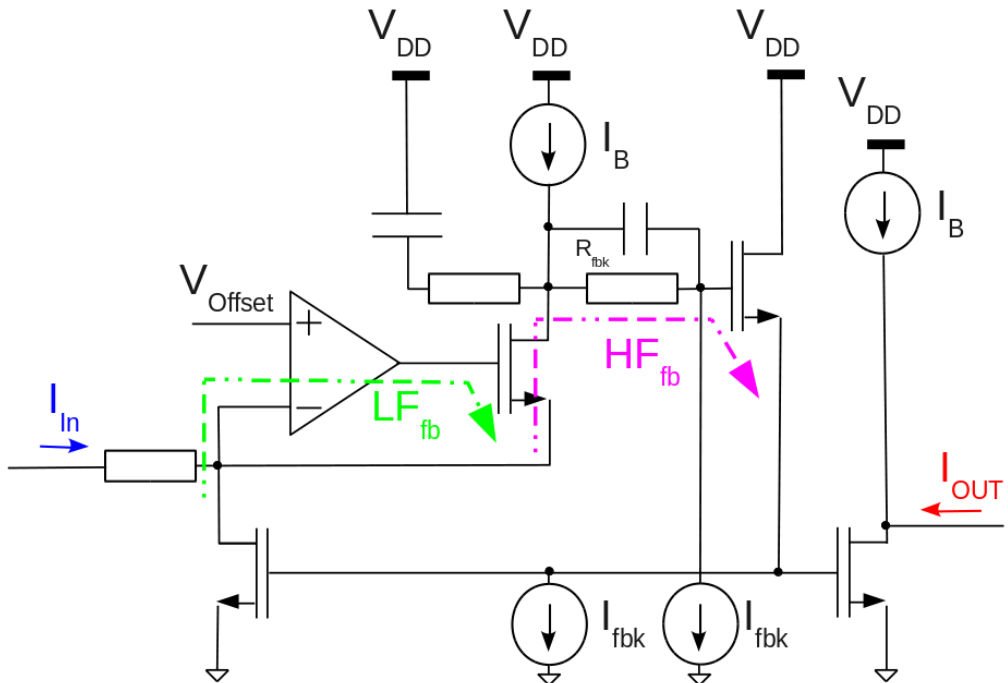


Figure 3.51: Current conveyor.

It provides a low input impedance in order to avoid affecting the timing behaviour of the SiPM and increasing the input current. The high frequency feedback path, HF_{FB} , keeps this input impedance constant in a certain frequency range. The second labelled path, LF_{FB} , will provide the DC voltage (V_{offset} in Fig. 3.51) of the input node using the virtual short circuit in the amplifier which will drive a follower in a lower frequency range. The design has been implemented taking into account the fact that the dominant pole should be set at the input node. The parasitic capacitance of the SiPM is in the

order of tenths of picofarads. In this way stability is not compromised when an important capacitance is added at the input.

The gain of the current conveyor is tunable by a factor of four to deal with different SiPMs and different operating conditions.

3.7.2.3 Shaper

The detector signals are not fully contained in one LHC clock period. There are two main factors which contribute to the long signal tail: light generation and propagation in the fibre; and SiPM recovery. The last factor depends completely on the SiPM. The role of this shaper is to perform tail cancellation prior to gated integration in order to minimise the spill over and the fluctuation of the integrated signal as function of the signal arrival time. *i.e.* to achieve a sufficient integration plateau.

The implementation consists of a double pole-zero shaper. The first time constant cancels the slowest time constant of the SiPM response, the one associated to the internal SiPM capacitances and quenching resistor. The second one cancels the fastest one which is related to the parasitic interconnect capacitance and the input impedance of the preamplifier. The proposed implementation is shown in Fig. 3.52. It is a closed loop shaper based on the same OTA³⁹ used for the transimpedance amplifier of the input stage with greater than 300 MHz GBW⁴⁰ and with high sourcing current capability (fast rising edge), and has low power consumption ($700 \mu\text{W}$). The pole and zero frequency of both shapers are tunable, and they have been calculated to be able to operate with the very different time constants of the Ketek and Hamamatsu SiPMs.

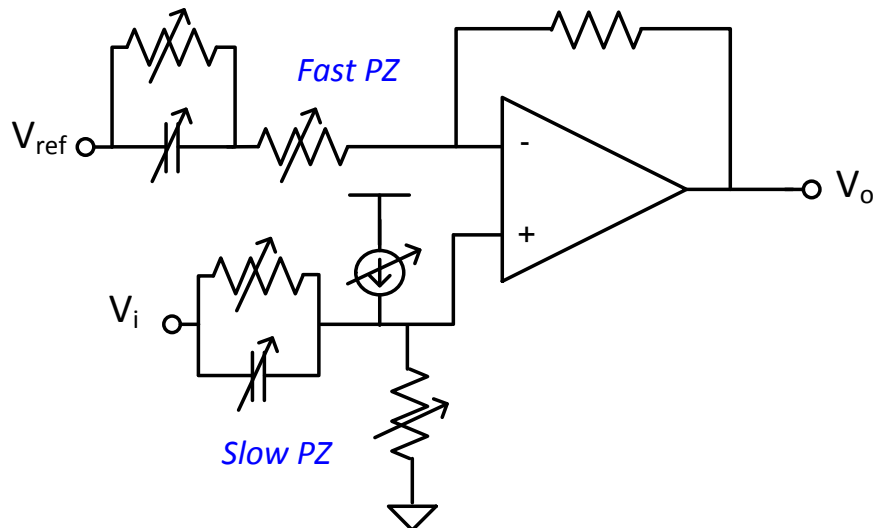


Figure 3.52: Fast shaper block diagram.

³⁹Operational transconductance amplifier.

⁴⁰Gainbandwidth product.

3.7.2.4 The Interleaved Gated Integrator

It has been decided to interleave two gated integrators, as shown in Fig. 3.53, to avoid any dead time during the acquisition.

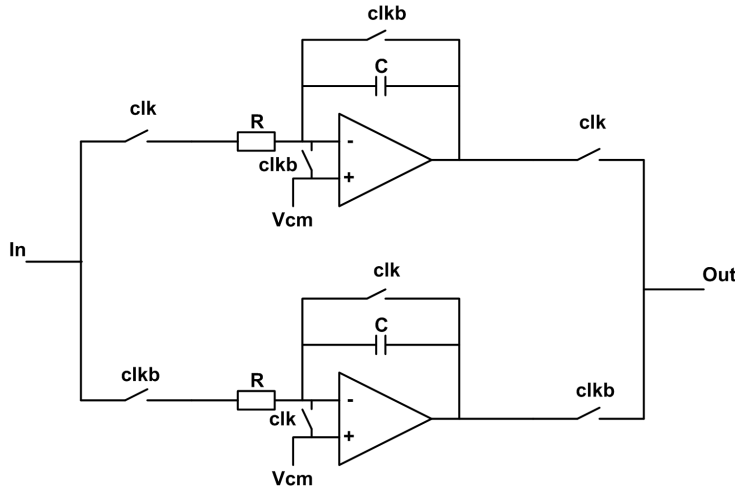


Figure 3.53: Interleaved gated integrators.

The principle of operation is as follows: when the first integrator is working, the second one is reset and vice versa. In order to fit in the 40 MHz general frequency, each gated integrator works at a frequency of 20 MHz. The ADC will convert the value at the output of the integrator each 25 ns just before the ADC switches from one integrator to the other one. With this solution, the integration is still available at the output of the channel even if the signal arrives between two clock cycles.

The integrator is composed of an amplifier, two switches, a resistor and a capacitor. This block performs the mathematical operation of integration. Equation 3.2 describes the relation between v_{in} and v_{out} :

$$v_{out}(t) = -\frac{1}{RC} \int_0^t v_{in}(t) dt - V_{cm} \quad (3.2)$$

As shown in Eq. 3.2, the maximum value of the output signal depends directly on the value of the resistor and the capacitor. The two switches allow the system to be reset by setting the value of the input and output voltages to the reference voltage (600 mV). The final values of R and C will be set when the choice of SiPM is made.

3.7.2.5 Pulse-height Information using Comparators

The digitisation of the analogue signal from the gated integrators is done with a 2-bit flash ADC with a non linear scale running at 40 MSample/s [84]. Three comparators are used with individual thresholds which are set using a 6-bit DAC. The threshold value is configurable for each SiPM channel in order to be able to cope with variations in the gain and the pedestals. This feature needs 2304 bits of configuration data per SiPM.

3.7.3 Data Processing

The large data volume from the PACIFIC chip needs to be significantly reduced before it can be transmitted to the AMC40 [31] boards⁴¹ in the counting house [28]. The compression is performed using a clusterisation algorithm [68] where the pulse-height information is necessary to achieve a resolution better than $100\mu\text{m}$ for clusters with more than one hit.

Monte-Carlo studies have shown that after clusterisation data rates below three clusters per SiPM in the highest occupancy region can be achieved, and that “cluster noise” can be kept below 2 MHz per SiPM [82]. The data format given in Sec. 3.7.3.2 allows for a maximum mean number of clusters of six per event. Therefore, executing a data clusterisation algorithm in the FE electronics will provide the desired data reduction.

3.7.3.1 Cluster Finding

The scheme shown in Fig. 3.47, adopting an FPGA for clusterisation, offers a flexible solution to the problem of data reduction. The hit finder and clusterisation procedure will be analogous to that used for the clusterisation of VELO and ST hits in the present TELL1 boards [85]. It is illustrated in Fig. 3.54, and uses four thresholds:

- *Seed threshold*: The first step in the clustering algorithm is to find cluster candidates with signals above the seed threshold. This condition alone is not sufficient to form a cluster. For a channel found above the seed threshold, its neighbours need to be tested.
- *Neighbour threshold*: Signals from neighbouring channels are included in the cluster if they are above the neighbour threshold which is lower than the seed threshold. This ensures that the maximum signal is measured as the signal are typically distributed over more than one channel.
- *High threshold*: Channels with signals above the high threshold are sufficient to form a cluster without any other conditions.
- *Cluster sum threshold*: The cluster is confirmed if the sum of the signals from the seed threshold channel and one or more neighbour threshold channels are above the cluster sum threshold. This removes a large fraction of the SiPM noise.

The cluster position is calculated by computing the barycentre b using a weighted average with a 2-bit inter-channel precision with

$$b = \sum_i i \times ADC(i) / \sum_i ADC(i), \quad (3.3)$$

where $ADC(i)$ is a configurable value representing the weight of the highest triggered threshold on the SiPM channel i . The implemented algorithm can handle up to four channels associated with a cluster, and larger clusters are split. Finally, a fixed length data

⁴¹The AMC40 is the standard read-out board for LHCb (mezzanine of the TELL40 board)

frame is recorded for each cluster containing its position, a 7-bit SiPM channel number and a 2-bit inter-channel position corresponding to 1/4 of a channel pitch; the number of hits in the cluster (2 bits); and 3 bits representing the sum of the ADC values in the cluster.

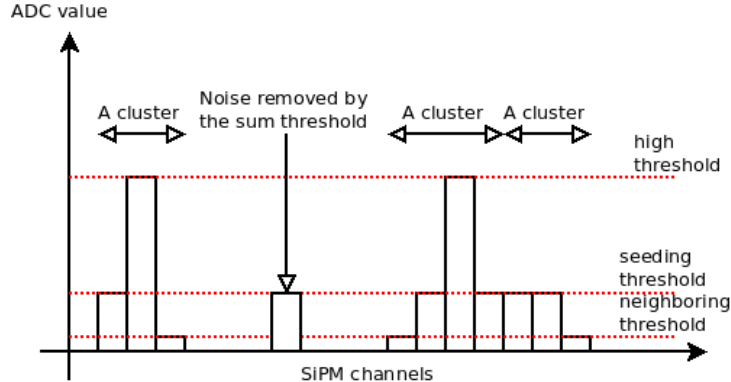


Figure 3.54: Graphical representation of the algorithm used to cluster neighbouring SiPM hits.

The choice of the FPGA and the implementation of the clusterisation algorithm in Fig. 3.54 have to deal with two main difficulties: the usage in a radiation environment and the limited amount of FPGA resources available. The radiation environment in which the FPGAs will have to operate was discussed in Sec. 3.2.3. The SciFi Tracker FE Boards will be in the same position occupied at present by the Outer Tracker FE Boxes. Detailed studies showing the feasibility of using Altera (Arria GX [86]) and Actel (ProAsic3 [87]) FPGAs in such environment were carried out in the framework of the upgrade of the straw-tubes FE electronics [88]. The usage of Smartfusion2/Igloo2 Microsemi FPGAs [89] is being considered at present. These flash-based FPGAs are expected to be more radiation hard [88] than the Actel ProAsic3, and also offer on-board fast transceivers where the GBT serialisation protocol could be embedded. Dedicated irradiation tests are foreseen.

3.7.3.2 Data Concentrator

As shown in Fig. 3.47, the data from four clustering FPGAs will be collected by a “Concentrator” FPGA with a larger number of I/O and logic resources. This FPGA format the data as required for serial transmission with the GBT [28], and will handle timing and fast control commands [29].

The data section of the 112-bit wide-bus GBT frame [77] will be split as shown in Table 3.13 [29], where the different formats generated in response to various TFC commands are also shown [79]:

- *Cluster data:* The compressed-data section will be filled with a sequence of cluster data using 16 bit words as it has been defined in Sec. 3.7.3.1 ;

Table 3.13: GBT frames

Cluster data:																								
Header	BCID												Number of clusters			Information								
Data	ADC charge	Cluster Size	SiPM	Cell								Fraction												
ADC data:																								
Header	BCID												Number of clusters			Information								
Data1	ADC charge	Cluster Size	SiPM	Cell								Fraction												
Data2	ADC0	ADC1	ADC2	ADC3	ADC4	ADC5	ADC6	ADC7																
Sync command:																								
Header	BCID												Information											

- *Non-zero suppressed data*: The SciFi Tracker FE electronics transmit all the ADC data (2-bit ADC data per SiPM channel, see Sec. 3.7.2) together with the cluster data ;
- *Sync command*: The full Bunch Crossing ID (BCID) is sent on in 12 bits in order to check the time alignment of the “Concentrator” FPGA with the AMC40.

Headers will be sent even if no clusters are found.

3.7.4 Back-end Processing

The data packets sent by the front-end (FE) boards through GBT optical links are received and processed on the back-end electronics side by TELL40 boards [31]. The TELL40 is an ATCA format board housing four AMC40 mezzanine boards, each of which handles 24 input optical GBT links from the front-end boards and up to 12 output optical links towards the DAQ farm. Most of the data packet processing is performed inside the AMC40 FPGA, which handles the following tasks:

1. The implementation of the GBT link reception module: deserialisation and error correction.
2. The incoming data packets from the 24 GBT links are realigned according to their BCID. Events are then repacked, and redundant headers are removed.
3. The events which are not rejected by the Low Level Trigger are concatenated into Multi-Event Packets (MEP) and stored in an on-board memory. Eventually, the MEPs are sent to the DAQ processor farm through one of the output optical links (typically, 10-gigabit ethernet links).

4. Monitoring of the data flow.

The development of the firmware for the AMC40 board is coordinated centrally with the aim to provide a generic code available for all the detectors of the LHCb experiment. However, if specific processing is required, it will still be possible to adapt the generic firmware to the needs of the SciFi Tracker.

In zero-suppressed mode, the SciFi Tracker front-end boards only send the list of all the detected clusters for a given BCID to their GBT links (see Sec. 3.7.3.1). It has been shown in Sec. 3.7.1.4 that the detector can be split in three regions in order to optimise the TELL40 board needs (see Table 3.14). For example, eight GBTs will be necessary to collect data from one FE board reading eight SiPMs in the high occupancy region. Therefore, each AMC40 will be able to handle data from three different FE boards, and each TELL40 ATCA board will handle data from 12 FE boards. On the other hand, in low occupancy regions, only the bandwidth of two GBTs is required to read out one FE board, and each AMC40 and TELL40 board will handle 6 and 48 FE boards respectively.

In any case, in either high, middle or low occupancy regions, the AMC40 firmware will have to be able to keep track of the original SiPM ID and SiPM channel for every data packet.

Table 3.14: AMC40 and TELL40 board needs assuming a dividing of the detector in three equal region (High, Middle and Low occupancy)

Zone	DAQ GBT link/FEB	FEB/AMC40	FEB/TELL40
High occupancy	8	3	12
Middle occupancy	4	6	24
Low occupancy	2	12	48
Needed for the detector	2592 links	120 AMC40	30 TELL40

3.7.5 Voltage Distribution

Each FE Board needs various Low Voltage (LV) lines: 1.2 V for the GBT-SCA and the PACIFIC chip, 1.5 V for the GBTs and the Microsemi FPGAs, 2.5 V for the optical links. The distribution of bias voltages to the FE electronics will follow the scheme adopted for the present tracking system [90]. Each FE Board will be provided with one LV line, and then a number of DC-DC voltage converters will be used to produce all necessary bias voltages. The SC01 DC-DC converters developed at CERN [91] for usage in radiation and magnetic field will be used ($<12\text{ V }V_{in} \rightarrow 0.6\text{-}5\text{ V}, 4\text{ A}, 1.8\text{ MHz}$). Positive-voltage prototypes have already been tested and found to meet the noise and stability requirements.

The Wiener MARATON (MAgnetic field and RAdiation TOleraNt) power supplies will be used. These are low-noise and low-ripple modular systems, and are already used in the present LHCb tracking detectors. The MARATON power boxes are mounted in 19-inch power bins located in the LHCb cavern in the concrete bunker below the tracking

system. This avoids high cable losses that would result from high current consumption in the FE electronics combined with the long distance between the experiment cavern and the counting room.

The power boxes are connected to rectifier modules (385 V DC) and controller boards located behind the wall separating the experimental area from the counting house (UX AB). Each power box has 12 channels (six power modules with two channels each); the power distribution scheme will be analogous to that presently used in the Outer Tracker [90] and it is illustrated schematically in Fig. 3.55. Each LV channel (300 W, 8 V \times 50 A) is routed with 35 mm² cables through a movable cable duct to the C-Frames, where it is distributed to various ROBs via a dedicated LV distribution box. The distribution system will be scaled to accommodate additional MARATON power supplies.

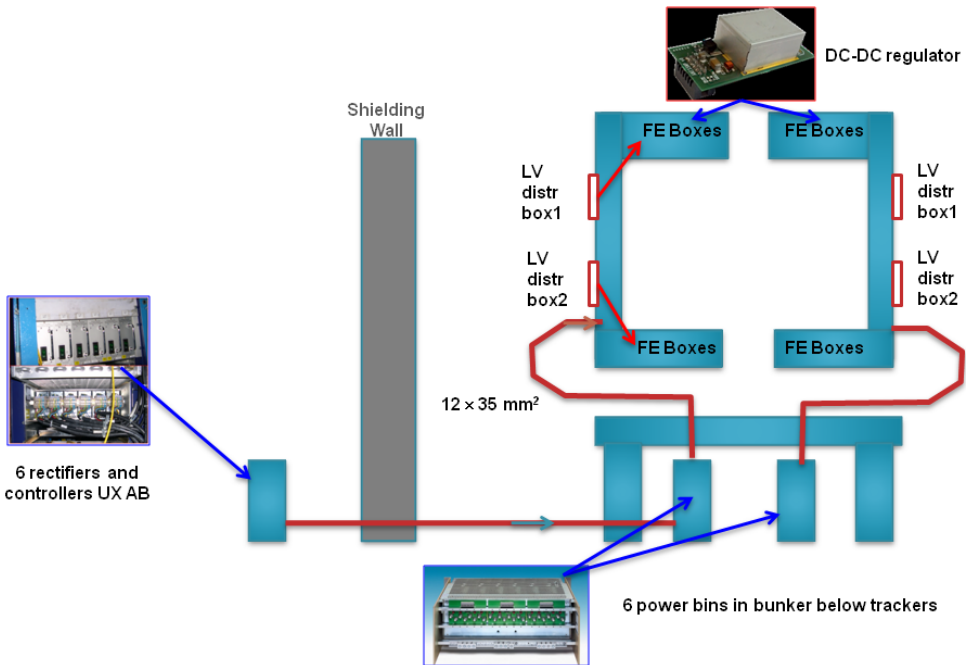


Figure 3.55: Low Voltage distribution in the Outer Tracker, from the power boxes in the concrete bunker to the ROB, through cable trays and specially designed distribution boxes in the C-Frames.

3.7.6 Slow and Fast Control

Each FE Board also has a complete interface for the distribution of Timing and Fast Control (TFC) signals, and signals from and to the Experiment Control System (ECS). Its design follows the specifications in Ref. [79]. Its implementation is based on the usage of a radiation-hard bi-directional optical link to transmit and receive timing, trigger and experiment control information, developed in the framework of the GBT project [77].

3.7.6.1 TFC

The necessary control, trigger and reset commands can be encoded from the 24 TFC bits [79]. This information will be received through the GBT Master.

3.7.6.2 ECS

A dedicated Slow Control Adaptor (SCA) chip [80] will be used for the slow control and monitoring of the FE electronics. The GBT-SCA system implements a point-to-multi-point connection between one GBT, henceforth called Master GBT, and several front end ASICs through dedicated 80 Mbps bidirectional ports. It is capable of handling 16 I²C busses, one JTAG controller port, an ADC to monitor up to eight external analogue signals, *etc.* Thus, it will be sufficient for each of the FE boards in Fig. 3.48 to host one GBT-SCA chip. In addition, a GBT-SCA chip next to the Master GBT will ensure the control of the Concentrator FPGAs, the optical links, the DC-DC regulators and, eventually, the GBTx data transmitters.

3.8 Infrastructure

3.8.1 Support Structures and Module Frames

The Scintillating Fibre Tracker will be installed in the volume occupied by the present downstream tracking system. It will have a similar geometrical layout with three tracking stations (T1-T3) each consisting of four detection planes (X,U,V,X).

The mechanical infrastructure necessary to support the Scintillating Fibre Tracker will be similar to the existing one. At present, the Inner and Outer Tracker detector modules are attached to C-Frames [92] with each C-Frame holding two half detection planes (XU or VX). Each tracking station consists of six C-Frames, three on either side of the beam-pipe: IT, OT-XU and OT-VX. These C-Frames are attached at the top to a stainless steel support structure called the “bridge” [93] and at the bottom to an aluminium structure called the “table” [94], in such a way that they can slide along the *x*-direction, and can be retracted away from the beam-pipe during maintenance periods. These movements are made possible by the nine rails, shown in Fig. 3.56, to which the C-Frames are attached by adjustable rail rollers. The Bridge and the Table are compatible with the Scintillating Fibre Tracker layout illustrated in Sec. 3.3 and thus can largely be re-used as they are with minor modifications that can be carried out *in situ*. Twelve C-Frames, six on each side of the beam-pipe, will support the scintillating fibre modules. These may use six of the existing rails, as shown in Table 3.15, which would allow a *z*-envelope 340 mm for each half station.

In principle, the aluminium C-Frames of the Outer Tracker shown in Fig. 3.57 could be re-used. However, the different geometry of the scintillating fibre modules (see Sec. 3.6) implies significant modifications: the dowel-pin holes would have to be accurately re-drilled and the layout of the read-out box region modified. These modifications would introduce a

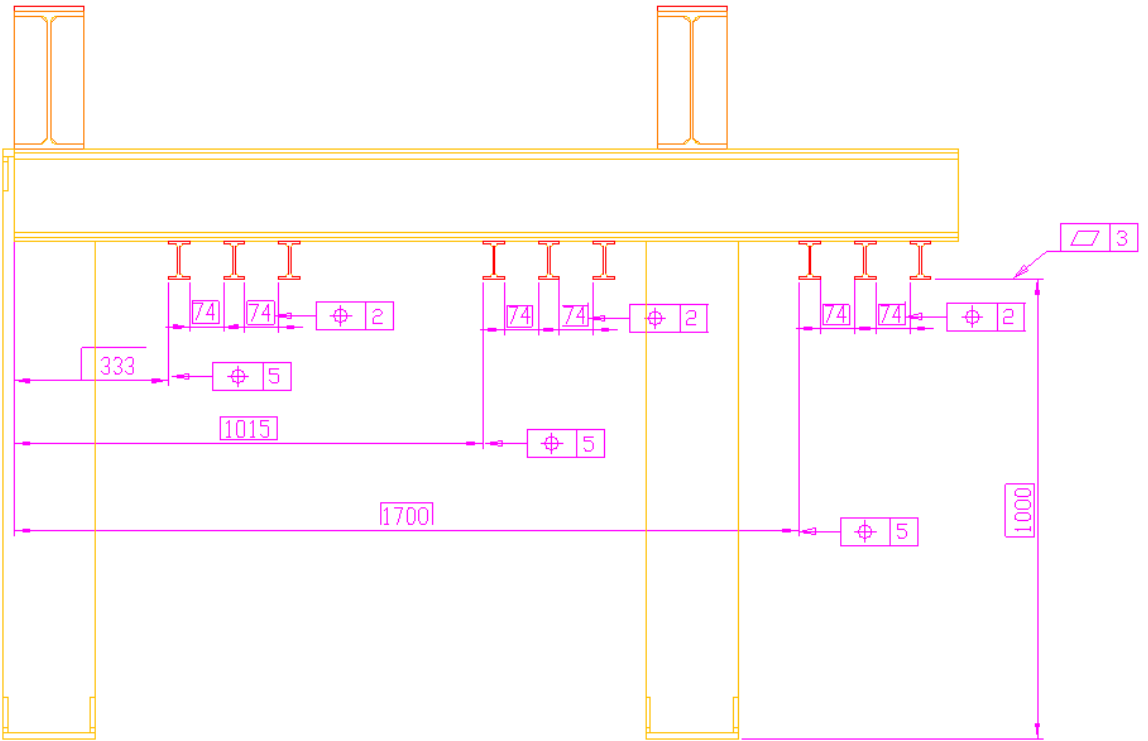


Figure 3.56: Side view of the IPE 20 i-beams attached to the Bridge, that function as rails along which the C-Frames slide with rail rollers.

further intermediate step in the installation procedure and are thus not desirable. Therefore, it was decided that new C-Frames will be produced and pre-assembled for installation, as was done for the present tracker.

3.8.2 Cooling

3.8.2.1 SiPM Cooling Infrastructure

The mechanical design of the SiPM cooling system should match the modular design of the SciFi Tracker. The system must be safe for the detectors in case of a failure, environmentally friendly and resistant to the mild radiation environment (<100 Gy, Sec. 3.2.3) at the level of the SiPM read-out. No particular constraints are imposed on the material budget at that level. The requirements on the temperature uniformity of the SiPM arrays are relatively weak (Sec. 3.5.3), while the required temperature stability of $\pm 0.5^\circ\text{C}$ is largely ensured by the constant ambient conditions in the LHCb cavern and the mostly passive nature of the heat load.

These and other design considerations, described in more detail in Ref. [95], led to the choice of a mono-phase liquid cooling technology, with a serial connection of ROBs in the cooling branches. The fluoroketone fluid 3MTM NovecTM649 [96] is the baseline option for

Table 3.15: Nominal positions of the Scintillating Fibre Tracker stations.

Half Station	C-Frames	Z position (mm)
T1-XU	T1-Q02-XU & T1-Q13-XU	7768
T1-VX	T1-Q02-VX & T1-Q13-VX	8008
T2-XU	T2-Q02-XU & T2-Q13-XU	8450
T2-VX	T2-Q02-VX & T2-Q13-VX	8690
T3-XU	T3-Q02-XU & T3-Q13-XU	9135
T3-VX	T3-Q02-VX & T3-Q13-VX	9375

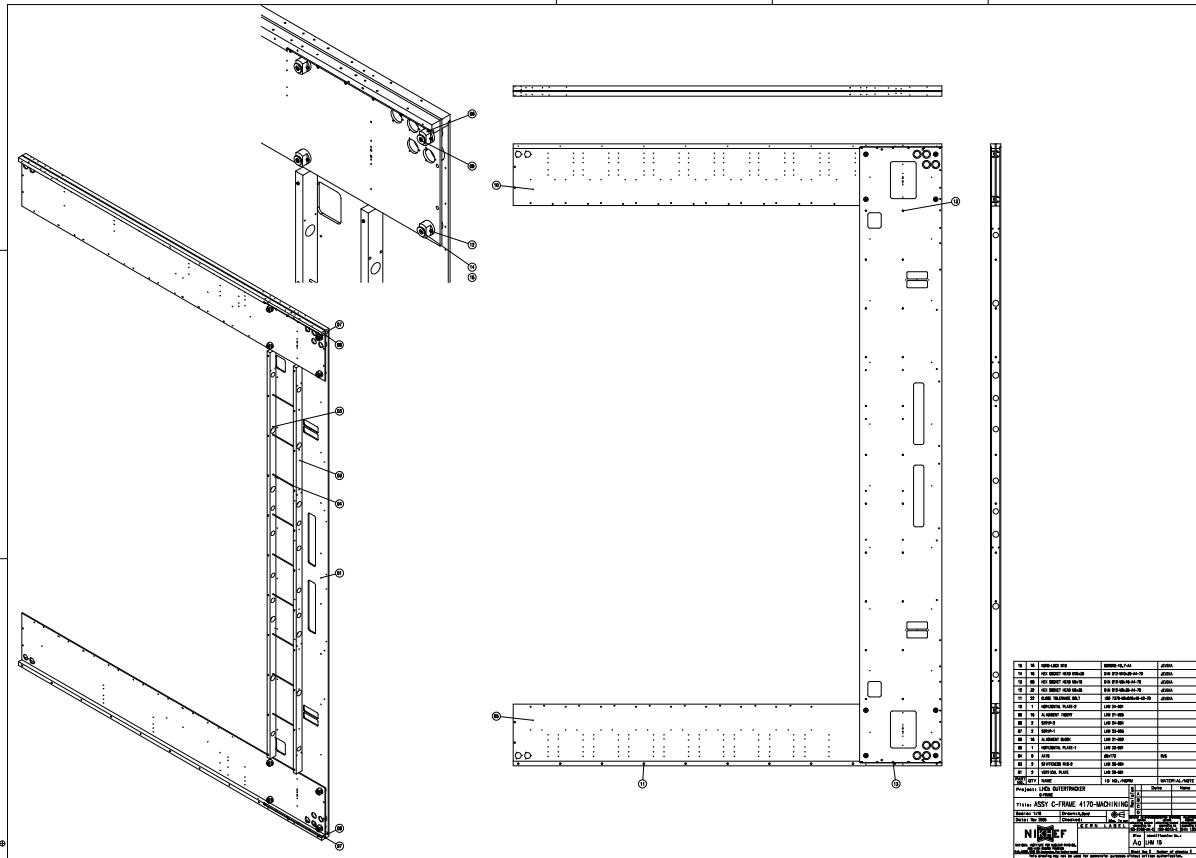


Figure 3.57: Design of the aluminium C-Frames supporting the Outer Tracker modules.

the coolant. This fluid has thermo-physical properties similar to perfluorohexane C_6F_{14} , widely used in detector cooling systems at the LHC (including four LHCb sub-systems). Like C_6F_{14} , it is non-flammable, non-irritating, dielectric, volatile and practically non-toxic. But in contrast with C_6F_{14} , which is a potent greenhouse gas (with the Global Warming Potential of 7400), Novec 649 has the GWP of about 1.⁴² Its stability under neutron and ionising radiation still remains to be tested. However, there are no *a priori* reasons for it to be different in that respect from C_6F_{14} . Because of the very similar density and viscosity properties of Novec 649 and C_6F_{14} , the latter remains the backup solution for the coolant.

The layout of the SiPM cooling system is described in Ref. [95] and is schematically shown in Fig. 3.58. It consists of the cooling plant located behind the LHCb shielding wall, the ≈ 100 m long foam- or vacuum-insulated transfer lines running through the shielding wall, and the detector cooling circuit distributing the coolant over the 48 local branches operated in parallel, each branch serving six consecutive ROBs in a quarter of one layer. The main design parameters and specifications are summarised in Table 3.16.

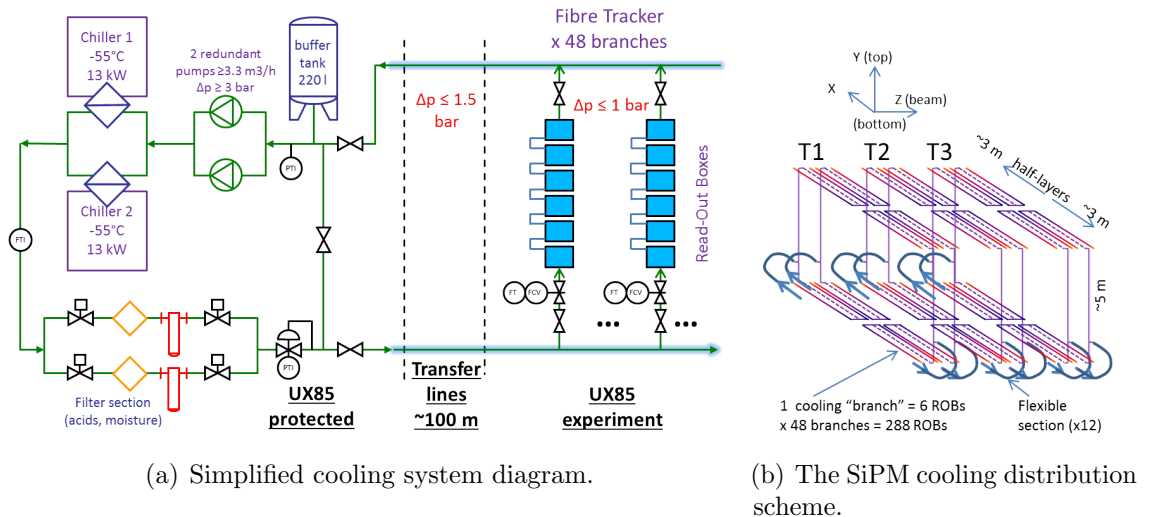


Figure 3.58: The SiPM cooling system.

The core of the cooling plant is an industrial chiller which will provide the required temperature stability and the absolute coolant temperature down to -55°C . At the minimal working SiPM temperature of -40°C in a cooling branch, the design coolant temperature drops (ΔT) are below 1K in the transfer line (assuming a pick-up of 12 W/m), less than 1K in the connection lines at the detector, and 3.6K over the branch (in the worst case scenario of 20 W heat load per ROB, see Sec. 3.6.5.3).

The system is sealed and runs at an over-pressure to simplify the overall design and ensure a favourable regime for the pump. The design pressure drop over the transfer and

⁴² The extremely short atmospheric lifetime of Novec 649 is due to the photolysis under UV occurring via rupture of the ketone group. This effect is excluded in the sealed cooling system.

Table 3.16: Preliminary design specification for the SiPM cooling system.

SiPM temperature range	$-40^{\circ}\text{C} \dots +40^{\circ}\text{C}$
Heat load per ROB	10–20 W at -40°C
Pump capacity	$\Delta p \geq 3 \text{ bar}; \geq 3.3 \text{ m}^3/\text{h}$
Chiller power	$\geq 13 \text{ kW}$ at -55°C
Temperature accuracy	$\pm 0.1\text{K}$
Total coolant mass/volume	min. 330 kg/213 l (Novec 649 at 40°C)
Transfer lines	DN32, $\approx 100+100 \text{ m}$; $\Delta T < (1\text{K} + 1\text{K})$
Heat pick-up in pipes	transfer: $\leq 2.4 \text{ kW}$; distribution: $\leq 2.5 \text{ kW}$
Manifolding scheme	1(transfer):12(flex):2(up-down):2(x-u/v)

distribution lines is below 1.5 bar, and around 1 bar over the cooling branches.

The filter group provides a continuous removal of the coolant decomposition products (notably, acids) and moisture from the cooling loop. The probability of moisture penetrating into the sealed system under normal operating conditions is low. However, trapping any moisture is particularly important for Novec 649 which is reactive with liquid water, forming perfluoropropionic acid by hydrolysis.

The principal components of the cooling plant (the chiller, the pump and the filter group) are duplicated.

All cooling branches have the same structure, with two manual valves permitting to isolate an individual branch, a manual flow regulation valve to equalise the coolant flow rates through all branches and a flow rate monitoring device (e.g., a differential pressure gauge on the flow valve). The ROBs in a branch are connected in series, in order to minimise the length of insulated connections and reduce six-fold the coolant flow rate, while keeping its ΔT over the branch at an acceptable level.

Given the layout of the cooling pipe inside the ROB described in Sec 3.6.5.3, the design heat transfer coefficient of $\approx 1000 \text{ W m}^{-2} \text{ K}^{-1}$ at the fluid velocity of 1.5 m/s will provide the coolant-to-wall ΔT of $\approx 3\text{K}$. The ΔT between the cooling pipe and the silicon die should not exceed 3K. Thus, at the chiller setting of -50°C , most of the SiPMs will be running at $< -40^{\circ}\text{C}$, except the ones at the extremities of the SciFi Tracker layers, where the temperature might be a degree or so higher, which is tolerable.

The cooling distribution lines on the SciFi Tracker (Fig. 3.58b) include 12 flexible two-way segments connecting the feed and return transfer lines to pairs of adjacent half-layers, as well as rigid segments conveying the coolant to the beginning of every branch (at $x = 0$) or returning the used coolant to the flexible return segments. The estimated heat pick-up in the pipelines represents a sizeable fraction of the overall system heat load, up to 7 kW, depending on the line parameters (pipe sizes, insulation, layout). The chiller is required to have the cooling power of 13 kW at about -55°C , to cope with the line losses and provide a sufficient performance margin for the SiPM cooling.

The SiPM cooling system will also include a dedicated air drying and conditioning station to provide the considerable amount of flushing gas ($\geq 30 \text{ m}^3/\text{h}$) required for the entire SciFi Tracker.

3.8.2.2 Cooling of Electronics

For the cooling of the FE electronics, the scheme presently used by the Outer Tracker, based on demineralised water at 19°C , will be adopted. Preliminary thermal simulation studies of the FE layout presented in Sec. 3.7.1 are shown in Fig. 3.59. The temperature can be limited to a maximum of 50°C at the location of the PACIFIC chips when water cooling is applied. A detailed estimate of the power budget that needs to be cooled is required in order to determine whether the capacity of the present cooling plant to dissipate 23 kW [97, 98] will be sufficient for the needs of the SciFi Tracker FE electronics. A worst-case scenario estimate, assuming low DC-DC conversion efficiency and largest number of components in the final design, gives a total value of about 30 kW , and indicates that a re-design of the demineralised-water cooling plant may become necessary.

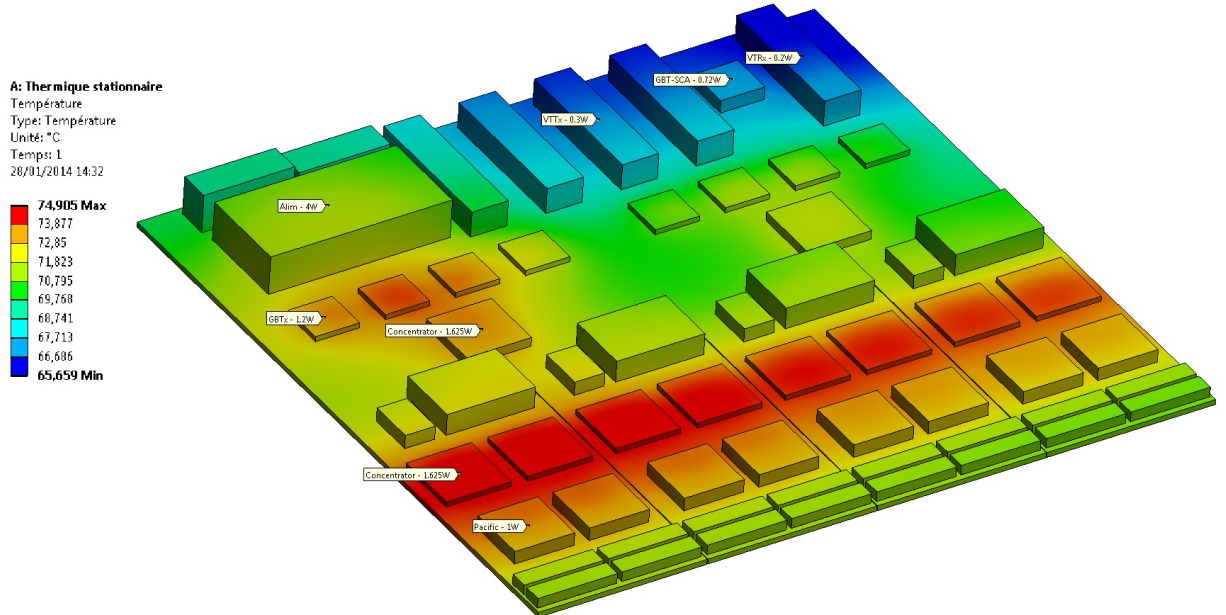


Figure 3.59: Thermal simulation of the FE board (without specific cooling) with the PACIFIC ASIC dissipating 1 W.

3.9 Simulation Results

This section is split into two main parts: the material description in the simulation is described in Sec. 3.9.1; and the digitisation which simulates the electronics response is described in Sec. 3.9.2. The tracking performances are reported in Chap. 4. To evaluate the robustness of the Tracker, a large set of physics channels were generated under various conditions. As these simulations are very time consuming, some of the properties described in the simulation are not identical to the current understanding derived from the latest detector development studies. Nonetheless, whenever possible, additional studies were conducted to ensure the simulation studies consider as much as possible the current design. The detector geometry is described in Ref. [99], and the digitisation is described in Ref. [100].

3.9.1 Material Description

The detector geometry in the simulation was described in Sec. 3.3. The physical properties of the material used in the geometry description and the implementation of the geometry in the software is described in Ref. [99]. The total mass of the SciFi Tracker was calculated to be 1166.4 kg. The geometry does not completely describe the detector design but provides the best estimate of the material at the time the simulation for performance studies was made.

The nuclear interaction length (λ_{int}) and the radiation length (X_0) are two parameters used to characterise the energy loss of hadrons, electrons and photons while traversing the detector material. The calculation of the radiation length is based on Ref. [101]. The value of the nuclear interaction length was calculated to be $\lambda_{int} = 1585$ cm and the radiation length is $X_0 = 796$ cm.

The total material seen by particles which pass through the current T1 station (z from 767.3 cm to 803.8 cm) is shown in Fig. 3.60 (top). The average material traversed is 4.0% of a radiation length (X_0). The material seen by particles passing through the upgraded T1 station is shown in Fig. 3.60 (bottom). The total material traversed is estimated to be 2.6% X_0 .

The fraction of particles that survive the passage through the SciFi Tracker has also been calculated. The calculation was made for particles passing along the z -axis perpendicular to the fibres. The fraction was found to be 96.9% for hadrons, 93.9% for electrons and 95.2% for photons.

3.9.2 Digitisation

The aim of the digitisation is to simulate the detector and electronic response taking into account radiation and ageing effects. The following effects are simulated using the constraints from the hardware side:

- Light yield of the fibres in term of photons.

- Attenuation of the light in fibre after irradiation, and the reflection at one end of the fibre.
- The geometric coupling of the fibres to the SiPM channels.
- Gain of the SiPMs in term of photoelectrons and its conversion in ADC counts.
- The thermal noise, and the noise from after pulses and spillover.
- The clustering algorithm as implemented in the front-end electronics.
- The encoding and decoding of the data format (banks) from the TELL40.

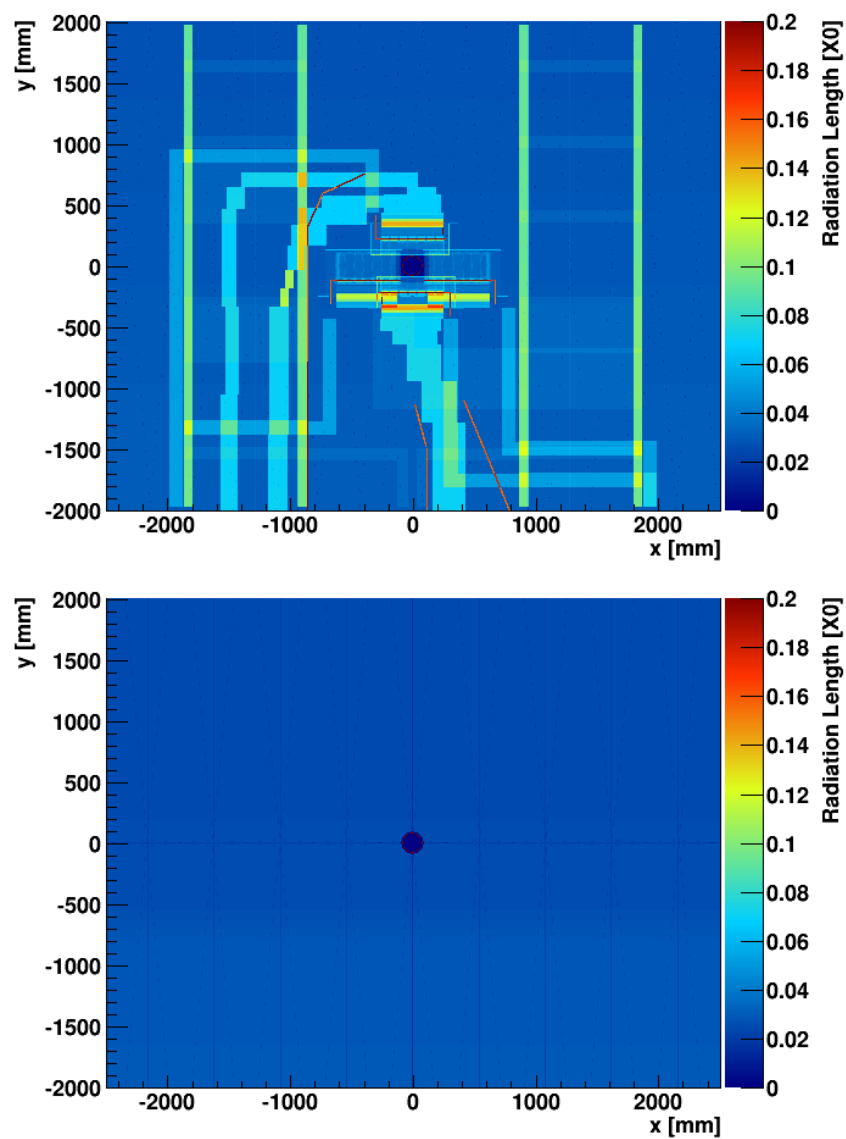


Figure 3.60: Distribution of material in T1 for the current (top) and upgraded (bottom) detector.

3.9.2.1 Description of the Light in the Fibres and SiPM Response

The individual fibres are not described in the geometry description. The smallest elements are the fibre mats. For this reason, a GEANT4 simulation was used to generate the entry and the exit points of particles in the fibre mats. The GEANT4 hits are the input to the digitisation. The attenuation factor of the light generated in the fibres is given by

$$a(l) = F_S e^{-(\frac{l}{\lambda_{short}})} + (1 - F_S) e^{-(\frac{l}{\lambda_{long}})} \quad (3.4)$$

where l defines the path length through the fibre, λ_{short} and λ_{long} are the attenuation length of the short and the long components, and F_S is the contribution of the short attenuation. A mirror at $y = 0$ of the fibres reflects the light back to the SiPMs, with a reflection coefficient C_R . In the current simulation the values for λ_{short} , λ_{long} , F_S and C_R are: 200 mm, 4700 mm, 0.18 and 0.7 respectively. The effect of the irradiation of the fibres is also simulated. The attenuation length of the fibres decreases as a function of the irradiation dose. The closer the fibre is to the beam-pipe, the more radiation it receives, leading to a negative gradient of the attenuation length towards the beam-pipe. In the worst case scenario, *i.e.* after collecting 50 fb^{-1} of data, the most irradiated region has a diamond shape in which the attenuation factor in one quadrant is represented in Fig. 3.61. The attenuation maps of the direct and reflected signals are shown in Fig. 3.62 as a function of the hit coordinates.

In the LHCb simulation, the energy deposited in each channel is converted into photoelectrons. Assuming that the SiPM detects 25 photoelectrons per MIP, the number of photoelectrons per MeV is set to 120. The number of photoelectrons is then converted

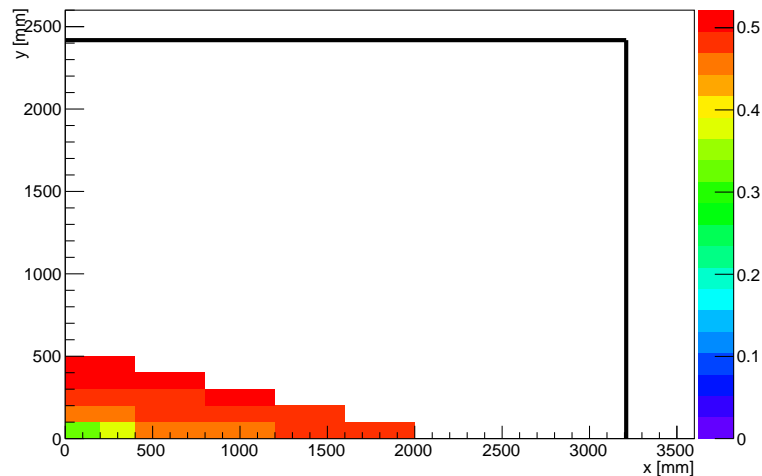


Figure 3.61: Correction factor obtained from the gradient of attenuation length associated to the fibre irradiation damage after 50 fb^{-1} of collected data. Black lines represent the edges of the layer.

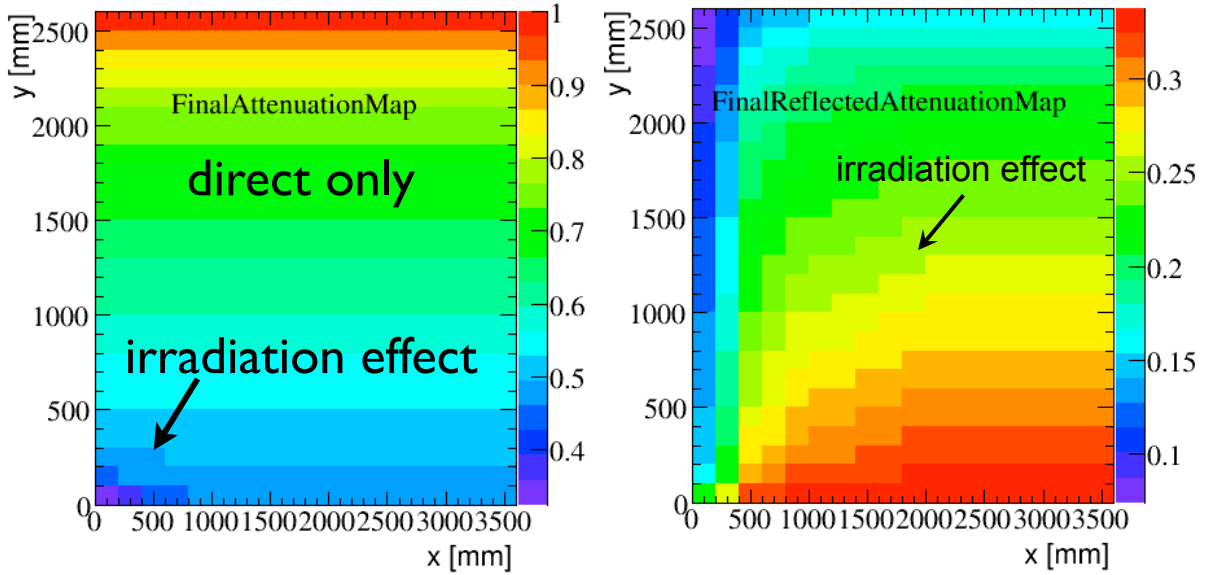


Figure 3.62: Correction factor applied to the hit energy as a function of the hit position in one quarter of a fibre layer. The plot on the left shows the effect of the scintillating fibre attenuation length on signal reaching directly the SiPM whereas the plot on the right gives the correction factor applied on the signal reflected by the fibre mirrors. Both figures include the fibre irradiation damage after 50 fb^{-1} of collected data.

into a 6-bit ADC number.⁴³

3.9.2.2 Time Description

The time of arrival of the photons at the SiPM is composed of

$$t_{\text{SiPM}} = t_{\text{spill}} + t_{\text{flight}} + t_{\text{scint}} + t_{\text{prop}}, \quad (3.5)$$

where t_{spill} is the time of the bunch crossing (-50 ns , -25 ns , 0 ns , 25 ns or 50 ns in the current simulation), t_{flight} is the time of flight of the particle from the pp interaction to the detection plane, t_{scint} is the decay time of the scintillation, and t_{prop} is the propagation time of the photons through the fibre. The intensity of the scintillation light follows an exponential decay law upon the passage of the particle. To determine t_{scint} , a random number is drawn from an exponential decay function with a decay time of 2.8 ns . To determine t_{prop} , the propagation time of the light is assumed to be 6.0 ns/m and the distance from the hit to the SiPM is used. For the reflected photons, the propagation time is always longer because the photons travel first to the mirror-end before travelling the full length of the fibre.

⁴³It was recently decided to replace the 6-bit ADC by the set of three comparators with 2-bit output described in Sec. 3.7.2. This will lead to a small loss in the resolution of the cluster position though the resolution will still be well within the required value (see Sec. 3.5.8, Table 3.6). The simulation will be updated to use the new digitisation scheme.

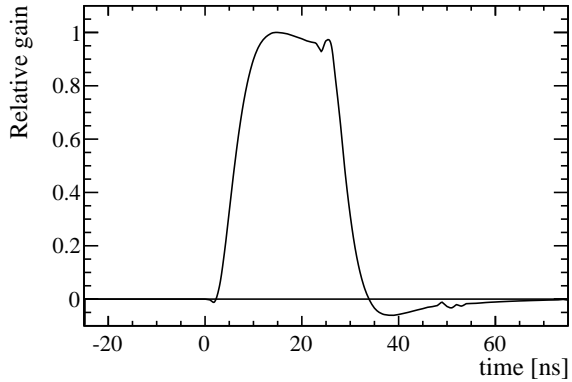


Figure 3.63: The time response function of the electronics on a single pulse. The arrival time of the pulse at the SiPM is arbitrary.

3.9.2.3 Simulation of the Spillover, Thermal Noise and After-pulse

Four types of noise can be distinguished:

Spillover is charge associated with real hits from previous or next bunch crossings that spill into the current integration window. The size of the electronic signal that is recorded after the shaper, integrator and ADC conversion on the front-end boards, depends on the time of arrival of the scintillation light at the SiPM. The sampling time of the integrator is chosen to get the largest signal gain for most of the particles. The reflected signal and the signals from previous bunch crossings will arrive at different times, resulting in lower gains for these contributions. The single pulse response function used in the simulation is shown in Fig. 3.63.

Cross-talk are additional photoelectrons released in neighbouring pixels due to UV radiation coming from an avalanche in the current pixel. The cross-talk is a charge enlargement of single photoelectrons, since most of the time the neighbouring pixels belong to the same read-out channel. Therefore, cross-talk is not considered as an independent source of noise, but rather added to dark noise and after-pulse noise to (statistically) increase the channel charge at the end.

Thermal noise depends on the temperature and irradiation of the SiPMs. The thermal noise rate per channel at $T = 20^\circ\text{C}$ increases from 100 kHz at 0 fb^{-1} to 250 MHz at 50 fb^{-1} . The noise rate increases by a factor of two for every 10°C . These numbers are obtained from *in situ* irradiation studies of the SiPMs [102].

After-pulses are due to charge carriers being trapped in the SiPM, and released after some time (mostly in following events). Since the after-pulses in the current event can come from many bunch crossings before, it is practically impossible to fully simulate all

these spillover events. Instead, the occupancy profile is taken from a fit to the channel hit occupancy. The after-pulse probability depends on the time after the original hit, and follows a double exponential with decay constants of 25 ns and 100 ns with equal probabilities. Furthermore, the intensity of the pulse depends on the recovery time of the pixel, resulting in a turn-on.

3.9.3 Simulation of the Electronics

The zero-suppression and clustering is already done on the front-end FPGAs before the data is sent to the TELL40 read-out boards. For this reason, the clustering algorithm needs to be emulated in the LHCb simulation. The simulated data is converted into a data format of 16-bit words that are sent to the TELL40.

3.9.4 Data Format

The data are optically sent from the front-end electronics to TELL40 read-out boards through GBT cards [77] whose transfer rate is limited to 4.8 Gb/s. The encoding of the clusters in the corresponding data format is emulated in the LHCb simulation. The decoding of the clusters was also implemented to be able to read the raw data for the track reconstruction.

The data format consists of an 8-bit bunch crossing ID (BCID), four bits for the number of clusters in the SiPM, and four bits for additional information. This means that the number of clusters in a 128 channel SiPM is limited to sixteen. After the header, the information encoded in the clusters is as follows: each cluster consists of 16 bits, of which three bits are for the cluster charge, two bits for the cluster size, two bits to identify the SiPM, seven bits for the channel number, and two bits for the fractional part.

3.9.5 Conclusion

In this chapter, the geometry of the Scintillating Fibre Tracker together with details of the proposed technology choices were presented. The main digitisation effects of the fibre detector are described in the simulation for the LHCb upgrade. This comprises the attenuation of the fibres after irradiation, the geometry of the fibres with respect to the SiPM channels, the gain of the SiPMs, the thermal noise, the noise from after-pulses and spillover, and the clustering. The simulation describes the expected performance of the detector after an integrated luminosity of 50 fb^{-1} . The performance of the pattern recognition algorithms can be found Chap. 4.

3.10 Project Organisation

3.10.1 Tasks

The institutes participating in the Scintillating Fibre Tracker project are listed in Table 3.17, and the division of responsibilities between the different institutes are listed in Table 3.18. The responsibility for the development of software is included in each sub-task. The development of the reconstruction software for the upgraded tracking system is handled by the LHCb Tracking and Alignment group to which the SciFi Tracker group contributes.

Table 3.17: List of institutes participating in the Scintillating Fibre Tracker project.

Country	Institute
Brazil (BR)	Centro Brasileiro de Pesquisas Físicas (CBPF)
China (CN)	Center for High Energy Physics, Tsinghua University, Beijing
France (FR)	Laboratoire de Physique Corpusculaire, Clermont-Ferrand (LPC) Laboratoire de l'Accélérateur Linéaire, Orsay (LAL) Laboratoire de Physique Nucléaire et de Hautes Energies, Paris (LPNHE)
Germany (DE)	RWTH Aachen Technische Universität Dortmund (TUD) Ruprecht-Karls-Universität Heidelberg (HD) Universität Rostock (RO)
The Netherlands (NL)	NIKHEF
Poland (PL)	National Center for Nuclear Research, Warsaw (NCBJ)
Russia (RU)	Petersburg Nuclear Physics Institute (PNPI) Institute of Theoretical and Experimental Physics (ITEP) Institute for Nuclear Research (INR) National Research Center Kurchatov Institute (NRC KI) Institute for High Energy Physics (IHEP)
Spain (ES)	Universitat de Barcelona (UB) Universitat de Valencia-CSIC (IFC)
Switzerland (CH)	CERN Ecole Polytechnique Fédérale de Lausanne (EPFL)
United Kingdom (UK)	Imperial College London (ICL)

Table 3.18 indicates where the institutes intend to contribute to the project as known at the time of this TDR. The exact distribution of responsibilities will be finalised when the results of requests to different funding agencies are known.

3.10.2 Schedule

A summary of the schedule for the upgrade of the tracker is shown in Fig. 3.64. The schedule covers the period from the publication of this TDR up to the start of data taking in 2020. The schedule includes the remaining R&D work, and the construction of the detector modules. It also covers the LHC Long Shutdown 2 (LS2) period between the

Table 3.18: Division of responsibilities between the participating institutes.

Task(s)		Institute(s)
Detector	SiPM assembly	EPFL
	SiPM QA	CERN, EPFL, NCBJ
	Fibre QA	CERN, NCBJ, RWTH, TUD, HD
	Fibre mat production	Russia, RWTH, TUD, HD
	Panel & module construction	Russia, RWTH, TUD, HD
	Read-out box	CERN, EPFL, LPC, NIKHEF, RWTH
Module testing (including electronics)		CBPF, NIKHEF
Electronics	PACIFIC ASIC	UB, IFC, LPC, NIKHEF, HD
	Front-end boards	EPFL, LPC, NIKHEF, RWTH, HD
	Tell40 board software	LPNHE, TUD
Infrastructure	Frames	CERN, EPFL, NIKHEF
	Cooling	CERN, RWTH
General	Installation	All institutes
	Non-read-out electronics, DAQ, ECS	All institutes
	Integration	All institutes
	Commissioning	All institutes
	Software	All institutes

middle of 2018 and the end of 2019 when the current tracker will be removed, and the SciFi Tracker will be installed.

3.10.2.1 Future R&D and Milestones

There will be further R&D work in the following areas:

Scintillating fibres: The qualification of fibres from Saint-Gobain will continue with new samples expected in April 2014. The irradiation tests will be repeated using larger components. The effects of annealing and dose rate will be studied to try to understand the differences in the current measurements. An EDR of the fibres will take place in Q3 2014.

Silicon photo-detector: New multi-channel SiPMs with trenches will be available from April 2014. The previous measurements on radiation hardness will be repeated. An EDR for the SiPMs is planned for Q3 2014. The procurement and Quality Assurance (QA) of the SiPMs will take place in 2015 and 2016.

Module-0: A full prototype module will be built and tested in 2014. This module will use all final components except for the read-out electronics. The design of the interface between the fibre panels and optical interface will be frozen by Q4 2014.

Electronics: The design and testing of the front-end electronics will continue until Q2 2016. First laboratory tests with the PACIFIC read-out are planned for Q3 2014.

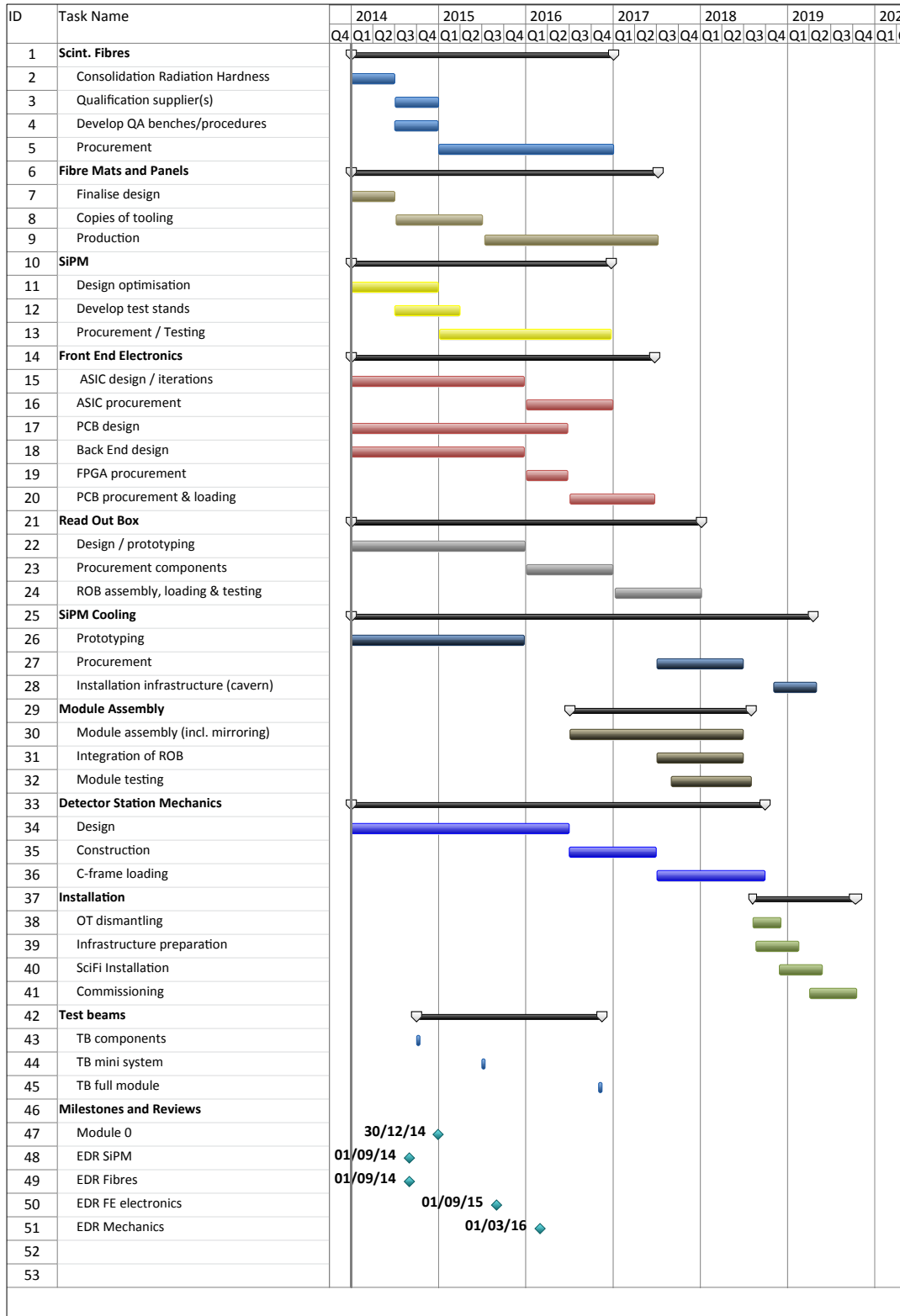


Figure 3.64: Schedule for the design, construction and installation of the SciFi Tracker.

An electronics EDR is planned for Q3 2015. The final production of the PACIFIC chip will take place in 2016.

Read-out Box: The design and prototyping of the Read-out Box will continue until the end of 2015. The design of this box also includes the R&D required for the light injection system, SiPM cooling, and the cooling of the front-end electronics.

Engineering Design: A full design of the station mechanics is expected by Q3 2016. An EDR of the mechanics will take place in Q1 2016.

A series of beam tests are planned to study the prototype electronics and detector modules. A mini-system test with beam will be made in Q1 2016.

3.10.2.2 Construction

The procurement of the scintillating fibres will take place in 2015 and 2016. The design of the fibre mats will be finalised by Q3 2014 and the tooling required will be made by Q3 2015. The final production of the fibre mats will commence in Q3 2015 and will run until the end of Q2 2017. The detector module assembly will start in Q2 2016, and the first modules will be loaded onto the C-frames in Q3 2017.

3.10.2.3 Installation and Commissioning

The beam-pipe and the current tracker will be removed in Q3 2018. The infrastructure will be prepared and the loaded C-frames will be installed from Q4 2018 to Q3 2019. The connection of all services and commissioning of the full system will start in Q2 2019. The detector will be available for commissioning tests with the other LHCb sub-detectors from the end of Q3 2019.

3.10.3 Costs

The costs of the Scintillating Fibre Tracker are listed in Table 3.19. The cost quoted is for a full fibre tracker and is split into three sections: detector, electronics and infrastructure. The estimates of the cost are based on current knowledge and include where possible quotes from industry. The costs include risk estimates, and 10% or 15% spares depending on the item. The total cost of the project is estimated to be 15.2 MCHF.

3.10.4 Operational Scenarios

The operation of the SciFi Tracker requires neither the circulation of detector gas nor the application of high voltage. Therefore, it is expected to be stable and robust, provided that the cooling system is able to maintain the SiPMs at the required temperature without condensation or frost formation.

Track reconstruction studies, based on test beam and cosmic ray data, show that the detector is fairly insensitive against the loss of single SiPM channels. In the unlikely event

Table 3.19: Cost of the SciFi Tracker, including risk estimates and spares.

Component		Cost (kCHF)
Detector	SiPMs (including packaging)	2600
	Fibre mats	2610
	Modules	2160
	Tooling	710
Sub-total		8080
Electronics	PACIFIC ASIC	1160
	Front-end boards	2510
	Tell40 boards	1440
	General Electronics	530
Sub-total		5640
Infrastructure	Mechanics	780
	Cooling	670
Sub-total		1450
Total		15170

that a complete SiPM array is lost, *e.g.* due to a faulty bias connection, this will create a dead region with a width of 3.2 cm in the acceptance, and could lead to a slight reduction in the track reconstruction efficiency. The replacement of an SiPM array, or rather a group of four SiPM arrays, is an intervention which can only be performed during Technical Stops of the LHC.

Periodic calibration of the detector will be required to verify and, if needed, to re-adjust the individual channel levels of the 2-bit ADC (*cf.* Sec. 3.6.5.2). These calibrations can be made during Technical Stops or between fills if they are required more frequently.

The leakage currents of the SiPM detectors provide a good measurement of the radiation damage due to the neutron flux. The radiation damage in the fibres is very inhomogeneous. It may be possible to measure the damage from the data by analysing the hit efficiency. However, a set of online dosimeters and test fibres will give more detailed and precise information.

The SciFi Tracker is designed to guarantee a fully adequate performance during the full lifetime of the experiment. The radiation damage in the fibres will be highly concentrated on the innermost modules closest to the beam-pipe. The 24 modules in this region will have six fibre layers and hence provide 20% higher light yield. The replacement of these modules with spares after about half the lifetime of the experiment is envisaged in case the effects of radiation damage have a larger impact than initially expected.

3.10.5 Safety

The SciFi Tracker will follow the relevant CERN safety rules and regulations defined by SAPOCO/42 [33]. The detector makes use of technologies and components which have already been used in high energy physics detectors. No major risks to the environment or to personnel have so far been identified. However there are some area of concerns which will require special attention to mitigate the risk to personnel and the environment, in agreement with CERN rules and regulations:

- The scintillating fibres are made of polystyrene which is known to be highly flammable, and to produce dense and toxic smoke. It is likely that the fibres which are to be used will not comply with CERN safety instruction IS41 [103]. The total volume of polystyrene to be installed is estimated not to exceed 0.4 m^3 . The fibres will be encapsulated in supporting panels, reducing then the risk of direct contact with ignition sources. Special care and attention will be given to the flammability of the material of the supporting panels.
- The power distribution and electronic circuits will follow the most recent IEC or CENELEC standards and recommendations. Low voltage return currents over long distance cables will be monitored and automatic actions taken in case of shorts to the ground.
- The installation of the detector is not expected to present special risks beyond those related to handling of long and heavy objects, and working at height.
- The risks associated to operation and maintenance arise from access difficulties and ionising radiation. The mechanical design of the detector shall take into account the need for safe and easy access to the detector components, to mitigate the risk of fall, and minimise the exposure of the personnel to ionising radiation. Further studies will be performed to assess the dose to the personnel during the various phases of the project.
- The SciFi Tracker is a light weight detector and it is not expected to contribute significantly to the total amount of radioactive waste produced during the LHCb upgrade. Further studies will be performed to assess the amount of radioactive waste produced.
- It is well known that fluorocarbons used in detector cooling contribute significantly to the carbon footprint of CERN. The design of the cooling system will avoid as much as possible the use of fluids with high Greenhouse Warming Potential (GWP) and alternative solutions will be investigated. In case an alternative solution cannot be found, the loss of fluids with high GWP will be minimised.

Chapter 4

Tracking Performance

4.1 Overview of the Tracking System

The current LHCb tracking system (Fig. 1.1) consists of a silicon micro-strip detector (Vertex Locator, VELO) surrounding the interaction point which provides measurements of R and ϕ ; one station with four layers of silicon strip detectors in front of the magnet (Tracker Turicensis, TT) arranged in a (x, u, v, x) configuration with $\pm 5^\circ$ stereo angle; and three stations (T-stations) located after the magnet with four layers in each. The layers in each station follow the same pattern as the TT with $\pm 5^\circ$ stereo angle. Each of the twelve layers consists of silicon micro-strip detectors (Inner Tracker, IT) close to the beam-pipe, and a straw tube detector (Outer Tracker, OT) in the outer region [1].

The same basic configuration is kept for the upgraded LHCb tracking system (Fig. 1.2). However, the individual detectors will all be replaced. The upgraded VELO detector will be a silicon pixel detector [24]. The TT will be replaced by the Upstream Tracker (UT) which was described in Chap. 2 and the tracking detectors in the T-stations will be replaced by the SciFi Tracker described in Chap. 3.

4.1.1 Track Types

The reconstructed tracks are divided into types which depend on the sub-detectors in which they are reconstructed (Fig. 4.1). The most valuable tracks for physics analysis are so-called *long* tracks which are reconstructed in the VELO and the T-stations. They have excellent spatial resolution close to the primary interaction and a precise momentum information due to the combined information of the track slope before and after the magnet. Tracks consisting of measurements in the T-stations alone are known as *T* tracks. They are not used in physics analyses, but are used as inputs to reconstruct so-called *downstream* tracks. These are tracks which have measurements in the UT (TT) and the T-stations. They are important for the reconstruction of the daughters of long-lived particles such as K_s^0 mesons or Λ baryons which decay outside the VELO. Tracks consisting of measurements in the VELO and in the UT (TT) are called *upstream* tracks. A preliminary momentum estimate is already possible ($\Delta p/p \sim 15 - 25\%$) because of the fringe field in the UT (TT).

The *upstream* tracks can be used to reconstruct low momentum particles which are bent out of the magnet before they reach the T stations. In addition, they can be used as input to further algorithms searching for *long* tracks. The so-called *VELO* tracks consist of measurements in the *VELO* only. In the forward direction they serve mainly to feed subsequent tracking algorithms which upgrade them to either *upstream* or *long* tracks. The *VELO* tracks in the backward direction are important for the unbiased reconstruction of the position of the primary vertices and for measurements of central exclusive production.

All tracks, except *VELO* tracks, are also used as input for the reconstruction algorithms of the RICH detectors.

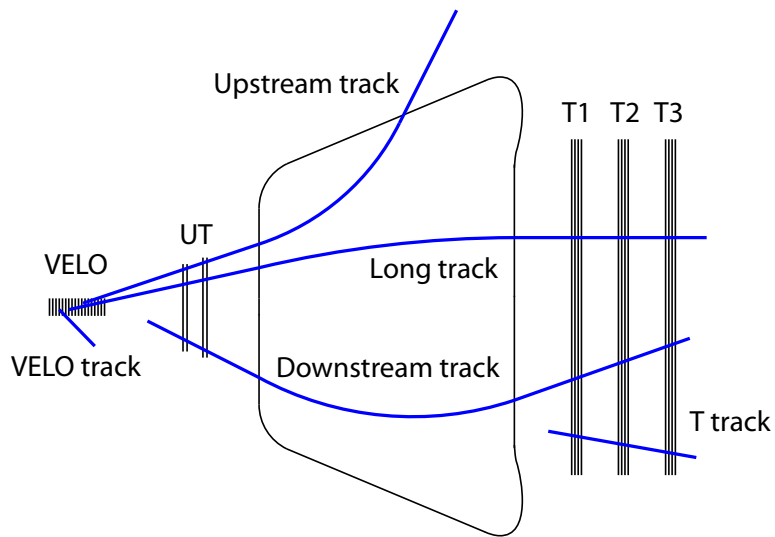


Figure 4.1: Reconstructed track types for the LHCb upgrade tracking system.

4.1.2 Figures of Merit to Evaluate Tracking Performance

The *Tracking* in the LHCb reconstruction sequence consists of two parts. The first is the pattern recognition, which combines individual measurements in the various tracking systems to form track candidates. The second part is to optimally determine the track parameters using a Kalman filter based fitting approach (called Kalman fit in the following). Various figures of merit for the pattern recognition and the track fit will be described in the following sub-sections, and then used to evaluate the tracking performance.

4.1.2.1 Efficiency

The reconstruction efficiency ε is measured using simulation by comparing the number of correctly reconstructed tracks with the number of tracks defined to be reconstructible. This is made possible by using truth information available in simulated samples. The definition of reconstructible depends on the pattern recognition algorithm which is evaluated (Table 4.1). The reconstruction efficiency is given by

$$\varepsilon = \frac{N(\text{reconstructed} \& \text{reconstructible} \& \text{!electrons})}{N(\text{reconstructible} \& \text{!electrons})}$$

where electrons are explicitly taken out of the definition as they are more challenging to reconstruct due to Bremsstrahlung. Additionally a cut of $2 < \eta < 5$ is applied for all reconstructible particles.

Table 4.1: Definition of reconstructible and reconstructed particles in the LHCb spectrometer.

Reconstructible in the VELO	Upgraded VELO: clusters are associated to a particle on three or more modules; Current VELO: three R and three ϕ sensors are required.
Reconstructible as T track	at least one x and one <i>stereo</i> cluster is associated to the particle in each T-station
Reconstructible as <i>long</i> track	reconstructible in the VELO & reconstructible as T track
Reconstructible in UT (TT)	At least one cluster is associated to a particle in each UT (TT) station
Reconstructible as <i>downstream</i> track	Reconstructible in the UT (TT) and as T track
Reconstructible as <i>upstream</i> track	Reconstructible in the VELO and in UT (TT)
Reconstructed (or associated)	At least 70% of the clusters on a track in each involved sub-detector are associated to the Monte Carlo particle

The efficiency definition is chosen such that only the pattern recognition part of the overall efficiency is evaluated. Particles passing through dead regions in several layers, or which are absorbed in the material, would not contribute to the set of reconstructible particles, and therefore have no impact on the quoted efficiency number.

4.1.2.2 Ghost Rate

A ghost track is a reconstructed track which cannot be associated to a Monte Carlo particle based on the definition given in Table 4.1. The ghost rate is the fraction of ghost tracks relative to all reconstructed tracks. It can be computed averaged by event or on a per track level. The second number gives more weight to high occupancy events and will result in a larger ghost rate. The numbers quoted in this section are track level ghost rates for reconstructed tracks in the nominal LHCb acceptance ($2 < \eta < 5$).

4.1.2.3 Clone Rate

If more than one track can be associated to the same Monte Carlo particle, only one of them is considered as properly reconstructed, while the others are counted as clones. The clone rate is the number of clone tracks relative to all reconstructed tracks. The fraction of clones for all studied pattern recognition algorithms is very low (0.1–1%). Therefore they are not listed explicitly for each algorithm.

4.1.2.4 Timing

The time taken to execute the pattern recognition in the tracking system does not dominate the time taken in the full offline LHCb reconstruction sequence. Therefore it is not a critical parameter when estimating the performance of the track reconstruction. It is, however, an essential parameter for the pattern recognition algorithms running in the trigger. The algorithms developed for the upgrade have so far, with one exception, only been tuned for operation offline. The Upstream tracking was explicitly tuned for use in trigger applications and will be described in Sec. 4.2.7. The offline time consumption is presented for all other algorithms, and the timing of each algorithm has been measured using the same machine to facilitate direct comparisons.¹

The algorithms used for the trigger and offline track reconstruction were almost identical during LHC Run 1 with only a few differences in the tuning of the selection parameters. For this reason, the relative time consumption of the algorithms used in the trigger is expected to scale in the same fashion as the time taken by the same algorithms offline. However, firm conclusions on the timing of the trigger can only be drawn after further studies which will be discussed in the upcoming LHCb Upgrade Trigger TDR.

4.1.2.5 Parameter Resolution

A precise vertex and good momentum resolution are the key ingredients for any analysis in the bottom and charm systems. The vertex resolution of a reconstructed track is mainly dominated by the first measurements in the VELO, while the momentum resolution is given by the precision of the slope in the VELO, the slope in the T-stations and, if available, by additional measurement points in the UT (TT) detector.

Details on the impact parameter and vertex resolution can be found in the LHCb VELO Upgrade TDR [24]. Only results on the momentum resolution will be reported in this TDR.

¹Single core 1.3 times speed of a 2.8 GHz Xeon. Depending on the machine, the timing can vary within 20%.

4.1.2.6 Data Samples

The default figures of merit have been evaluated using events simulated with the following running conditions:

- *Upgrade conditions*: Events with an average number of interactions per bunch crossing of $\nu = 3.8$ and $\nu = 7.6$ corresponding to instantaneous luminosities of $1 \times 10^{33} \text{ cm}^{-2}\text{s}^{-1}$ and $2 \times 10^{33} \text{ cm}^{-2}\text{s}^{-1}$, respectively, at a centre-of-mass energy of $\sqrt{s} = 14 \text{ TeV}$ and 25 ns bunch spacing (including spill-over).
- *Current (2011) conditions*: Events with an average number of interaction per bunch crossing of $\nu = 2$ at a centre-of-mass energy of $\sqrt{s} = 7 \text{ TeV}$ and no spill-over.

Samples of 50,000 $B_s \rightarrow \phi\phi$, $D^* \rightarrow D^0(\rightarrow K_s^0\pi\pi)\pi$ and minimum bias events have been simulated in these conditions. The simulation of the upgraded tracking system essentially describes the expected detector response after an integrated luminosity of 50 fb^{-1} . Unless otherwise stated the data sets are large enough that the statistical uncertainties on the quoted performance numbers are negligible. The absolute efficiencies to reconstruct B daughter tracks varies depending on the decay channel (*e.g.* due to different opening angles and momenta of the B daughters). The relative comparison for different running conditions does not however depend strongly on the decay channel. The D^* channel was explicitly chosen to validate the reconstruction of long-lived particles such as the K_s^0 . The minimum bias sample is only used to measure timing numbers for the upstream tracking in the software trigger, and the numbers are only given here for completeness.

The current detector with current running conditions is compared with the upgraded detector with upgrade conditions. Additionally the current detector and the upgraded detector are compared in the upgrade conditions. To the best of our knowledge the simulation reproduces all expected detector and event properties such as: occupancy, dead regions and single hit efficiencies. Additional studies of the effects of the degradation of these properties are summarised at the end of this Chapter.

Figure 4.2 shows the distribution of reconstructible primary vertices² in the different samples ($\nu = 2.0, 3.8, 7.6$). On average, it is expected that 13 particles from a minimum bias vertex are reconstructible as *long* tracks. The corresponding number for a B vertex is 20. The average momentum and transverse momentum for *long* reconstructible particles from a minimum bias event is $p = 13 \text{ GeV}/c$ and $p_T = 0.7 \text{ GeV}/c$ respectively. The average momentum is $p = 20 \text{ GeV}/c$ and the average transverse momentum is $p_T = 1.5 \text{ GeV}/c$ for the B daughters of the $B_s \rightarrow \phi\phi$ decay.

²In the upgrade reconstruction sequence the primary vertex algorithm is not yet in place, therefore the criteria of reconstructible primary vertex was introduced. A reconstructible primary vertex is a simulated primary vertex with at least five VELO reconstructible tracks. Primary vertices in this document refer to reconstructible primary vertices.

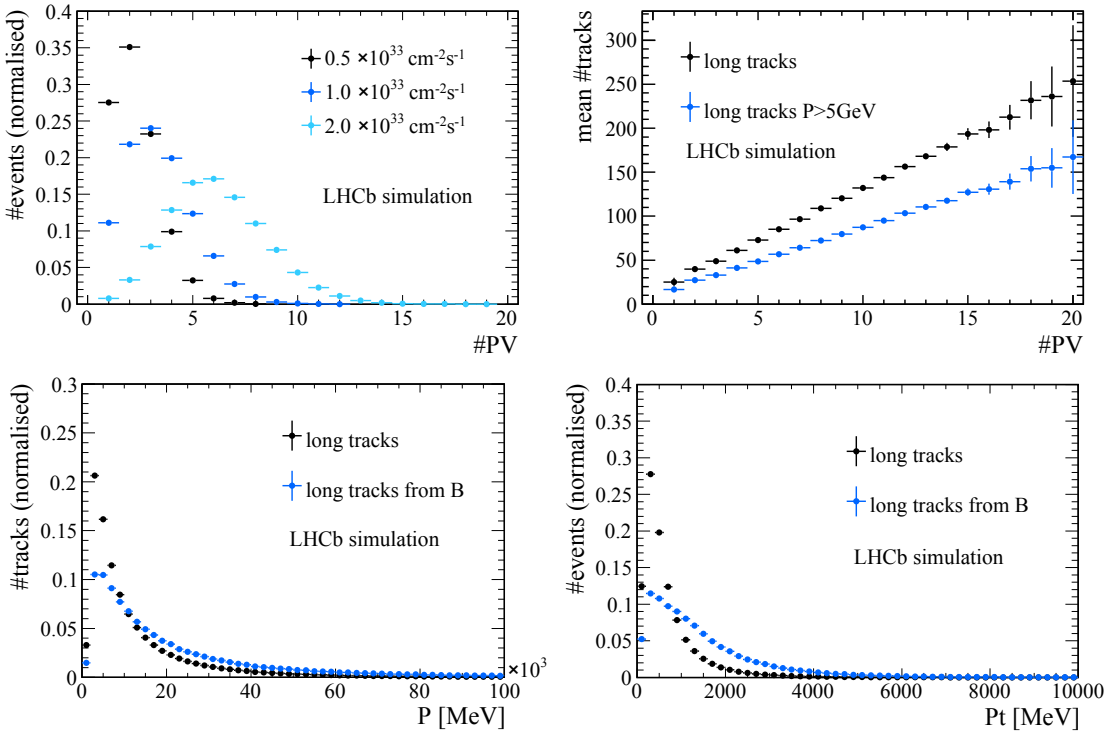


Figure 4.2: Top left: Number of primary vertices for simulated data samples generated with $\nu = 2$, $\nu = 3.8$ and $\nu = 7.6$. Top right: Number of reconstructible long tracks per primary vertex in an event. Bottom row: Momentum and transverse momentum distributions for all long reconstructible particles in $B_s \rightarrow \phi\phi$ events at $\sqrt{s} = 14 \text{ TeV}$.

4.2 Pattern Recognition Algorithms and their Performance

The tracking system of the upgraded LHCb detector is structured similarly to the that of the current detector. Therefore, the pattern recognition sequence is unchanged compared to that used for the current detector. However the individual algorithms are adapted to the new detector geometries. For comparison reasons, the performance numbers of the algorithms used in the current LHCb experiment are quoted for a sample of events with an interaction rate of $\nu = 2$. The figures of merit for the new algorithms for the upgraded tracking detectors are quoted for a sample of events at interaction rates of $\nu = 3.8$ and $\nu = 7.6$. Despite the challenging upgrade running conditions, the aim is to obtain, for each tracking algorithm in the upgraded experiment, comparable performance to that obtained with the current experiment in the current running conditions. However, it has to be taken into account that the current algorithms have been optimised and tuned over several years. The new algorithms have all been adapted and/or even completely rewritten in the last year, while details of the upgrade detector geometries were still modified. This means

that there is still room for improvement in the performance of the pattern recognition algorithms for the upgraded detector.

4.2.1 VELO Tracking

The pattern recognition for the upgraded VELO starts by looking for pairs of unused hits on neighbouring stations which are compatible with track slopes $|dx/dz| < 0.4$ and $|dy/dz| < 0.4$. These track candidates are extrapolated in the upstream direction and the closest hit within a search window around the predicted position on a sensor is added if it passes a cut on the maximal scattering angle. In case of tracks comprising only three hits, all hits are required to be unused by other track candidates. The corresponding results are quoted in Table 4.2. Significantly better performance with respect to the present conditions are obtained in all categories by the upgraded VELO. More details on the algorithm and its performance can be found in Ref. [24].

Table 4.2: Pattern recognition performance parameters for current and upgraded VELO. To be consistent with the VELO TDR, the numbers quoted here are for a sample of simulated $B^0 \rightarrow K^{*0} \mu^+ \mu^-$ events. The results are almost identical for other B decay channels.

	Current VELO [%]	Upgraded VELO [%]
	$\nu = 2$	$\nu = 7.6$
Ghost rate	6.2	2.5
Reconstruction efficiency		
VELO, $p > 5 \text{ GeV}/c$	95.0	98.9
long	97.9	99.4
long, $p > 5 \text{ GeV}/c$	98.6	99.6
b-hadron daughters	99.0	99.6
b-hadron daughters, $p > 5 \text{ GeV}/c$	99.1	99.8

4.2.2 Forward Tracking

The Forward tracking algorithm is based on a Hough transformation approach. It uses the *VELO*, or *upstream* (see later), tracks as input and searches for matching hits in the T-stations. The *VELO* track plus one additional x measurement in the T-stations after the magnet define the 3D trajectory of the particle. Projecting this trajectory on a reference plane, the x measurements corresponding to the *VELO* input form a cluster. For each identified Hough cluster a track candidate is formed. A simplified fit is used to remove outliers from the track candidates. If a minimum requirement on the number of hits is fulfilled, then the track candidates is passed on to the *stereo* search. Finally, a quality variable is computed out of the fit χ^2 and the number of associated x and *stereo* hits. If a minimum quality requirement is fulfilled, then the best candidate is accepted as a reconstructed *long* track by the Forward algorithm. In case the next best tracks are close

in quality they are accepted as well. The average performance to reconstruct *long* tracks by using the forward algorithm is listed in Table 4.3. Figure 4.3 illustrates the dependence of the efficiency on the momentum and the number of primary vertices. Acceptable performances are obtained in the full range studied, although a clear degradation of the performance as function of the number of primary vertices is seen. The ghost rate is significantly reduced, while keeping the efficiency almost unaffected (Table 4.4), by performing a full Kalman fit and applying a loose selection on the track χ^2 . Figure 4.4 shows the efficiency versus ghost rate for different χ^2 cuts. To achieve similar ghost rates for the upgrade experiment at $\nu = 7.6$ as in the current experiment at $\nu = 2$, a drop in efficiency of 5% would be required. If UT hits on the *long* track are requested, a similar ghost rate can be achieved with a drop in efficiency of only 4%. More on adding UT hits to *long* tracks can be found in the dedicated section.

The time spent in the pattern recognition algorithm is listed in Table 4.5. The time consumption of the Forward algorithm is proportional to the number of *VELO* input tracks and the number of hits in the T-stations. Therefore a quadratic dependence on the number of primary vertices is expected, which is roughly confirmed by the quoted timing numbers.

The efficiency and ghost rate as a function of number of primary vertices are compared for the current and upgrade detector using events generated with upgrade conditions at $\nu = 7.6$ for both detectors. Additionally, the efficiency as function of η of the tracks at the primary vertex is shown (Fig. 4.5). In this direct comparison of the same environment, the better performance of the upgrade detector can clearly be seen. While the algorithm of the current experiment aims for high efficiency in low occupancy events, the new algorithm is tuned to be stable as well at high occupancy with a decent ghost rate. The new algorithm of the upgrade detector could be tuned to low occupancy events as well. The range of $2 < \eta < 4$ corresponds mainly to tracks which pass through the area of the current OT detector, while the higher η range corresponds mainly to tracks which pass through the IT. This plot illustrates the superior performance of the SFT compared to the OT. In the range dominated by the IT, the performance is, as expected, similar in both detectors.

More details on the Forward pattern recognition algorithm and its performance can be found in Ref. [104].

Table 4.3: Pattern recognition performance parameters for *long* reconstructible particles reconstructed by the Forward tracking algorithm in the current and upgraded detector. Note that these numbers include the sum of the performance of the VELO and Forward pattern recognition.

	Current LHCb [%]	Upgrade LHCb [%]	
	$\nu = 2$	$\nu = 3.8$	$\nu = 7.6$
Ghost rate	25.4	21.4	38.2
Reconstruction efficiency			
long	91.9	87.5	85.2
long, $p > 5 \text{ GeV}/c$	96.1	93.6	92.3
b -hadron daughters	94.8	92.4	91.1
b -hadron daughters, $p > 5 \text{ GeV}/c$	96.8	95.6	94.7

Table 4.4: Pattern recognition performance parameters for *long* reconstructible particles reconstructed by the Forward tracking algorithm in the current and upgraded detector. Note that these numbers include the sum of the performance of the VELO and Forward pattern recognition. The tracks are fitted by a Kalman fit algorithm and a χ^2 cut of 5 is applied afterwards.

	Current LHCb [%]	Upgrade LHCb [%]	
	$\nu = 2$	$\nu = 3.8$	$\nu = 7.6$
Ghost rate	13.1	14.7	25.5
Reconstruction efficiency			
long	90.9	86.9	84.5
long, $p > 5 \text{ GeV}/c$	95.4	92.9	91.5
b -hadron daughters	93.9	91.9	90.6
b -hadron daughters, $p > 5 \text{ GeV}/c$	96.1	95.1	94.2

Table 4.5: Time spent on simulated $B_s \rightarrow \phi\phi$ events in the Forward pattern recognition algorithm.

	Current LHCb	Upgrade LHCb	
	$\nu = 2$	$\nu = 3.8$	$\nu = 7.6$
time [ms/event]	40	38	172

4.2.3 Seeding

The Seeding algorithm is a standalone track search in the T-stations. The reconstructed tracks are passed on to the Matching algorithm (see next section), which links them to *VELO* tracks. This is an alternative approach to the Forward algorithm to reconstruct *long* tracks. A clone killing algorithm is executed afterwards to remove one instance of the tracks found by both algorithms while keeping the complementary ones.

The second use of T tracks is to feed the so-called Downstream tracking, which searches for decay daughters of long-lived particles, such as K_s^0 mesons and Λ baryons.

The algorithm works in the following way. First, the projection of the track candidate in the $y=0$ plane is searched for. This is done by collecting a set of hits in the x -planes compatibles with a straight line that intersects the x -axis not further than a maximum value from the point of origin of the coordinate system. A parabola is fitted to the selected set of hits to take into account the impact of the magnetic field. Only the hits giving the best fit are kept, forming the x -projection of the track candidate. As a second step, the stereo-hits inside a tolerance value are added to the x -projection, and a new fit is performed in order to keep the best hits and transform the x -projection into a complete track. More information on the details of the algorithm can be found in Ref. [105]. Note that the Seeding algorithm used in the current experiment has a very bad timing behaviour for higher luminosity. Therefore a completely new and significantly simplified Seeding algorithm was written for the upgrade detector. Given the limited development time thus far, this algorithm is currently far from optimal. Several places in the code are identified, where part of the performance could potentially be recovered, especially for low momentum

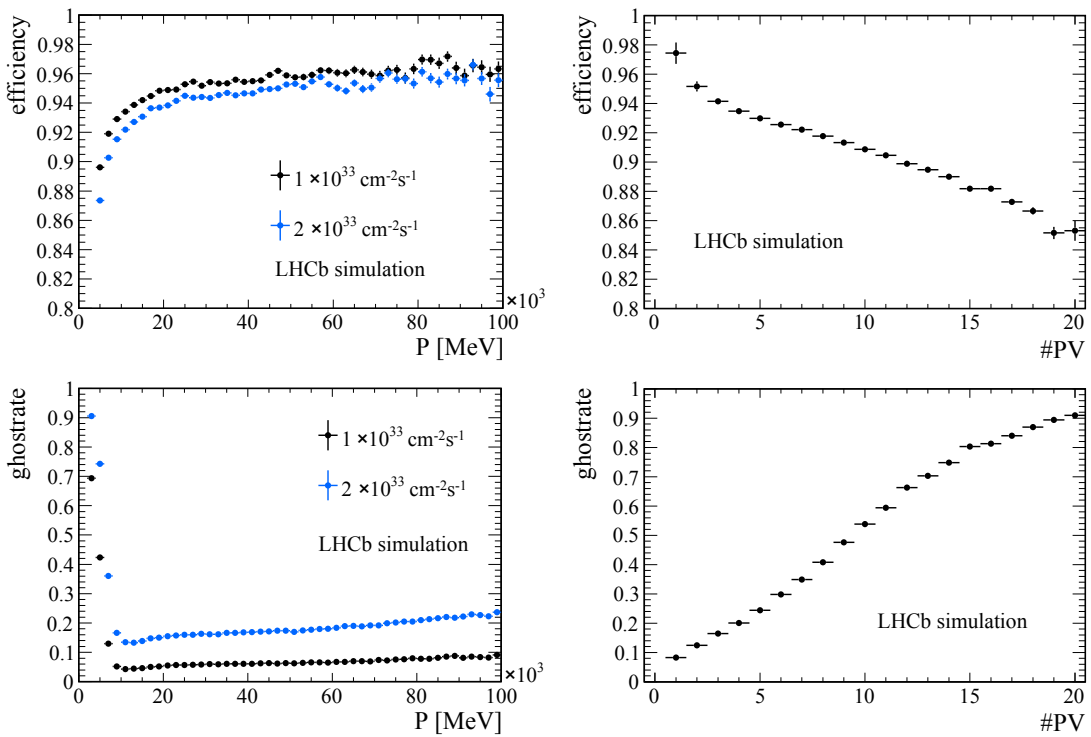


Figure 4.3: Forward tracking efficiency and ghost rate for *long* tracks in bins of momentum and number of primary vertices for samples of simulated $B_s \rightarrow \phi\phi$ events. Note that for the efficiencies a cut on the true momentum of $p > 5 \text{ GeV}/c$ is applied, while no cut is applied on the reconstructed momentum of the ghost tracks.

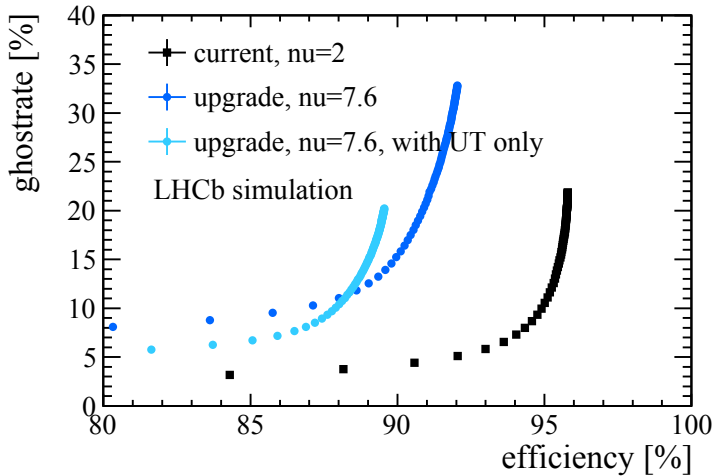


Figure 4.4: Ghost rate and efficiency of the Forward pattern recognition algorithm after the Kalman filter on samples of simulated $B_s \rightarrow \phi\phi$ for the current experiment at $\nu=2$ and the upgrade experiment at $\nu=7.6$. The individual points are obtained by different cuts on the track χ^2 after the Kalman filter. The efficiency given is for *long* reconstructible tracks with $p < 5 \text{ GeV}/c$.

tracks.

One additional complication in the upgrade detector for the Seeding algorithm is however related to the geometry. While the IT+OT combination of the current experiment gave an additional segmentation in y , the SciFi Tracker has uniform planes. For the Forward algorithm, this has no impact on the performance as y information is available from the *VELO* input tracks. However, the number of hit combinations to test for the Seeding is significantly increased with this design choice. Recent studies indicate that the high combinatorics are mainly caused by the densely populated track region at the inner acceptance, very close to the beam pipe. In the current fibre tracker design, the fibres extend over the maximum coverage, as close as possible to the beam line and even exceeding the current IT acceptance at large pseudorapidity. Studies have started which indicate that the observed ghost rate of the Seeding algorithm is closely linked to the exact position of the inner edge of the detector. This position is still being optimised and will likely result in a better Seeding performance than the one reported here.

Table 4.6 summarises the performance of the Seeding algorithm on a simulated sample of $B_s^0 \rightarrow \phi\phi$ events. The efficiency and ghost rate as function of the track momentum and the number of primary vertices is displayed in Fig. 4.6. Table 4.7 shows the performance for strange daughter tracks from $D^* \rightarrow D^0(\rightarrow K_s^0\pi\pi)\pi$ decays. The timing numbers can be found in Table 4.8.

To have a direct comparison of the current and the upgrade detector, the efficiency and ghost rate as a function of number of primary vertices are compared for events generated with upgrade conditions at $\nu = 7.6$ for both detectors. Additionally, the efficiency is shown

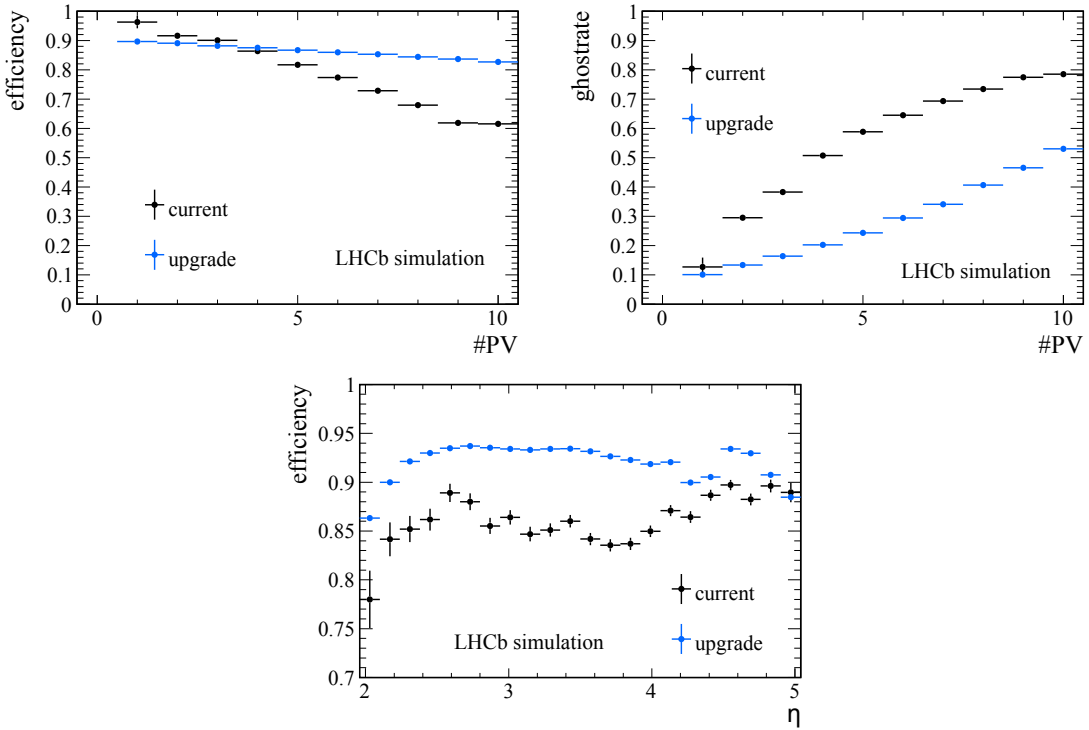


Figure 4.5: Ghost rate and efficiency of the Forward pattern recognition algorithm on samples of simulated $B_s \rightarrow \phi\phi$ events in upgrade running conditions at $\nu = 7.6$, for both the current detector and the upgrade detector. For the efficiency a cut of the track momentum of $p > 5$ GeV/c is applied.

as function of η of the tracks at the primary vertex (Fig. 4.7). It can be seen that the algorithms have different working points. One is optimised to work in a low occupancy environment while the other one is optimised for a reasonable efficiency and ghost rate in high occupancy events. The efficiency as function of η illustrates the better performance of the SciFi Tracker compared to the OT ($2 < \eta < 4$), but shows as well the advantage of the additional y segmentation in the range of the IT ($4 < \eta < 5$).

4.2.4 Track Matching

The track Matching algorithm takes T and *VELO* tracks as input. It extrapolates them all to the focal plane of the magnet and checks for a matching pair of tracks. The output of the algorithm are *long* tracks. This algorithm is an alternative approach to the Forward pattern recognition. The Forward algorithm is however the main algorithm used to reconstruct *long* tracks for physics analysis and for the trigger in the current experiment, and will also be the main algorithm in the upgrade experiment.

The performance of the Matching algorithm to reconstruct *long* tracks, including inefficiencies and ghost rates from the *VELO* and the Seeding algorithm, is given in

Table 4.6: Pattern recognition performance parameters for the Seeding algorithm in the current and upgraded detector on simulated $B_s \rightarrow \phi\phi$ events.

	Current LHCb [%] $\nu = 2$	Upgrade LHCb [%] $\nu = 3.8$	Upgrade LHCb [%] $\nu = 7.6$
Ghost rate	5.2	7.4	19.6
Reconstruction efficiency			
long	96.1	85.3	82.6
long, $p > 5 \text{ GeV}/c$	96.6	91.7	88.4
b -hadron daughters	96.9	89.3	87.6
b -hadron daughters, $p > 5 \text{ GeV}/c$	97.2	92.4	90.4

Table 4.7: Pattern recognition performance parameters for the Seeding algorithm in the current and upgraded detector on a sample of simulated $D^* \rightarrow D^0 (\rightarrow K_s^0 \pi\pi) \pi$ events. The ghost rates are identical to the ones obtained on the $B_s \rightarrow \phi\phi$ sample.

	Current LHCb [%] $\nu = 2$	Upgrade LHCb [%] $\nu = 3.8$	Upgrade LHCb [%] $\nu = 7.6$
Reconstruction efficiency			
long	96.2	84.8	82.1
long, $p > 5 \text{ GeV}/c$	96.6	91.5	88.1
strange daughter with UT (TT) hits	96.1	81.7	79.5
strange daughter with UT (TT) hits, $p > 5 \text{ GeV}/c$	96.6	91.2	88.4
strange daughter with UT (TT) hits from B or D	96.4	84.3	82.9
strange daughter with UT (TT) hits from B or D, $p > 5 \text{ GeV}/c$	96.9	91.7	89.7
strange daughter with UT (TT) hits from B or D and not VELO reconstructible	96.4	85.3	83.7
strange daughter with UT (TT) hits from B or D, $p > 5 \text{ GeV}/c$ and not VELO reconstructible	97.0	91.7	89.7

Table 4.8: Time spent in the Seeding algorithm on simulated $B_s \rightarrow \phi\phi$ events.

	Current LHCb $\nu = 2$	Upgrade LHCb $\nu = 3.8$	Upgrade LHCb $\nu = 7.6$
time [ms/event]	18	37	172

Table 4.9 and shown in Fig. 4.8. Note that the major contribution to the difference in efficiency of the Matching algorithm for low momentum tracks in the upgraded experiment at $\nu = 3.8$ and in the current experiment is inherited from the Seeding algorithm. The Matching algorithm itself is however sensitive to high occupancy for low momentum tracks.

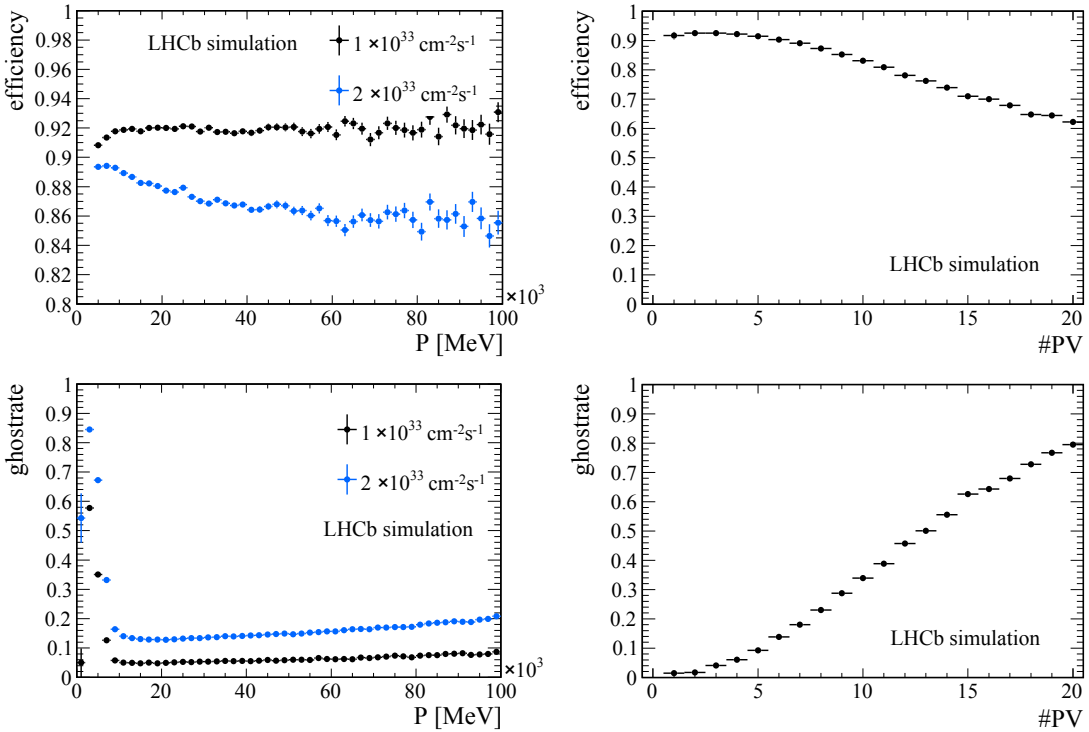


Figure 4.6: Seeding tracking efficiency for *long* reconstructible tracks and ghost rate in bins of momentum and number of primary vertices. Note that for the efficiencies a cut on the true momentum of $p > 5 \text{ GeV}/c$ is applied, while no cut on the reconstructed momentum of the ghost tracks is applied.

The *long* tracks of the Forward and the Matching algorithm are fitted by a Kalman fit. A clone killing algorithm is then used to remove duplicated or badly reconstructed tracks based on the number of associated hits and the track χ^2 . The combined performance of the Forward and the Matching algorithm after this clone killing step is given in Table 4.10 and illustrated in Fig. 4.9. The time spent in the Matching algorithm is given in Table 4.11.

4.2.5 Adding UT hits to *long* tracks

In the current pattern recognition sequence, UT hits are added to *long* tracks after they have been reconstructed by either the Forward or the Matching algorithm. The efficiency to add correct UT hits to non-ghost *long* tracks in the UT acceptance is about 99%. The efficiency to add UT hits to any reconstructed non-ghost *long* track is about 93%. Details are listed in Table 4.12 for the output tracks of the Forward algorithm at an interaction rate of $\nu = 7.6$. The results for the output tracks of the Matching algorithm as well as for samples with an interaction rate of $\nu = 3.8$ are very similar [106].

Adding UT (TT) hits to *long* tracks has two major advantages. Firstly, the momentum resolution after the Kalman fit is applied improves significantly. Figure 4.10 shows the

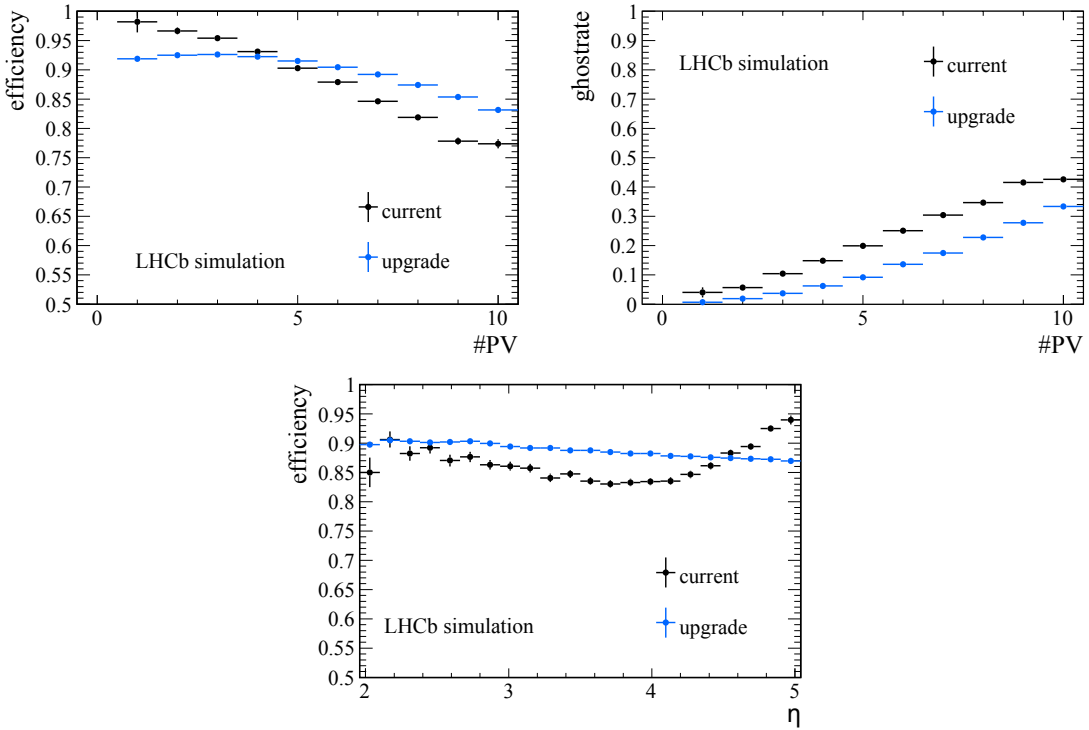


Figure 4.7: Ghost rate and efficiency of the Seeding algorithm on samples of simulated $B_s \rightarrow \phi\phi$ events in upgrade running conditions at $\nu = 7.6$, for both the current detector and the upgrade detector. For the efficiency a cut of the track momentum of $p > 5$ GeV/c is applied.

Table 4.9: Pattern recognition performance parameters for *long* reconstructible particles reconstructed by the Matching algorithm in the current and upgraded detector. Note that these numbers include the sum of the performance of the VELO, Seeding and Matching pattern recognition.

	Current LHCb [%] $\nu = 2$	Upgrade LHCb [%] $\nu = 3.8$	Upgrade LHCb [%] $\nu = 7.6$
Ghost rate	10.1	12.5	17.3
Reconstruction efficiency			
long	88.3	77.1	70.7
long, $p > 5$ GeV/c	92.5	85.7	80.1
<i>b</i> -hadron daughters	92.3	83.1	73.8
<i>b</i> -hadron daughters, $p > 5$ GeV/c	94.3	89.7	86.4

momentum resolution for Kalman fitted *long* tracks out of the forward algorithm³ and

³No attempt has been made to add UT (TT).

Table 4.10: Pattern recognition performance parameters for *long* reconstructible particles reconstructed by the Forward and/or the Matching algorithm in the current and upgraded detector. A cut on the track $\chi^2 < 5$ is applied.

	Current LHCb [%]	Upgrade LHCb [%]	
	$\nu = 2$	$\nu = 3.8$	$\nu = 7.6$
Ghost rate	14.8	16.8	27.3
Reconstruction efficiency			
long	94.6	89.5	87.3
long, $p > 5 \text{ GeV}/c$	96.8	94.4	93.2
b -hadron daughters	96.2	93.6	92.5
b -hadron daughters, $p > 5 \text{ GeV}/c$	97.3	96.2	95.6

the momentum resolution for the same tracks where UT (TT) hits have been successfully added. For comparison reasons, the momentum resolution for the current experiment and

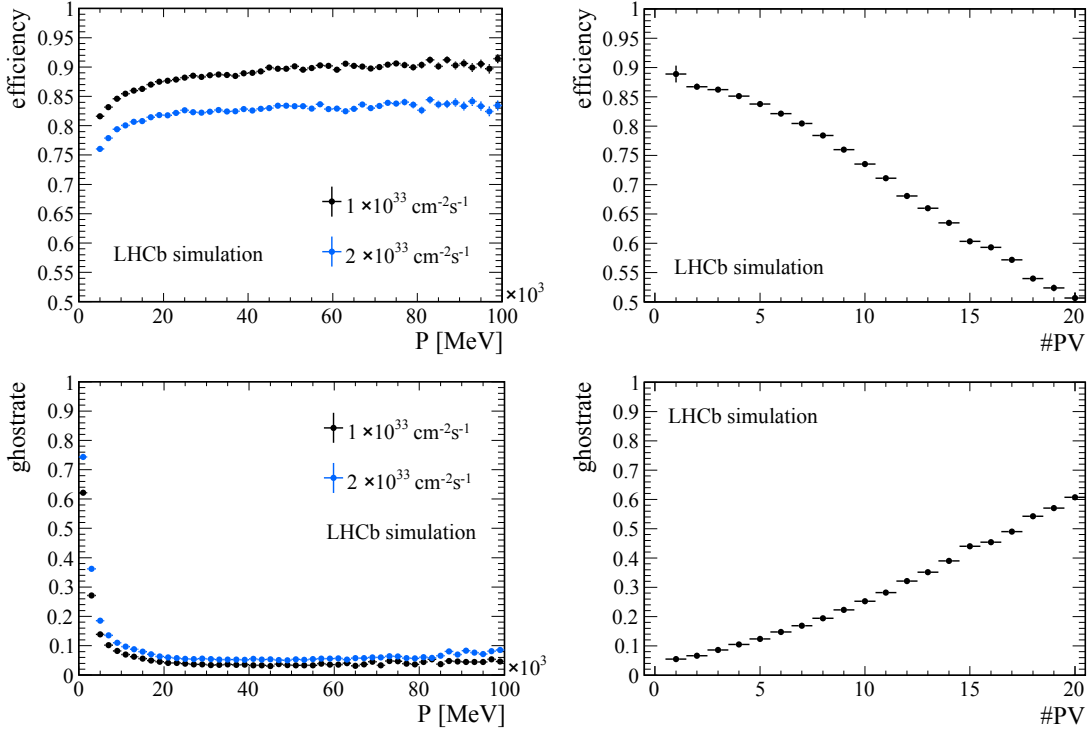


Figure 4.8: *Long* track efficiency and ghost rate for tracks reconstructed by the Matching algorithm in bins of momentum and number of primary vertices. Note that for the efficiencies a cut on the true momentum of $p > 5 \text{ GeV}/c$ is applied, while no cut on the reconstructed momentum of the ghost tracks is applied.

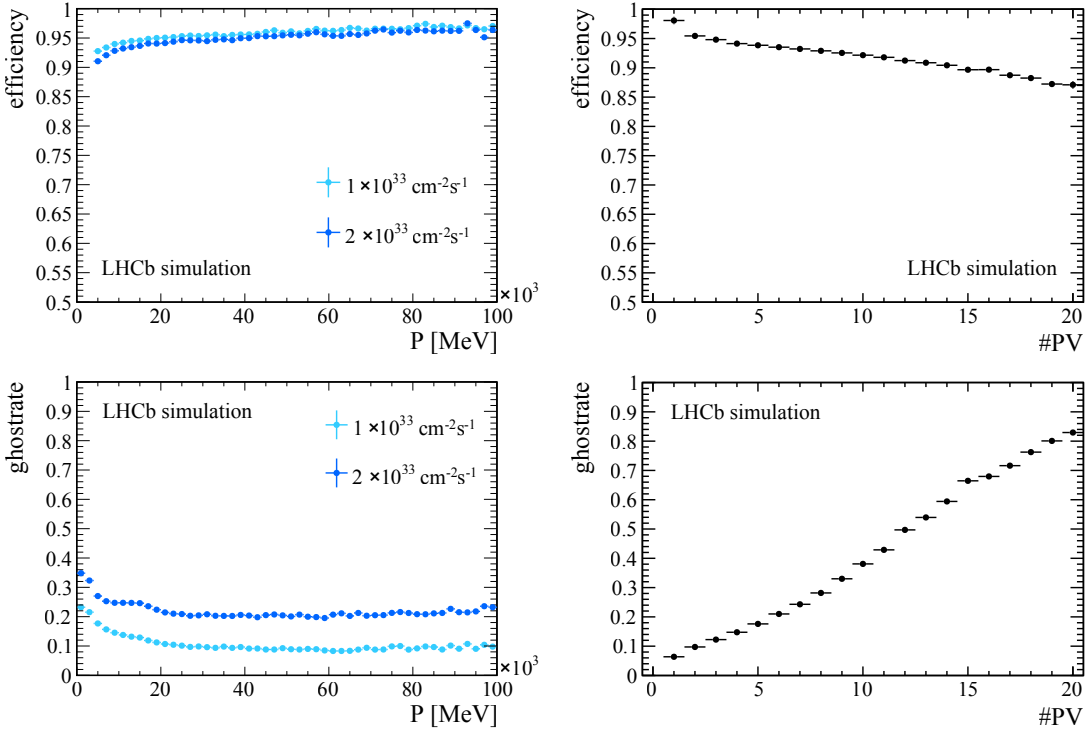


Figure 4.9: *Long* track efficiency and ghost rate for tracks reconstructed by the Matching and/or Forward algorithm in bins of momentum and number of primary vertices. Note that for the efficiencies a cut on the true momentum of $p > 5 \text{ GeV}/c$ is applied, while no cut on the reconstructed momentum of the ghost tracks is applied.

Table 4.11: Time spent in the Matching algorithm on simulated $B_s \rightarrow \phi\phi$ events.

	Current LHCb	Upgrade LHCb	
	$\nu = 2$	$\nu = 3.8$	$\nu = 7.6$
time [ms/event]	1.5	2.3	5.8

the upgraded detector is shown. The shape as function of p is rather similar, which implies that the main improvement in the upgraded tracking system comes from less material (in the entire tracking system including VELO + UT + SFT + support structure), which results in less multiple scattering.

The second advantage of adding UT hits to *long* tracks is that the lack of UT hits is a very good indicator for ghost *long* tracks. The requirement to have at least three UT hits picked up on a *long* track reduces the ghost rate of the Forward tracking algorithm by about a factor of 2, while keeping its efficiency almost unchanged (drop is smaller than 1%). The corresponding ghost rates are listed in Table 4.13 for *long* tracks reconstructed by the Forward algorithm. Similar results are shown for other pattern recognition algorithms [106].

Table 4.12: Reconstruction efficiency for adding correct UT hits to non-ghost *long* tracks reconstructed by the Forward algorithm on a sample of $B_s \rightarrow \phi\phi$ events simulated at an interaction rate of $\nu = 7.6$.

efficiency [%]	all	tracks in $2 < \eta < 5$	UT reconstructible
long	92.6	98.0	99.0
long, $p > 5 \text{ GeV}/c$	90.2	97.4	98.7
long from B	96.4	98.5	98.9
long from B, $p > 5 \text{ GeV}/c$	96.0	98.3	98.8

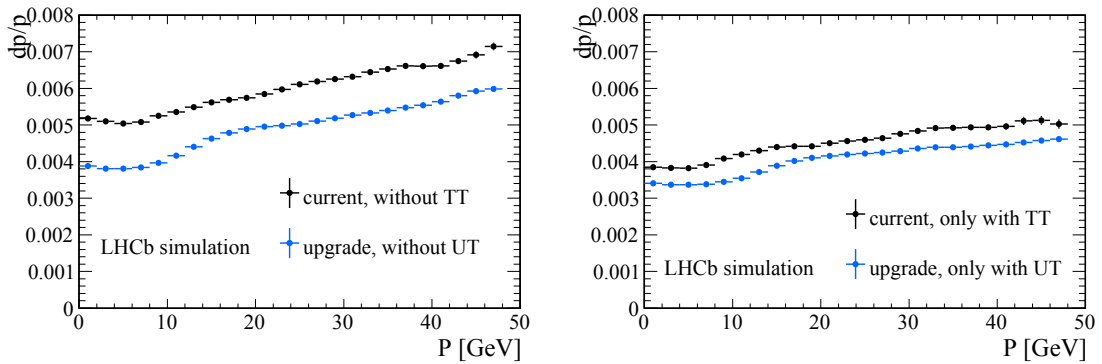


Figure 4.10: Momentum resolution of *long* tracks fitted with the Kalman fit without (left) and with (right) UT (TT) hits added in the current and in the upgraded tracking system, respectively.

The ghost rates with and without the UT hit requirement as a function of momentum and number of primary vertices are shown in Fig. 4.11.

4.2.6 Downstream Tracking

The Downstream tracking algorithm takes T tracks as input and extrapolates them into the UT (TT) where it tries to find matching hits. This algorithm is especially important for the reconstruction of daughter tracks of long lived particles such as K_s^0 mesons. The corresponding performance is listed in Table 4.14 and the timing in Table 4.15. The performance as a function of momentum and number of primary vertices is shown in Fig. 4.12. The extrapolation uncertainties of the T tracks relative to the cluster density in the innermost region of the UT are quite high. This is likely to be the main reason for the worse performance of the Downstream tracking in the upgrade experiment with upgrade running conditions. Therefore, a mild p_T selection cut, requiring the particles to pass through a less central region of the UT (TT), significantly improves the Downstream tracking performance. More details on the Downstream tracking algorithm can be found

Table 4.13: Ghost rate for *long* tracks reconstructed by the Forward algorithm which have at least three picked up UT hits on a sample of $B_s \rightarrow \phi\phi$ events simulated at an interaction rate of $\nu = 3.8$ and $\nu = 7.6$, respectively.

	$\nu = 3.8$		$\nu = 7.6$	
	no UT hit requirement	UT reconstructible	no UT hit requirement	UT reconstructible
Ghost rate [%]	21.4	14.1	38.2	23.8

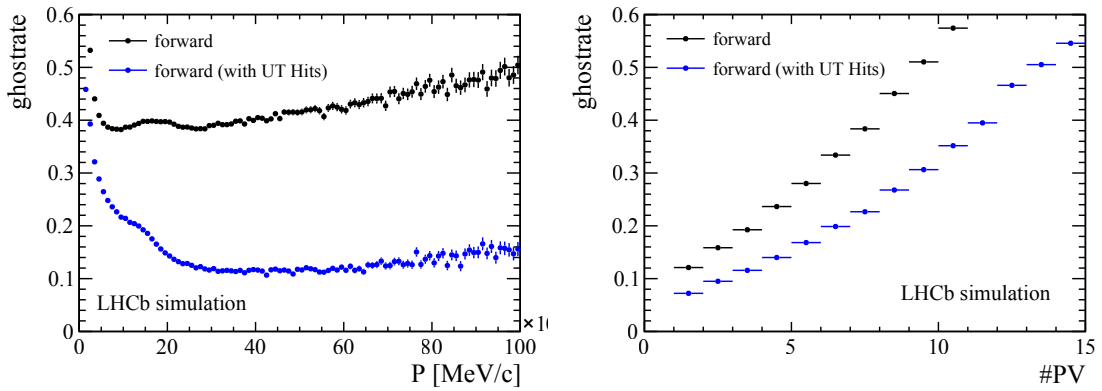


Figure 4.11: Ghost rate of *long* tracks reconstructed by the Forward algorithm with and without the requirement of at least three UT hits as a function of momentum and number of primary vertices for a sample of simulated $B_s \rightarrow \phi\phi$ events at an interaction rate of $\nu = 7.6$.

in Ref. [107].

4.2.7 Upstream Tracking

The Upstream tracking algorithm adds UT (TT) hits to *VELO* tracks. It serves two purposes. Firstly, there are low momentum tracks which are deflected out of the T-station acceptances by the magnetic field. These tracks can only be reconstructed by the Upstream tracking. The excellent performance of the *VELO* and the UT detector means that this algorithm results in a higher efficiency and comparable ghost rate for the upgraded detector (Table 4.16).

The second application of *upstream* tracks exploits the fringe field in the UT (TT) to add momentum information to the *VELO* tracks which are fed as input to the Forward tracking algorithm. The extra momentum has two advantages especially in view of applications for the trigger. A minimum momentum or transverse momentum cut can be applied, and the total number of *VELO* tracks passed to the Forward tracking algorithm can be significantly reduced. The extra momentum information helps to reduce the search window size in the Forward algorithm, and hence speed up the algorithm.

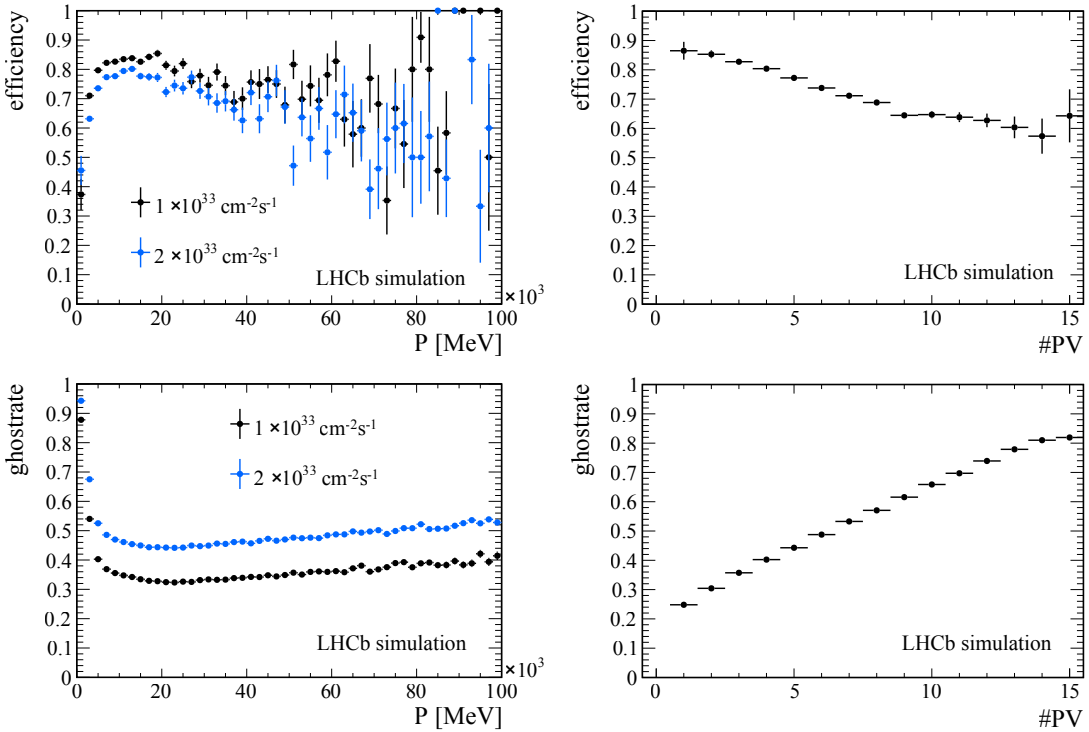


Figure 4.12: *Downstream* track efficiency and ghost rate for tracks reconstructed by the *Downstream* algorithm in bins of momentum and number of primary vertices. The efficiencies are calculated for particles containing a strange quark, stemming from a decay of a particle containing a charm or a bottom quark. Furthermore, the final state particles are required to not have enough information to be reconstructed in the *VELO*.

The Upstream algorithm works in the following way. It extrapolates *VELO* tracks to the z -position at the centre of the UT (TT). Hit candidates which fall within certain tolerances of the extrapolated track position, defined by the p and p_T cuts of the algorithm (currently $p > 3 \text{ GeV}/c$, $p_T > 0.5 \text{ GeV}/c$), are selected. The resulting UT (TT) hit candidates are clustered to form candidates, which consist of at least three UT (TT) hits on at least three UT (TT) layers with no more than one hit per layer. Each cluster is combined with the original *VELO* track to form a track candidate. It is possible to have many track candidates for a single *VELO* track. Finally, a simple fit is performed and the best track candidate is selected based on the number of hits on the track candidate and the χ^2 of the track fit.

The performance of the algorithm to reconstruct high momentum tracks is listed in Table 4.17. As this algorithm was not used in a similar way in the trigger of the current experiment, no comparison to the performance in the current detector is given.

Additionally, the impact on the Forward algorithm of using *upstream* tracks or *VELO* tracks as input, applying additional minimum momentum requirements similar to the

Table 4.14: Performance of the Downstream tracking algorithm on samples of simulated $D^* \rightarrow D^0(\rightarrow K_s^0\pi\pi)\pi$ events. Any inefficiency from the Seeding algorithm is not included in these numbers.

	Current LHCb [%]	Upgrade LHCb [%]	
	$\nu = 2$	$\nu = 3.8$	$\nu = 7.6$
Ghost rate	39.3	41.5	54.6
Reconstruction efficiency			
strange daughters	79.6	71.0	62.7
strange daughters, $p > 5 \text{ GeV}/c$	84.1	75.3	67.5
strange daughters, $p > 5 \text{ GeV}/c, p_T > 400 \text{ MeV}/c$	-	81.7	76.3
strange daughters from D or B	84.3	79.1	73.2
strange daughters from D or B, $p > 5 \text{ GeV}/c$	87.5	81.5	76.1
strange daughters from D or B, $p > 5 \text{ GeV}/c$ $p_T > 400 \text{ MeV}/c$	-	85.5	81.4

Table 4.15: Time spent in the Downstream algorithm on simulated $D^* \rightarrow (D^0 \rightarrow K_s^0\pi\pi)\pi$ events.

	Current LHCb	Upgrade LHCb	
	$\nu = 2$	$\nu = 3.8$	$\nu = 7.6$
time [ms/event]	8	21	100

Table 4.16: Performance of the Upstream tracking on simulated $B_s \rightarrow \phi\phi$ events. Any inefficiency from the VELO algorithm is included in these numbers.

	Current LHCb [%]	Upgrade LHCb [%]	
	$\nu = 2$	$\nu = 3.8$	$\nu = 7.6$
Ghost rate	19.5	15.3	20.3
Reconstruction efficiency			
VELO + UT(TT)	80.9	86.7	84.5
VELO + UT(TT) $p > 5 \text{ GeV}$	90.7	96.2	94.4
VELO + UT(TT) + not Long	66.6	69.6	67.9
VELO + UT(TT) + not long $p > 5 \text{ GeV}$	89.2	94.5	93.2

running mode on the planned trigger, is given in Tables 4.18 and 4.19, and shown in Fig. 4.13. Note that for *upstream* tracks the momentum is known and they are not passed to the Forward algorithm if they fail the momentum cuts. Both the reduction in input tracks and the reduced search windows speed up the Forward algorithm significantly. On the other hand, in the compared scenario where the *VELO* tracks are used as input instead, no momentum information is available. Therefore low momentum tracks will

also be passed to the Forward algorithm. The search windows correspond in this case to the minimum p and p_T requirements of the trigger. Due to the lack of competition with potential T-station track segments in the other detector regions, these tracks have a higher chance to form a ghost track. Therefore the ghost rate increases dramatically in this running scenario compared to the case where *upstream* tracks are used as input.

The timing numbers given in Table 4.19 are obtained using samples of simulated minimum bias events as they represent the majority of the events which will be processed by the trigger.

The Forward pattern recognition algorithm, using *upstream* tracks as input, results in an execution time per event and a ghost rate improved by a factor of three with around 1.5% loss in efficiency.

More details on the Upstream algorithm and its performance can be found in Ref. [108].

Table 4.17: Pattern recognition performance parameters for the Upstream tracking algorithm. Note that these numbers include the sum of the performance of the VELO and the Upstream algorithm.

	Upgrade LHCb [%]	
	$\nu = 3.8$	$\nu = 7.6$
Ghost rate $p > 3 \text{ GeV}/c, p_T > 0.5 \text{ GeV}/c$	5.2	7.9
Reconstruction efficiency long, b -hadron daughters, $p > 3 \text{ GeV}/c, p_T > 0.5 \text{ GeV}/c$	98.6	98.4

4.3 Robustness Tests

The simulated events used to study the track reconstruction in the upgraded detector include, to the best of our knowledge, both the geometry of the individual sub-detectors

Table 4.18: Pattern recognition performance parameters for the long track reconstruction using Forward tracking algorithm, with and without *upstream* tracks as input.

	VELO-Forward [%]	VELO-Upstream-Forward [%]	$\nu = 3.8$	$\nu = 7.6$	$\nu = 3.8$	$\nu = 7.6$
Ghost rate $p > 3 \text{ GeV}/c, p_T > 0.5 \text{ GeV}/c$	17.3	40.6	5.0	12.3		
Reconstruction efficiency long, b -hadron daughters, $p > 3 \text{ GeV}/c, p_T > 0.5 \text{ GeV}/c$	95.6	94.7	94.2	93.4		

Table 4.19: Timing numbers for the VELO-Forward and the VELO-Upstream-Forward reconstruction sequence. These numbers were obtained using samples of simulated minimum bias events.

time [ms/events]	VELO-Forward		VELO-Upstream-Forward	
	$\nu = 3.8$	$\nu = 7.6$	$\nu = 3.8$	$\nu = 7.6$
VELO	0.7	1.8	0.7	1.8
Upstream	-	-	0.9	2.2
Forward	4.0	22.5	1.2	4.1
Total	4.7	24.3	2.8	8.1

and the expected detector performance including all effects of radiation damage. It allows the performance of the track reconstruction after an integrated luminosity of 50 fb^{-1} to be estimated. Nevertheless, some additional scenarios describing “extreme” running conditions have been studied. Studies of the detector performance have been made separately for the SciFi Tracker and the Upstream Tracker.

4.3.1 Modified SciFi Tracker Performance

4.3.1.1 Impact of Hit Resolution

The current simulation has an average single hit resolution of $42 \mu\text{m}$. This corresponds to test measurements of short fibre tracker modules used in a cosmic ray experiment [38]. A 2-bit read-out scheme will be used for the SciFi Tracker which will result in a resolution of about $60 \mu\text{m}$ for signal only. Additional misalignment and noise can worsen the expected resolution further. Therefore, the momentum resolution is compared over the range from 42 to $100 \mu\text{m}$. Figure 4.14 shows the performance of the Forward pattern recognition algorithm with different single hit resolutions. As expected the momentum resolution for high momentum tracks degrades slightly for the worst single hit resolution.

4.3.1.2 Drop in Single Hit Efficiencies

The single hit efficiency of the SciFi Tracker at the beginning of the data taking is expected to be 99%, which is an artefact of the Poisson distribution of the number of emitted photons per charged particle traversing the detector and thresholds in the clustering.⁴ This efficiency is properly described in the simulation. Clusters have randomly been thrown away in the simulation to account for additional inefficiencies. The results can be found in Table 4.20. Note that *nominal* means no additional hits have been removed, and effectively corresponds to 99% single hit efficiency. The lines with $1.0 - 2.0\%$ correspond to the

⁴There are additional sources of inefficiencies such as dead regions in the modules or dead channels at the edges of photomultipliers. They are properly taken into account in the simulation but do not contribute to the single hit efficiency quoted here.

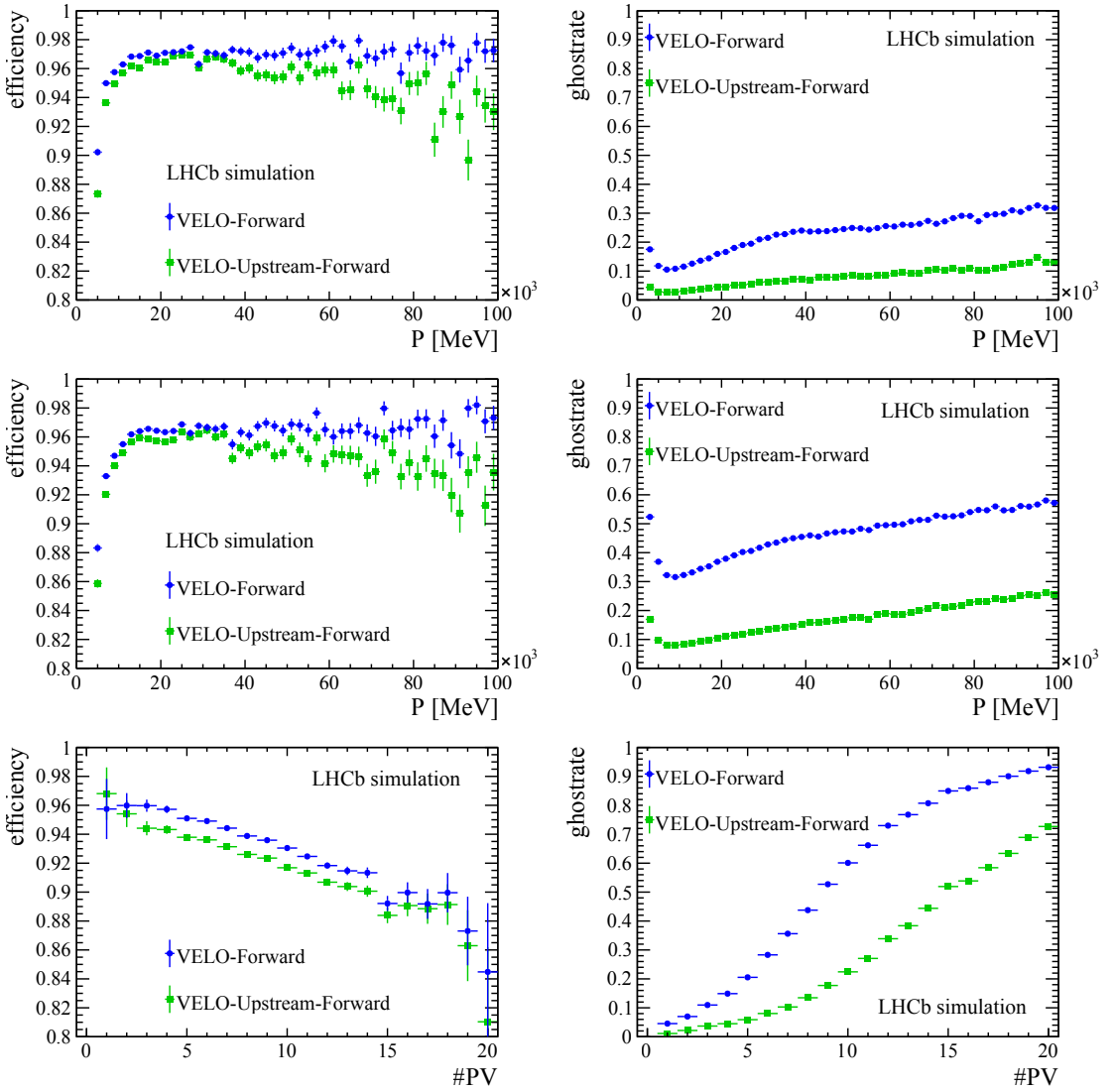


Figure 4.13: Long track efficiency and ghost rate for tracks reconstructed by the VELO-Forward and VELO-Upstream-Forward reconstruction sequence in bins of momentum and number of primary vertices. The upper row shows the performance on simulated $B_s \rightarrow \phi\phi$ events at $\nu = 3.8$, the second row shows the performance on the same events at $\nu = 7.6$. The bottom row shows the performance as a function of the number of primary vertices.

expected degradation to 97 – 98% single hit efficiency in the experiment over the planned running period. A loss of 1% single hit efficiency corresponds to about 2% loss in tracking efficiency. The pattern recognition performance is expected to go down by 2 – 4% over the entire period of data taking in upgrade conditions.

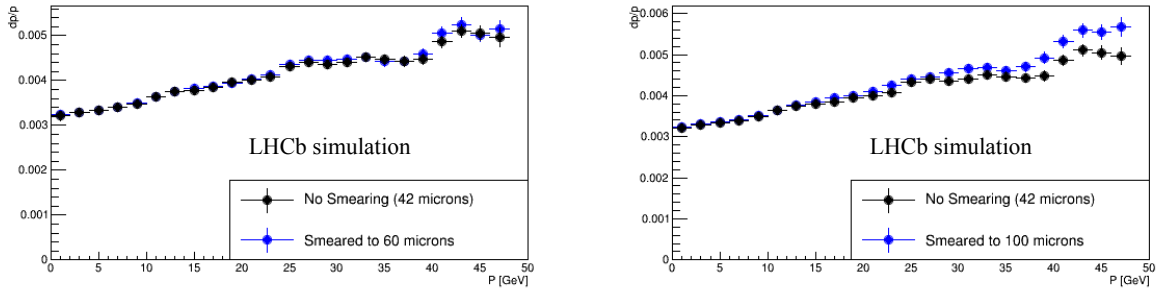


Figure 4.14: Momentum resolution of Kalman fitted *long* tracks reconstructed with the Forward algorithm for different single hit resolutions in the SciFi Tracker.

Table 4.20: Pattern recognition performance parameters for *long* reconstructible particles reconstructed by the Forward algorithm using a simulated sample of $B_s \rightarrow \phi\phi$ at $\nu = 7.6$. The quoted numbers correspond to additional inefficiencies introduced by throwing away random hits on top of the already existing 99% single hit efficiency in the simulated data samples.

Hit inefficiency [%]		Reconstruction inefficiency [%]
nominal	long tracks	0.0
	long tracks, $p > 5 \text{ GeV}/c$	0.0
0.5	long tracks	-0.4
	long tracks, $p > 5 \text{ GeV}/c$	-0.9
1.0	long tracks	-1.6
	long tracks, $p > 5 \text{ GeV}/c$	-1.8
1.5	long tracks	-2.6
	long tracks, $p > 5 \text{ GeV}/c$	-2.8
2.0	long tracks	-3.5
	long tracks, $p > 5 \text{ GeV}/c$	-3.8
2.5	long tracks	-4.5
	long tracks, $p > 5 \text{ GeV}/c$	-4.8
3.0	long tracks	-5.6
	long tracks, $p > 5 \text{ GeV}/c$	-5.9

4.3.1.3 Thermal Noise

A detailed study (see Ref. [100]) added the effect of thermal noise including after-pulsing and spillover as a function of temperature to the simulation. The simulated radiation damage corresponds to 10 years of nominal operation (50 fb^{-1}). The results on the tracking performance for the Forward and the Seeding algorithms are displayed in Fig. 4.15. It can be seen that the tracking efficiencies and the ghost rates remain acceptable for temperatures below -30°C . The planned operation temperature is -40°C .

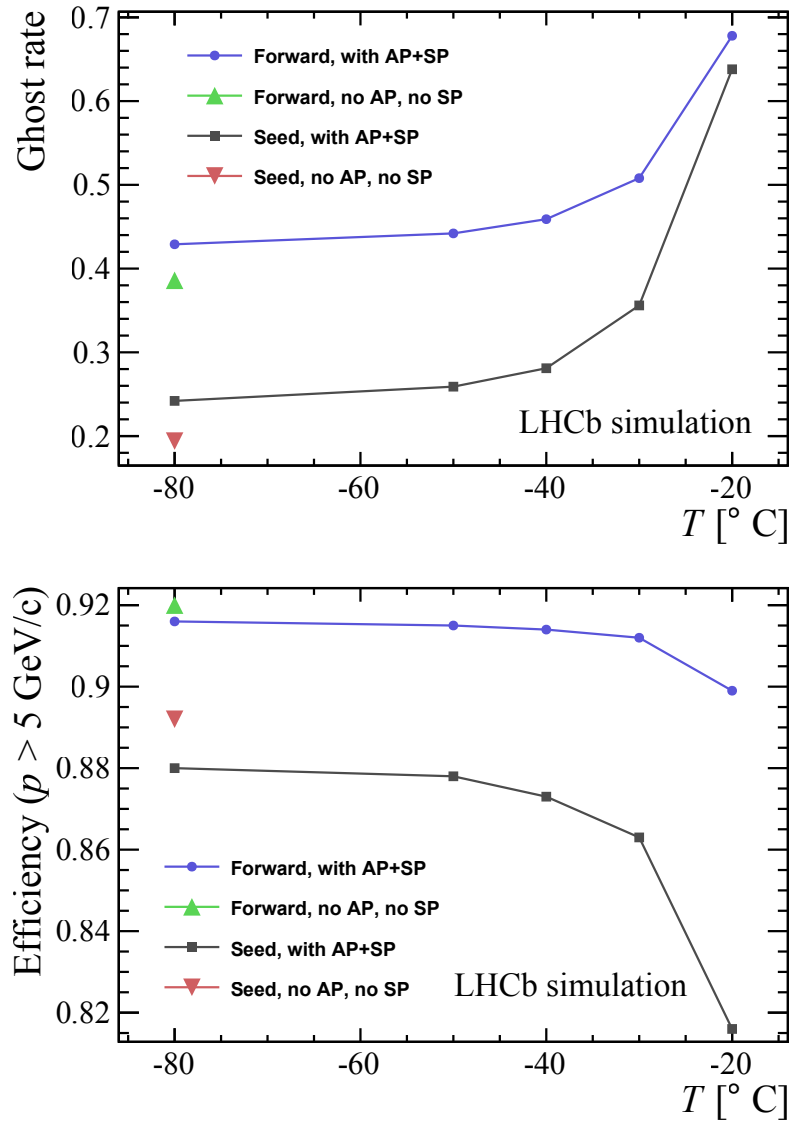


Figure 4.15: Effect of the thermal noise on the tracking performance, with after-pulsing (AP) and spillover (SP) and without after-pulsing and spillover. The results are obtained on a sample of simulated $B_s \rightarrow \phi\phi$ events with an interaction rate of $\nu = 7.6$ and a radiation damage corresponding to 50 fb^{-1} of data taking. The performance numbers have been obtained on a very small data sets, thus the absolute efficiency is slightly different from numbers quoted earlier for the Forward and the Seeding algorithm in this document. However the relative efficiencies as function of temperature are not affected by these fluctuations.

4.3.1.4 Higher Occupancy

In the current experiment, some tracking sub-detectors had higher occupancy in data compared to simulated events. The OT occupancy was affected by a difference of up to

30%. To estimate the impact of a potential higher occupancy data compared to simulation for the SFT, the performance of the Forward and the Seeding algorithm on a sample of simulated $B_s \rightarrow \phi\phi$ events generated with an interaction rate of $\nu = 11.4$ was studied. Note that it is likely that this study overestimates the effect, as the $\nu = 11.4$ sample not only increases the occupancy in the T-stations but in all (tracking) detectors. The corresponding performance numbers are listed in Table 4.21. The efficiency drops by 1–4%, and the ghost rate increases by a factor of about 1.5, compared to the nominal performance numbers given in Tables 4.3 and 4.6. However, no dramatic drop in performance is seen which would indicate that the pattern recognition is close to break down. Note that the algorithms have been tuned for samples with an interaction rate of $\nu = 3.8$ and are applied in this study without modifications to a sample with an interaction rate of $\nu = 11.4$. A better working point would be chosen if these conditions were to be faced in real data taking.

Table 4.21: Pattern recognition performance parameters for long reconstructible particles reconstructed by the Forward and the Seeding algorithm on a sample of simulated $B_s \rightarrow \phi\phi$ events at an interaction rate of $\nu = 7.6$ and $\nu = 11.4$, respectively.

Figure of merit	Forward tracking		Seeding	
	$\nu = 7.6$	$\nu = 11.4$	$\nu = 7.6$	$\nu = 11.4$
time [ms/event]	172	546	172	410
Ghost rate [%]	38.2	57.5	19.6	35.5
Reconstruction efficiency [%]				
long	85.2	82.7	82.6	78.4
long, $p > 5 \text{ GeV}/c$	92.3	90.9	88.4	83.1
b -hadron daughters	91.1	89.4	87.6	83.6
b -hadron daughters, $p > 5 \text{ GeV}/c$	94.7	93.7	90.4	86.0

4.3.2 Modified UT Detector Performance

Several parameters were modified simultaneously in the UT detector performance to mimic worse conditions and their impact has been studied on a sample of generated events at an interaction rate of $\nu = 7.6$. The single hit efficiency was decreased from 99.5% to 99.0%. Measurements in four randomly chosen ASICs in the x layers close to the beam-pipe were ignored to mimic potential dead regions. The cross-talk was raised from 5 to 7% and the noise level was increased from 1500 to 1800 electrons. Additionally, the gain which nominally corresponds to 1000 electrons per ADC count was varied randomly between 900 and 1100 electrons, following a Gaussian distribution with a central value of 1000 and a width of 50 electrons.

The performance of the Upstream and the Downstream algorithms on this sample with modified UT detector performance are compared to the performance of the nominal UT

Table 4.22: Performance of the Upstream tracking on a sample with nominal and degraded detector performance for the UT at an average interaction rate of $\nu = 7.6$.

	nominal	robustness test
Ghost rate [%] $p > 3 \text{ GeV}/c, p_T > 0.5 \text{ GeV}/c$	7.9	9.5
Reconstruction efficiency [%] long, b -hadron daughters, $p > 3 \text{ GeV}/c, p_T > 0.5 \text{ GeV}/c$	98.4	96.2

Table 4.23: Performance of the Downstream tracking on a sample with nominal and degraded detector performance for the UT at an average interaction rate of $\nu = 7.6$.

	nominal	robustness test
Ghost rate [%]	52.1	53.8
Reconstruction efficiency [%]		
K_s^0 daughters	65.6	59.9
K_s^0 daughters, $p > 5 \text{ GeV}/c$	65.2	61.1
K_s^0 daughters, $p > 5 \text{ GeV}/c, p_T > 300 \text{ MeV}/c$	72.0	67.9
K_s^0 daughters from D or B	74.6	69.3
K_s^0 daughters from D or B, $p > 5 \text{ GeV}/c$	74.6	72.4
K_s^0 daughters from D or B, $p > 5 \text{ GeV}/c, p_T > 300 \text{ MeV}/c$	79.1	76.2

in Tables 4.22 and 4.23 respectively. As expected the performance is slightly reduced but still reasonable. No significant change in the performance of adding UT hits to *long* tracks was observed in either configuration.

4.4 Conclusions

The LHCb tracking system will be replaced in the upgrade with detectors adapted to physics at high luminosity conditions. The expected performance of the new tracking system has been studied using simulated events generated for two upgrade scenarios ($\nu = 3.8$ or 7.6). These results have been compared to the tracking performance of the current detector using events generated with either 2011 data taking conditions ($\nu = 2$) or upgrade conditions ($\nu = 7.6$).

The most valuable reconstructed tracks for any physics analysis are *long* tracks. The main algorithm used to reconstruct these type of tracks is the Forward tracking algorithm. The efficiency to reconstruct *long* tracks using this algorithm is 2 – 4% lower for the upgraded detector running on events generated with the upgrade conditions compared to the efficiency found with the current detector and 2011 conditions. The difference is

largest for low momentum tracks. The Forward algorithm performs significantly better for the upgraded detector compared to the current detector when using events simulated with the same running conditions. It is expected that improvements to the new Forward tracking algorithm will ensure that the current efficiency and ghost rate can be achieved in the upgrade environment.

The reconstruction of *downstream* tracks is important for the reconstruction of stable daughters of long-lived particles such as K_s^0 mesons and Λ baryons. The Downstream tracking algorithm takes *T-tracks* produced by the Seeding algorithm, extrapolates them to the UT station and tries, if possible, to add UT hits to the track. The Seeding algorithm has been completely rewritten as the current algorithm was found to be too slow in the upgrade conditions. The new code running on events generated with the upgrade conditions is currently about 10% less efficient than the old code in 2011 running conditions especially for low momentum tracks. The drop in performance is expected as there is no y -segmentation in the SciFi Tracker, and the new algorithm has not yet been fully optimised. Further studies are required and an optimisation of the exact inner boundary position of the SciFi Tracker is currently being investigated. Additionally the Downstream algorithm shows some loss in performance due to the relative high density of UT measurements compared to the precision of the extrapolated *T* track.

The Upstream Tracker has a larger acceptance than the current Tracker Turicensis. This results in a highly efficient Upstream algorithm which allows the use of *upstream* tracks as input to the Forward tracking. This novel approach speeds up the *long* track reconstruction sequence for high momentum tracks by a factor of three and reduces the ghost rate significantly. This makes it a very interesting option for the software trigger. Requiring UT hits on *long* tracks reduces the ghost rate by almost a factor two with hardly any loss in efficiency.

The momentum resolution of the upgrade tracking system is about 10 – 20% better than that of the current one. This is the result of less material and therefore less multiple scattering in the VELO, UT and T-stations.

The studies presented in this Chapter demonstrate a robust and reliable track reconstruction with the planned Upstream and SciFi Tracker despite the challenging data taking conditions expected. For the majority of algorithms, it is expected that comparable, or even better, performance will be reached with the upgraded tracking system in upgrade running conditions compared to the current tracking system in 2011 data taking conditions.

Acknowledgements

We express our gratitude to the LHC vacuum group, in particular K. Vatansever for a study of the beam-pipe insulation and interface with UT, and to M. Gallilee for organising the discussions between LHCb and the LHC experts on this aspect of the design.

References

- [1] LHCb collaboration, A. A. Alves Jr. *et al.*, *The LHCb detector at the LHC*, JINST **3** (2008) S08005.
- [2] LHCb collaboration, R. Aaij, *et al.*, and A. Bharucha *et al.*, *Implications of LHCb measurements and future prospects*, Eur. Phys. J. **C73** (2013) 2373, [arXiv:1208.3355](https://arxiv.org/abs/1208.3355).
- [3] LHCb collaboration, R. Aaij *et al.*, *Framework TDR for the LHCb Upgrade*, CERN-LHCC-2012-007, LHCb TDR 12.
- [4] LHCb collaboration, *Updated sensitivity projections for the LHCb Upgrade*, LHCb-PUB-2013-015, CERN-LHCb-PUB-2013-015.
- [5] LHCb collaboration, *Expression of Interest for an LHCb Upgrade*, LHCC-G-139, CERN-LHCC-2008-007.
- [6] LHCb collaboration, R. Aaij *et al.*, *Letter of Intent for the LHCb Upgrade*, CERN-LHCC-2011-001, LHCC-I-018.
- [7] LHCb collaboration, *Outer Tracker Electronics Architecture Review Report*, EDMS ID 1350358, CERN, Geneva, Mar, 2013.
- [8] H. Dijkstra and E. van Herwijnen, *Simulation and tracking performance of the LHCb Tracker with a redesigned silicon inner tracker*, LHCb-PUB-2014-008 ; CERN-LHCb-PUB-2014-008 ; LHCb-INT-2013-048.
- [9] H. Dijkstra, V. Salustino Guimaraes, V. De Aguiar, and V. Rigo, *Airflow induced vibration of the Si-IT prototype*, LHCb-PUB-2014-011 ; CERN-LHCb-PUB-2014-011 ; LHCb-INT-2014-006.
- [10] S. Belogurov *et al.*, *Radiation environment and cooling of the Si option for the IT upgrade*, LHCb-PUB-2014-010 ; CERN-LHCb-PUB-2014-010 ; LHCb-INT-2014-005.
- [11] H. Dijkstra and S. Kandybei, *Report on SI-IT Prototype Modules R&D for the LHCb Upgrade*, LHCb-PUB-2014-009 ; CERN-LHCb-PUB-2014-009 ; LHCb-INT-2013-063.
- [12] LHCb collaboration, *SciFi Tracker: Viability Assessment Review*, EDMS ID 1358123, CERN, Geneva, 2013.

- [13] *LHCb Upgrade SciFi Tracker: Technology Validation Review*, EDMS ID 1358095, CERN, Geneva.
- [14] S. Löchner and M. Schmelling, *The Beetle Reference Manual*, CERN-LHCB-2005-105. LHCB-2005-105.
- [15] G. Battistoni *et al.*, *The FLUKA code: Description and benchmarking*, in *Proceedings of the Hadronic Shower Simulation Workshop 2006* (M. Albrow and R. Raja, eds.), AIP Conference Proceeding 896, pp. 31–49, 2007.
- [16] A. Fasso *et al.*, *FLUKA: a multi-particle transport code*, 2005. CERN-2005-10, INFN/TC05/11, SLAC-R-773.
- [17] M. Moll, *Radiation Damage in Silicon Particle Detectors*, PhD thesis, Fachbereich Physik der Universität Hamburg, 1999.
- [18] C. Elsasser *et al.*, *The LHCb Silicon Tracker*, JINST **9** (2014) C01009, CERN-LHCb-PROC-2013-056.
- [19] K. Vatansever, *LHCb Feasibility Study - Moving the TT Sensors closer to the beam pipe*, EDMS ID 1324474, CERN, Geneva, Oct, 2013.
- [20] M. Cepeda *et al.*, *Mechanical and cooling design studies for an integrated stave concept for silicon strip detectors for the super lhc*, ATLAS-UPGRADE-PUB-2008-001, 2008; G. Beck, T. Jones *et al.*, *Thermo-mechanical local support - barrel stave*, ATL-UPGRADE-PUB-2013-010, 2013.
- [21] B. Verlaat, A. Van Lysebetten, and M. Van Beuzekom, *CO₂ Cooling for the LHCb-VELO Experiment at CERN*, in *8th IIF/IIR Gustav Lorentzen Conference on Natural Working Fluids*, (Copenhagen, Denmark), 2008.
- [22] AMS-Tracker Collaboration, D. Rapin, *The AMS-02 silicon tracker: First year on ISS in space*, Nucl. Instrum. Meth. **A718** (2013) 524.
- [23] M. Capeans *et al.*, *ATLAS Insertable B-Layer Technical Design Report*, Tech. Rep. CERN-LHCC-2010-013. ATLAS-TDR-19, CERN, Geneva, Sep, 2010.
- [24] LHCb collaboration, R. Aaij *et al.*, *LHCb Velo Upgrade Technical Design Report*, CERN-LHCC-2013-021, LHCb-TDR-013.
- [25] G. Corti and L. Shekhtman, *Radiation background in the LHCb experiment*, Tech. Rep. LHCb-2003-083, CERN-LHCb-2003-083.
- [26] Y. Unno *et al.*, *Development of n-on-p silicon sensors for very high radiation environments*, Nucl. Instrum. Meth. **A636** (2011) 24.
- [27] M. Ullan *et al.*, *Embedded pitch adapters for the ATLAS Tracker Upgrade*, Nucl. Instrum. Meth. **A732** (2013) 178.

- [28] K. Wyllie *et al.*, *Electronics Architecture of the LHCb upgrade*, LHCb-2011-011.
- [29] F. Alessio and R. Jacobsson, *Readout Control Specifications for the Front-End and Back-End of the LHCb Upgrade*, CERN-LHCb-PUB-2012-017.
- [30] Y. Zhu *et al.*, *A 10-bit 100-MS/s Reference-Free SAR ADC in 90 nm CMOS*, IEEE Journal of Solid State Circuits **45** (2010).
- [31] J. Cachemiche *et al.*, *Readout board specifications for the LHCb upgrade*, EDMS ID 1251709, CERN, Geneva.
- [32] M. Firlej *et al.*, *Development of scalable frequency and power Phase-Locked Loop in 130nm CMOS technology*, JINST accepted for publication (2014).
- [33] SAPOCO 42, *SAFETY POLICY AT CERN*, EDMS ID 359387, CERN, Geneva, Nov, 2006.
- [34] M. Tobin *et al.*, *The LHCb Silicon Tracker*, Nucl. Instrum. Meth. **A732** (2013) 168, CERN-LHCb-PROC-2013-022.
- [35] D. van Eijk *et al.*, *Radiation hardness of the LHCb Outer Tracker*, Nucl. Instrum. Meth. **A685** (2012) 62.
- [36] R. Arink *et al.*, *Performance of the LHCb Outer Tracker*, JINST **9** (2014) P01002, arXiv:1311.3893.
- [37] LHCb collaboration, R. Antunes Nobrega *et al.*, *LHCb Reoptimized Detector Design and Performance Technical Design Report*, CERN-LHCC-2003-030, LHCb TDR 9.
- [38] B. Beischer *et al.*, *A High-resolution Scintillating Fiber Tracker With Silicon Photomultiplier Array Readout*, Nucl. Instrum. Meth. **A622** (2010) 542.
- [39] *Workshop on SiPM cooling for Fiber Tracker*, October, 2013. <https://indico.cern.ch/conferenceDisplay.py?confId=273434>.
- [40] *SciFi Tracker Electronics Architecture Review Report*, EDMS ID 1350337, CERN, Geneva.
- [41] N. Lopez March and M. Karacson, *Radiation studies for the LHCb tracker upgrade*, LHCb-PUB-2014-022, CERN-LHCb-PUB-2014-022, LHCb-INT-2013-003.
- [42] T. White, *Scintillating fibres*, Nucl. Instrum. Meth. **A273** (1988) 820.
- [43] R. C. Ruchti, *THE USE OF SCINTILLATING FIBERS FOR CHARGED-PARTICLE TRACKING*, Annual Review of Nuclear and Particle Science **46** (1996) 281.

- [44] M. Hoek, *Design and Construction of a Scintillating Fibre Tracker for measuring Hard Exclusive Reactions at HERMES*, PhD thesis, TU Dortmund, 2006, doi: 10.3204/DESY-THESIS-2006-027.
- [45] KAMI Collaboration, E. Cheu *et al.*, *An Expression of interest to detect and measure the direct CP violating decay $K_L \rightarrow \pi^0 \nu \bar{\nu}$ neutrino anti-neutrino and other rare decays at Fermilab using the main injector*, arXiv:hep-ex/9709026.
- [46] J. Flournoy, I. Berlman, B. Rickborn, and R. Harrison, *Substituted tetraphenylbutadienes as fast scintillator solutes*, Nucl. Instrum. Meth. **A351** (1994) 349.
- [47] I. Berlman *et al.*, *New fast organic scintillators using intramolecular bromine quenching*, Nucl. Instrum. Meth. **225** (1984) 78.
- [48] I. A. Berlman, *Handbook of Fluorescence Spectra of Aromatic Molecules*, Academic Press, New York and London, 2. ed., 1971.
- [49] C. D'Ambrosio *et al.*, *Organic scintillators with large stokes shifts dissolved in polystyrene*, Nucl. Instrum. Meth. **A307** (1991) 430 .
- [50] M. Deckenhoff, *Doctoral Thesis*, PhD thesis, TU Dortmund, 2014, to be completed 2014.
- [51] Saint Gobain Scintillating Fibres, 2014, as specified on the Saint Gobain web site: http://www.crystals.saint-gobain.com/Scintillating_Fiber.aspx.
- [52] Kuraray Plastic Scintillating Fibres, 2014, as specified on the Kuraray web site: <http://kuraraypsf.jp/psf/sf.html>.
- [53] Geant4 collaboration, S. Agostinelli *et al.*, *Geant4: a simulation toolkit*, Nucl. Instrum. Meth. **A506** (2003) 250.
- [54] Geant4 collaboration, J. Allison *et al.*, *Geant4 developments and applications*, IEEE Trans. Nucl. Sci. **53** (2006) 270.
- [55] M. Deckenhoff, *Signal Shape and Time of Light Propagation in Scintillating Fibre SCSF-78MJ from Kuraray*, Tech. Rep. LHCb-PUB-2014-016, CERN-LHCb-PUB-2014-016, LHCb-INT-2013-008, CERN, Geneva, Feb, 2013.
- [56] M. Deckenhoff, *Simulation of Scintillating Fibres in Geant4*, Tech. Rep. LHCb-PUB-2014-023, CERN-LHCb-PUB-2014-023, LHCb-INT-2014-009, CERN, Geneva, Jan, 2014.
- [57] C. Joram, *Technical specifications of the scintillating fibres*, LHCb-PUB-2014-019, CERN-LHCb-PUB-2014-019, LHCb-INT-2013-061.
- [58] C. Zorn, *A pedestrian's guide to radiation damage in plastic scintillators*, Nucl. Phys. B - Proc. Suppl. **32** (1993) 377.

- [59] S. Bruggisser, *Literature study on the radiation damage on KURARAY fibers*, <https://twiki.cern.ch/twiki/pub/LHCb/ScintFiber/FiberSummaryNew.pdf>, September, 2012.
- [60] C. Joram *et al.*, *Measurements and radiation tests on scintillating fibres for the LHCb SciFi project*, LHCb-PUB-2014-021, CERN-LHCb-PUB-2014-021, LHCb-INT-2013-002.
- [61] B. Leverington, C. Joram, and S. Baker, *Scintillating Fibre Irradiation with 22.9 MeV Protons*, Tech. Rep. LHCb-PUB-2014-024, CERN-LHCb-PUB-2014-024, LHCb-INT-2014-002, CERN, Geneva, Jan, 2014.
- [62] A. Dierlamm, *Irradiations in Karlsruhe*, 2010. Presentation at RD50 Workshop.
- [63] K. Hara *et al.*, *Radiation hardness and mechanical durability of kuraray optical fibers*, Nucl. Instrum. Meth. **A411** (1998) 31.
- [64] R. Brun and F. Rademakers, *Root - an object oriented data analysis framework*, Nucl. Instrum. Meth. **A389** (1997) 81.
- [65] Y. Musienko, *State of the art in SiPMs*, Talk given at Industry-academia matching event on SiPM and related technologies, CERN, Geneva, Feb. 2011, <http://indico.cern.ch/event/117424/>.
- [66] C. Joram and E. Gushchin, *Comparative Measurements of the Photon Detection Efficiency of KETEK SiPM Detectors for the LHCb SciFi Upgrade Project*, LHCb-PUB-2014-018, CERN-LHCb-PUB-2014-018, LHCb-INT-2013-062.
- [67] R. Greim *et al.*, *A New Measurement of the Cosmic-Ray Flux Below 5GV Rigidity with the PERDaix Detector*, in *Proceedings of the 20th ESA Symposium on European Rocket and Balloon Programmes and Related Research*, (Hyère, France), 2011.
- [68] A. Bay *et al.*, *Viability Assessment of a Scintillating Fibre Tracker for the LHCb Upgrade*, LHCb-PUB-2014-015, CERN-LHCb-PUB-2014-015, LHCb-INT-2013-004.
- [69] G. Haefeli and A. Gong, *LHCb VELO and ST clusterization on TELL1*, EDMS ID 690585, CERN, Geneva.
- [70] P. von Doetinchem *et al.*, *PEBS - Positron Electron Balloon Spectrometer*, Nucl. Instrum. Meth. **A581** (2007) 151.
- [71] N. P. Hessey and P. Werneke, *Choice of Korex core material for the next NIKHEF disc prototype*, NIKHEF Internal Note.
- [72] J. Nardulli and N. Tuning, *A Study of the Material in an Outer Tracker Module*, Tech. Rep. LHCb-2004-114. CERN-LHCb-2004-114, CERN, Geneva, Jan, 2005.

- [73] V. Fave, *Estimation of the material budget of the Inner Tracker*, Tech. Rep. LHCb-2008-054. CERN-LHCb-2008-054, CERN, Geneva, Oct, 2008.
- [74] C. Joram and T. Schneider, *Mirroring of fibre ends for the LHCb SciFi project*, LHCb-PUB-2014-020, CERN-LHCb-PUB-2014-020, LHCb-INT-2013-060.
- [75] E. Da Riva, *Final results of the project (SciFi Tracker cooling)*, EDMS ID 1343641, CERN, Geneva, 2014.
- [76] V. Vacek, M. Doubek, M. Erben *et al.*, *Summary of SiPM cooling tests in 2013*, https://twiki.cern.ch/twiki/pub/LHCb/SciFiDemoCooling/Summary_2013.pdf.
- [77] P. Moreira, *The GBT Project*, in *Proceedings of Topical Workshop on Electronics for Particle Physics*, 2009.
- [78] J. Troska *et al.*, *The Versatile Transceiver Proof of Concept*, in *Proceedings of TWEPP2009 (Topical Workshop on Electronics for Particle Physics)*, no. CERN-2009-006, (Paris, France), Sep, 2009.
- [79] F. Alessio and R. Jacobsson, *System Level Specifications of the Timing and Fast Control system of the LHCb Upgrade*, CERN-LHCb-PUB-2012-001.
- [80] A. Gabrielli *et al.*, *The GBT-SCA, a radiation tolerant ASIC for detector control applications in SLHC experiments*, in *Proceedings of Topical Workshop on Electronics for Particle Physics*, pp. 557 – 560, 2009.
- [81] F. Vasey, *Versatile Link Specification Part 2.1 Front-end Versatile Transceiver and Twin Transmitter*, EDMS ID 1140665 v1, CERN, Geneva.
- [82] O. Callot, *Acceptable noise rate in the SiPM of the Fibre Tracker*, LHCb-PUB-2014-017, CERN-LHCb-PUB-2014-017, LHCb-INT-2012-033.
- [83] A. Comerma, *Development of a multichannel integrated circuit for Silicon Photo-Multiplier arrays readout*, PhD thesis, Universitat de Barcelona, 2014.
- [84] S. Giani *et al.*, *Digitisation of SiPM signals for the LHCb Upgrade SciFi tracker*, LHCb-PUB-2014-025, CERN-LHCb-PUB-2014-025, LHCb-INT-2013-065.
- [85] G. Haefeli, *Contribution to the development of the acquisition electronics for the LHCb experiment*, PhD thesis, EPFL, 2004, CERN-THESIS-2004-036.
- [86] Arria GX Device Handbook, Volume 1, available from Altera web site, http://www.altera.com/literature/hb/agx/agx_5v1.pdf.
- [87] ProASIC3 Flash Family FPGAs Datasheet, available from Actel web site, http://www.actel.com/documents/PA3_DS.pdf.

- [88] *Mini-review OT FE electronics architecture*, March, 2013.
<https://indico.cern.ch/conferenceDisplay.py?confId=239292>.
- [89] IGLOO2 FPGAs datasheet, available from Microsemi web site,
http://www.microsemi.com/document-portal/doc_download/132042-igloo2-fpga-datasheet.
- [90] A. Pellegrino, *Low- and High-Voltage Systems of the LHCb Outer Tracker*, EDMS ID 938077, CERN, Geneva.
- [91] F. Faccio *et al.*, *Development of custom radiation-tolerant dc/dc converter asics*, JINST **5** (2010) C11016.
- [92] A. Pellegrino and H. Schuijlenburg, *Supply of Support Frames for the LHCb Outer Tracker Detector Modules*, January, 2006. CERN-LHCb-2005-026.
- [93] A. Pellegrino and H. Schuijlenburg, *Supply of Support Structure for the LHCb Outer Tracker - Upper Part*, EDMS ID 701347, CERN, Geneva, Nov, 2005.
- [94] A. Pellegrino and H. Schuijlenburg, *Supply of Support Structure for the LHCb Outer Tracker - Lower Part*, EDMS ID 696884, CERN, Geneva, Jan, 2006.
- [95] P. Gorbounov, E. Thomas, and E. Da Riva, *Requirements and design considerations for a SiPM cooling system of the SciFi Tracker*, CERN-LHCb-INT-2014-004. In preparation.
- [96] 3MTM Company, *3MTM NovecTM 649 Engineering Fluid, Product Information; Environmental properties of Novec 1230 Fluid, Technical Brief* and references therein (the 649 and 1230 are different commercial names of the same fluid),
http://solutions.3m.com/wps/portal/3M/en_US/3MNovec.
- [97] D. Gasser, *COOLING SYSTEMS FOR THE LHCb DETECTOR AND ITS INFRASTRUCTURE*, EDMS ID 480222, CERN, Geneva.
- [98] P. Guglielmini, *LHCb Outer Tracker cooling plant user manual*, EDMS ID 4861678, CERN, Geneva.
- [99] L. del Buono *et al.*, *Geometry of the Scintillating Fiber detector*, CERN-LHCb-PUB-2014-005.
- [100] E. Cogneras *et al.*, *The digitisation of the scintillating fibre detector*, CERN-LHCb-PUB-2014-003.
- [101] M. Gupta, *Calculation of radiation length in materials*, tech. rep., CERN-PH-EP, 2010, PH-EP-Tech-Note-2010-013.
- [102] M. Deckenhoff, PhD thesis, Technische Universität Dortmund, 2014, in preparation.

- [103] Safety Instruction IS41, Rev.1, *The use of plastic and other non-metallic materials at CERN with respect to fire safety and radiation resistance*, EDMS ID 335806, CERN, Geneva, Nov, 2005.
- [104] LHCb collaboration, Y. Amhis *et al.*, *Description and performance studies of the Forward Tracking algorithm for a scintillating fibre detector at LHCb*, LHCb-PUB-2014-001.
- [105] Y. Amhis *et al.*, *The Seeding tracking algorithm for a scintillating fibre detector at LHCb*, LHCb-PUB-2014-002.
- [106] P. Gandini *et al.*, *Adding UT hits to long tracks for the LHCb Upgrade*, LHCb-PUB-2014-004.
- [107] A. Davis *et al.*, *Downstream tracking for the LHCb Upgrade*, LHCb-PUB-2014-007.
- [108] E. Bowen *et al.*, *VeloUT tracking for the LHCb Upgrade*, LHCb-PUB-2013-023.